Nonlinear dynamics and control analysis of combustion instabilities based on the "Flame Describing Function" (FDF)

Frédéric Boudy

École Centrale Paris

THÈSE

présentée par

Frédéric BOUDY

pour l'obtention du

GRADE de DOCTEUR

Formation doctorale : Énergétique

Laboratoire d'accueil : Laboratoire d'Énergétique Moléculaire et Macroscopique, Combustion (EM2C) du CNRS et de l'ECP

Analyse de la dynamique non-linéaire et du contrôle des instabilités de combustion fondée sur la "Flame Describing Function" (FDF)

Soutenue le 21 décembre 2012

Directeur de thèse : Sébastien CANDEL
Codirecteur de thèse : Daniel DUROX
Co-encadrant de thèse : Thierry SCHULLER

Jury :

Mme	Françoise	BAILLOT	Professeure des Universités, Rouen	Présidente
MM.	Franck	NICOUD	Professeur des Universités, Montpellier	Rapporteur
	Thierry	POINSOT	DR CNRS, Toulouse	Rapporteur
	Sébastien	CANDEL	Professeur des Universités, Châtenay-Malabry	Examinateur
	Daniel	DUROX	IR CNRS, Châtenay-Malabry	Examinateur
	Philippe	LAFON	Ingénieur EDF, Clamart	Examinateur
	Nicolas	NOIRAY	Ingénieur Alstom Power, Baden, Suisse	Invité
	Thierry	SCHULLER	Professeur ECP, Châtenay-Malabry	Invité

École Centrale des Arts et Manufactures
Grand Établissement sous tutelle
du Ministère de l'Éducation Nationale
Grande Voie des Vignes
92295 Châtenay-Malabry Cedex
Tél : 33 (1) 41 13 10 00
Télex : 634 991 F EC PARIS

Laboratoire d'Énergétique Moléculaire et Macroscopique, Combustion (E.M2.C.)
UPR 288, CNRS et École Centrale Paris
Tél : 33 (1) 41 13 10 31
Fax : 33 (1) 47 02 80 35

2012ECAP0056

Remerciements

Pour commencer, je tiens à exprimer mes plus profonds remerciements à mes encadrants qui m'ont accompagné au cours de ces quatre années. Merci tout d'abord à Sébastien Candel pour m'avoir offert l'opportunité de travailler sur ce sujet qui ne m'est pas sans intérêt. Ses conseils ont toujours été très pertinents tout au long de ma thèse et malgré sa charge de travail, il a toujours su rester disponible, même par courriel tard le soir lorsque nous échangions des travaux à finaliser. Ses lectures et corrections de mes écrits ont toujours été constructives et enrichissantes. De même, son optimisme et ses conseils très aimables m'ont toujours guidé et appris à ne pas me fixer uniquement sur les détails qui ne convenaient pas. Mes pensées vont ensuite vers Daniel Durox que je remercie aussi énormément pour toute son aide et ses conseils durant les expériences. Ses astuces et ses connaissances ont toujours été fort utiles. Les manips, mais aussi les moments passés à côté de la thèse furent toujours très sympathiques. Je citerai notamment la fête de la science où je l'ai aidé pendant deux années consécutives. Cela restera toujours un excellent souvenir. Enfin, je tiens également à remercier Thierry Schuller qui a suivi mes travaux de thèse et pour toute son aide sur la partie théorique. Les discussions le soir dans le bureau ou dans sa salle de réunion m'ont également bien guidé dans la modélisation de certains phénomènes. Je garderai un très bon souvenir de cet encadrement, des connaissances que j'ai pu acquérir et également des nombreuses conférences et présentations auxquelles nous avons pu participer.

Je suis également très reconnaissant envers tous les membres du jury qui ont participé à l'évaluation de cette thèse. Merci à Thierry Poinsot et Franck Nicoud d'avoir été rapporteurs et d'avoir examiné avec tant d'attention mon travail. Je remercie également Françoise Baillot. Je suis très heureux de l'avoir eu comme examinatrice et présidente de jury. J'adresse aussi mes remerciements à Philippe Lafon pour avoir analysé mon travail avec intérêt. Je souhaite également remercier mon dernier examinateur, Nicolas Noiray, qui connaît très bien l'expérience sur laquelle j'ai travaillé, étant donné qu'il a effectué sa thèse dessus les années précédant mon arrivée à l'EM2C. L'avoir eu comme examinateur a été une occasion particulière et très intéressante pour moi.

Je remercie aussi mon laboratoire d'accueil, l'EM2C ainsi que le CNRS sans qui il n'aurait pas été possible d'accomplir tout ce travail. L'aide financière grâce au Septième Programme de la Communauté Européenne (FP7/2007-2013), dans le cadre du projet KIAI, a permis de réaliser la partie expérimentale de l'étude et a été très appréciable. Merci aussi à l'École Centrale Paris pour tous les moyens qu'elle a pu me fournir. Plus particulièrement, Géraldine Carbonel et Catherine Lhopital qui m'ont toujours apporté l'aide nécessaire au niveau de l'École Doctorale, notamment sur la fin lors du dépôt de la thèse, où le temps passe toujours trop vite.

Un grand merci aussi à tous les chercheurs que j'ai côtoyé et avec qui j'ai pu avoir des discussions scientifiques toujours intéressantes et plus spécialement, Franck Richecoeur et Marc Massot avec qui les instabilités sont toujours un sujet de réflexion passionnant et instructif. Je remercie aussi l'équipe de course du dimanche (et de la semaine), Deanna, Anne, Jean-Michel, Nicolas, Laetitia et Patrick qui ont participé à mon accueil lorsque je suis arrivé au laboratoire en 2008 et avec qui il était toujours agréable de parler ou travailler. Merci aussi à tous les thésards et postdocs que j'ai rencontré durant toutes ces années et qui ont fait que l'ambiance de travail est toujours sympathique. Plus spécialement j'adresse une pensée à tous mes collègues de bureau, et notamment Théo (arrivé en thèse le même jour que moi), Max, Paul, Tapish, Gaofeng (qui restait travailler aussi tard que moi), mais aussi Béné (toujours motivée et joyeuse), Alessandro (les discussions sur les "damper" ou encore les TD méca flu.), Raph, Antoine, Wenjie et PEB qui m'ont vu "garder" le bureau pendant la rédaction. Je n'oublie pas non plus Grunde Jomaas qui était en postdoc lorsque je suis arrivé et qui m'a aidé a réaliser mes premières manips, mais aussi Layal, François, Aymeric et Alexis avec qui il était souvent question de parler d'instabilités. Je ne peux pas non plus passer à côté de l'équipe des TD de mécanique des fluides qui ont rythmé mes années de thèse durant les mois de février et mars lorsque j'étais moniteur. La préparation deux fois par semaine, mais aussi les corrections de copies, étaient toujours des moments très prenants mais plus agréables lorsque l'on n'est pas seul.

Un merci très spécial aussi à tous mes amis d'ici et d'avant qui m'ont accompagné durant cette thèse lorsque nous arrivions à nous voir et que je ne restais pas concentré sur mes calculs. Leur contact a toujours su égayer ce travail parfois difficile.

Enfin, je tiens à remercier toute ma famille qui m'a toujours soutenu dans ce projet alors qu'ils ne me voyaient pas souvent, et bien évidemment Carole qui, même si elle connaît le vécu d'une thèse, m'a accompagné jusqu'à la fin et su m'arrêter quand je devais faire une pause.

Résumé

Analyse de la dynamique non-linéaire et du contrôle des instabilités de combustion fondée sur la "Flame Describing Function" (FDF)

Cette thèse de doctorat se concentre sur l'étude des instabilités de combustion dans un brûleur prémélangé. Le sujet des instabilités est étudié depuis de nombreuses années mais nécessite des développements constants en fonction notamment des progrès réalisés dans les technologies utilisées pour la propulsion ou pour la production d'énergie. Les instabilités sont généralement issues d'un couplage entre la combustion et les modes propres du système. La mise en résonance qui en résulte peut avoir des conséquences qui sont souvent dommageables, entraînant des vibrations, une fatigue des matériaux soumis à des charges acoustiques élevées et une intensification des flux de chaleur vers les parois de la chambre. Un premier objectif de cette thèse est de poursuivre le développement de méthodes de prévision des instabilités et des phénomènes non-linéaires qui en résultent comme par exemple le développement de cycles limites, les processus de déclenchement ("triggering"), la commutation de modes. Il s'agit à cet effet de comprendre les mécanismes physiques et de développer des méthodes analytiques de prévision. Le cadre général adopté est celui de l'"équivalent harmonique" bien connu dans le domaine du contrôle et qui a été exploré dans le domaine des instabilités de combustion dans des travaux récents du laboratoire EM2C. Par le biais de ce concept il est possible de tenir compte de l'évolution de la réponse de la flamme suivant l'amplitude à laquelle elle est soumise. Cette réponse de flamme en fréquence et amplitude généralise la notion de fonction de transfert et elle est désignée sous le nom de "Flame Describing Function" (FDF). On poursuit ici le développement des méthodes fondées sur la FDF. Le système envisagé est générique puisqu'il comporte sous une forme idéalisée tous les éléments que l'on trouve dans des configurations réelles : un conduit d'alimentation qui fournit un prémélange de méthane et d'air, un système d'injection multipoint composé d'une plaque perforée qui permet d'accrocher une collection de petites flammes coniques et un tube à flamme en quartz qui confine la zone de combustion. Le système est ouvert à son extrémité aval. Cette géométrie permet de simplifier l'analyse et d'obtenir une large gamme de configurations au moyen d'une variation con-

tinue de la longueur du conduit d'alimentation qui est limité en amont par un piston. On peut aussi échanger le tube à flamme et utiliser des longueurs différentes de cet élément. Une comparaison systématique entre des calculs théoriques et des expériences bien contrôlées est effectuée. Suivant la géométrie le système présente une très grande richesse de modes instables. Une étude exhaustive est réalisée pour répertorier les oscillations observées et déduire leurs propriétés. On utilise à cet effet les outils de la dynamique des systèmes. On montre que les cycles limites qui possèdent une amplitude constante sont bien décrits par la méthode unifiée fondée sur la FDF. Pour certaines configurations l'expérience fait apparaître des cycles limites dont l'amplitude et la fréquence ne se stabilisent pas au cours du temps. On observe notamment des oscillations plus complexes couplées par plusieurs modes pouvant soit donner lieu à des variations régulières ou à des fluctuations plus irrégulières avec un caractère "galopant" dans le temps. Pour ces oscillations particulières, la FDF fournit des indications sur les domaines d'apparition mais n'est pas en mesure de décrire complètement ces cycles limites complexes. Il faut dans ce cas recourir à une représentation temporelle qui n'est pas développée dans ce document. La base de données expérimentales pourra être utilisée pour guider ultérieurement ce type d'analyse. Le deuxième grand objectif de cette thèse est de rechercher des méthodes de contrôle des instabilités. On considère plus particulièrement des systèmes dynamiques utilisant des plaques perforées polarisées par un écoulement (BFP : "bias flow perforate"). Ces systèmes sont particulièrement intéressants pour atténuer les oscillations basse fréquence qui sont difficiles à réduire par des systèmes passifs. La conception de ces BFPs est fondée sur des travaux récents menés au laboratoire EM2C avec notamment l'objectif de robustesse, c'est-à-dire la possibilité de couvrir une large bande de fréquences. L'étude expérimentale et les calculs fondés sur la FDF menés en parallèle permettent de voir les possibilités de tels systèmes et de comprendre les conditions nécessaires à leur efficacité. Cette étude peut permettre de guider les applications qui pourraient être envisagées en pratique.

Mots-clés : instabilités de combustion, couplage thermoacoustique, cycles limites, régime non-linéaire, fréquences multiples, méthode de l'équivalent harmonique, contrôle des instabilités, plaques perforées polarisées.

Abstract

Nonlinear dynamics and control analysis of combustion instabilities based on the "Flame Describing Function" (FDF)

This doctoral thesis is concerned with an investigation of combustion instabilities in premixed combustors. This problem has been the subject of a continuous effort in relation with the many issues encountered in practical systems like those used in propulsion and energy production. Combustion instabilities usually arise from the coupling between combustion and acoustic eigenmodes of the system. In most cases such resonances lead to vibrations, structural fatigue and intensified heat fluxes to the chamber walls. The first part of this thesis pursues the development of prediction methods for combustion instabilities and the associated nonlinear phenomena such as limit cycles establishment, triggering, mode switching and hysteresis. The aim is to delineate physical mechanisms and develop analytical methods dedicated to prediction. The theoretical framework relies on the "harmonic balance" formalism well known in the domain of control and which has been adopted more recently in combustion instability studies carried out at EM2C, CNRS laboratory. Through this concept, it is possible to take into account the evolution of the flame response as a function of amplitude. This flame response, depending on frequency and amplitude, extends the flame transfer function principle and is designated as the "Flame Describing Function" (FDF). The development of the FDF framework is pursued in the present study. The experimental setup which exemplifies combustion instabilities and serves to validate the method has generic features as it comprises in an idealized version, all the parts found in practical systems : a feeding manifold delivering a mixture of methane and air, a multipoint injector made of a perforated plate anchoring a collection of small laminar conical flames and a flame tube made of quartz which confines the combustion zone. The downstream boundary of the system is open. This device allows a simplified analysis and provides a wide variety of configurations through the continuous modification of the feeding manifold length which is bounded by a piston on the upstream and through changes of the flame tube lengths. Systematic comparison between theoretical results and well controlled experiments is undertaken. Depending on the geometry, the setup exhibits a large variety

of unstable modes which are classified in terms of their limit cycle behavior using tools from dynamical system theory. It is shown that limit cycles with constant amplitude are well predicted by the unified FDF methodology. For some configurations, the experiment reveals limit cycles characterized by time variable amplitude and frequency. One finds situations where the oscillation is coupled by multiple modes leading either to regular amplitude variations or more irregular evolutions with a "galloping" pattern as a function of time. For this special type of limit cycle, the FDF indicates the range of the onset, but is not able to fully describe these complex limit cycles. These oscillations require a time domain state space analysis which is not addressed in this manuscript. The experimental database may be of value for further work in this direction. The second part of this thesis deals with control methods for instabilities. One specifically considers damping systems relying on perforated plates biased by a flow (BFP : "Bias Flow Perforate"). These systems are particularly interesting because they can be used to cancel low frequency oscillations which are otherwise difficult to reduce through passive control methods. This BFP design relies on recent work carried out at EM2C, CNRS laboratory which extends the frequency range where the system is effective. The experimental study and the associated FDF calculations are used to delineate the possibilities of such systems and uncover conditions required for an effective damping of oscillations. This study provides indications on the practical application of BFPs.

Keywords : combustion instabilities, thermoacoustic coupling, limit cycles, nonlinear regime, multiple frequencies, Describing Function, Flame Describing Function, control of instabilities, bias flow perforated screens.

Contents

List of Tables

List of Figures

Nomenclature

Latin symbols

$\mathcal{A}$	Surface area of one of the N flames	L^2
$\mathcal{F}$	Flame transfer function or describing function	
$\mathcal{P}$	Flame holder porosity	
$\boldsymbol{M}$	Matrix of the system (Model)	
$\boldsymbol{X}$	Vector of amplitudes of the waves	
A_c^+	Wave amplitude in the back cavity traveling in the $+z$ direction	
A_c^-	Wave amplitude in the back cavity traveling in the $-z$ direction	
A_n^+	Wave amplitude in the n-th tube traveling in the $+z$ direction	
A_n^-	Wave amplitude in the n-th tube traveling in the $-z$ direction	
a_0	Amplitude of vanishing growth rate (Case of 2 simultaneous modes)	
c	Speed of sound	LT^{-1}
C_{xy}	Coherence factor between the signals x and y	
c_p	Specific heat at constant pressure	$\mathrm{L}^2\mathrm{T}^{-2}\Theta^{-1}$
d	Square mesh of the damper	L
dB	Decibel	
D_1	Feeding manifold diameter	L
D_2	Confinement tube diameter	L
d_a	Holes diameter of the damper	L
d_e	Embedding dimension (Phase space representation)	
d_p	Holes diameter of the flame holder	L
E	Volumetric gas expansion ratio	
f	Frequency	T^{-1}
f_s	Sampling frequency	T^{-1}
f_1	Frequency of the first mode	T^{-1}
f_2	Frequency of the second mode	T^{-1}

f_3	Frequency of the third mode	T^{-1}
G	Gain of the flame response	
h	Pinching point altitude	L
H_{xy}	Transfer function between the signals of microphones x and y	
i	Imaginary unit ($i^2 = -1$)	
I_{OH^*}	Light intensity of OH^* radical	V
I_1	Modified Bessel function of the first kind	
k	Wave number	L^{-1}
K_R	Rayleigh conductivity	L
K_1	Modified Bessel function of the second kind	
k_{He}	Wave number of a Helmholtz resonator back cavity	L^{-1}
L	Unconfined burner size	L
l	Thickness of the flame holder	L
L_c	Back cavity length	L
L_1	Feeding manifold length	L
L_2	Confinement tube length	L
L_{1m}	Distance of microphone M_1	L
L_{2m}	Distance of microphone M_2	L
lb_f	Pound-force	MLT^{-2}
l_ν	Acoustic boundary layer thickness	L
$\dot{m}$	Mass flow rate	MT^{-1}
M_i	i-th microphone	
M_{spl}	Reference pressure microphone (Reflection coefficient measurement)	
N	Number of holes of the flame holder	
n	Amplification factor	
P	Power	W
p	Pressure	$\mathrm{ML}^{-1}\mathrm{T}^{-2}$
Q	Heat release	$\mathrm{ML}^2\mathrm{T}^{-2}$
q	Volumetric flow rate	$\mathrm{L}^3\mathrm{T}^{-1}$
R	Radius of the flame holder	L
r	Specific gas constant	$\mathrm{JM}^{-1}\Theta^{-1}$
R_c	Reflection coefficient in the back cavity	
R_n	Reflection coefficient in the n-th tube	
R_1	Radius of the feeding manifold	L
R_2	Radius of the confinement tube	L
r_a	Holes radius of the damper	L
r_p	Holes radius of the flame holder	L
S_L	Laminar burning velocity	LT^{-1}
S_p	Cross-sectional surface area of each hole of the flame holder	L^2

S_{xy}	Cross power spectral density between the signals of microphones x and y	
S_1	Cross-sectional surface area of the feeding manifold	L^2
S_2	Cross-sectional surface area of the confinement tube	L^2
S_{2p}	Cross-sectional surface area of the perforated plate (Flame holder)	L^2
S_{2r}	Cross-sectional surface area of the ring cavity	L^2
t	Time	T
T_f	Adiabatic flame temperature	Θ
T_r	Ring cavity temperature	Θ
T_1	Feeding manifold temperature	Θ
T_2	Confinement tube temperature	Θ
U	Velocity	LT^{-1}
u	Velocity	LT^{-1}
U_b	Bulk velocity	LT^{-1}
u_{cv}	Vortex convection velocity	LT^{-1}
V_n	n-th eigenvector	
z	Longitudinal coordinate	L
Z_n	Acoustic impedance in the n-th tube	$\mathrm{ML}^{-2}\mathrm{T}^{-1}$

Greek Symbols

α	Collective effect coefficient	
α	Damping rate	T^{-1}
Δ	Shoulder length supporting the confinement tube	L
δ	End correction	L
γ	Heat capacity ratio	
λ	Wavelength	L
λ_n	n-th eigenvalue	
ν	Kinematic viscosity	$\mathrm{L}^2\mathrm{T}^{-1}$
ω	Complex angular frequency	T^{-1}
ω_i	Growth rate	T^{-1}
ω_r	Real part of the complex angular frequency	$\mathrm{rad}\,\mathrm{T}^{-1}$
ϕ	Equivalence ratio	
φ	Phase of the flame response	rad
ϕ_n	Phase of the reflection coefficient in the n-th tube	rad
ρ	Density	ML^{-3}
σ_d	Damper porosity	
τ	Time delay	T

τ	Optimal time delay (Phase space representation)	T
Ξ	Acoustic coupling index	
ζ_n	Specific acoustic impedance in the n-th tube	

Dimensionless numbers

He	Helmholtz number	kL
$\mathrm{M_c}$	Mach number	u/c
Q	Resonance parameter	$(k/k_{\mathrm{He}})^2$
St	Strouhal number	$\omega r/u$

Subscript symbols

c	Back cavity
i	Imaginary part
$mean$	Mean value
n	Index of the cavity considered
p	Perforated plate (flame holder)
r	Real part
r	Ring cavity
rms	Root mean square
u	Unburned reactants

Superscript symbols

$\bar{}$	Mean value
$\dot{}$	Time derivative
$\sim$	Complex number (e.g. $\widetilde{a} = b\,e^{ic}$)
’	Fluctuating component

Operators

$\Re$	Real part
$\lvert\ \rvert$	Absolute value (or modulus)

Initials and acronyms

B-BH	B-Damper with Big Holes ($r_a = 2$ mm)
B-SH	B-Damper with Small Holes ($r_a = 0.5$ mm)
BFP	Bias Flow Perforates
DF	Describing Function
FDF	Flame Describing Function
FTF	Flame Transfer Function
GLC	Galloping Limit Cycle

ITHACA	Impedance Test bench at High ACoustic Amplitudes
LDV	Laser Doppler Velocimetry
LUM	Linearly Unstable Mode
MIC	Multiple Injection Combustor
NLUM	NonLinearly Unstable Mode
PM	PhotoMultiplier
PSD	Power Spectral Density
SPL	Sound Pressure Level
TF	Transfer Function
TMLC	Two Modes Limit Cycle
URANS	Unsteady Reynolds-Averaged Navier–Stokes

Introduction

Flame modeling constitutes a key element in combustion instability analysis. This issue is considered in the present thesis which is specifically focused on the development of suitable representations of the flame dynamics and their application in the analysis of instabilities in a generic configuration. One objective is to devise a prediction tool which could be used to define regions of instability, obtain instability characteristics, estimate limit cycle amplitudes and interpret the many nonlinear features which are manifested in practical systems such as mode switching, nonlinear triggering, frequency shifting. A second objective is to explore the possible suppression or reduction of instabilities which could be achieved with a special type of damper relying on bias flow perforates (BFP) backed by a cavity. These systems have interesting low frequency characteristics and have potential for practical applications. It is however necessary to see if dampers based on these principles can be effectively used. To reach these two objectives we combine experimentation with analysis and modeling and try to establish a dialog between theory and experiments. This can be achieved by making use of a well controlled generic configuration which represents in an idealized fashion the complex geometries found in practice which two examples are shown in Fig. 1.

The experimental system comprises the essential elements found in typical combustion installations but allows in addition variations of the geometrical dimensions, a feature which is extremely useful if one wishes to understand what is generally being observed for a fixed geometry. The resemblance between the experimental system and an aero-engine combustor is illustrated in Fig. 2 by placing side by side the Pratt & Whitney JT9D and the generic configuration of the present study. It is possible to see that the generic burner, shown on the right of this figure, involves the three main elements found in jet engines, i.e. a feeding manifold (1), an injector and combustion zone (2) and a flame tube (3). Jet engine combustors sometimes feature an annular cavity (2b) surrounding the flame, which changes the flame plane position in the exhaust tube. This is also found in the multiple flame combustor due to the thickness of the perforated plate, as shown in Fig. 2. A last part concerns the annular cavity surrounding the flame tube. This element can be seen in

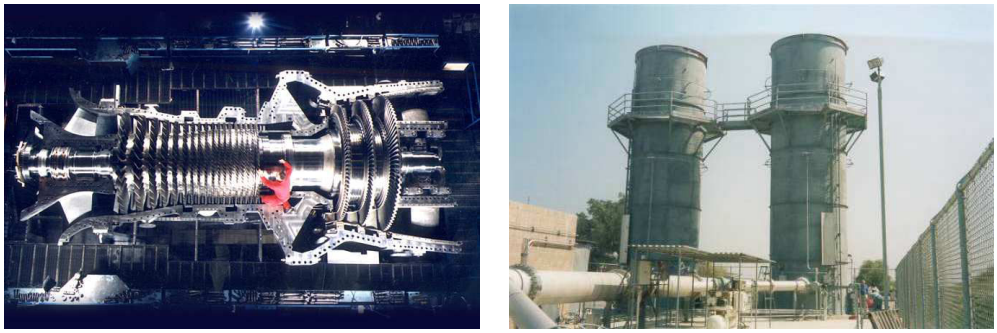

(a) (b)

Figure 1: *Typical combustion systems used in industry. (a) : 9FA model of the heavy duty gas turbines series from General Electric (GE). (b) : Flare station used to burn landfill gas. At 50 % of its maximum capacity, the system experienced a low frequency rumbling, from Pun (2001).*

the JT9D combustor appearing on the left of Fig. 2, but is not present in the model scale system used in the present study. Effects of the restriction for the cross section area, accelerating the flow at the combustor outlet of practical systems, are also not considered in the present thesis.

The thesis is a logical continuation of a work initiated by Noiray (2007); Noiray et al. (2008). It pursues the development of the flame describing function (FDF) framework explored in these previous studies. The FDF is used in what follows as the central tool for the description of the flame nonlinear dynamics.

At this point it is worth examining the state of the art in the field of combustion instability. An exhaustive review will not be attempted because the subject is already covered in many papers, for example in Candel (2002), in the book of Poinsot et al. (2012) or in a recent collection of papers edited by Lieuwen et al. (2005). We only give some historical highlights and consider more specifically work dealing with the flame dynamics and with the influence of oscillation amplitude on the flame response.

General background

The problem of combustion instability has been encountered in many combustion systems and more specifically in high performance devices. This is illustrated in Fig. 3 which exhibits different systems which underwent important failures due to combustion oscillations. Instability issues were identified during the early development of liquid rocket engines (see Crocco (1951)). It was rapidly found that there are many different types of oscillations in such systems. In this variety one may distinguish three main classes (Barrere et al. (1969)) :

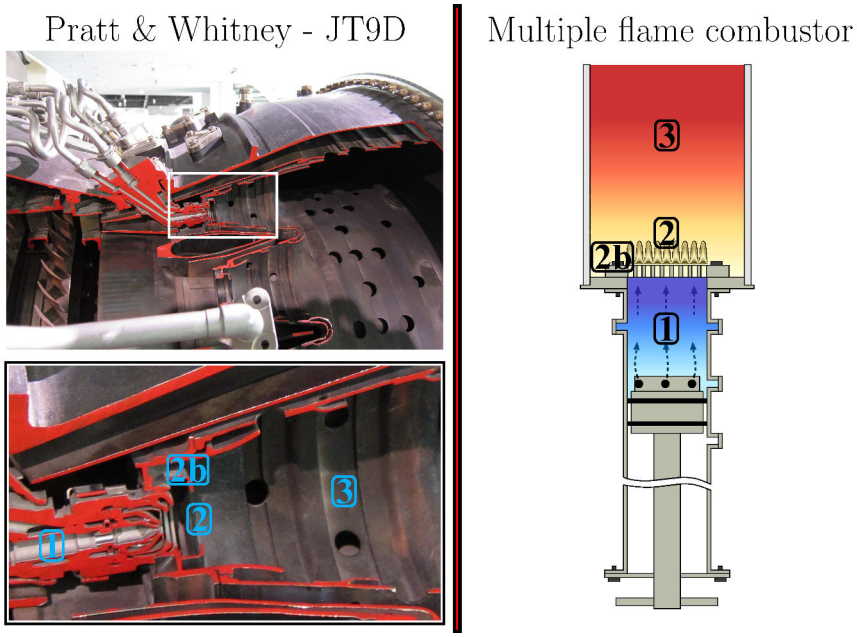

Figure 2: *Pratt & Whitney JT9D's jet engine combustor and the generic burner of the present study. The two configurations share the same essential components, i.e. a feeding manifold (1), a combustion zone (2) and a flame tube (3). The annular cavity (2b) surrounding the flame and changing its plane position in the exhaust tube is sometimes found in aero-engine combustors.*

- Chamber instabilities which essentially affect the combustion chamber are coupled by acoustic longitudinal or transverse modes. These instabilities generally occur in the high frequency range and the associated wavelength is smaller than the typical transverse dimension of the chamber $\lambda < D$;

- System instabilities which involve the various components in the combustion configuration including upstream manifold, chamber and exhaust duct. These instabilities are usually coupled by longitudinal modes, the wavelength is larger than the typical transverse dimension of the system $\lambda > D$ and they feature lower frequencies ;

- Instrinsic instabilities which correspond to motions induced by the flame in its own field like the Darrieus-Landau or the thermo-diffusive instabilities.

We focus in the present study on system instabilities and use to this purpose a configuration which comprises three components and typifies what is found in many practical devices.

Prediction of combustion instabilities has been a major issue for many decades (Candel (2002)). The problem has been tackled in various ways but it is possible to identify three broad classes of methods :

- Methods based on a modal expansion, used extensively in the rocket engine field, rely on a Galerkin projections on the eigenmodes of the system. This approach was developed in the 1970's (B. Zinn et al. (1971); F. Culick (1994)) and has mainly focused on the nonlinearity introduced by gas dynamics. One obtains a coupled set of nonlinear differential equations for the modal amplitudes and one can examine in this way the evolution of the system and the dynamics of the various modes. Culick has extensively contributed to the analysis of limit cycles using the modal expansion technique.

- Methods based on a frequency domain analysis. The acoustics of the system are described by a network analysis or by full Helmholtz solver calculations and the combustion response is represented by various models. This framework has been used in the rocket engine field by representing the combustion process with the so-called sensitive time lag model, also designated as the $n-\tau$ model. The more recent applications to aero-engines and gas turbines have focused on the combustion process unsteady response (Candel et al. (1996)) as the key mechanism and much effort has been expanded to document the flame response in terms of flame transfer functions (FTF) and characterize the flame unsteady behavior as a function of amplitude. It is known that com-

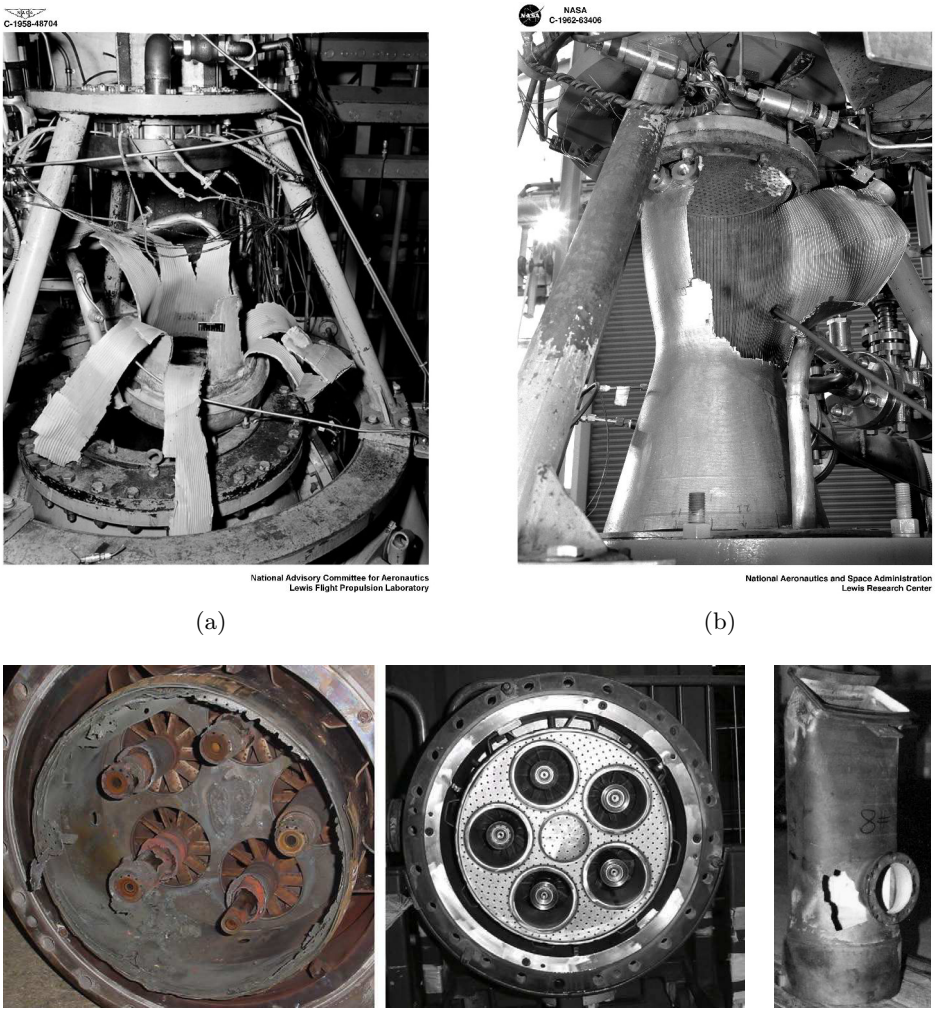

(a) (b)

(c) (d)

Figure 3: *Combustion systems which underwent important failures due to combustion oscillations. (a) and (b) : Rocket engines from NASA at Lewis research center (now Glenn research center, Cleveland). (a) is damaged by explosion on start, while (b) shows an engine producing 20000 lb_f of thrust shattered by blowout. (c) : Gas turbine combustor damaged after 6 months on the right and new burner assembly on the left, from Huang et al. (2009). (d) : A gas turbine transition piece destroyed by high thermal stresses and combustion driven oscillations, from Lieuwen et al. (2003).*

bustion instabilities also designated as "thermoacoustic instabilities" induce relative pressure oscillations p'/p_{mean} which are generally less than 10 %, whereas the velocity fluctuations u' may be of the order of the mean flow velocity $\bar{u}$. These velocity fluctuations induce heat release rate fluctuations which are such that the total reaction rate cannot become negative. This already induces a nonlinearity in the combustion response which corresponds to a saturation in amplitude of the heat release fluctuations. There are many other causes of nonlinearity and it is important to take them into account in the analysis of combustion instabilities. This point was made for example in Poinsot et al. (1989) where the study was aimed at the active control of combustion instabilities. Using the controller it was possible to obtain a stable regime and switch-off the driver unit to observe the oscillation growth from a stable operation. This indicated that the heat release rate fluctuation could be made to vanish during the unsteady motion but that the fluctuation in heat release rate were saturated leading to a limit cycle. It was concluded that the nonlinear effects are mainly caused by reacting flow processes and that the link to acoustic nonlinearity was less probable. Flame nonlinearities were studied independently by Lang (1991) in another multiple flame combustor controlled by a loudspeaker. It was found that harmonic frequencies arise when the oscillation amplitude increased indicating that energy is transferred to harmonics leading to a well defined limit cycle. The nonlinear flame response is known to play a key role in the triggering of oscillations in rocket engines but it was difficult to explain this phenomenon in terms of nonlinear gas dynamics (Wicker et al. (1996); Ananthkrishnan et al. (2005)). One possible extension of the frequency domain approach is offered by methods based on the harmonic balance approximation also designated as the describing function. These methods are used in the present work and related studies are reviewed in what follows.

- Methods based on numerical simulations. The simulation of combustion instabilities has been a long term goal in this field but the new developments in large eddy simulation have allowed considerable progress in this direction. There are many conditions to fulfill to devise methods which can be used in high fidelity simulations of combustion instabilities. It is in particular necessary to rely on tools which can be used to represent the flame motion and associated unsteady rate of heat release (Kaufmann et al. (2002); Giauque et al. (2005); Sensiau et al. (2009); Roux et al. (2009); Duchaine et al. (2011); Tay-Wo-Chong et al. (2010); Tay-Wo-Chong et al. (2011); Tay-Wo-Chong et al. (2012)) and acoustic field (Boudier et al. (2009); Gullaud et al. (2009)). Examples of this approach can be found in the recent literature (Selle et al. (2006); Wolf et al. (2012); Franzelli et al. (2012); Poinsot et al. (2012)).

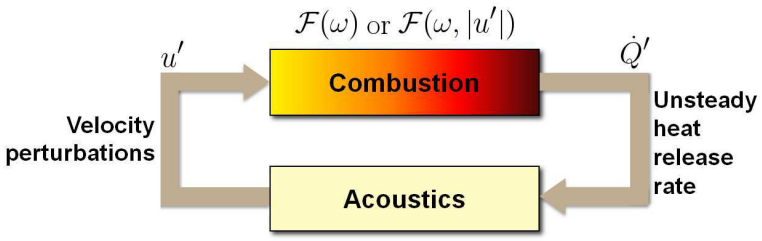

Figure 4: *Feedback loop representing the interaction of the flame with the acoustics of the system. The combustion response is either described by a Transfer Function ($\mathcal{F}(\omega)$) or a Describing Function ($\mathcal{F}(\omega, |u'|)$). The FTF or FDF are combined with an acoustic network representation of the wave motion in the system.*

The second approach is used in the present investigation which relies on the FDF concept in combination with an acoustic network description of the wave motion in the system. It is therefore logical to examine the literature dealing with the flame response in terms of transfer function (TF) and describing function (DF). This is done in the next section.

Flame transfer functions and describing functions

Under self-sustained combustion oscillations, the flame is subjected to velocity fluctuations and one can consider the interaction of the combustion process with the acoustics of the system as shown in Fig. 4. Thus, in many situations it is important to look at the flame response to harmonic oscillations in a broad range of frequencies. It is then natural to define a transfer function (the FTF) determined by taking the ratio of the fundamental normalized component of heat release rate fluctuations ($\widetilde{\dot{Q}}/\overline{\dot{Q}}$) to the fundamental normalized component of velocity fluctuations ($u'/\bar{u}$) at the flame base :

$$\mathcal{F}(\omega) = \frac{\widetilde{\dot{Q}}(\omega)/\overline{\dot{Q}}}{u'/\bar{u}}$$

In addition, the flame is submitted to a broad range of oscillation amplitudes and its response changes with the input level. One may then use an extension of the linear concept of transfer function and define an FDF which depends on frequency and on the amplitude of the input :

$$\mathcal{F}(\omega, |u'|) = \frac{\widetilde{\dot{Q}}(\omega, |u'|)/\overline{\dot{Q}}}{u'/\bar{u}}$$

This nonlinear dependence of the flame with respect to the input level produces the limit cycles observed in experiments. In addition, this nonlinearity gives access in many cases to the nonlinear features observed in practice as already shown in a range of previous studies and as will be confirmed in this investigation. There are some interesting indications on the processes which lead

to nonlinearities in the flame response for example in Schuller et al. (2003b), where variations of the rate of heat release are linked to the interaction between a "V"-flame and a wall or where a strong change in flame surface area is induced by the collapse of neighboring sheets in an "M"-flame. One may note that effects of amplitude of oscillation are generally not well documented and when they are, the description is often only qualitative. There are systematic investigation of the flame response to different amplitudes in some pioneering studies like Bourehla et al. (1998) where a conical (Bunsen) flame was subjected to a wide range of amplitudes. Light emission (chemiluminescence) was not recorded in this experiment but flame front analysis revealed that a convective wave was wrinkling the flame in a symmetric fashion for small amplitude levels ($u'/\bar{U} \leq 0.3$) whereas an asymmetric pattern was formed under more intense velocity perturbations. By operating at a higher frequency and using large amplitudes of modulation, the flame cone could be transformed into a hemispherical surface which became essentially insensitive to velocity fluctuations. This latter case was examined in further detail in Durox et al. (1997). Measurements of the flame response to different amplitude have been attempted in other studies (Lieuwen et al. (2002); Lee et al. (2003)) but they remain limited to a few frequencies.

The flame transfer function (FTF) of conical configurations was measured by Ducruix et al. (2000) and more recently for different forcing amplitudes by Durox et al. (2009b) and Karimi et al. (2009). This transfer function features a progressive drop in the gain as the perturbation amplitude is increased, whereas the phase is more sensitive to the amplitude and saturates for a certain level of modulation. Experiments and further analysis were carried out to include effects of the anchoring device on the flame response (see for example De Goey et al. (2011) for a recent review).

Nonlinear issues are considered in Baillot et al. (1996); Schuller et al. (2003a); Preetham et al. (2008). One may note that the analysis carried out in Preetham et al. (2008) essentially retrieves results obtained previously in the unified framework devised in Schuller et al. (2003a). These previous studies have stimulated work on nonlinearities in the flame response. Configurations investigated theoretically were also studied experimentally in Durox et al. (2005); A. Birbaud et al. (2007); Durox et al. (2009b) where a "V"-flame, an "M"-flame and a collection of small conical flames are considered. The "V"-flame (Durox et al. (2005)) features nonlinearities in the transfer function for increasing amplitude with a drop in the gain. This is linked to the vortices shed by the burner lip and interacting with the flame. On the other hand, the phase remains insensitive to amplitude. A further study (A. Birbaud et al. (2007)) reports effects of different confinement diameters and describes the possible interference between the flame and the side wall when the ratio of the injector diameter to the tube diameter exceeds a certain value. By decreasing the

tube diameter, the vortex interaction is modified and the nonlinear response is changed. The different flame geometries examined in Durox et al. (2009b) exhibit variations in gain as a function of amplitude, whereas only the collection of small conical flames features a phase sensitivity. A turbulent "V"-flame is analyzed in Balachandran et al. (2005). From measurements of heat release rate, it is concluded that the flame response is nonlinear even for low perturbation amplitudes and in the absence of local extinctions. It is found that leakage of energy takes place from the fundamental frequency to its harmonics as amplitude is increased. Numerical simulations with a URANS code in Armitage et al. (2006) indicate that the transition to the nonlinear regime occurs when well defined vortices are shed from the lips of the bluff body and distort the flame front.

Many current investigations concern swirling flames which are found in most gas turbine and aero-engine technologies. Dynamics of a premixed swirled combustor is considered for example in Bellows et al. (2003). The flame is submitted to various levels of modulation amplitudes for various air-fuel ratios. This reveals a saturation phenomenon in the FTF gain whereas the phase evolves linearly with frequency and is less sensitive to the fluctuation amplitude. This article also contains a list of potential processes which may be responsible for the saturation of the flame response.

Important features of swirling flames originate from the dynamics of the swirler. When this unit interacts with incident acoustic waves it generates a vorticity wave which is accompanied by transverse velocity oscillations. These in combination with the acoustic perturbations define the flame response. Acoustic velocity perturbations induce vortex roll-up from the injector lip, whereas azimuthal velocity fluctuations generated by the swirler are convected by the flow. The swirl number is modulated and this in combination with the vortex roll-up mechanism leads to flame surface area fluctuations and correspondingly heat release rate fluctuations (see for example Palies et al. (2010)). These mechanisms are sensitive to amplitude and heat release rate fluctuations are modified as the level of modulation is augmented. All these studies lead to the conclusion that the flame is sensitive to velocity fluctuations. Perturbations in real systems exciting one of the resonance frequencies may reach high amplitude levels. Wrinkling caused by acoustic modulations and convected azimuthal perturbations lead to separate contributions to heat release rate fluctuations and this affects the gain and phase of the transfer function.

Flame transfer functions (FTFs) have been used in linear stability analysis of complete systems. This provides predictions of unstable frequencies for small disturbances and yields exponential growth rates. The FTF is deduced from a model, from measurements (by making use of finite amplitude perturbations) or from simulations. The linear framework cannot be used to predict the limit

cycle amplitudes or to explain many features observed in practice and it only provides rough estimates of the oscillation frequency. This is exemplified in a linear stability analysis of an unconfined flame stabilized at the boundary of a burner (Noiray et al. (2006)). The unstable band was predicted, but it was not possible to explain mode switching arising when the burner geometry was modified. In addition the range of parameters corresponding to instability was overestimated. Similar issues are considered in another investigation due to Kim et al. (2009). Predictions are made for the first acoustic eigenmode of a swirled burner by using a FTF measured with a low modulation level $u'/\bar{u} = 0.10$. Frequency prediction relies on the phase of the FTF by considering an unstable frequency band. This provides an oscillation band which approximately matches experimental data but the level of oscillation is not available and the analysis provides no clues on the higher modes of the system. The flame response has also been measured under full engine conditions in Schuermans et al. (2010) and these data were used in a linear analysis to identify unstable ranges of a gas turbine combustor and predict staging effects and their influence on the regime of operation. In all these studies, the linear analysis is useful but incomplete. It was already mentioned by Crocco (1969) that "oscillations cannot grow indefinitely" and that predictions of amplitude and triggering need to be carried out in a nonlinear framework. The nonlinear flame response causes the bifurcations observed in practical devices an issue which is examined for example in Huang et al. (2009) in an extensive review of swirling flame dynamics. Bifurcations are revealed by changing combustor parameters (feeding manifold length, equivalence ratio, preheating temperature, etc.) (Lieuwen (2002)) and this can be used to identify self-sustained frequency-amplitude regimes and test prediction methods.

It is next logical to examine investigations of nonlinear combustion dynamics. One possible saturation mechanism giving rise to limit cycles is envisaged in Dowling (1997) to interpret experiments on a ducted flame stabilized on a bluff-body (Langhorne (1988)). In this analysis based on the describing function (DF) methodology borrowed from control theory, the flame gain saturates when the flow at the bluff-body is reversed. A more advanced model of the flame motion (Dowling (1999)) analyzed in the DF framework yields predictions of the unstable amplitude and frequency. The nonlinear transfer function concept is also used in Peracchio et al. (1999) to analyze the dynamics of a combustor submitted to equivalence ratio fluctuations. The transfer function was calibrated by making use of experimental data and suitable estimates of limit cycles were obtained by considering the mean air-fuel ratio as a bifurcation parameter. Observations of bifurcations in a swirled combustor are reported in J. Moeck et al. (2008) and interpreted with the nonlinear model defined in Peracchio et al. (1999). Describing function theory originates from nonlinear control theory developed during the second world war. Detailed presentation and applications can be found in Gelb et al. (1968). This theory is also known

as the "equivalent harmonic" and one also uses the term "harmonic balance" to designate methods based on this concept. In general the validity of this approach lies on the fact that there is a single nonlinear element (in the present case, this component is the flame) and that the other elements in the system filter out higher order harmonics so that the system stability is essentially governed by the fundamental component. The describing function is constituted by a family of transfer functions measured or calculated for a set of amplitudes (Schuller et al. (2003a); Bellows et al. (2003); Durox et al. (2005); A. Birbaud et al. (2007); Durox et al. (2009b); Karimi et al. (2009); Palies et al. (2010)).

A unified framework using the "Flame Describing Function" (FDF) concept was devised by Noiray et al. (2008) and applied to the analysis of the multiple open flame burner already examined with linear methods (Noiray et al. (2006)). The FDF model includes nonlinearities due to the flame and their impact on gain G and phase φ. The different amplitude-frequency couples found by changing the upstream size (used as a bifurcation parameter) of the open flame burner where well retrieved from calculations for the whole range of sizes. Experimental observations of hysteresis, triggering and mode switching were well predicted by calculations. Results found by Noiray et al. (2008) can be used to highlight the poor quality of a linear analysis. In essence, it comes down to narrow the full view of the whole amplitude range. The bifurcation diagram calculated by Noiray et al. (2008) is reproduced in Fig. 5. The comparison between predictions and experiments (open symbols) is drawn on the right hand side of the figure. By using the FDF, one obtains the positive growth rate (ω_i) regions plotted in the center of Fig. 5. These regions reveal the unstable range of the geometry and the associated unstable mode. By considering a linear analysis, one would obtain the result shown in Fig. 6. The FTF used to calculate the unstable range (for infinitesimally small amplitude here) gives positive growth rates (ω_i) on a narrow band of the whole amplitude panel. The gray area shows the hidden growth rates missed by the linear framework calculations. In this latter case, one would predict a first mode oscillation from $L = 0.10$ m to 0.15 m, followed by the second mode until $L = 0.22$ m. The second mode would also exist from $L = 0.25$ m to 0.43 m and would be followed by the third one until $L = 0.76$ m. This is depicted by horizontal colored lines at low amplitude ($u'_{rms}/\bar{u}$) on the right hand side of Fig. 6. It is then possible to see that the experimental points do not match the calculations where one expects a first mode oscillation from $L = 0.10$ m to 0.25 m followed by the second mode between $L = 0.29$ m and 0.63 m before switching to the third one until $L = 0.76$ m. The FDF methodology has also been applied to a turbulent swirled flame (Palies et al. (2011)) and calculations succeeded fairly well in predicting the limit cycles observed on the burner. In this latter study, the bifurcation parameter was the flame tube size. The system considered in Palies et al. (2011), operates like a Helmholtz resonator, and does not feature triggering and hysteresis characteristics.

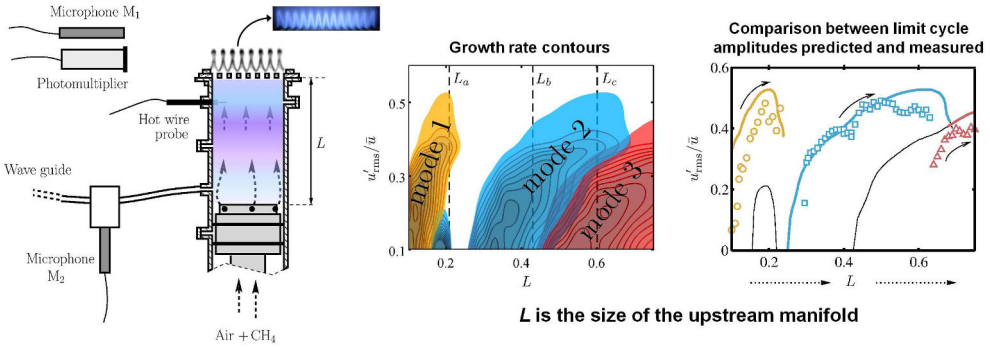

Figure 5: *Bifurcation diagram calculated by Noiray et al. (2008). The positive growth rate (ω_i) regions reveal the unstable range of the burner geometry. The three different colors are linked to the three first eigenmodes. On the right hand side, the bifurcation contours corresponding to $\omega_i = 0$ are compared with experiments data plotted as open symbols.*

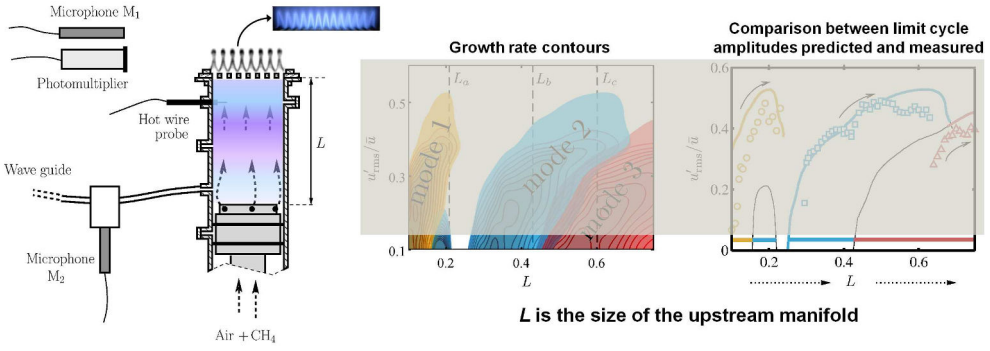

Figure 6: *The bifurcation diagram from Noiray et al. (2008) shows the results that one would find by using a linear analysis with a FTF measured for infinitesimally small amplitudes. The gray area shows that much of the system response is missed, giving access to a narrow region in the diagram and hiding the real dynamics of the burner.*

The present study is aimed at testing the FDF methodology in a generic configuration where the flame is confined and is therefore closer to real systems. Experiments and calculations have already been reported in Boudy et al. (2011b) and Boudy et al. (2011a). Two confinement tubes featuring different lengths have been mounted on the open burner investigated by Noiray et al. (2008). It was found that amplitude, frequency, hysteresis, triggering and mode switching, observed by changing the burner feeding manifold length were fairly well retrieved for the different confinement tube sizes. The FDF framework was however less successful in predicting the unstable behavior observed with the longest confinement tube (Boudy et al. (2011b)). Systematic experiments and calculations considered in what follows by making use of confinement tubes up to $L_2 = 0.40$ m exhibit many types of limit cycles including *variable amplitude* oscillations featuring special sound signatures. This is illustrated in Fig. 7 which shows typical signals encountered during various experiments on the multiple flame combustor equipped with different confinement tube sizes. It is worth noting that similar characteristics were observed for example in Sterling (1993) and a nonlinear modeling was proposed by introducing an n-τ flame response with an amplitude dependent gain n or delay τ. It was suggested that the quasi-periodic oscillations observed were linked to interactions of two acoustic eigenmodes. A more recent investigation (Kabiraj et al. (2012)) reports observations of different types of oscillations in a multiple flame combustor equipped with a perforated plate comprising a small number of holes. The flame tube size is used as bifurcation parameter providing access to a variety of limit cycles. J. P. Moeck et al. (2012) recently analyzed the dynamics of a combustor featuring multiple linearly unstable modes and defined conditions for the existence and stability of single or multiple mode oscillations by using the describing function framework.

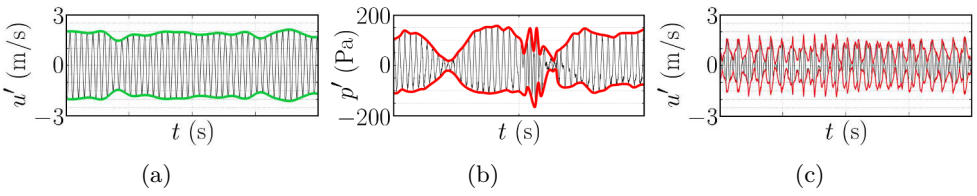

Figure 7: *Typical signals found in experiments on self-sustained combustion oscillations with the multiple flame combustor equipped with different sizes of confinement tube. (a) : Signal usually recorded for most of the burner geometries with a nearly constant amplitude. The signal envelope is drawn in green. (b) and (c) : Variable amplitudes of different kinds arising for certain ranges of the upstream manifold size. The signal envelope, drawn in red, reveals variations in amplitude.*

Thesis objectives and organization

As already indicated this investigation addresses issues in nonlinear combustion dynamics. These issues may be subdivided in two groups :

- The first group aims at extending the Flame Describing Function (FDF) methodology to generic configurations and provide an interpretation of the various types of limit cycles encountered in experiments.

- The second group deals with control methods and is intimately linked to predictions derived from the FDF framework. It centers on the reduction of oscillations by means of a bias flow perforated plate backed by a cavity (BFP). This control method is used in both experiments and calculations. The FDF analysis allows to interpret experimental data and predict system effectivness.

The first part of this document describes the experimental setup. The second part gives a detailed account of the FDF model. Results of calculations are compared with the experimental data in part three. Reduction of combustion oscillations using optimized bias flow perforates is envisaged in part four. A more detailed description of the successive chapters is given in what follows.

Chapters details

- The first chapter describes the experimental configuration which comprises a feeding manifold of length L_1 connected to a multipoint injector which anchors a collection of small laminar conical flames. These flames are enclosed in a quartz tube of length L_2 open to the atmosphere.

- Typical regimes of operation of this device are reported in the second chapter. Various flow rate and geometrical parameters are considered. This shows that the burner is flexible and allows a continuous variation of the feeding manifold size L_1 and discrete changes in confinement tube length L_2.

- The third chapter presents two other setups used to investigate the acoustic signature of the burner and the flame response.

- The analysis of the generic burner system is carried out in Chapter 4. The configuration is represented as two connected ducts and can be analyzed as an acoustic network by specifying boundary conditions and matching conditions at the duct interface.

- The flame model is introduced in Chapter 5 by closely following the presentation proposed by Noiray et al. (2008). Two flow rates are investigated and the flame responses are measured by making use of har-

monic perturbations generated by a driver unit (loudspeaker). A link is made at the end of the chapter with the flame reflection coefficient and an impedance tube methodology based on multiple microphones is used to determine this reflection coefficient under reacting flow conditions.

- The acoustic network and the flame response are combined to model the system in Chapter 6. Two models are derived. The first considers ideal boundary and matching conditions and is named "model A", while the second entitled "model B" includes the characteristics of these elements. The models emphasize the use of the FDF and include the injection element composed of a perforated plate. This latter is represented with a relation derived from Melling (1973).

- The basic model entitled "Model A" is applied in Chapter 7 to predict unstable combustion regimes observed with two configurations of the burner. This chapter is a combination of two articles presented at the ASME turbo expo of 2010 held in Glasgow, UK (Boudy et al. (2011b)) and at the 33^{rd} International Symposium on Combustion held in Beijing, China (Boudy et al. (2011a)). These two papers report calculations carried out for short and intermediate confinement tube sizes up to $L_2 = 0.20$ m. Systematic comparisons are carried out with experimental data. These results generally match with a few differences arising in the switching zone between mode 1 and mode 2.

- The same procedure is used in a modified configuration examined in Chapter 8. In the new configuration, the confinement tube length L_2 covers a broader range. The flame holder is thickened to increase the damping in the system (it was shown previously that a thicker injection system enhances damping Noiray et al. (2007)). It allows to measure FDF values in a confined environment with a small quartz tube of $L_2 = 0.10$ m without loosing loudspeaker efficiency. It is shown that the mismatch observed between experimental data and analytical results is not caused by the FDF and that the model accuracy is enhanced by a better representation of boundary and matching conditions. A better estimate of frequencies and amplitudes measured in the burner is obtained in this way.

- By doing the analysis of combustion regimes with different configurations of the burner, a new class of limit cycles is uncovered. This class is typified by a variable amplitude of oscillation. These unsteady amplitudes take different forms and require some dynamical systems analysis. This is reported in Chapter 9 where experimental results are those described in Chapter 8. The analysis in Chapter 9 is based on two papers presented at the 3^{rd} INCA conference held in Toulouse, France in 2011 (Boudy et al. (2013)) and at the ASME turbo expo of 2012 held in

Copenhagen, Denmark (Boudy et al. (2012)). The describing function methodology is used to identify conditions giving rise to phenomena observed in experiments.

- Chapter 10 of the manuscript is dedicated to control issues. A bias flow perforated plate backed by a cavity (BFP) is tested in order to cancel the self-sustained combustion oscillations. The analysis relies on the FDF framework and is based on calculations and systematic experiments which are carried out to understand the physical processes. This investigation uses the possibility to easily modify the geometry of the system to identify the potential and limitations of the bias flow perforated plate controller. It is shown that damping is accessible for a broad range of frequencies by optimizing the plate in the low Strouhal number approximation devised in Scarpato et al. (2012). The damping bandwidth is broader than that obtained in the high Strouhal number regime examined in Hughes et al. (1990). This latter method yields a more compact system, but is only effective in a narrow band of frequencies. The chapter is fairly long because it accounts for experiments and calculations. It also contains interpretations of various phenomena observed in practice, like the occurrence of self-sustained oscillations at frequencies which should be damped. This interpretation is made possible by the FDF methodology which provides a useful account of flame behavior as the oscillation frequency changes.

- The dynamics of the system is profoundly modified by the presence of the control device. Calculations confirm the ability of the flame to oscillate on a shifted frequency. This highlights the difficulty to anticipate the real behavior of the system even if the acoustic eigenmodes are known. This is the reason why we consider an idealized configuration in Chapter 11 to identify possible decoupling effects. This phenomenon is induced by the upstream boundary condition when the reflection coefficient is close to zero. This is used to explain observations reported in Chapter 10 indicating that it is not always possible to act on instabilities which are coupled by resonances in the confining tube and decoupled from the feeding manifold. Another interesting point is also investigated. It deals with particular geometries which promote the decoupling of the flame tube even if the reflection coefficient is not close to zero.

The various parts of the thesis are illustrated synthetically in Tab. 1. The main pictures picked up from each part allow to have a preview of the elements or results which will be exposed.

Table 1: *Illustration of the thesis content for each part of the manuscript.*

Part I	Part II	Part III	Part IV
Burner geometry	**Relevant elements**	**Nonlinear stability analysis**	**Passive control approach**
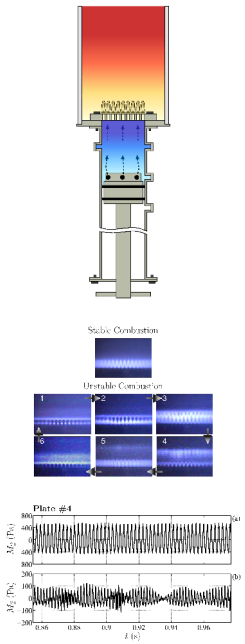	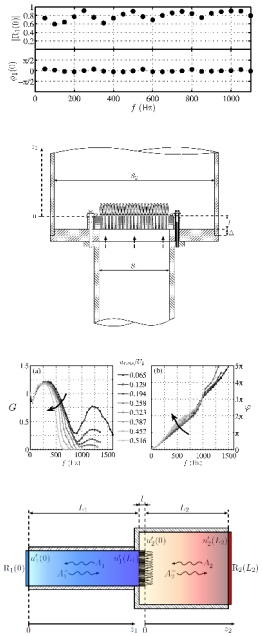	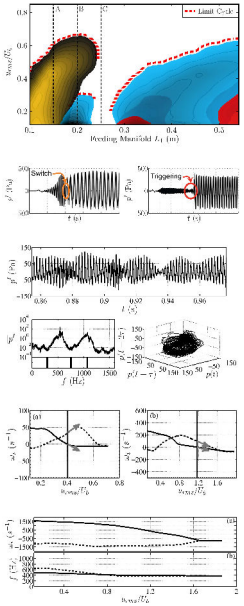	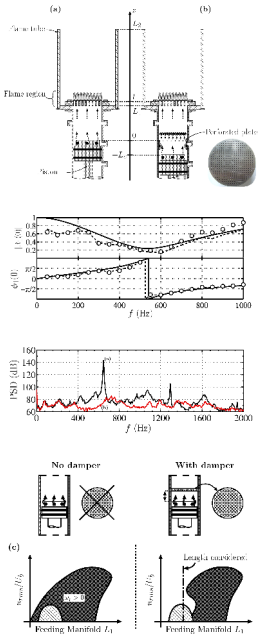
➡ Experimental setup ➡ Combustion regimes	➡ Burner acoustics ➡ Flame dynamics ➡ Modeling strategy	➡ Basic model ➡ Detailed model ➡ Variable amplitudes	➡ Bias Flow Perforates ➡ Cavity decoupling

Publications associated with the thesis

Boudy, F.*, D. Durox, T. Schuller, G. Jomaas, and S. Candel. 2011. "Describing function analysis of limit cycles in a multiple flame combustor" *J. Eng. Gas Turb. Power* 133 (6): 061502.1–061502.8. doi:10.1115/1.4002275

Boudy, F.*, D. Durox, T. Schuller, and S. Candel. 2011. "Nonlinear mode triggering in a multiple flame combustor." *Proc. Combust. Inst.* 33 (1): 1121–28. doi:10.1016/j.proci.2010.05.079

Duchaine, F., F. Boudy*, D. Durox, and T. Poinsot. 2011. "Sensitivity analysis of transfer functions of laminar flames." *Combust. Flame* 158 (12): 2384–94. doi:10.1016/j.combustflame.2011.05.013

Boudy, F.*, D. Durox, T. Schuller, and S. Candel. 2012. "Nonlinear flame describing function analysis of galloping limit cycles featuring chaotic states in premixed combustors." In *Proceedings of the ASME Turbo Expo, paper GT2012-68998*, New York: American Society of Mechanical Engineers.

Boudy, F.*, D. Durox, T. Schuller, and S. Candel. 2013. "Analysis of limit cycles sustained by two modes in the flame describing function framework." C. R. Mec. 341 (1–2): 181–90. doi:10.1016/j.crme.2012.10.014

* Permanent email : frederic.boudy@graduates.centraliens.net

Part I

Thermoacoustic coupling in a premixed combustion chamber equiped with a multipoint injector

Chapter 1

Experimental setup

Combustion instabilities are usually examined in configurations which represent in an ideal fashion industrial systems. The configuration used in the present study has generic features allowing an analysis of fundamental interest. In this configuration the flame is confined in an open ended tube. The aim of experiments carried on this system is to provide a data base for the analysis and and prediction of self-sustained combustion oscillations. The burner offers a wide variety of settings through easily adjustable feeding manifold and flame tube lengths. Combustion oscillations are characterized as the geometry is changed by varying the position of a piston defining the boundary of the upstream manifold. This chapter describes the experimental configuration and associated diagnostics.

1.1 Burner geometry and operating conditions

The experimental setup is sketched in Fig. 1.1. It is derived from a previous burner used by Kagiya 2000. The FDF framework was initially developed on a similar configuration but with an unconfined flame (Noiray et al. (2008)). These previous studies were motivated by industrial applications of radiant burners in which self-sustained combustion oscillations are often observed. Thanks to its generic arrangement, the system facilitates a theoretical analysis and has been modified with the aim of acquiring detailed insights on combustion instabilities for a confined combustion geometry. In most practical configurations combustion takes place in a closed environment as exemplified in gas turbines. It is then interesting to examine a system having similar features. While there are many studies of combustion dynamics and instabilities there is a need for systematic experimentation and modeling.
The burner can be divided in three parts. A feeding manifold of radius $R_1 = 0.035$ m ended by a perforated plate which delivers the premixed streams. A perforated plate anchors a collection of small laminar conical flames. The third element is an open ended quartz tube of radius $R_2 = 0.065$ m, enclosing the

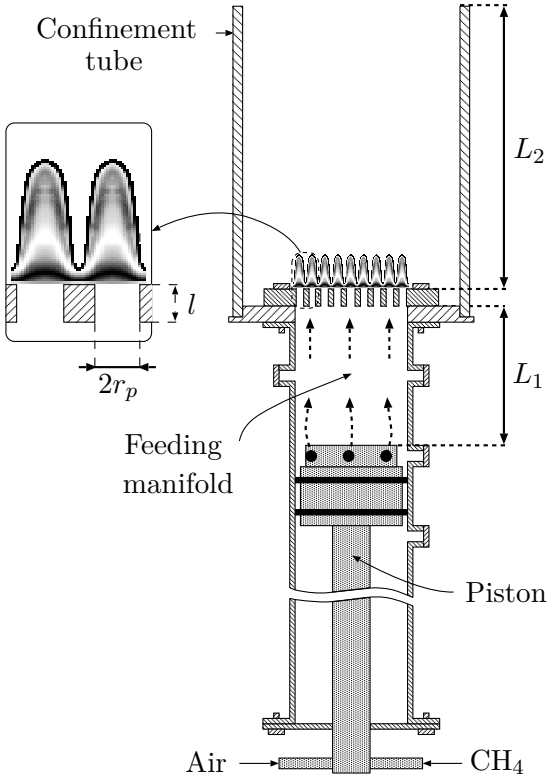

Figure 1.1: *Experimental setup used to characterize self-sustained combustion oscillations in a confined combustion environment. Reactants are premixed inside a movable piston used to change the feeding manifold length L_1. A perforated plate anchors a collection of small laminar conical flames. The flame tube L_2, made of quartz confines the combustion zone. Four flame tube sizes L_2 are used in the present investigation.*

combustion zone. Reactants are premixed in the piston before being injected in the feeding manifold through six apertures machined on the head periphery (see Fig. 1.1).

Combustion instabilities involve a resonant feedback between the heat release rate fluctuations and the acoustics of the burner. Experiments on the same configuration but with an unconfined combustion zone have already shown a variety of couplings between the unsteady flame and the injection manifold (Janardan et al. (1976); Schuller et al. (2003b); Durox et al. (2005); Noiray et al. (2008); Durox et al. (2009a)). With confined combustion, it was demonstrated in some early studies that the injection manifold or the flame tube influences the "singing" character of a flame (Putnam (1971), p. 9-16). The piston used in the present investigation facilitates the length modification of the feeding manifold. This length L_1 measured between the upstream side of the perforated plate and the head of the piston, can be varied in discrete steps all the way from $L_1 = 0.11$ m to 0.55 m. By using an additional tube, it is possible to sweep the feeding manifold length from $L_1 = 0.11$ m to 0.77 m. The

Table 1.1: *Geometrical parameters of the perforated plates (dimensions in mm).*

Plate	***#1***	***#2***	***#3***	***#4***
Thickness l	3			15
Holes radius r_p	0.85	1.5	1	
Number of holes N	601	189	421	
Porosity $\mathcal{P}$	0.35	0.34		

head of the piston is designed to offer a nearly perfect reflecting boundary for acoustic waves. It is machined with a shoulder and 6 holes on its periphery to allow flow of the reactants to be injected through the piston. The flame tube of size L_2, can also be changed. Four quartz tubes of different lengths are used ranging from $L_2 = 0.10$ m to $L_2 = 0.40$ m by steps of 0.10 m.
The perforated plate located at the top of the feeding manifold and confined within the quartz tube, anchors a collection of small laminar conical flames. The different geometries of this element are gathered in table 1.1. The main configuration examined in the present study pertains to plate #4. It has a thickness $l = 15$ mm and a diameter $2R = 70$ mm. It is made of stainless steel and comprises $N = 421$ holes of diameter $2r_p = 2$ mm arranged on a 3 mm square mesh, resulting in a global porosity $\mathcal{P} = N\pi r_p^2/\pi R^2$ of 0.34.
In a first exploration, the feeding manifold length is swept in both ways with a confinement tube $L_2 = 0.10$ m. Then, another flame tube is used in a second set of tests and so on until $L_2 = 0.40$ m. For all confinement tubes, the flame oscillates for a wide range of feeding manifold lengths L_1 and is only stable in some narrow intervals. Three operating conditions have been tested depending on the perforated plate set in this investigation. These flow rates are gathered in Tab. 1.2 for each perforated plate. The air is delivered by a filtered network at a pressure of 6 bars. The G20 methane is stored on site.

Table 1.2: *Flow rate conditions used with the different perforated plates anchoring the small laminar conical flames.*

Plate	***#1***	***#2***	***#3***	***#4***
Flow rate $\dot{m}$ (g.s^{-1})	3.65	3.65 or 2.2	4.7	
Equivalence Ratio ϕ	0.9		1.03	
Power P (kW)	9.1	9.1 or 5.4	13.3	

1.2 Diagnostics

The experimental setup is equipped with different probes allowing measurements of velocity, pressure and heat release rate fluctuations. Figure 1.2 shows the burner and associated diagnostics and sensors.
Five quantities are measured in this experiment. Velocity fluctuations are determined by means of a hot wire probe 3 cm below the perforated plate. Three microphones are used to record pressure fluctuations at different locations on

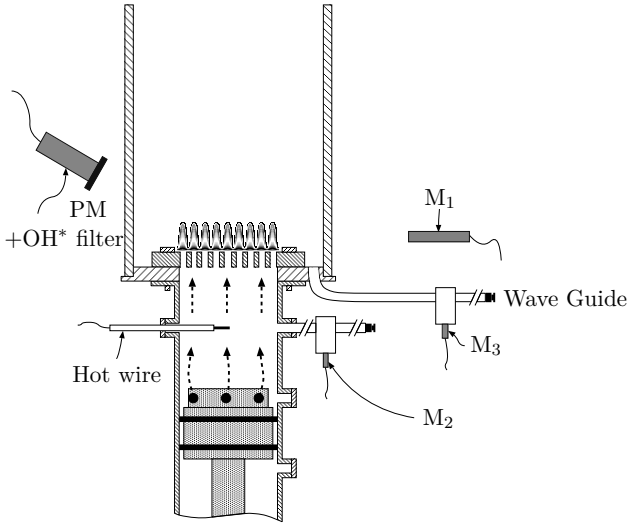

Figure 1.2: *Experimental setup used to characterize self-sustained combustion oscillations and associated diagnostics. Three microphones are used to measure the pressure fluctuations. Microphone* M_1 *is located 25 cm away from the burner axis while microphones* M_2 *and* M_3 *are connected on 25 m waveguides. Hot wire probe measures the velocity fluctuations in the feeding manifold. A photomultiplier equipped with an OH* filter views the flame from outside the quartz tube and measures the hydroxyl radical fluctuations radiated by the flame.*

the burner. Microphone M_1 acquires the sound radiated by the burner, 25 cm away from the burner axis. In experiments carried out in the present configuration, walls, ceiling and floor are sufficiently distant from the flame to assume that the records are weakly influenced by acoustics reflections. Two microphones are connected on 25 m waveguides to measure pressure fluctuations inside the burner. The waveguides are sufficiently long to avoid reflection of the wave. Microphone M_2 is connected to the feeding manifold while M_3 is plugged on the waveguide connected to the flame plane. This latter allows measurements of combustion noise. Feeding manifold plugs are separated by 5 cm from each other and microphone M_2 is plugged on the first one facing the hot wire. The length of the waveguide between the plug location and the microphone M_2 is 12 cm while the one of microphone M_3 is 11.5 cm. A photomultiplier equipped with an OH^* filter (λ=308 nm) records free radicals emissions from the flame which are almost proportional to the heat release rate (Hurle et al. (1968); Higgins et al. (2001)). It is important to note that this can be assumed with a perfectly premixed flame under lean or stoichiometric condition. Measurements are processed with LabVIEW® and Matlab®. Characteristics of the different diagnostics are gathered in Tab. 1.3.

Table 1.3: *Materials and diagnostic tools characteristics.*

Equipment	**Manufacturer**	**Reference**
Flow-controller (Air)	Bronkhorst	F202AC-FAC55V, 5 Nm^3h^{-1} with C_3H_8
Flow-controller (CH_4)	Bronkhorst	F201AC-FAC33V, 50 $Nl\,min^{-1}$ with N_2
Microphone (5Hz-20kHz, 50mV/Pa)	Brüel & Kjaer	4189
Microphone preamplifier	Brüel & Kjaer	2669
Microphone amplifier	Brüel & Kjaer	Nexus Conditioning Amplifier
Hot wire probe	Dantec Dynamics	55P16
Power supply	Dantec Dynamics	Mini CTA 54T30
Photomultiplier	Electron Tubes Limited	91295B
Current to voltage convertor	Electron Tubes Limited	Transimpedance Amplifier A1
Loudspeaker	Focal	4K211
Sinusoidal wave generator	Hameg	HM8040
Loudspeaker amplifier	Europsonic	PA-9402

Chapter 2

Dynamical behavior of the combustion system

The system examined throughout this study exhibits a variety of combustion regimes. These are revealed by changing the geometry and flow rate conditions. Typical regimes are described in this chapter. The experimental procedure is explained in a second step. A special combustion regime is considered in the last part of this chapter. Phenomena which are here briefly reviewed will be analyzed in further detail in the following chapters.

2.1 Typical combustion regimes

The experimental investigation begins by setting a confinement tube L_2 with the head of the piston L_1 close to the perforated plate. Then, the system is ignited and the piston can be moved from minimum to maximum extension with a predefined step. Another sweep can be done by retracting it in the reverse direction. Depending on the piston position L_1 and the confinement tube L_2 selected, combustion is either stable or unstable.
In a stable case, flames exhibit a conical shape with a low level of noise reaching about 100 dB at microphone M_2 (reference pressure 2×10^{-5} Pa). This is illustrated in Fig. 2.1. In this case, $L_1 = 0.25$ m and $L_2 = 0.10$ m and the burner is equipped with the perforated plate #3 ($l = 3$ mm see Tab. 1.1). The flow rate is fixed to $\dot{m} = 4.71\times10^{-3}$ kg.s^{-1} at an equivalence ratio $\phi = 1.03$, providing a thermal power of 13.3 kW. These conditions induce a bulk velocity $U_b = 3.1$ m.s^{-1} in each channel of the perforated plate.
In the unstable case, all the flames move in a regular fashion with formation and collapse of fresh reactant pockets as illustrated in Fig. 2.1. In this latter case, the combustion chamber features the same perforated plate (#3) and $L_2 = 0.10$ m but the feeding manifold length $L_1 = 0.29$ m. This oscillation exhibits a frequency $f = 750$ Hz and induces a strong level of noise which

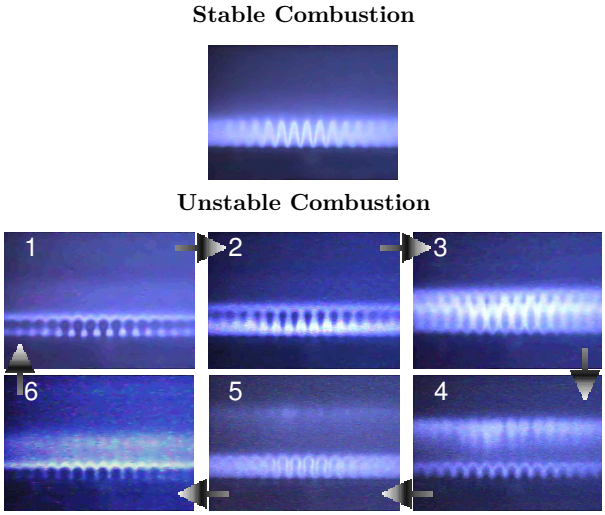

Figure 2.1: *Stable and unstable combustion regimes for an equivalence ratio $\phi = 1.03$. These records illustrate typical flame behaviors. They are recorded for $L_2 = 0.10$ m with the perforated plate #3. Stable combustion corresponds to feeding manifold length $L_1 = 0.25$ m while the unstable one is acquired for $L_1 = 0.29$ m.*

exceeds 140 dB at microphone M_2 (reference pressure 2×10^{-5} Pa). For longer flame tubes, larger oscillation levels may be reached during unstable operation and the flame motion is often more complex.
In these experiments, the pressure is essentially harmonic, indicating that the acoustic field remains in the linear range. Typical pressure and heat release rate fluctuations recorded in the system are plotted in Fig. 2.2. The pressure signal remains sinusoidal whereas OH* radicals light intensity, corresponding to the heat release rate, shows asymmetrical oscillations, revealing the nonlinearity of the flame response.

2.2 Frequency-amplitude sweep

The protocol used to determine the stability margins is the same for all flame tubes. The experimental procedure is initiated with the head of the piston close to the perforated plate (minimum extension) and consists of recording the sensor signals at limit cycles. Then, the piston is retracted in increments of one centimeter all the way to a manifold length $L_1 = 0.55$ m (maximum extension) with signals being acquired for each step. The piston is then moved in the reverse direction (maximum to minimum extension) using the same increment and acquiring the same set of signals. As a result, the oscillation frequencies and the amplitudes of pressure oscillations are obtained for a range of manifold lengths. These experiments are repeated for the different flame tubes $L_2 = 0.10$ m, 0.20 m, 0.30 m and 0.40 m. An unconfined combustion layout is also investigated.

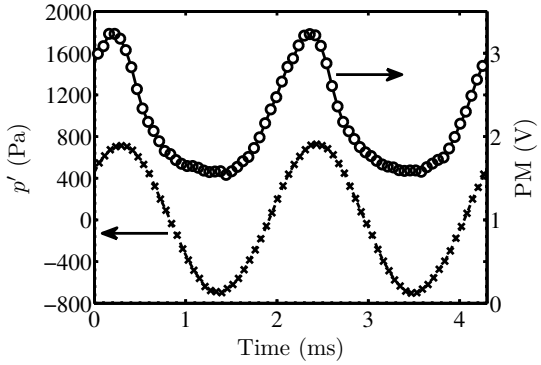

Figure 2.2: *Pressure signal from microphone* M_2 *(left vertical axis) and OH* radicals light intensity (right vertical axis) under self-sustained oscillations. The burner is equipped with the thin perforated plate* $l = 3$ *mm (#3). The feeding manifold is adjusted to* $L_1 = 0.51$ *m with the flame tube* $L_2 = 0.20$ *m.*

Sweeps of the piston in two directions have been done for conditions presented in Tabs. 1.1 and 1.2. Typical evolutions of frequency and amplitude are displayed in Fig. 2.3. The plate #1 (601 holes of diameter $2r_p = 1.7$ mm, thickness $l = 3$ mm) is used in all the confined and unconfined conditions. Frequency and amplitude are plotted as a function of the burner size for L_1 between 0.16 m and 0.55 m. The amplitude is determined by integrating the pressure signal which provides the root mean square (rms) value of the oscillation and allows calculation of the Sound Pressure Level (SPL). The power spectral density of the pressure is calculated by using Welch's method of averaging with a Hanning windowing.

Regarding the amplitude, one finds that it mostly evolves around 140 dB, indicating that the flame is strongly unstable. The spectrum shows the peak frequency of the oscillation. One should note that the combustion process induces oscillations at frequencies which lie in the neighborhood of the acoustic eigenmodes of the system. These eigenmodes are calculated by considering a network of coupled cavities. Ideal boundary conditions and different temperatures inside each element are considered for the calculation of the eigenmodes. The feeding manifold temperature is fixed to $T_1 = 300$ K while the flame tube value T_2 depends on the length L_2 of the flame tube. This mean temperature T_2 is estimated from measurements by using a K-thermocouple. One finds $T_2 = 900$ K for $L_2 = 0.10$ m, $T_2 = 1100$ K for $L_2 = 0.20$ m, $T_2 = 1300$ K for $L_2 = 0.30$ m and finally $T_2 = 1400$ K for $L_2 = 0.40$ m. It is important to note that the perforated plate used as a flame holder and the unsteady behavior of the flame are not included in the calculation of these eigenmodes.

A stable band appears for the unconfined case between $L_1 = 0.23$ m and 0.27 m. A narrower stable band, between $L_1 = 0.30$ and 0.31 m, is retrieved for the confined case with $L_2 = 0.20$ m. Stable combustion is characterized by a "low" level of noise around 100 dB at microphone M_2. For unconfined or small

confinement tube situations, the oscillation frequency is not precisely locked on the eigenmode but lies in its vicinity. Nevertheless, as the flame tube size is greater than 0.10 m the frequency is displaced away from the eigenmode. This is exemplified in the case $L_1 = 0.20$ m to 0.35 m with $L_2 = 0.30$ m in Fig. 2.3.

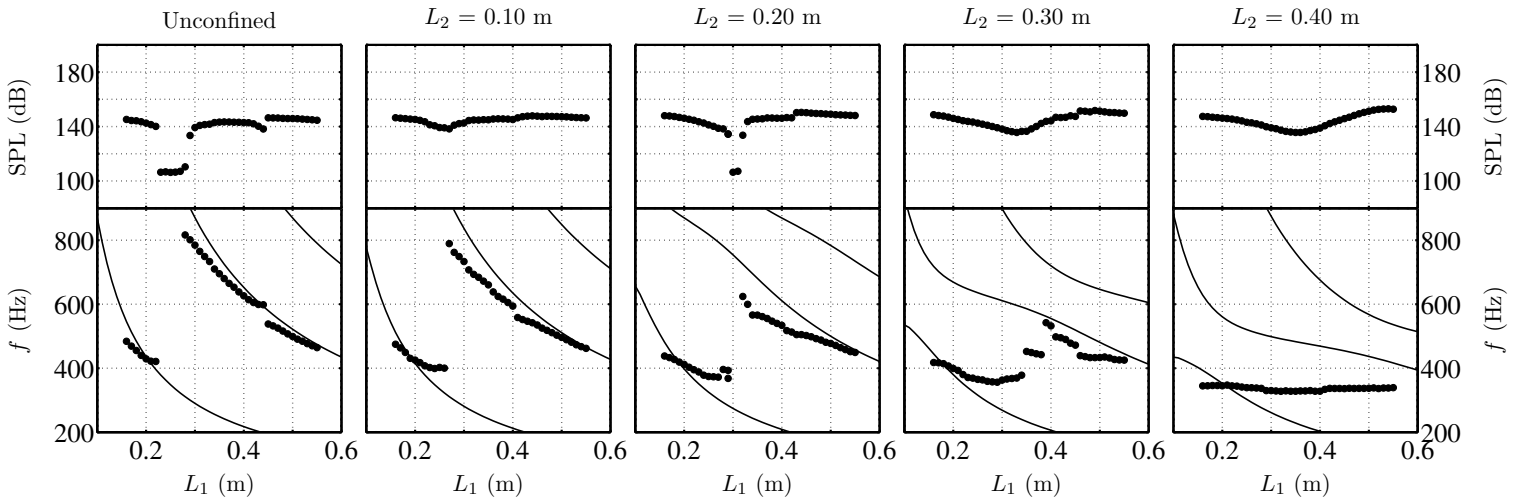

Figure 2.3: *Amplitude and frequency evolution for the different confinement tube sizes L_2. Multipoint injector and operating conditions are set with plate #1 (601 holes of diameter $2r_p = 1.7$ mm, see Tabs. 1.1 and 1.2). Top subfigure displays the Sound Pressure Level (SPL) measured by microphone M_2. Lower subfigure shows the main frequency peak observed in the power spectral density of the pressure signal measured by microphone M_2. The feeding manifold length is swept from $L_1 = 0.16$ m to 0.55 m. The three first acoustic eigenmodes calculated in the absence of a flame response and without taking into account the perforated plate are also shown as bold lines. The flame tube temperature T_2 differs from that assigned to the feeding manifold T_1. $T_1 = 300$ K, $T_2 = 900$, 1100, 1300 and 1400 K correspond respectively to $L_2 = 0.10$, 0.20, 0.30 and 0.40 m.*

Similar experiments have been carried out for the other plates listed in Tab. 1.1. Figures 2.4 and 2.5 show the burner behavior in an amplitude-frequency chart for plate #2 (189 holes of diameter $2r_p = 3$ mm, thickness $l = 3$ mm) with the two flow rates given in Tab. 1.2, i.e. $\dot{m} = 2.2$ and 3.65 g.s^{-1}. It is interesting to note that the amplitude evolution is roughly different from the preceding plate investigated. The lower flow rate experiment, shown in Fig. 2.4, reveals stable combustion for all the feeding manifold lengths L_1 in the unconfined and first confined ($L_2 = 0.10$ m) conditions. For longer flame tubes, unstable combustion is retrieved with the levels as observed for plate #1 (see Fig. 2.3). This is not the case in Fig. 2.5 where the increased flow rate induces unstable combustion for unconfined and confined situations, but this time with lower amplitudes. Regarding the frequencies, the shift with respect to the acoustic eigenmodes is observed for the two flow rates. It is also interesting to see that frequencies between two modes exist for the highest flow rate with $L_2 = 0.30$ m (see Fig. 2.5).

It is found from these experiments that the system exhibits various types of self-sustained combustion oscillations. Amplitudes and frequencies depend on the injector type, the feeding manifold length, the flame tube length and on the mass flow rate.

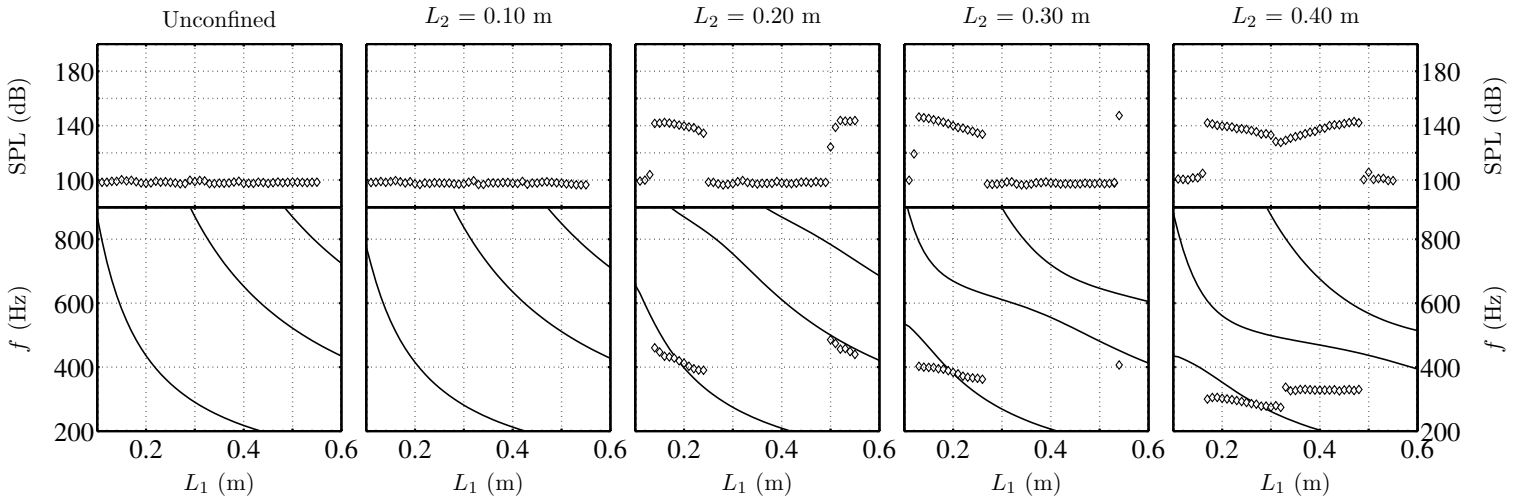

Figure 2.4: *Amplitude and frequency evolution for the different confinement tube sizes L_2. Multipoint injector and operating conditions are set with plate #2 (189 holes of diameter $2r_p$ = 3 mm, see Tab. 1.1). The flow rate is set to 2.2 $g.s^{-1}$. Top subfigure indicates the Sound Pressure Level (SPL) measured by microphone M_2. Lower subfigure displays the main frequency peak observed on the power spectrum density of the pressure signal measured by microphone M_2. The feeding manifold length is swept from L_1 = 0.16 m to 0.55 m. The three first acoustic eigenmodes calculated in the absence of a flame response and without taking into account the perforated plate are also shown as bold lines. T_1 = 300 K, T_2 = 900, 1100, 1300 and 1400 K correspond respectively to L_2 = 0.10, 0.20, 0.30 and 0.40 m.*

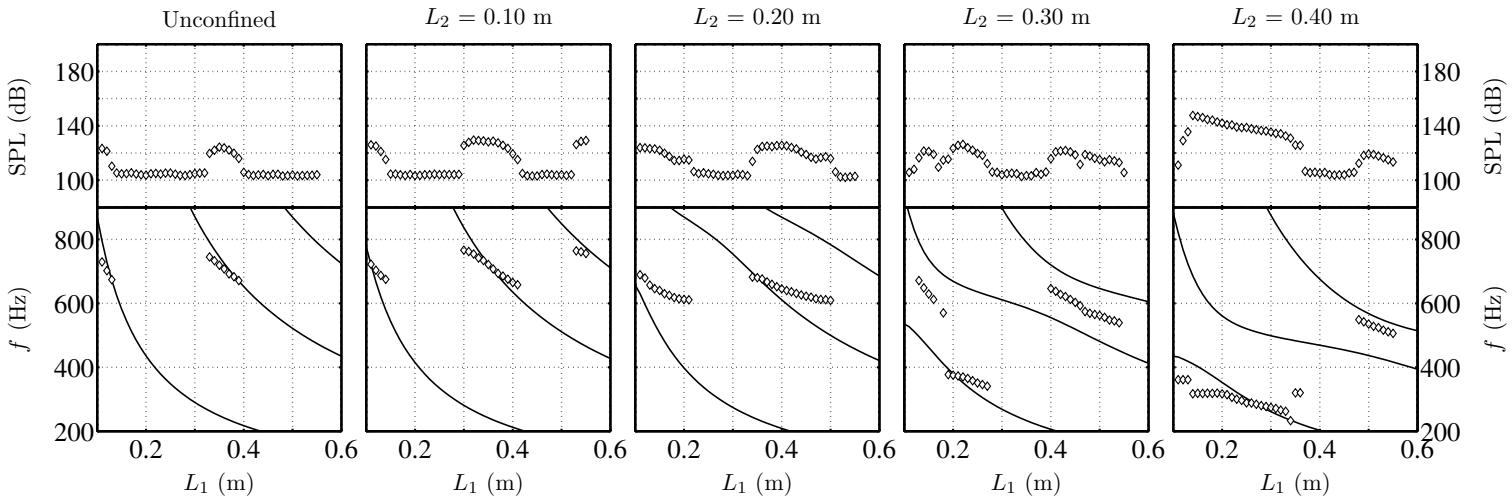

Figure 2.5: *Amplitude and frequency evolution for the different confinement tube sizes L_2. Multipoint injector and operating conditions are set with plate #2 (189 holes of diameter $2r_p$ = 3 mm, see Tab. 1.1). The flow rate is set to 3.65 $g.s^{-1}$. Top subfigure indicates the Sound Pressure Level (SPL) measured by microphone M_2. Lower subfigure displays the main frequency peak observed on the power spectrum density of the pressure signal measured by microphone M_2. The feeding manifold length is swept from L_1 = 0.16 m to 0.55 m. The three first acoustic eigenmodes calculated in the absence of a flame response and without taking into account the perforated plate are also shown as bold lines. T_1 = 300 K, T_2 = 900, 1100, 1300 and 1400 K correspond respectively to L_2 = 0.10, 0.20, 0.30 and 0.40 m.*

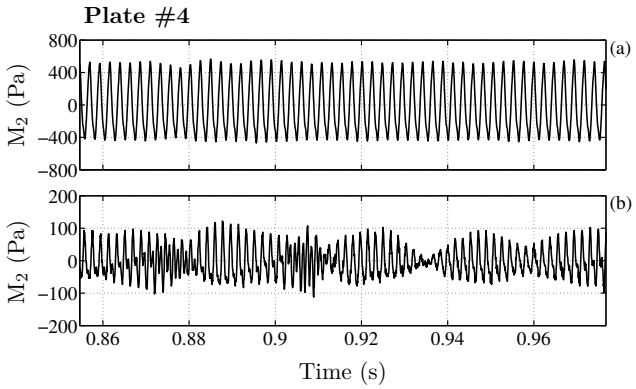

Figure 2.6: *Typical limit cycles recorded by means of microphone* M_2 *with plate #4 and confinement tube* $L_2 = 0.20$ *m. (a)* $L_1 = 0.18$ *m. The frequency shift reaches 100 Hz with respect to the acoustic eigenmode. (b) Limit cycle acquired for* $L_1 = 0.21$ *m. The amplitude evolves in an irregular manner as a function of time.*

2.3 Amplitude modulations

Figures 2.3, 2.4 and 2.5, discussed in the preceding section, show the evolution of the oscillation frequency as a function of the burner geometry. By analyzing results corresponding to the different flame tube sizes L_2, one finds that the frequency lies in all cases in the vicinity of the acoustic eigenmodes of the geometry but one also notes that for certain values of L_1 the frequency shift between the eigenmode and the observed oscillation is quite large. This is exemplified for flame tubes $L_2 = 0.30$ m and 0.40 m in Figs. 2.3, 2.4, 2.5 ; see for example $L_1 = 0.35$ m to 0.38 m with the flame tube $L_2 = 0.30$ m in Fig. 2.3. These cases are characterized by a noisy sound signature which notably differs from the pure tone radiated in most other cases.

This behavior is well revealed by time traces of the pressure signal detected by microphone M_2. Two cases are plotted in Fig. 2.6. These pressure evolutions have been measured for feeding manifold lengths $L_1 = 0.18$ m and 0.21 m by using plate #4 with the flame tube $L_2 = 0.20$ m. It is seen that the amplitude, recorded in Fig. 2.6(a), is almost constant, while the one in the lower graph (b) is perturbed in a more random fashion. In this case, the main frequency observed in the pressure spectrum is displayed in the amplitude-frequency chart (see for example $L_1 = 0.35$ m to 0.38 m with the flame tube $L_2 = 0.30$ m in Fig. 2.3). In examining these situations, one notes that time trace analysis is essential to characterize the oscillations observed in the burner. The corresponding limit cycles can be roughly divided in two classes. In the first one, the amplitude is nearly constant as observed in many previous investigations (Schuller et al. (2003b); Durox et al. (2005); Noiray et al. (2008); Durox et al. (2009a)), whereas in the other class, the amplitude is variable a feature which is also noted in various other thermoacoustic coupling studies (Sterling (1993); Lamraoui et al. (2011); Kabiraj et al. (2012); J. P. Moeck et al. (2012)).

In the following chapters, the analysis will focus on these two classes of limit cycles. The stable amplitude case will be characterized experimentally and investigated theoretically in order to predict the amplitude value for all the geometries considered. Then, situations exhibiting a broader band of sound with unstable amplitude will be examined in the same way. It will be seen that there are many distinct types of oscillation featuring a broad spectral band of frequencies, regularly modulated signal sustained by two modes or even multiple well defined frequencies. In these cases, the comparison between model and experiments indicates that some predictions are possible but that the interpretation is less easy.

Part II

Analysis of the setup

Chapter 3

Setup for diagnostics

The burner presented in Chapter 1 is typified by specific conditions on its boundaries and the connection between the two ducts. These specificities need the use of other devices to determine the reflection coefficient of the combustor outlet or the flame response when the flow is submitted to disturbances. These systems are described in this chapter.

3.1 Impedance tube device

The boundary conditions can be modeled or characterized experimentally. In the present case this latter method has been applied. An experimental setup, presented in Fig. 3.1, is used to estimate the reflection coefficient. It is derived from the "ITHACA impedance tube" apparatus developed by Tran (2009) to characterize the acoustic response of perforated plates.
In the present configuration, it is specifically used to estimate the reflection coefficient of the piston head. This latter is submitted to acoustic waves of increasing amplitude levels. The configuration comprises a long cylindrical manifold connected to a loudspeaker at the end and a set of plug holes equipped with flush mounted microphones M_1 to M_3. The loudspeaker, fed by a wave generator and an amplifier, is used to produce harmonic modulations of the upstream flow which leaks from holes located near the loudspeaker. Assuming plane wave propagation, the impedance $Z_1(0)$ located at $z = 0$ can be measured for different forcing levels imposed by the loudspeaker using a three microphones measurement technique described by Chung and Blaser (Chung et al. (1980a); Chung et al. (1980b)). In the configuration displayed in Fig. 3.1, the specific acoustic impedance $\zeta_1(0) = Z_1(0)/(\rho_1 c_1)$ at the location $z = 0$ can be obtained from the pressure traces measured by microphones M_1 and M_2 :

$$\zeta_1(0)(\omega) = i\frac{\sin(\omega L_{2m}/c_1) - H_{12}(\omega)\sin(\omega L_{1m}/c_1)}{H_{12}(\omega)\cos(\omega L_{1m}/c_1) - \cos(\omega L_{2m}/c_1)} \tag{3.1}$$

where H_{12} stands for the transfer function between microphones M_1 and M_2. The quantities L_{1m} and L_{2m} are the distances of microphones M_1 and M_2 with

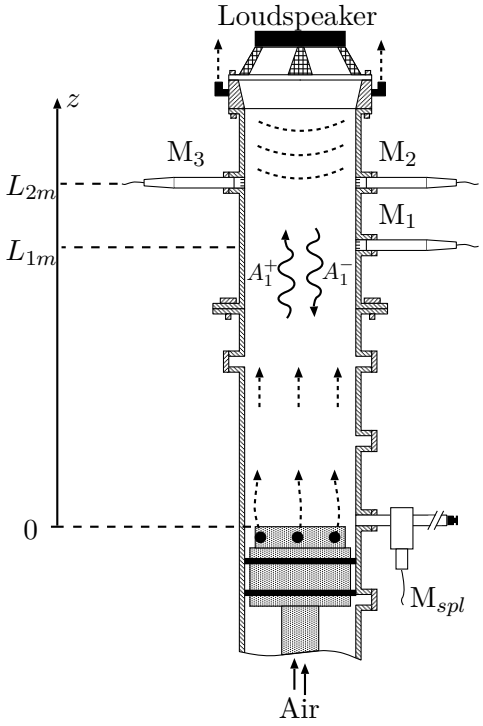

Figure 3.1: *Impedance tube device used to measure the reflection coefficient of the piston with an air flow condition equivalent to the methaneair premixture.*

respect to the piston head. The transfer function is estimated with the measurements of microphones M_1 and M_2 as $H_{12} = S_{12}/S_{11}$, where S_{12} designates the cross power spectral density between the two microphones at the forcing angular frequency ω and S_{11} the power spectral density of microphone M_1.
The loudspeaker is located 0.17 m from microphones M_2 and M_3. The sound level is controlled by a microphone M_{spl} mounted on a waveguide at the piston head plane. The three microphones M_1, M_2 and M_3 are flush mounted on the tube.
The reflection coefficient is measured with the same flow rate as the one used in the exploration of self-sustained combustion oscillations, i.e. 4.7 g.s^{-1}. Nevertheless, as the flame is not present, the methane air premixture is replaced by an equivalent flow rate of air. Air flows through the tube and is evacuated from radial orifices near the loudspeaker. As explained in Scarpato et al. (2012), two criteria have been considered to set positions L_{1m} and L_{2m} of the three microphones M_1, M_2 and M_3. Firstly, the interspace between microphones M_1 and M_2 should be chosen to set less than an half wavelength between the 2 microphones, i.e. $L_{2m} - L_{1m} \leq c/2f_{max}$. For 1.1 kHz, $L_{2m} - L_{1m} \leq 0.15$ m. In the present case, it is set to 0.05 m to ensure accurate measurements on a frequency range up to 3.4 kHz. The second criterion concerns the maximum length for L_{1m}. It is fixed by the first pressure node and thus the shorter

wavelength established in the tube. For a frequency $f = 1.1$ kHz one has to set $L_{1m} \leq 0.31$ m. In the measurements performed here $L_{1m} = 0.23$ m. The fourth microphone M_{spl} mounted on a waveguide at the piston plane $z = 0$ is used to control the Sound Pressure Level (SPL) imposed by the loudspeaker. It ensures measurements of the reflection coefficient at the same amplitude for all frequencies. For each forcing condition, a total of 65536 data points are acquired with a sampling frequency of $f_s = 16384$ Hz. Data are post processed with Matlab® and Welch's method of averaging with a Hanning windowing.
The determination of the impedance defined by Eq. (3.1) is quite sensitive to errors on distances L_{1m} and L_{2m}, which must be precisely determined. It is also important to have a correct estimate of the sound speed c_1 in the manifold, which was taken here equal to $c_1 = 346$ m.s^{-1} and the fluid characteristic impedance $Z_0 = \rho_1 c_1$ taken equal to $Z_0 = 410$ kg.m^{-2}.s^{-1} in these experiments. Accurate determination of the transfer function H_{12} requires a suitable calibration in both gain and phase of the data acquisition system. While calibration in gain is quite straightforward, phase distorsions are more difficult to reduce. The difficulty may be overcome with a microphone switching technique (Chung et al. (1980b)). A first transfer function H_{12}^o is computed for an experiment with all microphones set at their original location. The same experiment is then repeated in a switched configuration where the microphone M_2 is placed at L_{1m} and M_1 at L_{2m} (all other parameters remaining fixed). A second transfer function H_{12}^s is computed in the switched configuration. The transfer function H_{12} appearing in Eq. (3.1) is then determined as the geometric mean of these transfer functions $H_{12} = (H_{12}^s H_{12}^o)^{1/2}$. The signal to noise ratio can be further improved using an additional microphone M_3 located at L_{2m}. A coherence factor C is evaluated between the three microphones M_1 to M_3 in the original ($n = o$) and switched ($n = s$) configurations : $C^n = C_{23}^n/(C_{12}^n C_{31}^n)$, where $C_{xy} = |S_{xy}|^2/(S_{xx}S_{yy})$. The transfer function H_{12} in Eq. (3.1) is in this case replaced by the following expression : $H_{12} = [C^o H_{12}^o C^s H_{12}^s]^{1/2}$ (Chung et al. (1980a)). This last expression is useful for a precise determination of the impedance resistive and reactive parts in noisy environments as can be the case in a turbulent burner under unstable regimes (Tran et al. (2009a); Tran et al. (2009b)). The reflection coefficient of the element set at $z = 0$ is given here as a function of the specific acoustic impedance as defined later in Eq. (4.6):

$$R_1(0) = \frac{\zeta_1(0) + 1}{\zeta_1(0) - 1} \tag{3.2}$$

where $\zeta_1(0)$ corresponds to the specific acoustic impedance defined in Eq. (3.1). The impedance measurement setup and the corresponding processing tools are first validated using a known impedance before measuring the piston response to ensure accurate measurements of the reflection coefficient. The experimental procedure consists in replacing the piston with a rigid plate to obtain the response of a closed end duct. Measurements with the closed end tube are performed by increments of 100 Hz on a frequency range comprised between 100

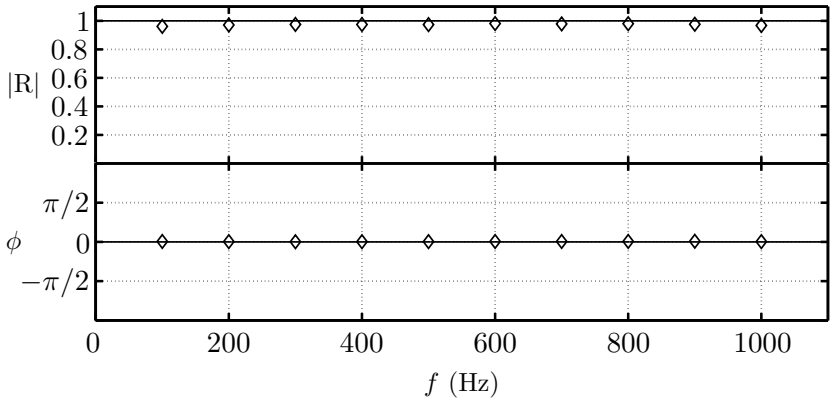

Figure 3.2: *Reflection coefficient of the closed end tube measured with the impedance tube device. ◇ symbols indicate measurements, whereas bold lines correspond to the theoretical expected values. One can see that the modulus* |R| *nearly matches the theory with* |R| = *1 while the phase is perfectly equal to 0.*

Hz and 1000 Hz. Figure 3.2 shows measurements executed with an amplitude of 110 dB controlled by M_{spl}.
Measurements yield values for the modulus of the reflection coefficient ranging between 0.96 and 0.98 and matching well the expected theoretical value of a rigid plate |R| = 1. The phase of the reflection coefficient does not exceed 0.01 radian. One can thus safely use this setup to measure the reflection coefficient of the piston head for frequencies lower than 1000 Hz.

3.2 Setup for the flame response

3.2.1 Materials and working conditions

The experimental setup sketched in Fig. 3.3 is used to measure the flame response for different amplitudes.
This burner corresponds to a reduced version of the one used in the study by keeping the same ratio between the perforated plate and the confinement tube diameters. These reduced sizes allow Laser Doppler Velocimetry (LDV) measurements as the laser beams cannot cross at the flame base in the real case. A perforated plate of thickness l = 3 mm or 15 mm is set to anchor a collection of small laminar conical flames. It comprises 129 holes of diameter $2r_p$ = 2 mm placed on a 3 mm square mesh. A methane/air mixture feeds the burner at the bottom (see Fig. 3.3). The flow rate has been adapted to keep the same mean flow velocity U_b and equivalence ratio ϕ of 1.03, as the one used in the experiments presented in Chapter 2. The length of the quartz tube L_2 is set to 0.10 m and the diameter to 0.07 m. It allows to keep the control through the loudspeaker, as longer confinement tube induces start of self-sustained combustion oscillations.

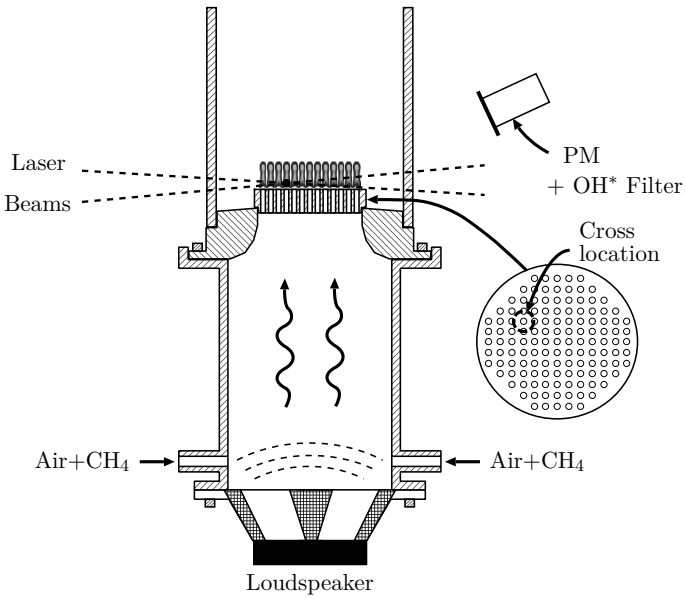

Figure 3.3: *Experimental setup used to measure the FDF. A loudspeaker is placed at the bottom of the burner and subjects the flame to harmonic fluctuations. Velocity is measured by means of LDV at the base of one flame 0.6 mm above the hole. A photomultiplier equipped with an OH* filter collects free radicals emissions.*

The loudspeaker produces velocity oscillations in a chosen frequency range which is swept between 0 and 1600 Hz. The relative fluctuation amplitude u_{rms}/U_b is varied from 0.065 to 0.516 for $l = 3$ mm (plate #3) and 0.065 to 0.774 for $l = 15$ mm (plate #4). In the experiments, the flame is enclosed with a quartz tube and a confined FDF is therefore acquired. Nevertheless, these measurements with a quartz tube were only achieved with the thickest perforated plate $l = 15$ mm. This latter adds some damping in the system and avoids start of self-sustained oscillations. In the other case $l = 3$ mm, the FDF is only estimated in an unconfined configuration. Finally, it is interesting to compare the influence of the confinement tube on the FDF. This is done with the thickest perforated plate by measuring the flame response without the quartz tube.

3.2.2 Diagnostics

Velocity oscillations are measured by means of LDV at the base of one flame 0.6 mm above the hole. The hole of crossing is selected as close to the center as possible by avoiding reflexions (see Fig. 3.3). A continuous laser, with a beam at 514.5 nm and a mixing with a Bragg cell set to 10 kHz, is used to ensure the LDV measurements. Micro-metric oil droplets (diameter $\approx 2\ \mu m$) are created with a perfume atomizer to seed the premixture (Durox et al. (1999)). A photomultiplier is used to detect the droplets passing in the volume

where the laser beams cross. A convex lens focuses the light emitted to the photomultiplier equipped with a pin hole and a filter centered on the laser wavelength. The counting rate is around 50 kHz with a validation of 60 % for plate #3 and 35 kHz with a validation of 40 to 47 % for plate #4. For the unconfined configuration with plate #4, the mixing of the Bragg cell is set to 0.2 MHz. The counting rate is in this case between 30 and 35 kHz with 35 to 40 % of validation.
A photomultiplier, equipped with an OH^* filter ($\lambda = 308$ nm) measures free radicals emissions. It gives an estimate of heat release rate fluctuations through the fluctuations of light intensity (Hurle et al. (1968); Higgins et al. (2001)).
The flame frequency response linked to a set of FTFs obtained at different amplitudes is called the Flame Describing Function (FDF) which is defined as the ratio of the relative heat release rate fluctuations to the relative velocity fluctuations. Signals are acquired with a sampling frequency $f_s = 32768$ Hz over a duration of 2 seconds. The measurements are processed with LabVIEW® to obtain the gain and the phase of the FDF which can be written as follow :

$$\begin{aligned} \mathcal{F}\left(\omega_r, u_{rms}/U_b\right) &= \frac{\widetilde{\dot{Q}}/\bar{\dot{Q}}}{u_{rms}/U_b} = \frac{\widetilde{I}_{OH^*}/\bar{I}_{OH^*}}{u_{rms}/U_b} \\ &= G\left(\omega_r, u_{rms}/U_b\right) e^{i\varphi(\omega_r, u_{rms}/U_b)} \end{aligned} \tag{3.3}$$

where ω_r indicates the angular forcing frequency and u_{rms} the root mean square velocity fluctuation measured by LDV.

Chapter 4

Acoustical key points

It is first useful to consider the acoustics of the burner configuration. This is accomplished by examining the different parts of the system separately. The duct acoustics is examined in a first step. Due to the system dimensions and the frequencies observed experimentally, only plane waves are considered to travel in the system. Then, boundary and matching conditions between the tubes are examined. Boundary conditions reveal that the piston head and the open-ended flame tube feature non-ideal reflection coefficients i.e. that the piston has a reflection coefficient which differs from a perfectly reflecting wall and that the open end differs from a pressure node. A model is proposed for the matching conditions in the injection zone hinged on the perforated plate which takes into account the ring cavity which surrounds the multipoint injection unit. This configuration is often found in practice (for example in gas turbine combustors), where the flame is not located at the junction plane between upstream and downstream cavities and it is therefore interesting to consider this aspect in further detail. An expression is derived for this specific geometry.

4.1 Duct acoustics

Thermoacoustic instabilities observed in the system under investigation involve unsteady combustion coupled to acoustic disturbances. It is then natural to begin the analysis by examining the burner acoustics. The system is characterized by low frequency unstable modes (see Chapter 2) and one may thus consider that the wave motion is longitudinal and takes place in the axial direction z. The pressure oscillations detected remain relatively weak compared to the mean pressure ($p'/p \approx 1$ %) and the analysis may be carried out by assuming that acoustic disturbances are linear. Moreover, the system operates at a low Mach flow number ($U_b/c_u \leq 0.01$) so that flow effects can be neglected in the analysis of acoustic propagation.
In each referenced tube n, temperature, density, velocity and pressure are all

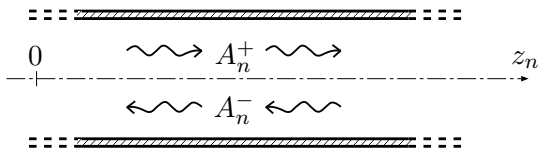

Figure 4.1: *Acoustic waves propagating in the n^{th} tube section.*

subscripted with their respective tube number. Flow variables are decomposed in terms of a mean and a fluctuating component : $a(z,t) = \bar{a}(z) + a'(z,t)$. The mean temperature $\overline{T_n}$ and density $\overline{\rho_n}$ are considered uniform in each section n. Pressure and velocity disturbances associated to sound waves propagate in the two directions as illustrated in Fig. 4.1. These perturbations are considered as harmonic functions of time, $a'(z,t) = \widetilde{a}(z)\exp(-i\omega t)$, where ω stands for the angular frequency $\omega = 2\pi f$. The modal distribution associated to these waves for the n^{th} tube is given by :

$$\begin{aligned} \widetilde{u}_n(z_n) &= \frac{1}{\rho_n c_n}\left(A_n^+ \, e^{ik_n z_n} - A_n^- \, e^{-ik_n z_n}\right) \\ \widetilde{p}_n(z_n) &= A_n^+ \, e^{ik_n z_n} + A_n^- \, e^{-ik_n z_n} \end{aligned} \tag{4.1}$$

where z_n stands for the position, $k_n = \omega/c_n$ denotes the wave number and c_n corresponds to the speed of sound which differs in the feeding manifold and the flame tube. It is worth noting that the signals detected by various sensors correspond only to the real component of these complex quantities. In the expressions developed in this manuscript, the longitudinal position in each tube is referenced with respect to the beginning of the element. The use of different origins avoids writing lengthy expressions in acoustic relations. This is illustrated in Fig. 4.2 with two tubes connected at their extremities. In the case of a single origin corresponding to the first element, the sound pressure in the second tube would be given by :

$$\widetilde{p}_2(z_2) = A_2^+ \, e^{ik_2(z_2 - z_1)} + A_2^- \, e^{-ik_2(z_2 - z_1)} \tag{4.2}$$

Using different origins, it is possible to replace $z_2 - z_1$ in Eq. (4.2) by z_2 yielding simpler expressions.

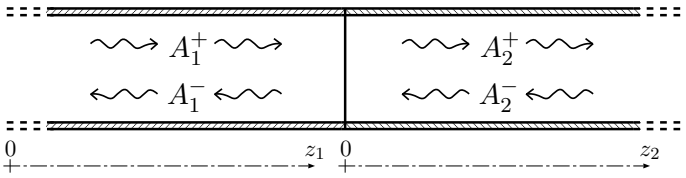

Figure 4.2: *Acoustic waves propagating in two ducts.*

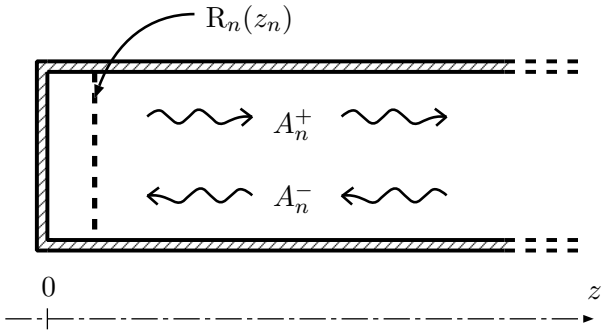

Figure 4.3: *Acoustic waves propagating in a duct and reflection coefficient defined at a location z_n.*

4.2 Interactions with the system boundary

Interaction of sound waves with the extremities of the combustor are characterized by the impedance of this section defined as the ratio of acoustic pressure to acoustic velocity (Morse et al. (1986), p. 261) :

$$Z_n(z_n) = \frac{p(z,t)}{u(z,t)} = \rho_n c_n \frac{A_n^+ \, e^{ik_n z_n} + A_n^- \, e^{-ik_n z_n}}{A_n^+ \, e^{ik_n z_n} - A_n^- \, e^{-ik_n z_n}} \tag{4.3}$$

By considering the characteristic impedance of the medium defined by $\rho_n c_n$, one can define the specific acoustic impedance in a given section by:

$$\zeta_n(z_n) = \frac{Z_n(z_n)}{\rho_n c_n} = \frac{A_n^+ \, e^{ik_n z_n} + A_n^- \, e^{-ik_n z_n}}{A_n^+ \, e^{ik_n z_n} - A_n^- \, e^{-ik_n z_n}} \tag{4.4}$$

Using the convention defined in Fig. 4.3, the reflection coefficient R_n of the n^{th} tube at z_n is given by (Rienstra et al. (2010)) :

$$R_n(z_n) = \frac{A_n^+ \, e^{ik_n z_n}}{A_n^- \, e^{-ik_n z_n}} \tag{4.5}$$

The reflection coefficient and the specific acoustic impedance of Eq. (4.4) are linked by the following expression :

$$R_n(z_n) = \frac{\zeta_n(z_n) + 1}{\zeta_n(z_n) - 1} \tag{4.6}$$

4.2.1 Upstream boundary condition

The piston head response has been characterized by making use of an impedance tube testing as described in Chapter 3. The piston is set in the feeding manifold as depicted in Fig. 3.1 and its reflection coefficient is measured in two cases. The first series of measurements is carried out without flow. The

second set of data corresponds to the nominal flow condition in which the mass flow rate is fixed at 4.7 g.s^{-1}. Results obtained for the piston reflection coefficient without flow are displayed in Fig. 4.4. Regarding the modulus |R|, it is confirmed that the head does not fully reflect the incoming sound waves. For some frequencies, the modulus |R| is less than 0.8. The phase also differs from zero, indicating that the piston head induces a small time lag in the reflected waves. It is interesting to see that the larger deviations, with respect to a perfectly reflecting boundary, take place at low frequencies.
Effects of the mean flow in the perforations are now examined in Fig. 4.5. The modulus still features a wavy shape over the frequency range investigated. Its values evolve between |R| = 0.6 and 1, but this variation is more regular than in the absence of flow. Deviations of the phase lag with respect to zero are also attenuated. These experiments indicate that the piston head does not fully reflect incoming waves. This is taken into account in the stability analysis carried out in the following chapters by linking the amplitude of the reflected pressure wave A_1^+ at the piston head, to the incoming wave amplitude A_1^- by the reflection coefficient $R_1(0)$:

$$A_1^+ = A_1^- \, |R_1(0)| \, e^{i\phi_1(0)} \tag{4.7}$$

where $|R_1(0)|$ and $\phi_1(0)$ are defined by the data presented in Fig. 4.5. Additional measurements have been carried out to determine the input level influence on the reflection coefficient values of the piston head. The range of frequencies presented in Fig. 4.5 was swept by increasing the amplitude up to 130 dB at the location of microphone M_{spl}. Results were found to be independent of the input level, indicating that the modulus $|R_1(0)|$ and phase $\phi_1(0)$ of the reflection coefficient only depend on the frequency as shown in Fig. 4.5. These values will be considered to be applicable in the whole amplitude range and used as such in the nonlinear stability analysis of the system.

4.2.2 Downstream boundary condition

The combustion zone is enclosed in quartz tubes of different lengths which are open to atmospheric conditions. Different approximations can be used to model this open outlet, which are briefly presented below.
Considering an open duct as shown in Fig. 4.6, a first possibility is to neglect the inertia of the column of gas at the exit of the confinement tube by considering that the tube outlet constitutes a pressure node $\widetilde{p}_2(L_2) = 0$. This crude model however does not take into account the part of acoustic energy which is radiated outside the tube. When sound is radiated at the tube outlet, the internal acoustic field is modified in turn. One generally uses an end correction to take this phenomenon into account. In this model, the pressure node is slightly displaced to a point which is further away from the tube outlet : $\widetilde{p}_2(L_2 + \delta_2) = 0$. For long tubes, the end correction corresponds to a fraction of the tube radius and depends on the Mach number of the flow, Strouhal and Helmholtz

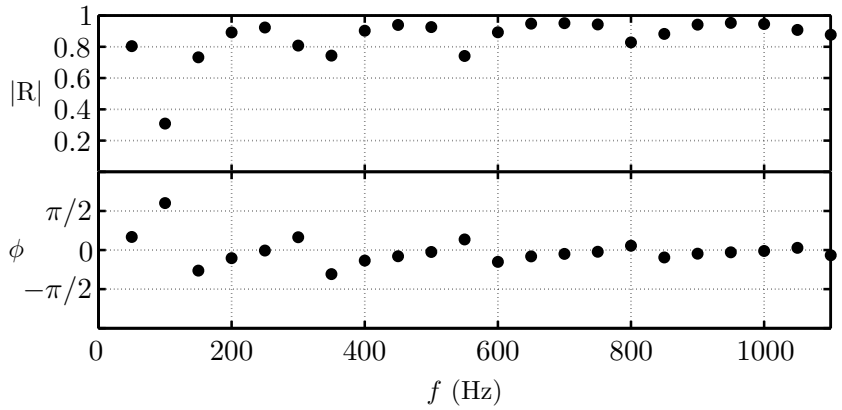

Figure 4.4: *Reflection coefficient of the piston head measured with the impedance tube in the absence of flow. Filled circle symbols (•) indicate measurements. One can see that the modulus* |R| *does not correspond to* |R| = 1 *while the phase differs from 0. Large differences pertain to low frequencies.*

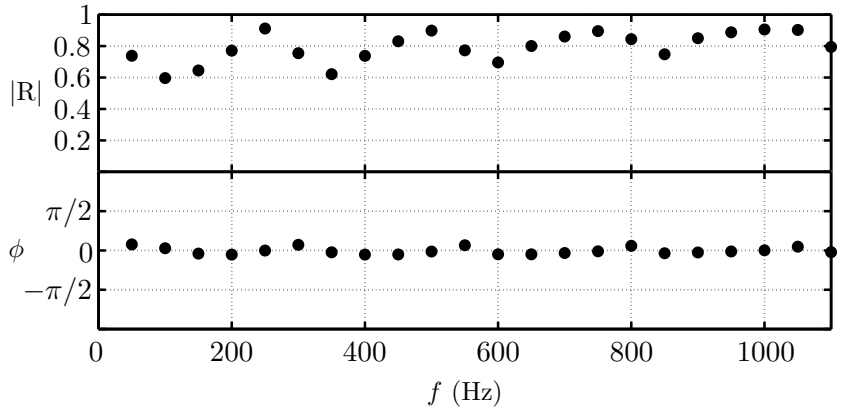

Figure 4.5: *Reflection coefficient of the piston head measured with the impedance tube for a nominal flow rate of 4.7 g.s*$^{-1}$*. Filled circle symbols (•) indicate measurements. One can see that the modulus* |R| *does not correspond to* |R| = 1 *while the phase slightly differs from 0.*

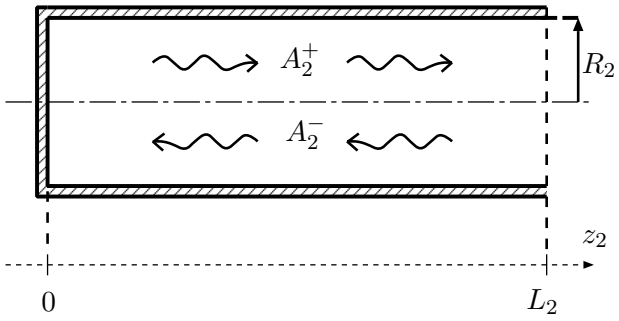

Figure 4.6: *Open-ended duct with two waves propagating in the two directions. The speed of sound is designated as c_2.*

numbers (Rienstra et al. (2010)). For an unflanged pipe traversed by a low Mach number flow, one generally uses $\delta_2 = 0.61\,R_2$, where R_2 designates the radius of the tube (Levine et al. (1948)) as depicted in Fig. 4.6. This model has been used as a first approximation in many calculations carried out in the present work. It was then reconsidered when detailed comparisons between experiments and predictions indicated that it was more adequate to use at the flame tube outlet, a condition varying as a function of frequency.
The radiation impedance was used to this purpose. For low frequency sound waves in an unflanged open pipe, one can use a first approximation valid in the limit $k_2 R_2 \ll 1$ (Levine et al. (1948); Rienstra et al. (2010))[1] :

$$\zeta_2(L_2) = \frac{1}{4}\left(\frac{\omega R_2}{c_2}\right)^2 - i\,0.61\,\frac{\omega R_2}{c_2} \tag{4.8}$$

The corresponding reflection coefficient writes :

$$\mathrm{R}_2(L_2) = \frac{A_2^- e^{-ik_2 L_2}}{A_2^+ e^{ik_2 L_2}} = \frac{\zeta_2(L_2) - 1}{\zeta_2(L_2) + 1} \tag{4.9}$$

The reflection coefficient is plotted in Fig. 4.7 for the frequency range of interest when the temperature in the flame tube is set to $T_2 = 900$ K. It will be shown in the following chapters that this mean temperature pertains to small confinement tubes.
This figure indicates that the amplitude of the reflected waves is reduced as the frequency increases. Low frequency waves are reflected with a phase lag of $-\pi$ with respect to the incoming waves that is progressively reduced when the frequency increases. At 1000 Hz, the phase lag of the reflected wave lies around $-\pi/2$ while the amplitude equals 0.8 times that of the incoming wave.

[1] It should be noted that the imaginary component is negative here, while the formula given in Rienstra et al. (2010) considers a positive value. This is due to different conventions used for the acoustic waves ($p(x,t) = \Re(\widetilde{p}\exp(i\omega t))$ instead of $p(x,t) = \Re(\widetilde{p}\exp(-i\omega t))$ used here).

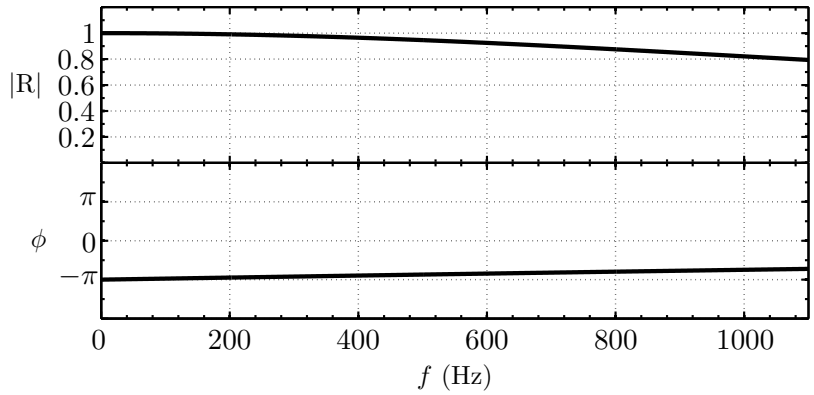

Figure 4.7: *Reflection coefficient* $\mathrm{R}_2(L_2)$ *of the confinement tube outlet. The temperature is fixed to* $T_2 = 900$ *K. For the increasing frequency, the modulus* $/\mathrm{R}_2(L_2)/$ *drops down regularly while the phase lag* $\phi_2(L_2)$ *is reduced.*

4.3 Multipoint injection zone

The methane/air mixture is injected in the flame tube through a perforated plate of thickness l which is used to anchor a collection of small laminar conical flames. A schematic of this injection unit is presented in Fig. 4.8. Acoustic propagation in this element is considered in the present section. It is first important to note the location of the combustion zone in the flame tube. Combustion takes place at the perforation outlets in a plane which is slightly different than that corresponding to the bottom of the flame tube. The perforated plate protrudes in the flame tube and forms a ring cavity around the combustion zone. The upstream and downstream cavities feature distinctive temperatures T_1 and T_2 while the ring cavity could be considered to have a different value T_r. For the sake of simplicity in modeling, it is assumed in what follows that $T_r = T_2$. The second aspect that should be considered in the model is the effect of the perforated plate.

4.3.1 The ring cavity

Acoustic propagation in the ring cavity is taken into account in the modal analysis of the system. The cavity extends over a length l equal to the thickness of the perforated plate located in the center of the flame tube (see Fig. 4.8). The acoustic pressure in the ring cavity is noted $\widetilde{p}_r$. The sound pressure above the perforated plate is noted $\widetilde{p}_p$. It is possible to build a one dimensional representation of these elements by matching the acoustic pressure and the acoustic flowrate.
The acoustic pressure is considered uniform over the section area S_2 :

$$\widetilde{p}_r(l) = \widetilde{p}_p(l) = \widetilde{p}_2(0) \tag{4.10}$$

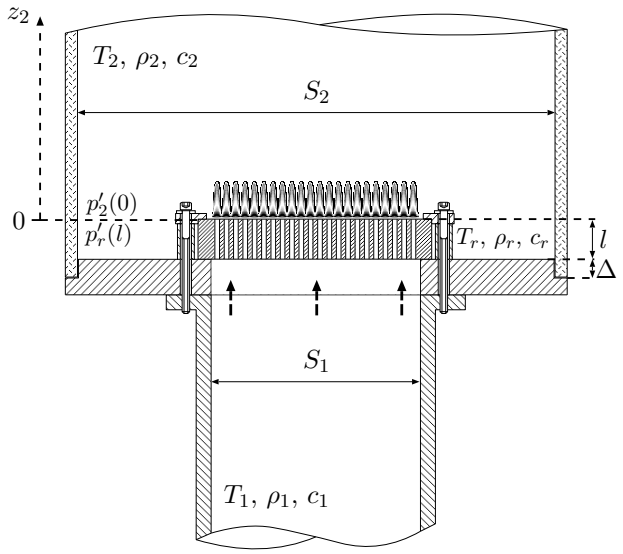

Figure 4.8: *Details of the injection zone. The perforated plate and the shoulder supporting the quartz tube decrease the confinement tube length L_{quartz} seen by the flame. In the anchoring flame plane, the confinement length L_2 corresponds to L_{quartz} - $(l + \Delta)$.*

A balance for the acoustic volume flow rate inside the flame tube yields :

$$S_2\widetilde{u}_2(0) = S_{2r}\widetilde{u}_r(l) + S_{2p}\widetilde{u}_p(l) \tag{4.11}$$

where S_{2r} and S_{2p} respectively designate the ring cavity surface area and the perforated plate surface area. Thus, the flame can be introduced by considering a balance for the acoustic volume flow rate between the downstream and upstream parts. The balance takes place between $S_{2p}\widetilde{u}_p(l)$ and $S_1\widetilde{u}_1(L_1)$. This point will be examined in the following chapter. It is useful to combine these expressions to determine the corresponding impedance $\zeta_2(0)$ of these elements that will be used in the one dimensional modal analysis with a compact treatment of the flame tube inlet. One obtains :

$$\frac{S_2}{\zeta_2(0)} = \frac{S_{2r}}{\zeta_r(l)} + \frac{S_{2p}}{\zeta_p(l)} \tag{4.12}$$

where $\zeta_r(l)$ is the specific impedance of the ring cavity and $\zeta_p(l)$ denotes the specific impedance at the perforated plate outlet. This latter component will be examined in the next section. The specific acoustic impedance of the ring cavity corresponds to that of an annular duct perfectly closed at one extremity and open on the other one. At the bottom of the ring cavity, the acoustic velocity must vanish yielding :

$$\widetilde{u}_r(0) = 0 \tag{4.13}$$

Using Eq. (4.13) to determine velocity and pressure fluctuations at $z = l$, one obtains the following expression for the specific acoustic impedance of the ring cavity :

$$\zeta_r(l) = \frac{e^{ik_2 l} + e^{-ik_2 l}}{e^{ik_2 l} - e^{-ik_2 l}} = \frac{-i}{\tan(k_2 l)} \tag{4.14}$$

4.3.2 The perforated plate

The mean flow injected from the piston head in the feeding manifold passes through the small circular channels of the perforated plate used to anchor the flame. This latter element influences the relation of pressure and velocity disturbances across the perforations. Different models were proposed to consider pressure and velocity relations across perforations (Howe (1979); Crandall (1926); Melling (1973)). The model devised by Howe (1979) takes into account a vortex street shed at the perforation outlet which is responsible for sound absorption. It is well appropriate for the design of acoustic dampers (see for example Scarpato et al. (2012)). In the present case, flames are anchored on the perforated plate and hinder the creation of vortices (Schuller et al. (2009)). Acoustic dissipation does not take place at the perforation outlet but it is merely due to viscous effects inside the channels. Crandall (1926) derived a model for acoustic perturbations in a single channel that was later used by Melling (1973) to analyze sound absorption by perforated plates by taking into account dissipation in the shear layer of the perforations. This model was adapted by Noiray (2007) to represent the dynamics of a perforated plate with a set of flames anchored on the top. The reflection coefficient of this arrangement comprising a perforated plate and a set of flames was later characterized by Schuller et al. (2009). Experiments confirmed predictions over the low frequency range up to 1000 Hz and for different forcing levels. The same model is used in the present study to link acoustic disturbances across the perforated plate. As the wavelength of disturbances considered are long compared to the perforated plate thickness, the acoustic velocity perturbations oscillate in a bulk mode in the perforations. Pressure fluctuations across the perforations are linked by :

$$\widetilde{p}_p(l) - \widetilde{p}_p(0) = i\,\omega\rho_1 l \left[1 + \frac{l_\nu}{r_p}(1+i)\right] \widetilde{u}_p \tag{4.15}$$

where $l_\nu = (2\nu/\omega)^{1/2}$ designates the acoustic boundary layer thickness, $\widetilde{u}_p$ denotes the bulk velocity oscillation in the perforation of radius r_p and length l. A balance for the acoustic flow rate also yields :

$$S_1\widetilde{u}_1(L_1) = NS_p\widetilde{u}_p \;\Leftrightarrow\; \widetilde{u}_1(L_1) = \mathcal{P}\widetilde{u}_p \tag{4.16}$$

where N denotes the number of perforations, $S_p = \pi r_p^2$ is the cross section area for one hole and $\mathcal{P}$ stands for the perforated plate porosity. It is worth noting

that the pressure disturbances at the perforation extremities also correspond by continuity to the pressure oscillation in the feeding manifold $\widetilde{p}_p(0) = \widetilde{p}_1(L_1)$ and the pressure fluctuation at the flame tube inlet $\widetilde{p}_p(l) = \widetilde{p}_2(0)$. Combining Eqs. (4.15) and (4.16), the specific acoustic impedance of the perforated plate can be determined as follows :

$$\zeta_p(l) = \frac{\widetilde{p}_p(l)}{\rho_2 c_2 \widetilde{u}_p} = \frac{\mathcal{P}}{\rho_2 c_2}\left\{\frac{i\,\omega\rho_1 l}{\mathcal{P}}\Big[1 + \frac{l_\nu}{r_p}\,(1+i)\Big] + \frac{\widetilde{p}_1(L_1)}{\widetilde{u}_1(L_1)}\right\} \tag{4.17}$$

Chapter 5

Flame dynamics and "harmonic equivalent" formalism

The determination of the Flame Describing Function (FDF) is discussed in this chapter. The setup presented in Chapter 3 is first used to measure the velocity profile in a perforation of the flame holder. FDF measurements are then carried out in confined and unconfined environments. The FDFs are determined in situations where self-sustained oscillations are absent. Such oscillations would hinder any control from the loudspeaker. FDF data obtained in confined and unconfined situations are then compared. It is found that the gain G and phase φ are nearly identical in the two cases. The two FDFs considered for the study of plate #3 and #4 are consequently presented. Finally, the reflection coefficient of the flame is introduced. This quantity is measured for some selected situations and compared to the one deduced from the FDF. This indicates that it is possible to determine the flame response with two different techniques and confirms that the presence of the flame tube does not influence the response.

5.1 Flame dynamics and velocity profile

The experiments presented in Chapter 2 indicate that the flame is susceptible to self-sustained oscillations by coupling with the acoustics of the system. Energy derived from the flame oscillations feeds the acoustic modes, closing the loop of the self-sustained oscillations as shown in Fig. 4 presented in the introduction of this document. To represent the link between the flow perturbations and the heat release rate fluctuations one may use the concept of flame transfer function (FTF). Considering the sensitivity of the flame to velocity oscillations, it is possible to determine its response in term of heat release rate fluctuations for various frequencies. The FTF is defined as the fundamental

normalized component of heat release rate fluctuations ($\widetilde{\dot{Q}}/\overline{\dot{Q}}$) over the fundamental normalized component of velocity fluctuations (u_{rms}/U_b) at the flame base:

$$\mathcal{F}(\omega) = \frac{\widetilde{\dot{Q}}(\omega)/\overline{\dot{Q}}}{u_{rms}/U_b} \tag{5.1}$$

Nevertheless, as explained in the introduction of the manuscript the flame response changes with the amplitude of oscillation. It is important to take this into account and use the FDF which depends on frequency and amplitude of the input :

$$\mathcal{F}(\omega, |u_{rms}/U_b|) = \frac{\widetilde{\dot{Q}}(\omega, |u_{rms}/U_b|)/\overline{\dot{Q}}}{u_{rms}/U_b} \tag{5.2}$$

The FDF is determined experimentally by using the setup presented in Chapter 3, Fig. 3.3. In a first step, it is important to estimate the bulk velocity U_b inside the perforations of the flame holder. This gives the dimensionless parameter u_{rms}/U_b for the FDF. This velocity ratio sets the position for each series of measurements acquired in the frequency range of interest and defines the FDF evolution as a function of the amplitude u_{rms}/U_b. A laser Doppler velocimeter (LDV) system is used to measure velocities above a perforation and allows to determine the velocity profile along the radius of one hole. Figures 5.1 and 5.2 exhibit the profiles respectively acquired on the thin and the thick perforated plates 0.7 mm above the hole. The flame is present and flow rate is set according to the conditions defined in Sec. 3.2.1. The loudspeaker is turned off and no harmonic forcing is applied to the flow. Measurements are carried out upstream the flame front in the volume of fresh gas.

It is interesting to note the effect of the boundary layer thickness on the velocity profile. For the thickest perforated plate, the boundary layer is developed as viscous effects are more important in the longer channels. This yields a parabolic mean profile reaching 6 m.s^{-1} in the center. For the thinner perforated plate, the profile is flattened in the center, limiting the amplitude to 4.8 m.s^{-1}. Nevertheless, the distribution over the surface area is almost the same in the two cases, and one calculates a bulk velocity of 3.03 m.s^{-1} for the thin perforated plate and 3.23 m.s^{-1} for the thick one. By considering the flow rate for a channel of the flame holder determined from the massflow controller indications, one finds $U_b = 3.1$ m.s^{-1}, which allows to estimate a relative error to measurements. One finds 2 % for the thin perforated plate and 4 % for the thick one. Based on that, the bulk velocity inside the perforations is fixed to $U_b = 3.1$ m.s^{-1} for the rest of the study.

Regarding the rms values, it is seen that the fluctuation amplitude is located at the edges of the hole for the thin perforated plate, where the velocity gradient is the steepest. Thus, one may argue that the flame surface will move in a different fashion between the thin and the thick perforated plate, indicating a

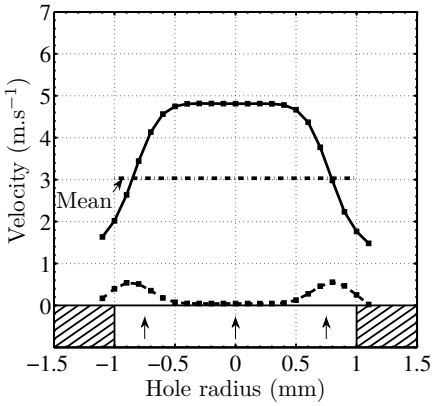

Figure 5.1: *Velocity profile above one hole for the thin perforated plate l = 3 mm. The bold line indicates the mean velocity profile while dashed line is linked to the remanent rms value in this unforced situation. The dash-dotted line is used to mark the mean value calculated from the mean profile on the complete hole surface area.*

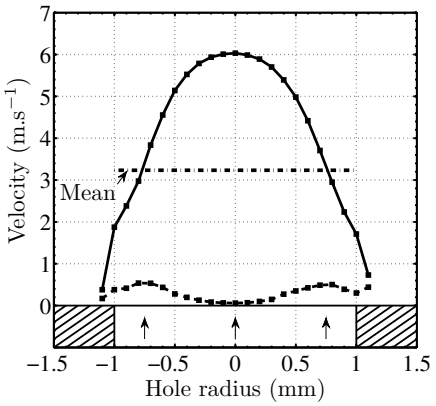

Figure 5.2: *Velocity profile above one hole for the thick perforated plate l = 15 mm. The bold line indicates the mean velocity profile while dashed line is linked to the remanent rms value in this unforced situation. The dash-dotted line is used to mark the mean value calculated from the mean profile on the complete hole surface area.*

change in the flame response. This point will be examined in the next section with the FDF measurements.

5.2 FDF measurements

The FDF has been determined for forcing frequencies ranging from 0 to 1600 Hz. A first examination is carried out by comparing gain and phase between the unconfined and confined configurations equipped with the thickest perforated plate l = 15 mm. Results for gain and phase are plotted in Fig. 5.3. Six amplitudes u_{rms}/U_b have been considered. The unconfined values appear as gray lines (**–**) while the confined case is displayed as black lines (**–**).
First of all, one finds that the gain and phase nearly match in all cases. It should be noted that whilst the amplitude level is increased, the frequency range where measurement are feasible diminishes. This is due to a lack of efficiency of the loudspeaker at high amplitude and high frequency. Regarding the gain, the agreement is well marked for lower fluctuation levels. The bounce above unity between 0 and 550 Hz exhibits higher values in the unconfined case from $u_{rms}/U_b = 0.32$ to the largest amplitudes. Nevertheless, the decreasing part above 550 Hz is close to the confined case. The phase is almost the same for all amplitudes over the range of frequencies between 0 to 850 Hz. The lower fluctuation level allowing measurements at higher frequencies, it is possible to distinguish higher phase values in the unconfined situation beyond 850 Hz.

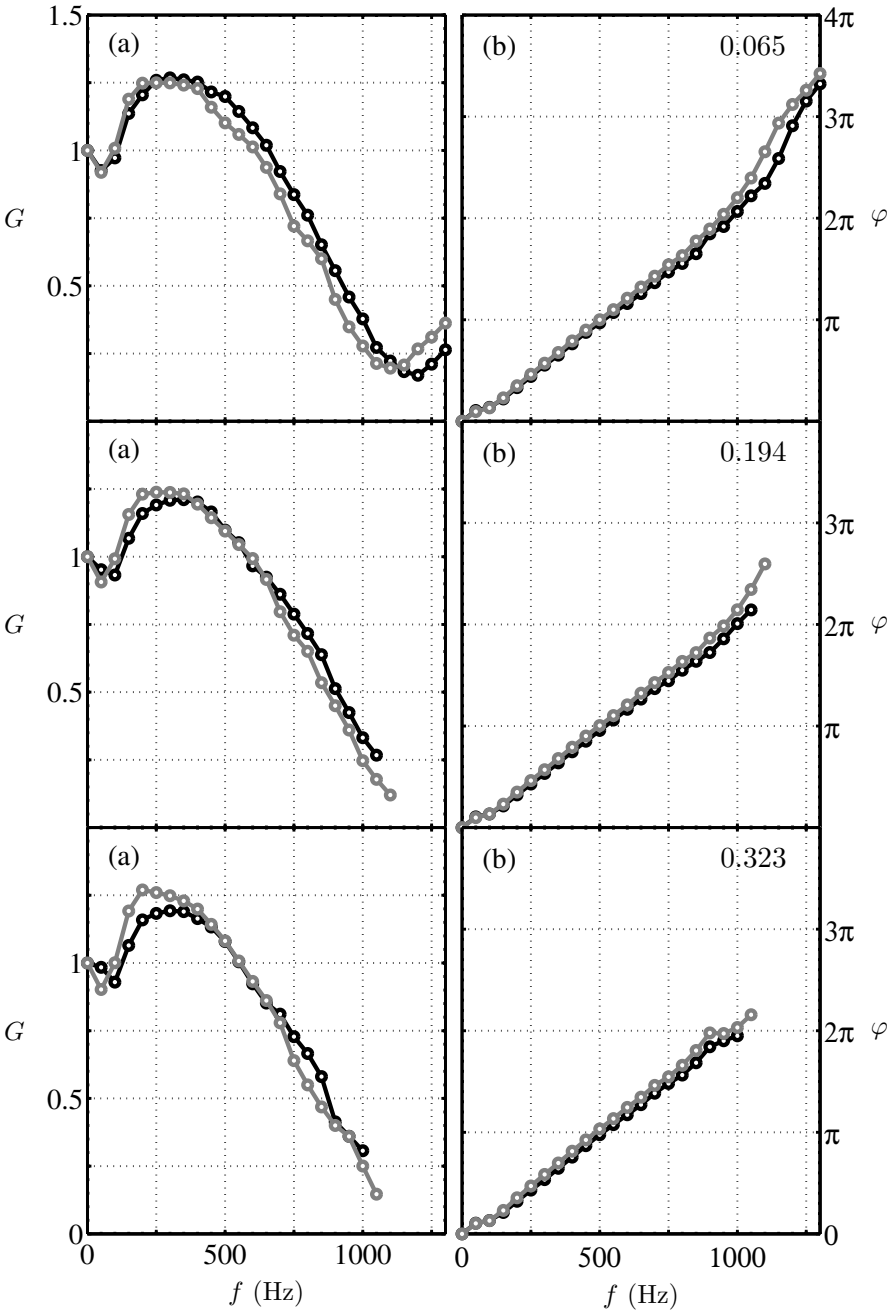
(a)
(b)
0.065
0.194
0.323
G
φ
f (Hz)
1.5
1
0.5
0
4π
3π
2π
π
500
1000

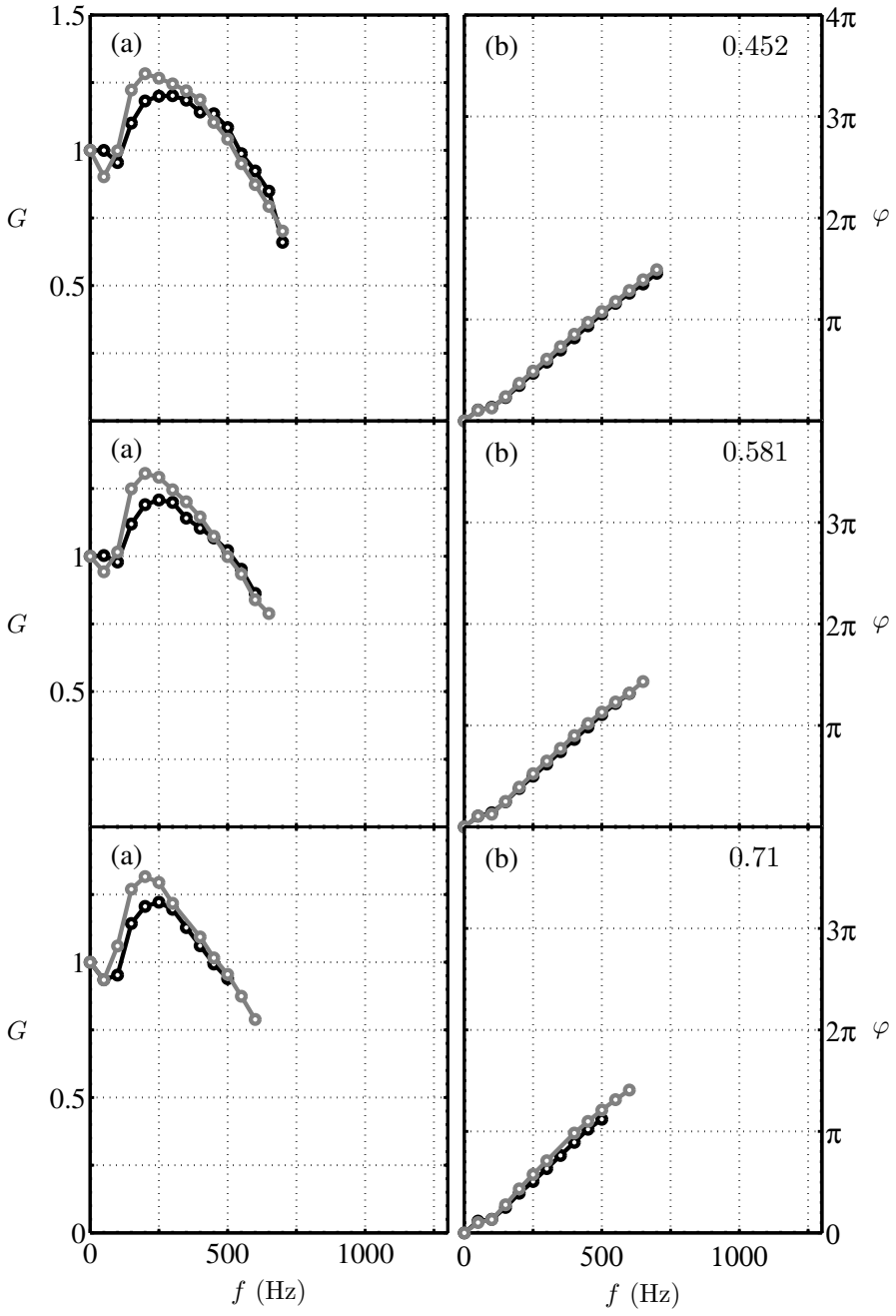

Figure 5.3: *FDF measurements in confined and unconfined situations. The black line (—) pertains to the confined configuration with $L_2 = 0.10$ m while the unconfined flame measurements are plotted as gray lines (—). Different amplitudes have been considered. Each relative fluctuation level u_{rms}/U_b is indicated on the phase graph (b). The corresponding gain is displayed on the left hand side (a).*

However, this difference is negligible. Based on that, one may consider that the flame response remains the same and does not depend on the upstream condition. It must be stressed that this case corresponds to a flame response with a collection of small laminar conical flames embedded in a confinement tube of larger diameter. One might not infer the same conclusions for other configurations. For example, the nonlinear flame response of A. Birbaud et al. (2007) is modified in case C when the flame tube diameter is decreased and interacts with the flame front. The flame response is also modified when the burnt gases cannot fully expand as demonstrated in the recent analysis of Cuquel et al. (2013).

It is now interesting to examine measurements of the flame response over a range of fluctuation amplitudes. Two FDF are considered in what follows. The first relates to the perforated plate of small thickness $l = 3$ mm, while the second is linked to the thick flame holder $l = 15$ mm. Figure 5.4 displays the different series of data for the thin perforated plate $l = 3$ mm. The fluctuation level u_{rms}/U_b is indicated in the center. The measurements have been carried out without confinement tube to prevent the establishment of self-sustained combustion oscillation. The gain G is drawn on the left (a) while the phase φ appears on the right (b).

When the amplitude increases, the gain G drops and phase lag φ is shifted and increases its slope, confirming the nonlinear behavior of the flame. As it is shown in Fig. 5.3, FDF data are limited due to a lack of efficiency of the loudspeaker at high amplitude and high frequency. The flame acts as a low pass filter with a significant overshoot at higher frequencies and low fluctuation amplitudes. This behavior was demonstrated to result from interfering phenomena (Schuller et al. (2003a); Durox et al. (2009b); Kornilov et al. (2009)). The phase evolves in a quasi linear fashion with the frequency and is sensitive to the fluctuation level.

The second FDF is drawn in Fig. 5.5. Measurements have been carried out with a small flame tube $L_2 = 0.10$ m and the perforated plate of thickness $l =$ 15 mm. On the one hand, phase and gain evolution feature the same trends as the one observed with the thin perforated plate. The gain drops while the phase shifts as a function of the increasing amplitude. On the other hand, it is possible to note some differences. Regarding the gain curve for the first amplitude with $l = 3$ mm, a minimum is reached at 900 Hz (see Fig. 5.4). This minimum is found for 1200 Hz with the thick perforated plate $l = 15$ mm. Hence, the finite gain covers a wider frequency range. Besides, the phase slope is smaller. It reaches 4π at 1600 Hz, while this value is passed around 1200 Hz with the thin perforated plate. Concerning the amplitude, one can see that the phase sensitivity is less visible.

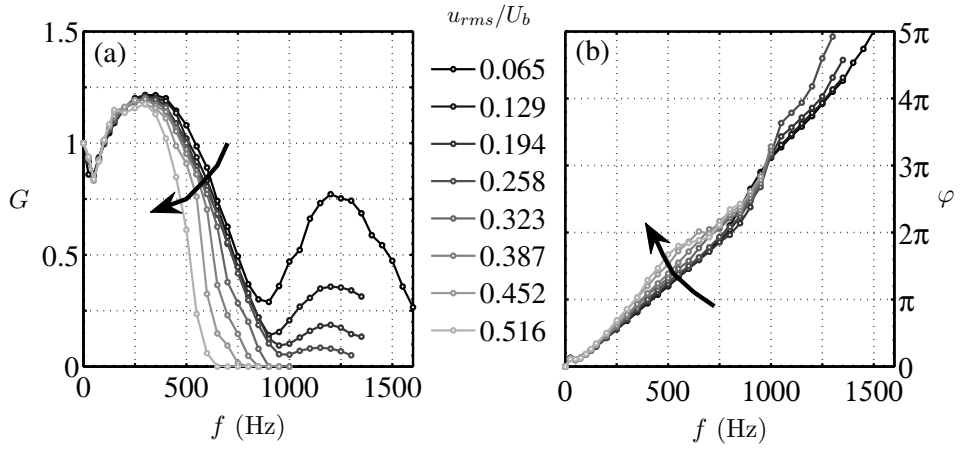

Figure 5.4: *FDF measurements for the whole range of amplitudes and frequencies. The perforated plate thickness is set to l = 3 mm in an unconfined situation. A gray scale shows the increasing level of fluctuations. (a) shows the gain G, while (b) corresponds to the phase φ. One can see that the gain drops and the phase shifts as the amplitude grows. This is indicated by the arrows in the graphs.*

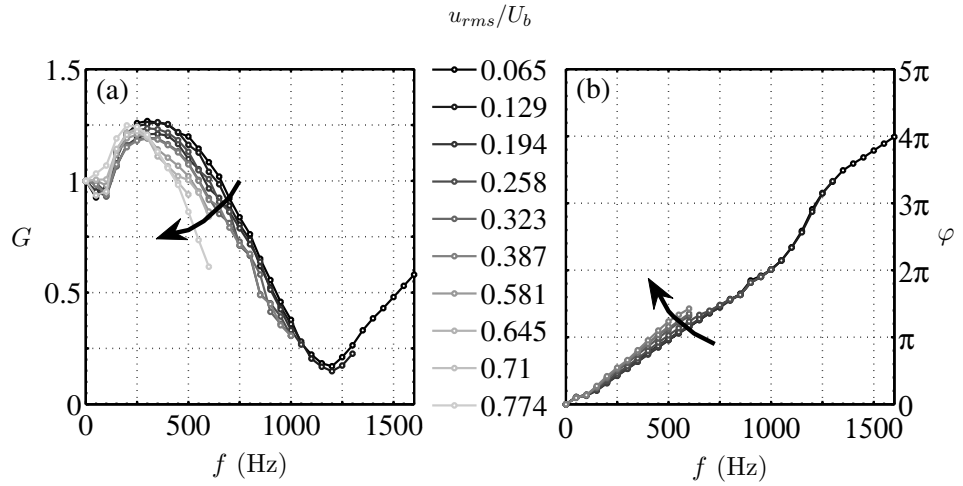

Figure 5.5: *FDF measurements for the whole range of amplitudes and frequencies. The perforated plate thickness is set to l = 15 mm with a small flame tube L_2 = 0.10 m. A gray scale shows the increasing level of fluctuations. (a) shows the gain G, while (b) corresponds to the phase φ. The decrease of the gain as a function of frequency is more spread compared to data obtained for the thinner perforated plate, while the phase slope is smaller and its amplitude sensitivity less visible.*

5.3 Jump condition between two sections of the burner and FDF

The acoustic jump condition between the upstream and downstream components of the combustor includes the flame located at the interface of the two cavities. This jump condition can be derived from an integration of the wave equation for a compact reacting flows. A simple analysis can be found in Blackshear Jr. (1953), but a more detailed derivation is presented in Le Helley (1994) or Poinsot et al. (2012) (Chapter 8). By considering the characteristics of the present configuration, the wave equation is linearized in the same way. In addition, it is well known that for low Mach number reactive flows, pressure disturbances remain unchanged across the reaction zone. Thus, from this isobaric condition, the integration of the linearized wave equation leads to the condition between the two sections separated by the flame. The acoustic volume flow rate experiences a jump through the flame region fixed by :

$$S_2\widetilde{u}_2(0) - S_1\widetilde{u}_1(L_1) = \frac{\gamma-1}{\rho_1 c_1^2}\widetilde{\dot{Q}} \tag{5.3}$$

where S_1 represents the surface area of the upstream part linked to the feeding manifold and S_2 the surface area of the flame location. For the present burner, which features a change of surface area between the upstream and downstream parts, it is important to note that the flame location can be modeled in two manners. This has been examined in Chapter 4 where it was shown that the ring cavity surrounding the flame location could be included by dividing S_2 in two surface areas. This induces two different jump conditions for the conservation of the acoustic volume flow rate. In the first one, the surface area S_2 corresponds to the section of the confinement tube and does not involve the ring cavity. The jump condition for the acoustic volume flow rate is devised as detailed in Eq. (5.3). In the other case, one divides the acoustic volume flow rate of the downstream part in two components as shown in Eq. (4.11) of the preceding chapter. So, the value $S_2\widetilde{u}_2(0)$ of Eq. (5.3) is replaced by $S_{2p}\widetilde{u}_p(l)$, limiting the flame influence to the perforated plate :

$$S_{2p}\widetilde{u}_p(l) - S_1\widetilde{u}_1(L_1) = \frac{\gamma-1}{\rho_1 c_1^2}\widetilde{\dot{Q}} \tag{5.4}$$

where γ is the specific heat ratio and $\widetilde{\dot{Q}}$ denotes heat release rate fluctuations. The right hand side term of Eq. (5.3) can be expressed by taking into account the response of the flame to velocity fluctuations with a Flame Describing Function (FDF). FDF measurements are plotted in Figs. 5.4 and 5.5 in terms of gain G and phase φ defined as :

$$\mathcal{F}\left(\omega_r, u_{rms}/U_b\right) = \frac{\widetilde{\dot{Q}}/\overline{\dot{Q}}}{u_{rms}/U_b} = G\left(\omega_r, u_{rms}/U_b\right) e^{i\varphi(\omega_r, u_{rms}/U_b)} \tag{5.5}$$

where $\overline{\dot{Q}}$ stands for the mean value of the heat release rate and U_b denotes the bulk flow velocity in a perforation. The FDF depends on both the angular frequency $\omega_r = 2\pi f$ and the relative fluctuation amplitude u_{rms}/U_b. The modifications of the gain and phase with the amplitude emphasize the need of a nonlinear stability analysis. The nonlinear behavior of the gain corresponds to a transfer of energy to higher harmonics as the amplitude increases. For a fixed forcing frequency, the phase lag increases with the forcing level indicating that the flames become more compact at high forcing amplitudes and that the time lag describing the interaction with incoming velocity disturbances is reduced.

To use the FDF measurements for a stability analysis, one has to interpolate and extrapolate the available data to cover missing areas. Considering the right hand side in Eq. (5.3) and the FDF representation in Eq. (5.5), these quantities are linked by :

$$\begin{aligned} \frac{\gamma-1}{\rho_1 c_1^2}\,\widetilde{\dot{Q}} &= \frac{\gamma-1}{\rho_1 c_1^2}\,\frac{\widetilde{\dot{Q}}\big/\overline{\dot{Q}}}{\widetilde{u}_{rms}/U_b}\,\frac{\widetilde{u}_{rms}/U_b}{1\big/\overline{\dot{Q}}} \\ &= \frac{\gamma-1}{\rho_1 c_1^2}\,\overline{\dot{Q}}\,\mathcal{F}\left(\omega_r, u_{rms}/U_b\right)\frac{\widetilde{u}_{rms}}{U_b} \end{aligned} \tag{5.6}$$

where the bulk velocity in the perforation U_b is determined from the mass flow rate across one hole. In the present study, air and methane are considered to be ideal gases. In this case, the speed of sound is given by $c_1^2 = \gamma r T_1$ and the specific heat at constant pressure writes $c_p = \gamma r/(\gamma - 1)$. In these expressions, r is assumed to be constant. This approximation is reasonable for air combustion systems due to the large dilution of the reactants and products by nitrogen. The specific heat c_p and specific heat ratio γ are in principle functions of temperature. A mean value is considered in the present calculations with $\gamma = 1.4$. The mean heat release rate may be written as $\overline{\dot{Q}} = \dot{m} c_p (T_f - T_1)$, where $\dot{m} = \rho_1 N S_p U_b$ denotes the mixture mass flowrate in the set of perforations and T_f is the adiabatic flame temperature (equal to $T_f = 2000$ K for the equivalence ratio used in these experiments). Combining these expressions, one obtains a matching condition for the acoustic volume flow rate. The jump across the flame sheet depends on both FDF gain G and phase φ :

$$S_2\widetilde{u}_2(0) - S_1\widetilde{u}_1(L_1) = G\,e^{i\varphi}\,S_1\left(\frac{T_f}{T_1} - 1\right)\widetilde{u}_1(L_1) \tag{5.7}$$

where G and φ depend on both angular frequency ω_r and relative amplitude u_{rms}/U_b.

5.4 FDF and flame reflection coefficient

Another interesting approach to characterize the flame response to flow perturbations is linked to the reflection coefficient $\mathrm{R}_1(L_1)$ of the flame anchored on its

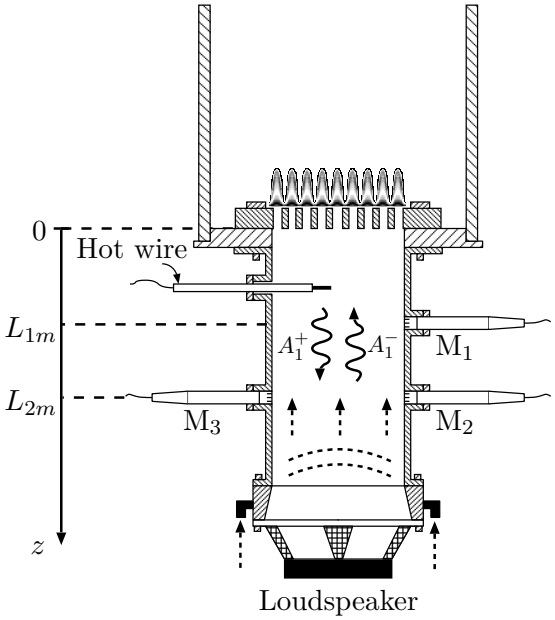

Figure 5.6: *Impedance tube configuration used to measure the reflection coefficient of the flame with its perforated plate. The system is fed with a methane-air mixture at the nominal flow rate used in the experiments on self-sustained combustion oscillations, i.e 4.7 g.s^{-1}.*

perforated plate. The reflection coefficient is related to the impedance of the device and defines the ratio between the reflected and incoming waves. This point has already been considered by B. T. Zinn et al. (1982) to measure the response of solid propellant by adapting an impedance tube. The unconfined version of the present burner has also been characterized for some amplitudes by Noiray (2007) to initiate a linear analysis of the combustion-acoustic coupling. Results indicate that the flame response was fairly well obtained by means of this technique and it is therefore considered in the confined version of the burner.

5.4.1 Experimental setup

The experimental setup relies on an impedance tube configuration like the one presented in Chapter 3, Sec. 3.1. Nevertheless, microphones are placed in a different manner because one wishes to determine the reflection coefficient of the perforated plate and flame. This is shown schematically in Fig. 5.6.
The experimental procedure remains the same, compared to the one applied in Sec. 3.1. One determines the transfer function H_{12} by using the three microphones M_1, M_2 and M_3 (Tran (2009)). This transfer function is then used to compute the specific acoustic impedance $\zeta_1(0)$ and deduce the reflection coefficient $R_1(0)$ of the flame with its perforated plate.

The three microphones are placed at positions which are in agreement with the two criteria mentioned in Sec. 3.1. The distance between microphone M_1 and M_2 is not changed and still satisfies $L_{2m} - L_{1m} \leq 0.15$ m. The second criterion $L_{1m} \leq 0.31$ m is also fulfilled as $L_{1m} = 0.06$ m.
The flame response evolves with the amplitude and one expects the same for the flame reflection coefficient. Measurements have to be controlled in amplitude to ensure the same perturbation level for all frequencies. This is done by using a hot wire probe placed 3 cm below the perforated plate (see Fig. 5.6). This sensor is used during the frequency sweep from 100 Hz to 1000 Hz to keep the same level of disturbances from the loudspeaker. Once sweeping has been done for one amplitude, another can be used for the same frequency range. The precise level is however controlled after the frequency exploration by using a reconstruction technique of the velocity signal $u_1'(0)$ by means of the microphones and the transfer function H_{12}. This reconstruction uses the harmonic signal $\widetilde{p}_1(L_{1m})$ at microphone M_1 location and the transfer function H_{12} between microphones M_1 and M_2 (M_3 in front of M_2 is used to improve the signal to noise ratio). This yields :

$$u_1'(0) = \Re\left\{ \frac{i}{\rho_1 c_1} \frac{H_{12}\cos(k_1 L_{1m}) - \cos(k_1 L_{2m})}{\sin[k_1(L_{1m} - L_{2m})]} \widetilde{p}_1(L_{1m})\, e^{-i\omega t} \right\} \tag{5.8}$$

where $\widetilde{p}_1(L_{1m})\, e^{-i\omega t}$ stands for the Hilbert transform of the pressure measurement. Then, the records of the three microphones are processed to obtain the flame reflection coefficient and results are compared to the reflection coefficient calculated from the FDF as done in Noiray (2007) and Schuller et al. (2009).

5.4.2 Flame reflection coefficient

The acoustic relations describing the burner acoustics introduced in Chapter 4 allow to write the flame reflection coefficient depending on the FDF. The FDF value is taken at the amplitude calculated from Eq. (5.8). One derives the reflection coefficient of the flame $R_1(0)$ by using the downstream zone of the burner. It comprises the flame tube L_2, the ring cavity and the outlet impedance $\zeta_2(L_2)$ defined in Chapter 4. Equations (4.11), (4.15) and (4.9) are combined to obtain an expression which may be cast in the following form :

$$R_1(L_1) = \frac{\Xi\left[1 + Ge^{i\varphi}\left(\frac{T_f}{T_1} - 1\right)\right] + \mathcal{A}_1\left[\mathcal{R} + i\left(1 - \frac{S_1}{S_2}\right)\tan(k_2 l)\right]}{\Xi\left[1 + Ge^{i\varphi}\left(\frac{T_f}{T_1} - 1\right)\right] - \mathcal{A}_2\left[\mathcal{R} + i\left(1 - \frac{S_1}{S_2}\right)\tan(k_2 l)\right]} \tag{5.9}$$

where $\Xi = (S_1/S_2)(\rho_2 c_2/\rho_1 c_1)$, $\mathcal{A}_1$ and $\mathcal{A}_2$ stand for the terms in Melling's relation and $\mathcal{R}$ is a ratio involving the reflection coefficient of the flame tube

outlet $R_2(L_2)$ defined by :

$$\mathcal{A}_1 = 1 + \frac{i\omega l}{\mathcal{P}c_1}\left[1 + \frac{l_\nu}{r_p}(1+i)\right],\ \mathcal{A}_2 = 1 - \frac{i\omega l}{\mathcal{P}c_1}\left[1 + \frac{l_\nu}{r_p}(1+i)\right],$$
$$\mathcal{R} = \frac{R_2(L_2)e^{ik_2L_2} - e^{-ik_2L_2}}{R_2(L_2)e^{ik_2L_2} + e^{-ik_2L_2}} \tag{5.10}$$

It should be noted that the reflection coefficient is designated differently between measurements made with the multiple flame combustor presented in Chapter 1 and calculations done here. This is linked to a modification in the origin of the longitudinal coordinates. The origin used in the impedance tube device is located at the perforated plate and named $R_1(0)$, while it is on the piston head in the experiment used to characterize self-sustained combustion oscillations. In this latter case, the flame reflection coefficient is designated as $R_1(L_1)$. Nevertheless, by using the suitable system of coordinates, one retrieves the expression given in Eq. (5.9).

Table 5.1: *Values of the coefficients used for the coupling factor to determine the impedance of the unconfined flame.*

Variable	Value	Units
A	$1.9\,10^{-5}$	m^2
α	104	-
E	6.67	-
h	6.5	mm
$\mathcal{P}$	0.344	-
ρ_1	1.18	$kg\,m^{-3}$
S_L	0.35	$m\,s^{-1}$
U_b	3.1	$m\,s^{-1}$

Two configurations have been investigated. The first is linked to the flame reflection coefficient of the unconfined burner. The second deals with the confinement tube set to $L_2 = 0.20$ m. The main trend of this experiment concerns the possibility to compare a reflection coefficient calculated from the FDF and one measured with three microphones without any optical diagnostic. This point has also been considered by Schuermans et al. (2010) in a more complex configuration and it was shown that a good agreement could be achieved with optical measurement methods.
In addition, a second important point centers around the use of a unique FDF to obtain the flame reflection coefficient of the confined and unconfined burners. Indeed, it has been seen in Sec. 5.2 that the FDF does not change with the flame tube. Thus, it is interesting to see if it is possible to calculate the reflection coefficient for these two burners with the same flame response. The FDF has been measured in a confined configuration with a small tube $L_2 = 0.10$ m while

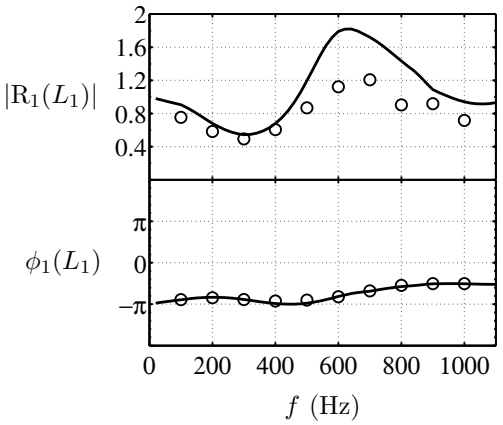

Figure 5.7: *Flame reflection coefficient measured on the unconfined burner for an amplitude $u_{rms}/U_b = 0.6$. Calculations from the FDF appear as a bold line while measurements are shown as open circle symbols (∘).*

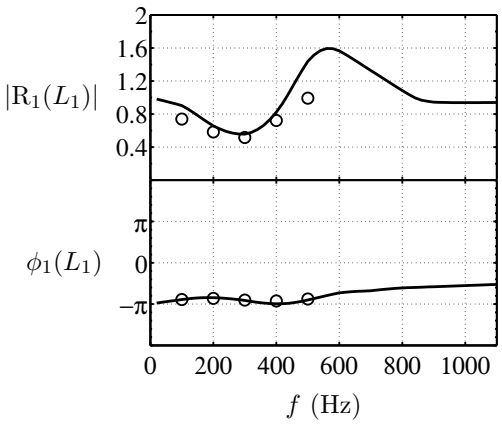

Figure 5.8: *Flame reflection coefficient measured on the unconfined burner for an amplitude $u_{rms}/U_b = 0.8$. Calculations from the FDF appear as a bold line while the measurements are shown as open circle symbols (∘).*

the one used here is longer $L_2 = 0.20$ m. Hence, on the basis of the previous FDF data, the flame response is supposed to remain the same with this longer tube. One will be able to verify this fact by using the flame reflection coefficient. It is important to note that this comparison is made up to $u_{rms}/U_b = 0.8$ due to a lack of efficiency from the loudspeaker at higher amplitudes. The flame reflection coefficient of the unconfined burner is calculated with the impedance of the flame anchored on its perforated plate. This relation has been derived by Noiray (2007) and is recalled here for completeness :

$$Z_1(L_1) = \frac{\widetilde{p}_1(L_1)}{\widetilde{u}_1(L_1)} = -i\omega\alpha\frac{\rho_1\,(E-1)\,S_L}{4\pi h}\frac{\bar{\mathcal{A}}}{U_b\mathcal{P}}\,G\,e^{i\varphi} \\ -i\frac{\omega\rho_1 l}{\mathcal{P}}\Big(1+\frac{l_\nu}{r_p}\,(1+i)\Big) \tag{5.11}$$

where values used in the coupling factor of the combustion noise are given in Tab. 5.1.

The unconfined results are presented in Figs. 5.7 and 5.8. They display evolutions of the reflection coefficient for $u_{rms}/U_b = 0.6$ and $u_{rms}/U_b = 0.8$ between 0 Hz and 1100 Hz. One observes a perfect match for the phase $\phi_1(L_1)$ over the whole frequency range in both cases. In addition, the modulus $|\mathrm{R}_1(L_1)|$ reveals a fairly good agreement. There are some differences between 500 Hz and 900 Hz for $u_{rms}/U_b = 0.6$, but the main trend is retrieved for all frequencies. The reflection coefficient is now examined for a confined flame, using $L_2 = 0.20$ m. The results are attempted for the same amplitudes, but due to a noisy signal, a precise value with the hot wire probe is less easy to obtain and the pressure post-processing reveals slight deviations from the expected level. It was found

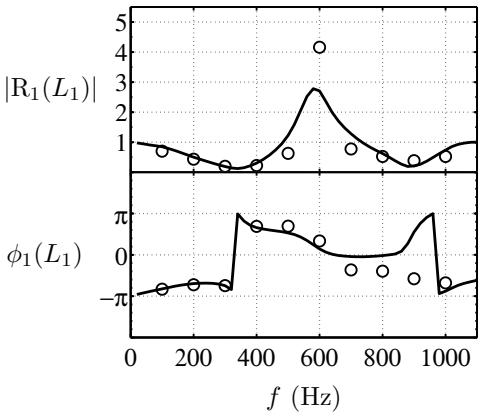

Figure 5.9: *Flame reflection coefficient measured on the confined burner with $L_2 = 0.20$ m for an amplitude $u_{rms}/U_b = 0.4$. Calculations from the FDF appear as a bold line while the measurements are shown as open circle symbols ($\circ$).*

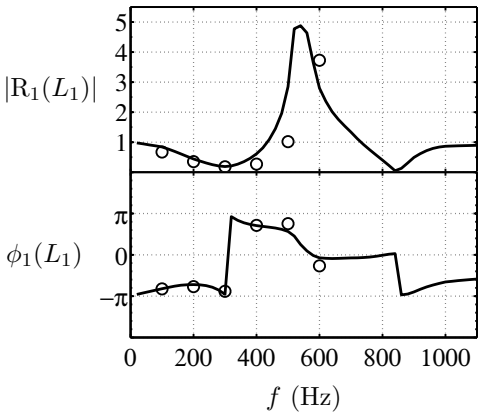

Figure 5.10: *Flame reflection coefficient measured on the confined burner with $L_2 = 0.20$ m for an amplitude $u_{rms}/U_b = 0.7$. Calculations from the FDF appear as a bold line while the measurements are shown as open circle symbols ($\circ$).*

that measurements could be carried out for $u_{rms}/U_b = 0.4$ and $u_{rms}/U_b = 0.7$, which remain close enough to 0.6 and 0.8. This is respectively shown in Figs. 5.9 and 5.10.

Regarding the modulus, one obtains a good agreement in both cases, except around 600 Hz for the lowest amplitude $u_{rms}/U_b = 0.4$, where the calculated value is 30 % lower than the measured quantity. The phase also agrees fairly well and there is a perfect match until 600 Hz. Beyond 600 Hz, the trend is still good and differences arise around 900 Hz for the lowest amplitude.

In light of these two cases, it is seen that the reflection coefficient can be used to retrieve the flame response with a good agreement. This has been done for confined and unconfined situations without any optical diagnostic. Besides, it is interesting to see that a unique FDF can be handled in these two situations. This indicates the reliability of this FDF when other flame tubes are fitted on the same burner. It also shows that the FDF can be measured by making use of the small confinement tube $L_2 = 0.10$ m. This reflection coefficient technique needs the determination of the oscillation level on the flame plane to fix the measurements on the amplitude scale. It has been demonstrated that this can be anticipated with a hot wire probe placed in the upstream cavity and cross checked by microphone measurements.

Chapter 6

Modeling strategy

The analysis of the different elements of the burner − undertaken in the two previous chapters − is now used to model the burner dynamics. The purpose of this model is to reproduce the different unstable regimes recorded in the experiments. The objective is to develop predictions of oscillation for a given geometry and operating conditions and possibly avoid this phenomenon. Two models are delineated. The first implements simplified conditions while the second aims to take into account the detailed response of the different elements composing the burner. This gives rise to nonlinear dispersion relations. Methods providing the roots of these relations are explained. It is then shown that the calculated eigenfrequencies are notably influenced by the temperature T_2 of the burnt gases in the different flame tubes of the study. This temperature needs to be estimated to obtain an accurate modeling of the system. It is found, and this may be counterintuitive that the average temperature in the flame tube takes larger values when the length of the tube is augmented.

6.1 Modal analysis

The acoustic response of the different elements composing the burner have been analyzed in Chapters 4 and 5. It is then possible to analyze the response of the complete system.

The system is modeled as an acoustic network of compact elements. This method is widely used to analyze thermoacoustic coupling (see for example Keller (1995); Poinsot et al. (2012)). The configuration retained is presented in Fig. 6.1. The burner comprises two cylindrical cavities, a flame zone with its ring cavity between these two elements, and two boundary conditions at the system inlet and exhaust. Two models with different levels of approximation are examined. The first one corresponds to a simplified version of the burner acoustics and is named “model A”. It does not account for the real value of the piston head reflection coefficient which is replaced here by a perfectly rigid

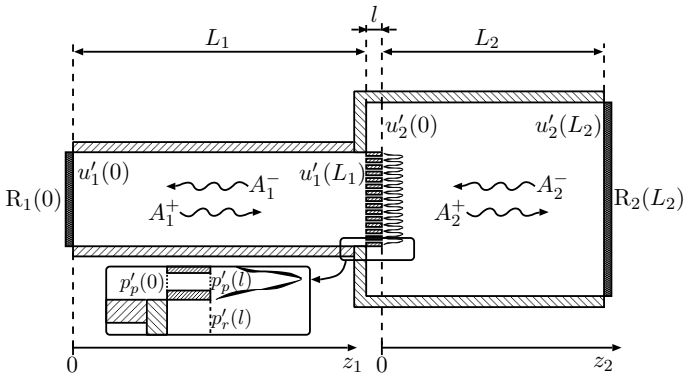

Figure 6.1: *Burner and symbol convention used for the theoretical acoustic analysis.*

wall constituting a velocity node. Acoustic radiation of the flame tube outlet is also neglected and this section is represented by a pressure node. The flame response is characterized by a jump condition of the acoustic variables without taking into account the effect of the ring cavity surrounding the flame. Dissipation within the perforations of the flame holder is however included by a relation derived from Melling (Melling (1973)). The second model designated as "model B" includes an improved description of the inlet and outlet boundary conditions, and it accounts for the effect of the ring cavity surrounding the flame. The characteristics of these two models are gathered in Tab. 6.1.

Table 6.1: *Details of the two models devised for the acoustic analysis of the burner.*

	R piston	***R outlet***	***Pressure jump***	***Velocity jump***
model A	$R_1(0) = 1$	$R_2(L_2) = -1$	Melling model	No ring cavity
model B	$R_1(0) = R(f)$ (measured)	$R_2(L_2) = R(f)$ (modeled)	Melling model	Ring cavity

6.1.1 The simplified model : "model A"

In model A, the reflection coefficient of the piston head is $R_1(0) = 1$ and the pressure is assumed to vanish at the flame tube outlet $R_2(L_2) = -1$. These two assumptions are idealized versions of reality. It is known from measurements shown in Fig. 4.5, that the value of $R_1(0)$ is nearly constant beyond 600 Hz and lies around 0.8 for the modulus while the phase almost equals 0. Thus, the approximation of $R_1(0) = 1$ can be used for a burner featuring high frequencies of oscillation. This is precisely the case for the thin perforated plate $l = 3$ mm and the small confinement tubes. The effect of sound radiation at the outlet can partly be accounted for by including in the description the imaginary contribution of the radiation impedance. This leads to artificially increasing the size of the flame tube with an end correction. This is achieved by replacing

L_2 by $L_2^c = L_2 + 0.61R_2$. The previous conditions applied at the inlet and outlet define the ratios of the wave amplitudes in the upstream manifold and flame tube :

$$\begin{aligned} \mathrm{R}_1(0) &= \frac{A_1^+}{A_1^-} = 1 \\ \mathrm{R}_2(L_2) &= \frac{A_2^- e^{-ik_2 L_2}}{A_2^+ e^{ik_2 L_2}} = -1 \end{aligned} \tag{6.1}$$

The acoustic response of the flame zone is modeled without taking into account the effect of the ring cavity surrounding the flame. In this case, the jump condition for the acoustic volume flow rate across this region corresponds to Eq. (5.3) which may be cast in the following form :

$$S_2 \widetilde{u}_2(0) - S_1 \widetilde{u}_1(L_1) = \frac{\gamma - 1}{\rho_1 c_1^2} \widetilde{\dot{Q}} \tag{6.2}$$

This is a reasonable approximation when the plate thickness is small compared to the acoustic wavelengths of interest (the frequency encountered in calculations does not exceed 1300 Hz). This approximation is valid for the thin flame holder $l = 3$ mm, but it will be shown that it is advisable to include the effect of the ring cavity when $l = 15$ mm. Equation (5.5) is then used to link the heat release rate fluctuation $\widetilde{\dot{Q}}$ to the FDF presented in Chapter 5, as shown previously in Eq. (5.6).
The pressure also experiences a jump across the perforated plate used as a flame holder. Viscous dissipation takes place in the channels of this perforated plate. This is described by using a relation derived from Melling (1973) which is detailed in Eq. (4.15). By considering the acoustic pressure $\widetilde{p}_1(L_1)$ at the feeding manifold outlet and the pressure $\widetilde{p}_2(0)$ one obtains :

$$\widetilde{p}_2(0) - \widetilde{p}_1(L_1) = \frac{i\,\omega \rho_1 l}{\mathcal{P}} \Big[1 + \frac{l_\nu}{r_p} (1 + i) \Big] \widetilde{u}_1(L_1) \tag{6.3}$$

where $\mathcal{P}$ denotes the perforated plate porosity of thickness l with holes of radius r_p, while $l_\nu = (2\nu/\omega)^{1/2}$ is the acoustic boundary layer thickness.

Equations (6.1) to (6.3) combined with the FDF, as shown in Eq. (5.6), may be written in a matrix form to describe the dynamics of the system :

$$\begin{pmatrix} 1 & -1 & 0 & 0 \\ 0 & 0 & e^{ik_2 L_2} & e^{-ik_2 L_2} \\ \mathcal{A}_1 e^{ik_1 L_1} & \mathcal{A}_2 e^{-ik_1 L_1} & -1 & -1 \\ \mathcal{B} e^{ik_1 L_1} & -\mathcal{B} e^{-ik_1 L_1} & -1 & 1 \end{pmatrix} \begin{pmatrix} A_1^+ \\ A_1^- \\ A_2^+ \\ A_2^- \end{pmatrix} = 0 \tag{6.4}$$

where $\mathcal{A}_1$, $\mathcal{A}_2$ and $\mathcal{B}$ correspond to :

$$\mathcal{A}_1 = 1 + \frac{i\omega l}{\mathcal{P}c_1}\left[1 + \frac{l_\nu}{r_p}(1+i)\right],\ \mathcal{A}_2 = 1 - \frac{i\omega l}{\mathcal{P}c_1}\left[1 + \frac{l_\nu}{r_p}(1+i)\right],$$

$$\mathcal{B} = \frac{S_1}{S_2}\frac{\rho_2 c_2}{\rho_1 c_1}\left[1 + Ge^{i\varphi}\left(\frac{T_f}{T_1} - 1\right)\right]$$

where $\Xi = (S_1/S_2)(\rho_2 c_2/\rho_1 c_1)$ designates the acoustic coupling index between the cavities separated by the perforated plate and the flame (Schuller et al. (2012)). For the present conditions, the index lies between $\Xi = 0.13$ and 0.17, depending on the flame tube temperature T_2. This indicates that the cavities remain coupled.
A trivial solution of the system Eq. (6.4) is obtained by setting A_n^+ and A_n^- to 0. Nontrivial solutions are sought by cancelling the determinant of this system. Model A features a fairly simple matrix form to develop the determinant. It is then possible to obtain an explicit dispersion relation which describes the dynamics of the system :

$$\begin{aligned}&\frac{S_1}{S_2}\frac{\rho_2 c_2}{\rho_1 c_1}\left[1 + Ge^{i\varphi}\left(\frac{T_f}{T_1} - 1\right)\right]\sin(k_1 L_1)\sin(k_2 L_2)\\ &- \cos(k_1 L_1)\cos(k_2 L_2)\\ &+ \frac{\omega l}{\mathcal{P}c_1}\left[1 + \frac{l_\nu}{r_p}(1+i)\right]\cos(k_2 L_2)\sin(k_1 L_1) = 0\end{aligned} \tag{6.5}$$

In this expression, the FDF represents the flame response in terms of a gain and a phase $G\exp(i\varphi)$, and this relation depends on the perturbation amplitude u_{rms}/U_b. The objective is to find complex roots $\omega = \omega_r + i\omega_i$ yielding oscillation frequencies $f = \omega_r/2\pi$ and growth rates ω_i of perturbations as a function of this amplitude. This is done by solving the dispersion relation for each FDF amplitude. Positive values of ω_i indicate that perturbations grow, while negative ones correspond to decaying disturbances. The burner can be equipped with different confinement tube sizes L_2 and a continuously variable feeding manifold lengths L_1 allowing to follow unstable frequencies with respect to this parameter. This provides a considerable insight as compared to a fixed geometry which only gives partial indications the behavior of the system. Solutions of the nonlinear dispersion relation are considered in four cases, corresponding to four confinement tubes L_2. For one flame tube L_2, an iterative algorithm is used to find the set of solutions for the angular frequency ω_r and growth rate ω_i as a function of the following parameters :

- The feeding manifold length L_1 ;
- The amplitude of perturbation u_{rms}/U_b ;

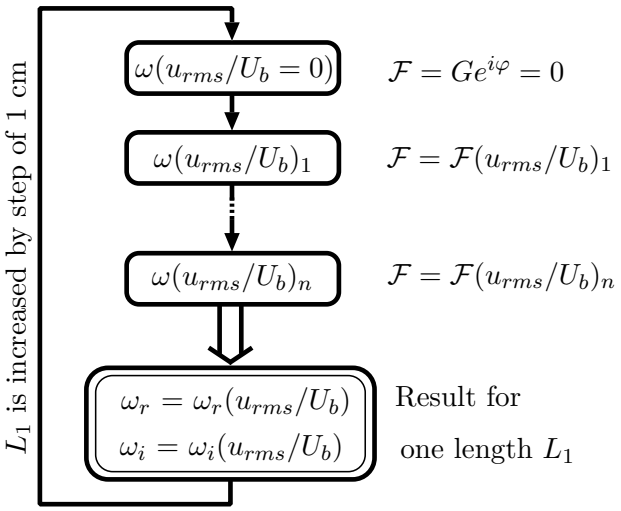

Figure 6.2: *Sequential solution of the nonlinear dispersion relation including the FDF.* $(u_{rms}/U_b)_n$ *designates the* n^{th} *amplitude of the FDF. This algorithm is used for each flame tube* L_2 *treated separately. This loop is effected for each eigenmode calculated in the absence of unsteady combustion and handled one by one. The feeding manifold length* L_1 *is varied for the eigenmodes under consideration. The loop is then repeated for another flame tube size* L_2*.*

- For each acoustic eigenmode of the system in the absence of unsteady combustion.

This procedure is repeated for each flame tube configuration L_2 and each eigenmode, following the algorithm presented in Fig. 6.2 where the methodology is described as a sequential chart. Roots of the dispersion relation Eq. (6.5) are first determined in the absence of unsteady combustion ($G = 0$), leading to a set of acoustic eigenmodes (the three first modes for instance) for a fixed geometrical configuration, i.e. for a flame tube L_2 and a set of feeding manifold lengths L_1. The chart in Fig. 6.2 is then repeated for each of these eigenmodes calculated separately while taking into account unsteady combustion effects. A new root associated to a certain acoustic eigenmode is calculated by accounting for the FTF (the FDF at a certain amplitude) determined for a small perturbation level $\mathcal{F} = \mathcal{F}(u_{rms}/U_b)_1$. This leads to a new complex angular frequency $\omega = \omega(u_{rms}/U_b)_1$ associated to this perturbation level $(u_{rms}/U_b)_1$, which serves now as an initial state to find the solution of the dispersion relation for a higher amplitude ($(u_{rms}/U_b)_2$). One considers an increasing level until the maximum amplitude $(u_{rms}/U_b)_n$ is reached. This yields a set of roots changing as a function of the amplitude $\omega = \omega(u_{rms}/U_b)$ for each eigenmode. The geometrical configuration is then modified by changing the feeding manifold length L_1 and the procedure from small to high amplitudes is repeated as indicated in Fig. 6.2.

Solutions of the dispersion relation are determined numerically by finding minima of the modulus of the left hand side of Eq. (6.5). This problem is solved with Matlab® and the Nelder-Mead simplex algorithm by using the function "fminsearch". A starting point for the angular frequency ω_r and the growth rate ω_i is necessary to initiate the algorithm. As indicated previously, this is done by setting $G = 0$ in Eq. (6.5) to obtain the acoustic eigenmodes of the system in the absence of a flame response.
This first step corresponding to $G = 0$ is treated with the same optimization algorithm ("fminsearch"). Initial solutions are taken to be the quarter wave modes $(2n-1)c/4L$ ($n \in \mathbb{N}$) of the burner. A few iterations yield the acoustic eigenmodes of the burner corresponding to the bold lines in Figs. 2.3, 2.4 and 2.5 of Chapter 2. These eigenmodes are then used to start the continuation methodology described in Fig. 6.2.
It should be noted that the algorithm presented in Fig. 6.2 is used differently for some confined configurations L_2. When the roots of the dispersion relation, determined for the small perturbation level $(u_{rms}/U_b)_1$, are largely shifted from the acoustic eigenmodes ($G = 0$), the solving for the growing amplitude (Fig. 6.2) is reversed. The acoustic eigenmode still serves as an initial state but the first root is sought for the highest amplitude $(u_{rms}/U_b)_n$. Then, this latter solution serves as an initial state for a lower level $(u_{rms}/U_b)_{n-1}$ and so on until the lowest value. The roots are easily found in this way. This is linked to the decrease of gain G for the highest amplitudes. As the gain falls, the frequency shift decreases, which helps the software algorithm to determine the minima of the dispersion relation modulus. This procedure is more suitable for the longest confinement tubes L_2 where the roots of the dispersion relation are more prone to shift.

6.1.2 An improved model

Model B aims to improve predictions of the combustor dynamics by including a better description of the boundary and matching conditions between the two cavities. Measurements gathered in Chapter 4 for the reflection coefficient of the piston head (see Fig. 4.5) are included in this "model B". The reflection coefficient of the outlet is represented by taking into account sound radiation from an unflanged open pipe (see Eqs. (4.8) and (4.9)).
The contribution from the ring cavity surrounding the flame is taken into account and this modifies the jump condition on the acoustic volume flow rate at the flame :

$$\begin{aligned} S_{2p}\widetilde{u}_p(l) - S_1\widetilde{u}_1(L_1) &= \frac{\gamma-1}{\rho_1 c_1^2}\widetilde{\dot{Q}} \\ S_2\widetilde{u}_2(0) &= S_{2r}\widetilde{u}_r(l) + S_{2p}\widetilde{u}_p(l) \end{aligned} \tag{6.6}$$

The pressure experiences the same jump as the one derived in model A from the relation of Melling. Combining the two reflection coefficients and the different

matching conditions for pressure and velocity, one obtains the following system of equations written in a matrix form :

$$\begin{pmatrix} 1 & -\mathrm{R}_1(0) & 0 & 0 \\ 0 & 0 & \mathrm{R}_2(L_2)e^{ik_2L_2} & -e^{-ik_2L_2} \\ \mathcal{A}_1 e^{ik_1L_1} & \mathcal{A}_2 e^{-ik_1L_1} & -1 & -1 \\ \mathcal{B}e^{ik_1L_1} & -\mathcal{B}e^{-ik_1L_1} & \mathcal{C}_1 & \mathcal{C}_2 \end{pmatrix} \begin{pmatrix} A_1^+ \\ A_1^- \\ A_2^+ \\ A_2^- \end{pmatrix} = 0 \quad (6.7)$$

where the complex coefficients $\mathcal{A}_1$, $\mathcal{A}_2$, $\mathcal{B}$, $\mathcal{C}_1$ and $\mathcal{C}_2$ correspond to :

$$\mathcal{A}_1 = 1 + \frac{i\omega l}{\mathcal{P}c_1}\left[1 + \frac{l_\nu}{r_p}(1+i)\right],\ \mathcal{A}_2 = 1 - \frac{i\omega l}{\mathcal{P}c_1}\left[1 + \frac{l_\nu}{r_p}(1+i)\right],$$

$$\mathcal{B} = \frac{S_1}{S_2}\frac{\rho_2 c_2}{\rho_1 c_1}\left[1 + Ge^{i\varphi}\left(\frac{T_f}{T_1} - 1\right)\right],$$

$$\mathcal{C}_1 = i\left(1 - \frac{S_1}{S_2}\right)\tan(k_2 l) - 1,\ \mathcal{C}_2 = i\left(1 - \frac{S_1}{S_2}\right)\tan(k_2 l) + 1$$

The same algorithm is used to determine nontrivial solutions of this system of equations but it is more difficult to derive an analytical form of the determinant. Thus, it is calculated numerically with Matlab®.
The procedure described in Fig. 6.2 is also used for the present model.
The two models developed in this Chapter are applied to different configurations of the burner in the next chapters. It is however interesting to examine the acoustic eigenmodes of the system in the absence of combustion coupling by setting $G = 0$ in the dispersion relation while the temperature T_2 in the flame tube is varied.

6.2 Influence of the flame tube temperature

The temperature T_2 inside the flame tube differs from the temperature T_1 in the feeding manifold. Using different temperatures between the confinement tube and the feeding manifold, acoustic eigenmodes will slightly differ with respect to uniform temperature calculations. This is exemplified in Fig. 6.3 for the smallest flame tube $L_2 = 0.10$ m. The three first eigenmodes of the system calculated in the absence of unsteady combustion with model B are represented for two flame tube temperatures T_2. Bold lines correspond to calculations with a uniform temperature in the burner fixed to $T_1 = T_2 = 300$ K pertaining to the fresh gas. Dashed lines correspond to calculations where the burnt gas temperature is raised to $T_2 = 900$ K to illustrate modifications induced by increasing T_2.
This figure shows that the modal distribution is quite sensitive to the temperature chosen for the burnt gases. Differences between calculations carried out for 300 K and 900 K may lead to a shift of the order of 100 Hz for the modal frequency. It is thus important to have a good estimate of the gas temperature

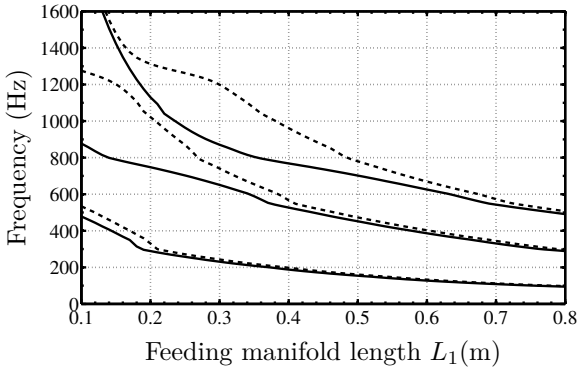

Figure 6.3: *The first three acoustic eigenmodes of the burner without unsteady combustion process calculated by using "model B". The feeding manifold temperature T_1 is set to 300 K. Bold lines (**—**) correspond to calculations with T_2 = 300 K while dashed lines (- -) are used for T_2 = 900 K.*

T_2 inside the flame tube. This temperature was therefore measured with a K-thermocouple at different locations to estimate a mean value. These values are gathered in Tab. 6.2 for each flame tube L_2 explored. They indicate that an increase of the flame tube length L_2 is associated to a temperature increase for T_2.

Table 6.2: *Mean temperature of the hot gases in the different confinement tubes L_2.*

***Tube length* (m)**	***0.10***	***0.20***	***0.30***	***0.40***
Temperature (K)	900	1100	1300	1400

Part III

Nonlinear modeling of combustion-acoustic coupling

Chapter 7

Basic modeling of stable limit cycles and triggering

Nonlinear stability of the combustion system presented in Part I is now examined theoretically with model A devised in Chapter 6. In a first step, the model is used to predict experimentally observed combustion oscillations in terms of frequency and amplitude at the limit cycle. In a second section, frequency shift during transients, nonlinear instability triggering, hysteresis and mode switching observed in the experiments are compared to results of calculations.

7.1 Describing Function analysis of stable limit cycles in a multiple flame combustor

This section corresponds to a publication presented at the *ASME Turbo expo 2010* and published in *Journal of engineering for gas turbine and power* in 2011 :

Boudy, F., D. Durox, T. Schuller, G. Jomaas, and S. Candel. 2011. "Describing function analysis of limit cycles in a multiple flame combustor" *J. Eng. Gas Turb. Power* 133 (6): 061502.1–061502.8. doi:10.1115/1.4002275

For the sake of clarity, the present chapter has been shortened compared to the journal publication. The introduction has been reduced to the organization of the work carried out in this chapter. The abstract, description of the experimental setup and the model derivation were kept to allow an easier reading of the contents, but these sections can be skipped since they are described in the preceding chapters.

7.1.1 Abstract

A recently developed nonlinear Flame Describing Function (FDF) is used to analyze combustion instabilities in a system where the feeding manifold has a variable size and where the flame is confined by quartz tubes of variable length. Self-sustained combustion oscillations are observed when the geometry is changed. Regimes of oscillation are characterized at the limit cycle and also during the onset of oscillations. Theoretical predictions of the oscillation frequencies and levels are obtained using the FDF. This generalizes the concept of flame transfer function by including a dependence on the frequency and on the level of oscillation. Predictions are compared with experimental results for two different lengths of the confinement tube. These results are in turn used to predict most of the experimentally observed phenomena and in particular the correct oscillation levels and frequencies at limit cycles.

7.1.2 Introduction

The present work focuses on the prediction of combustion instabilities using the FDF framework. This is applied to a generic configuration comprising a feeding manifold, an injection unit, a flame anchoring system and a confinement tube. The flame holder comprises a thin perforated plate $l = 3$ mm. Emphasis will be put on the prediction of oscillation limit cycle frequencies and levels as a function of modifications of the burner geometry. The experimental set-up is described in Section 7.1.3. Self-sustained combustion oscillations are characterized in section 7.1.4. The nonlinear analysis with model A is developed in Section 7.1.5. This section also provides the FDF data determined in forced flow experiments. These data are used in a thermoacoustic model of the combustor to obtain the unstable frequencies and amplitude levels at the limit cycles. Theoretical predictions are systematically compared with experiments in Section 7.1.6 by changing the length of the upstream manifold and by making use of two flame tube sizes.

7.1.3 Experimental setup and combustion regimes

This section describes the experimental setup and the combustion regimes detailed in Part I of the present manuscript. The reader can skip this section but it is worth recalling that the thin flame holder $l = 3$ mm is used in the present study.

The experimental setup is sketched in Fig. 7.1. The three main elements of the burner are the feeding manifold, a perforated plate which delivers the premixed streams and anchors the flames and the quartz confinement tube. The combustion zone is placed in this quartz tube. The reactants are premixed in the piston before they are injected inside the enclosing manifold. The piston also facilitates changes in the length of the feeding manifold. The perforated

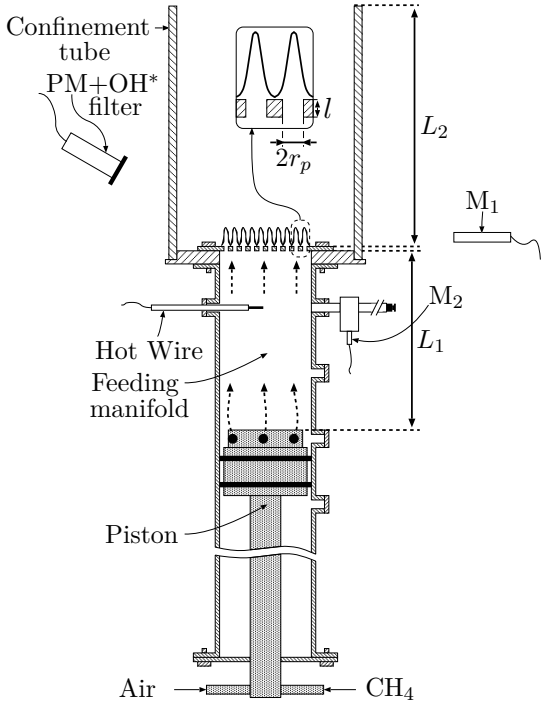

Figure 7.1: *Experimental setup used to characterize self-sustained instabilities.*

plate, which is confined within a quartz tube at the top of the feeding manifold, anchors an ensemble of small laminar conical flames. It has a thickness of $l = 3$ mm and a diameter of $2R = 70$ mm. It is made of stainless steel and comprises $N = 421$ holes of diameter $2r_p = 2$ mm placed on a 3 mm square mesh, resulting in a global porosity $\mathcal{P} = N\pi r_p^2/\pi R^2$ of 0.34. Four quantities are measured in this experiment. The fluid velocity in the feeding manifold is determined with a hot wire probe 3 cm below the perforated plate. A photomultiplier equipped with an OH^* filter ($\lambda = 308$ nm) views the flames from outside the confinement and provides a signal almost proportional to the heat release rate (Hurle et al. (1968)). The pressure fluctuations are measured inside the feeding manifold with the microphone M_2 placed in a waveguide in front of the hot wire and another microphone M_1 outside the confinement tube 24.5 cm away from the burner axis detects the radiated sound pressure level. The length of the feeding manifold, as measured between the upstream side of the perforated plate and the head of the piston, can be varied in discrete steps all the way from $L_1 =$ 0.15 m to 0.54 m. The piston head is designed to offer a quasi-perfect reflecting boundary for acoustic waves. Two lengths of confinement tubes are used in the present study. In the first set of experiments, the length of the feeding manifold is swept with a confinement tube $L_2 = 0.10$ m. Then, another tube $L_2 = 0.20$ m is used in a second set of exploration. The flow rate of the methane/air mixture is $\dot{m} = 4.71\times10^{-3}$ kg/s at an equivalence ratio $\phi = 1.03$, providing a

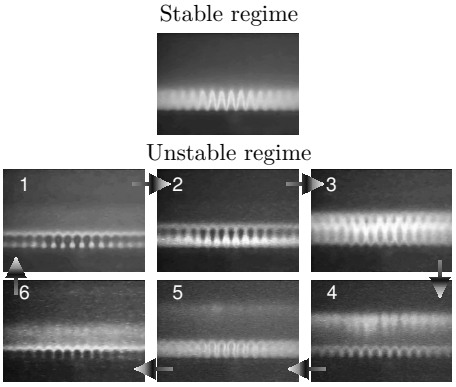

Figure 7.2: *Stable (L_1 = 0.25 m) and unstable (L_1 = 0.29 m) combustion regimes at 750 Hz for an equivalence ratio ϕ = 1.03 and a confinement tube L_2 = 0.10 m.*

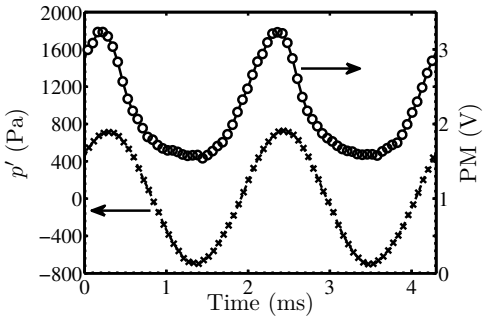

Figure 7.3: *Pressure signal from microphone M_2 (left vertical axis) and OH* radicals light intensity (right vertical axis) for one length of feeding manifold L_1 and flame tube L_2 = 0.20 m under self-sustained oscillations.*

thermal power of 13.3 kW.

For both confinement tubes, the system is unstable for a wide range of feeding manifold lengths (L_1) and only stable for some values. In a stable case, as shown in Fig. 7.2, flames have a conical shape. In the unstable cases, all the flames move in a regular fashion with formation and collapse of fresh reactant pockets as illustrated in Fig. 7.2. This behavior causes a strong level of noise, which can exceed 110 dB measured by microphone M_1 (with a reference pressure 2×10^{-5} Pa). The experimental procedure is initiated with the head of the piston at L_1 = 0.15 m from the perforated plate (minimum extension) and consists of recording the sensor signals at limit cycles. Then, the piston is retracted in increments of one centimeter all the way to a manifold length L_1 = 0.54 m (maximum extension) with signals being acquired for each step. The piston is then moved in the reverse direction (maximum to minimum extension) using the same increment and acquiring the same set of signals.

As a result, the oscillation frequencies and the amplitudes of pressure oscillations are obtained for a range of manifold lengths. These experiments are repeated for the two flame confinement tubes L_2 = 0.10 m and 0.20 m.

In these experiments, the pressure is essentially harmonic, indicating that the acoustic field remains in the linear range. Typical pressure and heat release rate fluctuations recorded in the system are plotted in Fig. 7.3. The pressure signal remains sinusoidal whereas OH* radicals light intensity, corresponding to the heat release rate, shows asymmetrical oscillations, revealing the nonlinearity of the flame response.

Another set of experiments is conducted to get the response of the flame ensemble to velocity fluctuations and determine the FDF (Noiray et al. (2008); Durox et al. (2009b)). This system, shown in Fig. 7.4, allows measurements of heat

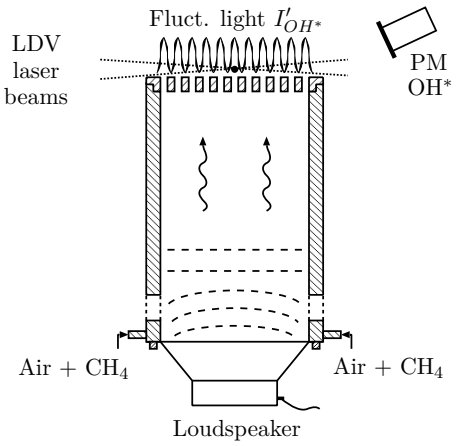

Figure 7.4: *Forced flow setup used to determine the FDF. The forced flow fluctuations are created by a loudspeaker placed at the bottom of the burner. Velocity fluctuations are measured by LDV at the base of one flame, 0.6 mm above the hole and heat release rate fluctuations are deduced from I'_{OH^*} measured by the photomultiplier.*

release rate fluctuations through the values of the light emission fluctuations of the OH* radical recorded by a photomultiplier (PM). Velocity fluctuations are obtained from LDV (Laser Doppler Velocimetry) measurements inside one flame 0.6 mm above the hole.

7.1.4 Experimental results

The first set of data correspond to the $L_2 = 0.10$ m flame confinement tube. Figure 7.5 illustrates the evolution of frequency and pressure for different lengths of feeding manifold. The dashed lines represent the acoustic eigenmodes evolution for a variable feeding manifold length L_1. For a range, between $L_1 = 0.23$ m and 0.27 m, the system is stable and the pressure measured by microphone M_2 falls under 120 dB which is the noise level corresponding to that of the flow and combustion alone. The sound pressure level, 24.5 cm away from the center of the burner (M_1), reaches 120 dB for the unstable regimes and 95 dB in the stable cases. It is noteworthy that the frequency evolves differently for the two directions of piston movement (min to max vs. max to min). When the feeding manifold cavity length L_1 is increased (min to max) the frequency evolves around the first mode ($L_1 = 0.15$ m to 0.22 m), reaches a stable band, and then switches to the second mode ($L_1 = 0.27$ m to 0.54 m). In the reverse direction (max to min) the frequency remains close to that of the second mode between $L_1 = 0.54$ m to 0.26 m, as it should, reaches a stable band, and then continues on the second mode from $L_1 = 0.22$ to 0.18 m before finally switching to the first mode for $L_1 = 0.17$ m to 0.15 m. It is therefore established that unstable modes present a hysteresis in this confined configuration when the feeding manifold geometry is changed. In a second

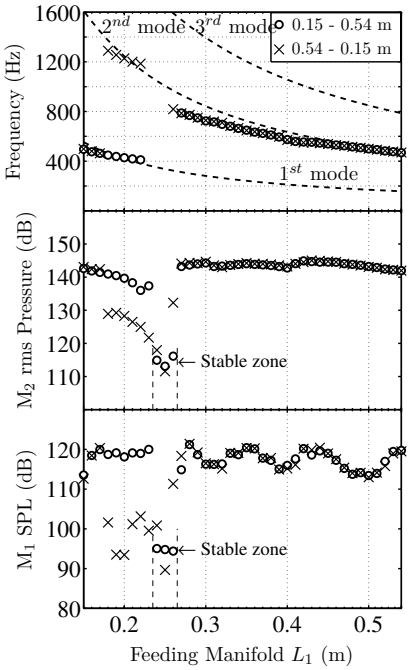

Figure 7.5: *Frequency and pressure level evolution with the L_2 = 0.10 m confinement tube, swept from 0.15 m to 0.54 m (○) and from 0.54 m to 0.15 m (×) of feeding manifold. The acoustic eigenmodes without combustion are plotted as dashed lines.*

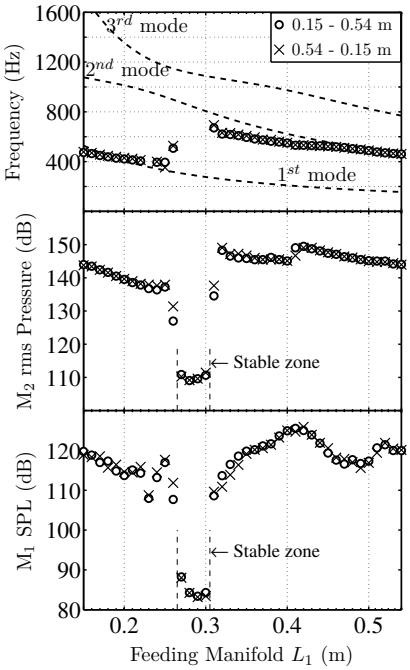

Figure 7.6: *Frequency and pressure level evolution with the L_2 = 0.20 m confinement tube, swept from 0.15 m to 0.54 m (○) and from 0.54 m to 0.15 m (×) of the feeding manifold. The acoustic eigenmodes without combustion are plotted as dashed lines.*

set of experiments, the flame confinement tube was changed to $L_2 = 0.20$ m. The evolution of the oscillation frequency and pressure level are presented in Fig. 7.6. The stable zone still exists in this configuration but its appearance is delayed until the length of the manifold reaches $L_1 = 0.26$ m and the system remains stable until $L_1 = 0.30$ m. Thus, the change of the downstream confinement length has altered the system stability. For the short manifold lengths $L_1 = 0.15$ m to 0.25 m, the frequency evolution still closely matches the first mode, and after the stable zone, the second mode arises for $L_1 = 0.31$ m to 0.54 m. The reverse evolution of the piston gives the same set of data, which indicates that there is no hysteresis for this confinement tube length $L_2 = 0.20$ m. Features of this type, like the oscillation level and hysteresis phenomena cannot be anticipated if one only uses classical linear stability analysis. The data can be used to validate the FDF nonlinear analysis.

7.1.5 Nonlinear analysis

This section describes model A derived in Chapter 6 to analyze the dynamics of the system. The reader can skip this section.

A nonlinear analytical model is needed to capture the rich physics behind the observed phenomena. In addition, such a model will be of value for predicting and understanding mechanisms of frequency switching or hysteresis in this system. In the following analysis, fluctuating quantities are written as a sum of a mean quantity and a fluctuation : $a = \bar{a} + a'$. The analysis is carried out in the frequency domain and each fluctuating quantity takes the form : $a' = \widetilde{a}e^{-i\omega t}$ where $\omega = \omega_r + i\omega_i$, ω_r corresponds to the angular frequency $(2\pi f)$ and ω_i is the growth rate. A perturbation grows for positive values of growth rate while it decays for negative ones. The analytical work carried out in this section follows that developed previously by Noiray et al. (2009) where a dispersion relation is derived and combined with the FDF to analyze the dynamics of a confined system. Given the low unstable frequencies observed in the experiments, the wavelengths are long compared to the dimensions of the system to consider other acoustic waves than longitudinal ones. The flame is thus compact. The different elements of the system are modeled as an acoustic network. The influence of the flames is taken into account in the matching condition between the feeding manifold and the confinement tube through the expansion of gases. This method is widely used to analyze thermoacoustic coupling phenomena (see for example Poinsot et al. (2012); Dowling et al. (2003); F. E. C. Culick (2006)). The burner is modeled as illustrated in Fig. 7.7. In each tube section, temperature, density, velocity and pressure are all subscripted with their respective numbers and mean quantities $(\bar{T}, \bar{\rho})$ are considered uniform. The

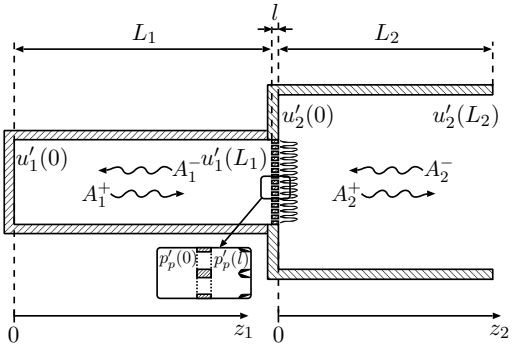

Figure 7.7: *Burner and symbol convention used for the analytical model.*

pressure and velocity fluctuations are written as follows for the n^{th} tube :

$$\begin{aligned} \widetilde{u}_n(z_n) &= \frac{1}{\rho_n c_n}\left(A_n^+ e^{ik_n z_n} - A_n^- e^{-ik_n z_n}\right) \\ \widetilde{p}_n(z_n) &= A_n^+ e^{ik_n z_n} + A_n^- e^{-ik_n z_n} \end{aligned} \tag{7.1}$$

where z_n stands for the position within the system, $k_n = \omega/c_n$ denotes the wave number and c_n indicates the speed of sound which differs in the premixer $c_1 = 340$ m/s and in the flame tube $c_2 = 850$ m/s.
These relations are completed by matching and boundary conditions. The head of the piston offers a quasi-perfect reflecting boundary condition which gives $\widetilde{u}_1(0) = 0$. At the combustor outlet, sound radiation is neglected and the pressure fluctuation vanishes , which yields $\widetilde{p}_2(L_2) = 0$. In this model, no end correction is taken into account, but it would be easy to include as all it does is to augment the length of the confinement tube by a factor of 0.61 times the radius. The unsteady flow in the perforated plate is considered with bulk oscillations of velocity in the apertures. Based on Melling's work (Melling (1973)), a relation that links the pressure between the upstream and downstream sides of the perforated plate can be derived :

$$\widetilde{p}_p(l) - \widetilde{p}_p(0) = i\,\omega\rho_1 l\left(1 + \frac{l_\nu}{r_p}(1+i)\right)\widetilde{u}_p \tag{7.2}$$

where $l_\nu = (2\nu/\omega)^{1/2}$ stands for the viscous acoustic boundary layer thickness and ν the kinematic viscosity. Pressures and velocities on each side of the perforated plate are linked with the sound waves in the upstream and downstream cavities by :

$$\widetilde{p}_p(0) = \widetilde{p}_1(L_1)\ , \quad \widetilde{p}_p(l) = \widetilde{p}_2(0)\ , \quad S_1\widetilde{u}_1(L_1) = NS_p\widetilde{u}_p \tag{7.3}$$

where S_1 is the surface area of the feeding manifold section, S_p is the surface area of one aperture and N corresponds to the number of holes. Combining

Eqs. (7.2) and (7.3) it is possible to find the pressure jump condition between the upstream and downstream cavities :

$$\widetilde{p}_2(0) - \widetilde{p}_1(L_1) = i\,\omega\rho_1 l \left(1 + \frac{l_\nu}{r_p}(1+i)\right) \frac{\widetilde{u}_1(L_1)}{\mathcal{P}} \tag{7.4}$$

As the perforated plate is thin with a high porosity, one expects that its influence on the acoustic field will be weak. The acoustic volume flow rate experiences a jump through the unsteady flame region :

$$S_2\widetilde{u}_2(0) - NS_p\widetilde{u}_p = \frac{\gamma-1}{\rho_1 c_1^2}\widetilde{\dot{Q}} \tag{7.5}$$

where S_2 represents the confinement section surface area, γ is the heat capacity ratio and $\widetilde{\dot{Q}}$ denotes the heat release rate fluctuation. The right hand side term of Eq. (7.5) can be expressed by taking into account the response of the flame to velocity fluctuations with a Flame Describing Function (FDF). This quantity is obtained with the setup presented in Fig. 7.4. The conical flames are subjected to harmonic oscillation of increasing rms fluctuation levels up to 51 % of the bulk velocity in the perforation for a range of frequencies up to 1600 Hz. FDF measurements are plotted in Fig. 7.8 in terms of gain G and phase φ defined as :

$$\begin{aligned}\mathcal{F}\left(\omega_r, u_{rms}/U_b\right) &= \frac{\widetilde{\dot{Q}}/\bar{\dot{Q}}}{u_{rms}/U_b} \\ &= G\left(\omega_r, u_{rms}/U_b\right) e^{i\varphi(\omega_r, u_{rms}/U_b)}\end{aligned} \tag{7.6}$$

where $\overline{\dot{Q}}$ stands for the mean value of the heat release rate fluctuation and U_b the mean flow velocity in one hole. The FDF depends on both the frequency ω_r and the fluctuation amplitude u_{rms}/U_b as shown in Fig. 7.8. When the amplitude increases, the gain G drops and the phase φ shifts confirming the nonlinear behavior of the flame. This is the key point of the nonlinear stability analysis. As shown in this figure, the FDF data are limited by the lack of efficiency from the loudspeaker at high frequency and amplitude. The forcing root mean square velocity level u_{rms} is determined by a Fourier transform and U_b stands for the mean value of the velocity profile measured 0.7 mm above one hole by means of LDV. It is equal to $U_b = 3.1$ m.s^{-1}. The normalized ratio between the fluctuation of OH* radical light intensity and the velocity yields the gain G and phase φ of the flame response. The flame acts as a low pass filter with a significant overshoot for higher frequencies and low fluctuation amplitudes. This behavior is also noted by other authors (Schuller et al. (2003a); Durox et al. (2009b); Kornilov et al. (2009)). The phase evolves in a quasi linear fashion with the frequency and is sensitive to the fluctuation level.

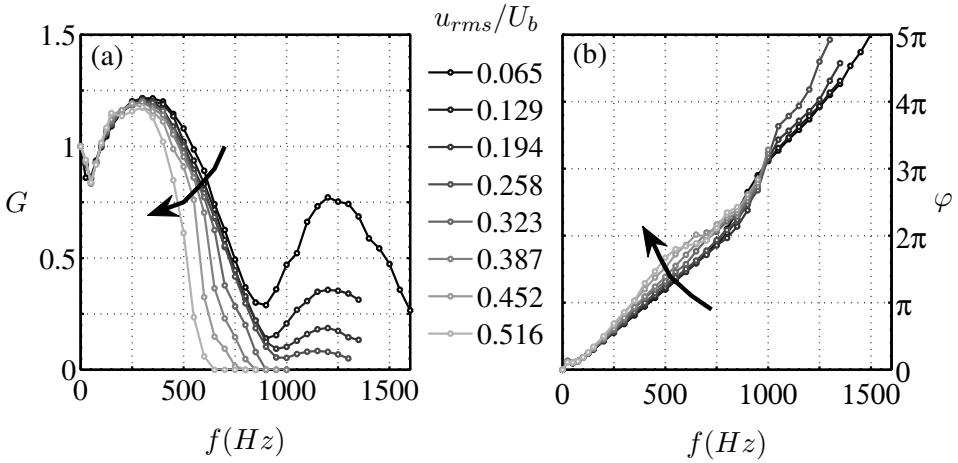

Figure 7.8: *Experimental measurements of the gain G and phase φ of the FDF. u_{rms} corresponds to the rms value of the fluctuation amplitude and U_b the mean flow velocity within one hole.*

With the aim of using these measures for stability analysis, data are interpolated and extrapolated in missing areas. Considering the right hand side of Eq. (7.5) and the FDF Eq. (7.6), one can write :

$$\frac{\gamma-1}{\rho_1 c_1^2}\widetilde{\dot{Q}} = \frac{\gamma-1}{\rho_1 c_1^2}\frac{\widetilde{\dot{Q}}\Big/\overline{\dot{Q}}}{\widetilde{u}_p/\overline{u}_p}\frac{\widetilde{u}_p/\overline{u}_p}{1\Big/\overline{\dot{Q}}} \tag{7.7}$$

In the present study, air and methane are considered to be ideal gases yielding, $c_1 = \sqrt{\gamma r T_1}$, $\overline{\dot{Q}} = \dot{m} c_p (T_f - T_1)$, $c_p = \gamma r/(\gamma - 1)$, $\dot{m} = \rho_1 N S_p \overline{u}_p$, where r is the specific gas constant for dry air, $\dot{m}$ is the mixture mass flow rate in one hole, c_p denotes the specific heat at constant pressure and T_f is the adiabatic flame temperature. Combining Eqs. (7.5) to (7.7), the velocity relation of Eq. (7.3) and the ideal gas relations, one obtains an expression for the acoustic volume flow rate jump condition across the flame sheet depending on the FDF :

$$S_2\widetilde{u}_2(0) - S_1\widetilde{u}_1(L_1) = G e^{i\varphi} S_1 \left(\frac{T_f}{T_1} - 1\right)\widetilde{u}_1(L_1) \tag{7.8}$$

The preceding set of equations can be used to obtain the following linear system :

$$\begin{pmatrix} 1 & -1 & 0 & 0 \\ 0 & 0 & e^{ik_2L_2} & e^{-ik_2L_2} \\ \mathcal{A}_1 e^{ik_1L_1} & \mathcal{A}_2 e^{-ik_1L_1} & -1 & -1 \\ \mathcal{B}e^{ik_1L_1} & -\mathcal{B}e^{-ik_1L_1} & -1 & 1 \end{pmatrix} \begin{pmatrix} A_1^+ \\ A_1^- \\ A_2^+ \\ A_2^- \end{pmatrix} = 0 \tag{7.9}$$

where $\mathcal{A}_1$, $\mathcal{A}_2$ and $\mathcal{B}$ corresponds to :

$$\mathcal{A}_1 = 1 + \frac{i\omega l}{\mathcal{P}c_1}\left[1 + \frac{l_\nu}{r_p}(1+i)\right],\ \mathcal{A}_2 = 1 - \frac{i\omega l}{\mathcal{P}c_1}\left[1 + \frac{l_\nu}{r_p}(1+i)\right],$$

$$\mathcal{B} = \frac{S_1}{S_2}\frac{\rho_2 c_2}{\rho_1 c_1}\left[1 + Ge^{i\varphi}\left(\frac{T_f}{T_1} - 1\right)\right]$$

The determinant of this system must equal zero, to obtain non-trivial solutions. This condition provides the dispersion relation describing the dynamics of the system :

$$\begin{aligned} &\frac{S_1}{S_2}\frac{\rho_2 c_2}{\rho_1 c_1}\left[1 + Ge^{i\varphi}\left(\frac{T_f}{T_1} - 1\right)\right]\sin(k_1 L_1)\sin(k_2 L_2) \\ &- \cos(k_1 L_1)\cos(k_2 L_2) + \frac{\omega l}{\mathcal{P}c_1}\left[1 + \frac{l_\nu}{r_p}(1+i)\right] \\ &\cos(k_2 L_2)\sin(k_1 L_1) = 0 \end{aligned} \tag{7.10}$$

The objective is to find complex roots $\omega = \omega_r + i\omega_i$ yielding oscillation frequencies $f = \omega_r/2\pi$ and growth rates ω_i of perturbations.

7.1.6 Theoretical and experimental comparison

The nonlinear analysis described in the previous section is now used to investigate the stability of the system. It is interesting to compare the experimental results from the self-sustained instabilities described in Sec. 7.1.4 with the theoretical predictions of the oscillation frequencies and amplitudes at the limit cycle. Therefore, the FDF is used to calculate roots of the dispersion relation Eq. (7.10) for each driving amplitude. This yields ω_r and ω_i couples for each burner geometry and driving amplitude. For the different lengths of feeding manifold and the $L_2 = 0.10$ m confinement tube, calculations for the three first oscillation modes give the growth rate evolutions displayed in Fig. 7.9. This figure represents positive values of growth rate corresponding to unstable regions. Negative growth rates corresponding to stable zone are displayed through white color regions. Each color is dedicated to an oscillation mode; the first mode is drawn in yellow, the second in blue, and the third in red. Red dashed lines indicate the limit cycle corresponding to vanishing values of the growth rate.

From the different growth rate trajectories, it is possible to find, for each geometry, the evolution of the oscillation frequency of an instability up to the limit cycle. As presented in Fig. 7.9, the growth rates reveal three types of evolution. The first type of trajectory (for example dashed line “A” obtained

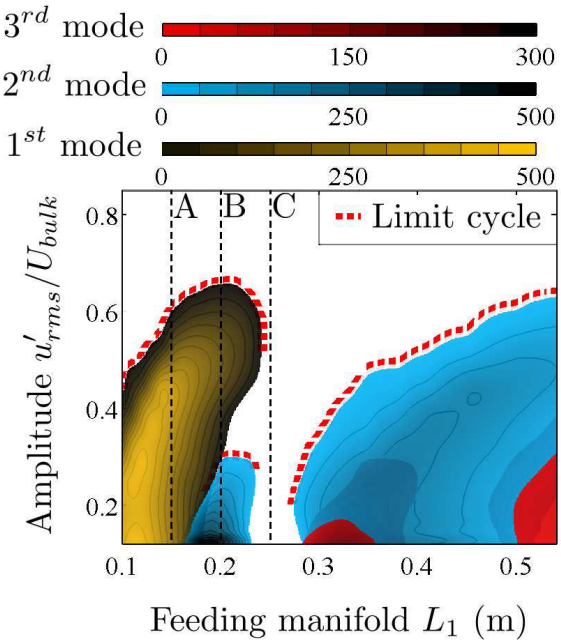

Figure 7.9: *Positive values of the growth rate (in s^{-1}) for the L_2 = 0.10 m confinement as function of the length of the feeding manifold and the relative fluctuation level, u'_{rms}/U_{bulk}.*

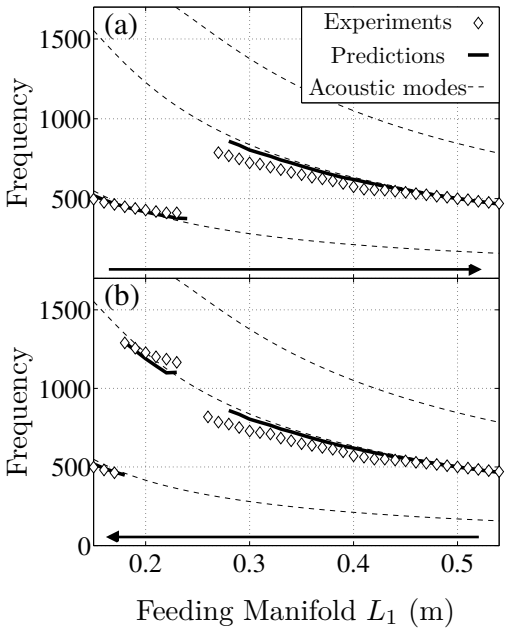

Figure 7.10: *Experimental and predicted oscillation frequencies of self-sustained instabilities for the L_2 = 0.10 m confinement tube for increasing (a) and decreasing (b) sweeps of the feeding manifold length L_1.*

for $L_1 = 0.15$ m) is positive for a small level of perturbation ($u_{rms}/U_b = 0.1$) and vanishes for a finite amplitude ($u_{rms}/U_b = 0.6$), and, as such, defines the limit cycle of the system. In this case, the system is linearly unstable. For the second type (for example dashed line "B" obtained for $L_1 = 0.20$ m), the growth rate of the first mode (yellow zone) is negative for small perturbation amplitudes but becomes positive at an amplitude of $u_{rms}/U_b = 0.3$ and finally vanishes for a higher amplitude ($u_{rms}/U_b = 0.65$). This yields a limit cycle that can be triggered by a finite level of perturbation. Indeed, a small level of perturbation cannot trigger an instability whereas a high oscillation level can. These limit cycles are nonlinearly unstable and linearly stable. The last type (for example dashed line "C" obtained for $L_1 = 0.25$ m) yields negative values of growth rate for all perturbation levels. In this case, the system is unconditionally stable. Moreover, it can be deemed as both linearly and nonlinearly stable. In summary, it is found that the calculations show three types of growth rate evolutions.

By analyzing the growth rate for each length of feeding manifold L_1 it is possible to find the limit cycle obtained when $\omega_i = 0$ and extract at the same time the oscillation frequency using the angular frequency ω_r. The limit cycle is reached when the growth rate is equal to zero. The acoustic damping α is not taken into account in these calculations. For systems featuring large damping, limit cycles are reached when $\omega_i - \alpha = 0$. In the present case, the influence of α is weak because growth rates take high values typically about 500 s^{-1} whereas α in this system was estimated to be around 10 to 50 s^{-1} and does not significantly influence the results.

Figure 7.10 displays the evolution of the predicted oscillation frequencies and the experimental measurements. These predictions were obtained by analyzing the growth rate as detailed herein. In these figures, the acoustic eigenmodes, without flame ($G = 0$ in the dispersion relation of Eq. (7.10)), are drawn as thin dashed lines. The frequencies predicted at the limit cycle using the nonlinear analysis are represented by bold lines and the measurements are plotted as diamond signs. For each length of feeding manifold, (L_1), the frequency is extracted from the oscillations of the pressure signal (M_2). As presented in Fig. 7.5, for the $L_2 = 0.10$ m confinement case there are two types of frequency evolutions. When the manifold length is increased (min to max) (Fig. 7.10(a)), the oscillation frequency evolves around the first eigenmode with a change around the second eigenmode after the stable zone between $L_1 = 0.24$ m and 0.26 m. In the reverse movement (max to min) (Fig. 7.10(b)), the frequency lies close to the second eigenmode until it becomes stable at $L_1 = 0.26$ m, but resumes around the second eigenmode for $L_1 = 0.23$ m to 0.18 m before it finally switches to the first mode for the last three lengths $L_1 = 0.17$ m to 0.15 m.

This behavior, defined as hysteretic, is well described by the growth rate analysis (see Fig. 7.9). When the piston is moved in the reverse direction (L_1 decreasing), the oscillation vanishes for three lengths of feeding manifold L_1

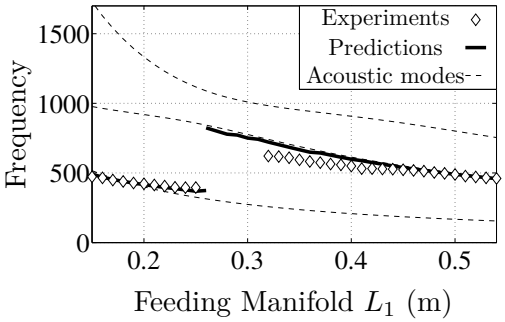

Figure 7.11: *Experimental and predicted oscillation frequencies of self-sustained instabilities for the L_2 = 0.20 m confinement tube. Increasing and decreasing L_1 has the same influence on the frequency evolution.*

= 0.26, 0.25 and 0.24 m. After the stable zone, linearly unstable trajectories for the second mode yield a weak limit cycle between L_1 = 0.23 m and 0.18 m (blue zone). For shorter lengths $L_1 < 0.18$ m, the system is unstable on the first mode (yellow zone) as presented in Fig. 7.10(b). At the beginning, when the manifold cavity was increased from L_1 = 0.15 m to 0.54 m, the system oscillates at high amplitudes for the first length interval L_1 = 0.15 m to 0.17 m. In this case, the instability remains on the first mode even if the growth rate trajectories of this mode become nonlinearly unstable between L_1 = 0.18 m and 0.23 m. The nonlinear impulse, needed to trigger the first mode, comes from the high oscillation amplitude reached at the previous length.
The origin of this hysteresis is linked to the nonlinear behavior of the flame. Indeed, it is possible to predict the hysteresis by analyzing the FDF phase at the acoustic eigenmodes frequencies around the stable zone. If the phase of the FDF is comprised between π and 2π modulo 2π, the instability may develop (Durox et al. (2009a); Noiray et al. (2009)). For the L_2 = 0.10 m confinement case, when the instability evolves on the first mode at high amplitude (increasing L_1) the phase is in the right band between π and 2π (see Fig. 7.8) at L_1 = 0.23 m where f = 400 Hz whereas this is not the case for the second mode f = 1100 Hz. When the cavity length L_1 decreases, as the system leaves the stable zone at L_1 = 0.23 m, the phase for low oscillation amplitude lies in the right band for the high frequency f = 1100 Hz of the second mode. This is the reason why the instability frequency takes on second mode values.

The growth rate evolution was also computed for the L_2 = 0.20 m confinement tube and its reading yields the different limit cycle oscillation frequencies. These results are presented in Fig. 7.11. For this second confinement case, the evolution is simpler. When the feeding manifold length L_1 is increased, the instability frequency changes from the first mode between L_1 = 0.15 m to 0.25 m to the second mode between L_1 = 0.32 m to 0.54 m after a stable zone. When L_1 is decreased, the instability evolves in the same way. Thus, in this case, no

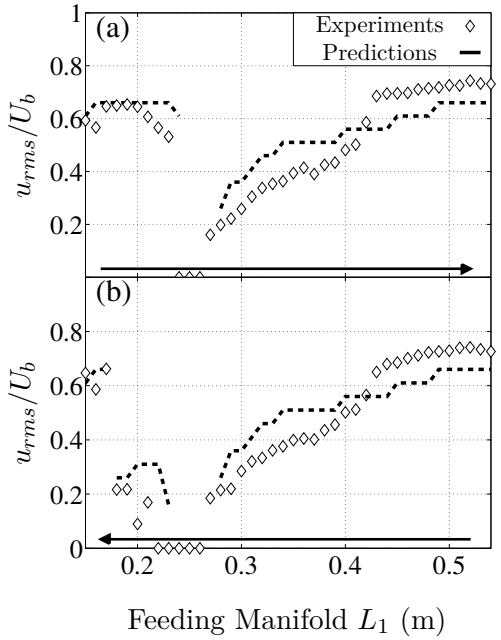

Figure 7.12: *Experimental and predicted amplitudes of the instabilities for the L_2 = 0.10 m confinement tube for increasing (a) and decreasing (b) sweeps of the feeding manifold length L_1.*

hysteresis is observed. The theoretical analysis in terms of phase shows that the frequency of the second mode does not yield phase values in the right band at low or at high amplitude after the stable band at $L_1 = 0.25$ m. This is the reason why the system lies always on the first mode for perturbations at high or low amplitude. In this case, calculations are less reliable, as some oscillation frequencies are predicted in the stable zone. By analyzing the growth rate, it is shown that the model gives positive values for these lengths. These discrepancies can be linked to the accuracy on the experimental determination of the FDF, showing the importance of getting the right flame response.

One advantage of the FDF methodology, is that, in addition to providing the limit cycle frequency, the growth rate analysis also predicts the amplitude. For each length of feeding manifold L_1 and each confinement tube length L_2, it is possible to find the oscillation amplitude when the instability oscillation is established. These results are presented in Fig. 7.12 for the $L_2 = 0.10$ m confinement tube. The predictions are plotted as dashed lines whereas the experimental values, obtained by the hot wire probe, appear as diamond signs. Fig. 7.12(a) represents the evolution of the amplitude when L_1 is increased. The oscillation evolves at high amplitude for L_1 comprised between 0.15 m and 0.23 m. After the stable zone $L_1 = 0.24$, 0.25 and 0.26 m, the oscillation grows from a level around $u_{rms}/U_b = 0.2$ to 0.7 for the longer feeding manifold length at $L_1 = 0.54$ m. By decreasing L_1, the oscillation evolves in the same

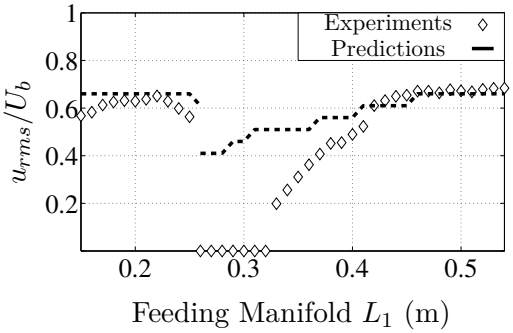

Figure 7.13: *Experimental and predicted amplitudes of the instabilities for the L_2 = 0.20 m confinement tube. Increasing and decreasing L_1 has the same influence on the amplitude evolution.*

way until the stable zone at $L_1 = 0.26$, 0.25 and 0.24 m. Then, the amplitude switches to a very low level around $u_{rms}/U_b = 0.10$, or nearly close to zero for the hot wire values at $L_1 = 0.23$ m and 0.22 m. After $L_1 = 0.18$ m, the level increases abruptly to $u_{rms}/U_b = 0.7$. The dashed lines, which represent the results of calculations, are in good agreement with the levels measured in the expriments.
For the longer confinement tube $L_2 = 0.20$ m, the evolution is drawn in Fig. 7.13. In this case, the evolution is the same when the feeding manifold length L_1 is increased or decreased. From $L_1 = 0.15$ m to 0.25 m the amplitude lies around $u_{rms}/U_b = 0.6$. It falls to 0 from $L_1 = 0.26$ m to 0.32 m. Then, the instability appears again with an increasing amplitude until it reaches $u_{rms}/U_b = 0.7$ for the longer cavities. Predictions are again in agreement with experimental data except in a range of $L_1 = 0.26$ m to 0.40 m. This is probably due to the fact that the predicted self-sustained oscillations occur in a frequency band where the gain drops rapidly and the phase of the FDF is less well defined with the consequence that the stability analysis becomes less reliable. It should be noted however that this only affects a small interval of feeding manifold sizes.

7.2 Nonlinear mode triggering in a multiple flame combustor

This section corresponds to a second publication presented at the *33rd international symposium on combustion* and published in the *Proceedings of the Combustion Institute* in 2011 :

Boudy, F., D. Durox, T. Schuller, and S. Candel. 2011. "Nonlinear mode triggering in a multiple flame combustor." *Proc. Combust. Inst.* 33 (1): 1121–28. doi:10.1016/j.proci.2010.05.079

The experimental setup and model (model A) used in this analysis are the same as those presented in Sec. 7.1. Thus, only experimental results revealing triggering in the system are presented together with the comparison between measurements and predictions delineated from model A. The abstract is kept to highlight the highlights of this section. Then, the text jumps directly to the experimental results.

7.2.1 Abstract

A nonlinear analysis of combustion instability is carried out by making use of the Flame Describing Function (FDF) framework. Predictions are compared with data obtained from experiments on a multipoint injection combustor. The burner comprises a premixer manifold of variable length, an injection system and a flame tube. This device features several types of self-sustained oscillation and its dynamics is characterized by nonlinearities like transient frequency shifting, mode switching, mode triggering and hysteresis phenomena which cannot be anticipated from a classical linear stability analysis. It is shown that many of these phenomena can be suitably predicted by including the amplitude dependent response of the flame in a matrix analysis of the system dynamics. More specifically, the present work centers on processes which cannot be anticipated from linear analysis such as mode switching linked to a triggering by the nonlinear flame response.

7.2.2 Experimental results

Experiments were carried out with the flame tube $L_2 = 0.10$ m. The measurements of the oscillation frequencies and the corresponding sound levels are plotted in Fig. 7.14 as a function of the feeding manifold length L_1.
Open circles correspond to data gathered when the manifold length is augmented (from 0.15 m to 0.54 m) while cross symbols correspond to data collected when L_1 is diminished (0.54 m to 0.15 m). The dashed lines show the first three acoustic eigenfrequencies of the burner calculated by taking into account the temperature difference between the upstream manifold and the flame tube. The system features self-sustained oscillations for all cavity lengths L_1 except between 0.24 and 0.26 m where combustion is stable. Results obtained by increasing the manifold length indicate that the oscillation frequency lies around the first acoustic mode when L_1 ranges from 0.15 m to 0.23 m, then the oscillation vanishes in the band $L_1 = 0.24$ m to 0.26 m. The peak frequency then evolves around the second acoustic mode for longer cavity depths ($L_1 =$ 0.27 m to 0.54 m). The corresponding pressure level at M_2 lies around 142 dB when the system is unstable and is roughly independent of L_1. When the piston is moved in the reverse direction, the peak oscillation frequency remains locked to the second mode from $L_1 = 0.54$ m to 0.26 m and the oscillation level is about equal to that found in the previous case. The oscillation then

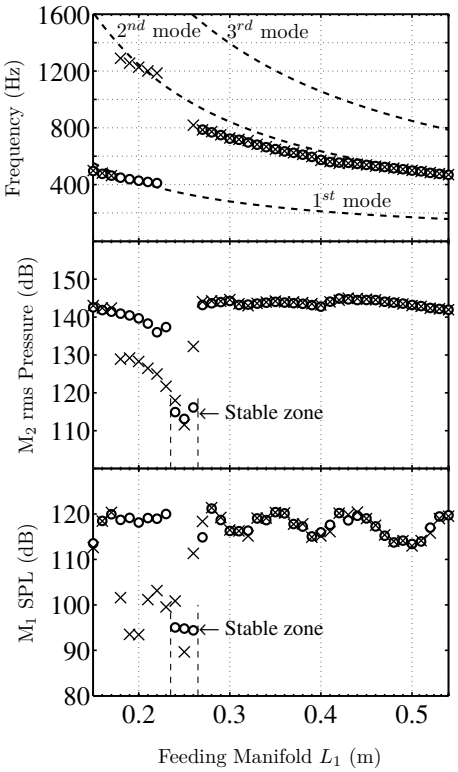

Figure 7.14: *Frequency and pressure level evolution obtained by sweeping L_1 from 0.15 m to 0.54 m (○) and from 0.54 m to 0.15 m (×). Flame tube size L_2 = 0.10 m. Acoustic eigenmodes determined by taking into account the temperature variation in the system are plotted as dashed lines.*

vanishes in the stable band, but from $L_1 = 0.22$ m to 0.18 m the frequency is still locked on the second acoustic mode with a moderate amplitude level. The peak frequency finally switches to the first acoustic mode for the shortest cavity sizes $L_1 = 0.17$ m to 0.15 m with an oscillation level equal to that found in the first set of experiments. The system clearly features an hysteresis for the range of feeding manifold lengths comprised between 0.18 and 0.22 m where the oscillation frequency and level depend on the manifold length variation history. Such features cannot be anticipated from a linear stability analysis and they constitute a good benchmark for validation of the FDF nonlinear methodology. As indicated in section 7.1.3, acoustic oscillations remain in the linear range and the only nonlinearity considered in the following stability analysis is that of the flame response.

7.2.3 Triggering and limit cycles analysis

The nonlinear stability analysis developed in section 7.1.5 is now used to obtain oscillation frequencies and associated limit cycle amplitudes and compare these predictions to experimental data. Figure 7.15 maps the growth rates determined from the dispersion relation Eq. (7.10) where only positive values are indicated and plotted as a function of the manifold size L_1 and the perturbation amplitude u_{rms}/U_b. This map has been plotted by subtracting a damping $\alpha = 20$ s^{-1} from ω_i to account for acoustic attenuation in the system. The value of α comes from a measurement not presented in this study. Regions indicated by different gray levels correspond to one of the oscillation modes, which are calculated separately. Light, medium and dark gray respectively correspond to oscillation frequencies lying around the first, second and third acoustic modes. The dark bold lines delimiting the contour of these regions indicate stable oscillation equilibria, i.e. the limit cycle reached for $\omega_i = \alpha$, whereas the dashed part of these lines designates unstable equilibria for the same modes considered separately.
Figure 7.15 indicates that regions associated to different oscillation modes can be superimposed depending on the size L_1 of the feeding manifold. Thus two unstable modes may coexist for the same feeding manifold length and the observed mode will be determined by examining the growth rate evolution as a function of perturbation level. This can be easily analyzed by plotting vertical cuts in Fig. 7.15 at different manifold lengths. The growth rate then follows three types of trajectories :

- The first type of trajectory always yields negative growth rates for all perturbation levels (line B in Fig. 7.15). In this case, the system is linearly and nonlinearly stable. This is for example the case for $L_1 = 0.24$ m to 0.26 m as shown in Fig. 7.14 where the system is effectively stable.

- The second type, illustrated for $L_1 = 0.10$ m (corresponding to the y-

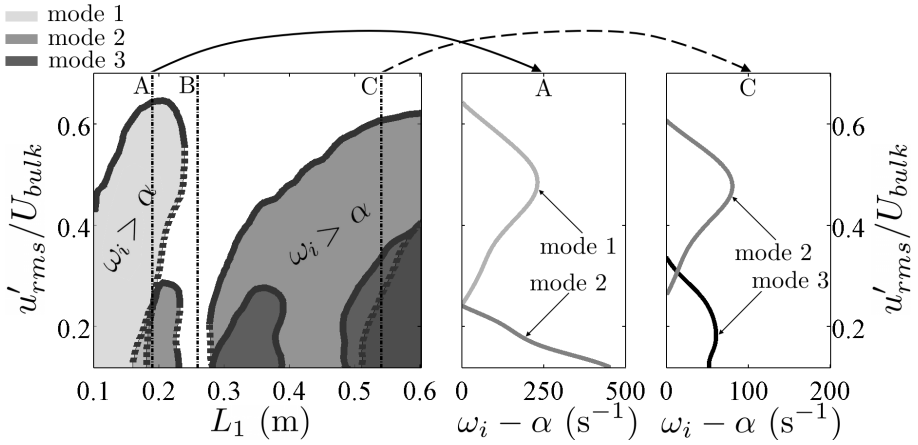

Figure 7.15: *Positive values of growth rate ($\omega_i - \alpha$ in s^{-1}) calculated from the dispersion relation as function of the feeding manifold length, L_1 and the relative fluctuation level, u'_{rms}/U_{bulk}. A damping α of 20 s^{-1} is considered in this figure. Two slices in the growth rate are plotted on the right. The first "A" corresponds to $L_1 = 0.18$ m and the second "C" pertains to $L_1 = 0.54$ m.*

axis in Fig. 7.15), features positive growth rates for small perturbation levels and a vanishing growth rate for a finite amplitude $u_{rms}/U_b = 0.45$. This corresponds to a supercritical bifurcation where the system is linearly unstable. The instability grows from an infinitesimal perturbation and reaches a limit cycle with an oscillation frequency locked around the first acoustic mode.

- The third type of trajectory is illustrated by taking a slice through the growth rate map at point A. In this case, mode 1 is linearly stable. A linear analysis would predict a stable operation for this mode. A deeper analysis of the subplot A in Fig. 7.15 shows that mode 1 features positive growth rates for perturbation levels u_{rms}/U_b higher than 0.20 and then reaches a limit cycle around $u_{rms}/U_b \simeq 0.65$. Mode 1 corresponds to a subcritical bifurcation with a system linearly stable on this mode, but nonlinearly unstable. This type of mode can be triggered by another supercritical mode or by an external perturbation if the threshold level is exceeded as detailed in the following part.

Subcritical bifurcations can now be used to explain some of the experimental observations and in particular the nonlinear mode triggering phenomenon. This is illustrated for two lengths $L_1 = 0.18$ m and 0.54 m. For $L_1 = 0.18$ m, the subplot A in Fig. 7.15 shows that the first mode features a subcritical bifurcation (nonlinear instability) and the second mode a supercritical bifurcation (linear instability). The two trajectories cross for $u_{rms}/U_b \simeq 0.25$ close to $\omega_i = \alpha$. The following scenario can be predicted. An infinitesimal oscillation

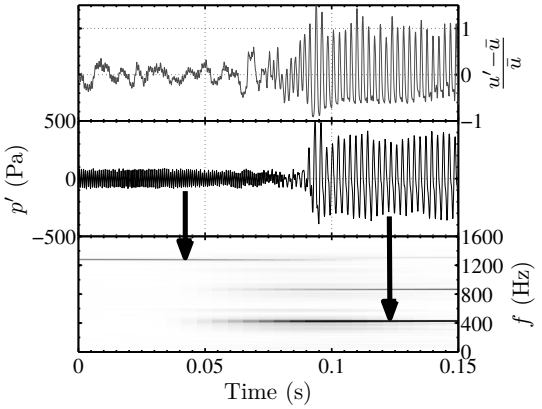

Figure 7.16: *Temporal signals of the self-sustained instability for $L_1 = 0.18$ m. Upper boxes display normalized velocity measured by the hot wire probe and pressure of microphone M_2. Lower box corresponds to the short-time Fourier spectral density of the pressure signal.*

starts to grow with an oscillation frequency locked on mode 2 and reaches an oscillation level $u_{rms}/U_b \simeq 0.25$. The mode trajectory then crosses that of mode 1 which features growth rates values around α. In this case, by adding a perturbation, mode 1 growth rate is greater than the damping α and the oscillation frequency switches to mode 1 until the mode reaches a new limit cycle for $u_{rms}/U_b \simeq 0.65$ when $\omega_i = \alpha$. Figure 7.16 displays the temporal signals recorded by the different sensors for this manifold length $L_1 = 0.18$ m. The velocity fluctuation signal measured by the hot wire below the perforated plate is displayed in the upper subfigure.

The signal measured by microphone M_2 is plotted in the central subfigure. The lower plot shows the short-time Fourier power spectral density of the pressure signal as a function of time. From $t = 0$ to 0.08 s, the frequency found in the pressure trace ($f_2 \simeq 1290$ Hz) corresponds to the calculated oscillation frequency $f_2 = 1292$ Hz determined from the dispersion relation Eq. (7.10) for mode 2 with a small oscillation amplitude. At $t = 0.08$ s, an external perturbation is introduced by blowing on the flame and the system quickly switches to a new limit cycle with a lower oscillation frequency $f_1 \simeq 449$ Hz and a larger fluctuation amplitude. It can be seen in Fig. 7.14 that this frequency closely matches that calculated. This corresponds to the scenario deduced from the nonlinear analysis, where an external perturbation was required to initiate the transition from mode 2 to mode 1. This is so because trajectories cross at a point where growth rates are close to the damping value α.

It is thus worth examining if nonlinear triggering may also take place without requiring an external disturbance. This can be obtained for a manifold cavity length $L_1 = 0.54$ m. The growth rates trajectories for modes 2 and 3, plotted in subfigure C in Fig. 7.15, feature subcritical and supercritical bifurcation. Their trajectories cross for a positive growth rate $\omega_i - \alpha$ of 13 s^{-1}.

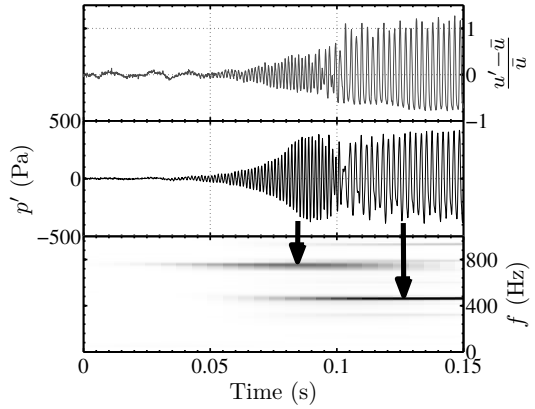

Figure 7.17: *Temporal signals of the self-sustained instability for $L_1 = 0.54$ m. Upper boxes display normalized velocity measured by the hot wire probe and pressure of microphone M_2. Lower box corresponds to the short-time Fourier spectral density of the pressure signal.*

An oscillation then naturally develops from an infinitesimal perturbation and is locked on mode 3 which is linearly unstable. When the velocity oscillation amplitude reaches $u_{rms}/U_b \simeq 0.30$, the oscillation switches on mode 2 which is nonlinearly unstable and features higher growth rates than mode 3 for higher perturbation levels. It then reaches a limit cycle $u_{rms}/U_b \simeq 0.60$ and remains locked on mode 2 with a predicted oscillation frequency $f_2 = 465$ Hz deduced from Eq. (7.10). Figure 7.17 shows the corresponding temporal evolutions of the measured signals. The time-frequency analysis shows that a switch in frequency occurs during the onset of oscillation. From $t = 0$ to 0.09 s an oscillation slowly grows with a frequency corresponding to that calculated for the third mode $f_3 \simeq 765$ Hz. At time $t \simeq 0.09$ s, the oscillation level reaches $u_{rms}/U_b \simeq 0.20$ and the frequency suddenly switches to the second mode in about 0.015 s without external actuation. The system then evolves to a new limit cycle with an oscillation frequency $f_3 = 465$ Hz in agreement with that predicted, and with fluctuation level u_{rms}/U_b of the order of 0.6 comparable to the fluctuation predicted thanks to the dispersion relation for $L_1 = 0.54$ m.

7.2.4 Conclusion

Calculations of limit cycles based on the FDF framework for combustion instability analysis have been undertaken with "model A" in order to predict these thermoacoustic oscillations. The system studied herein is close to a real configuration in the sense that it features a feeding manifold that is used to feed a multipoint injector and features a combustion region in a confined environment. The FDF, determined experimentally, exhibits nonlinearities of the flame response. This is used to derive a nonlinear dispersion relation providing predictions of the stable or unstable behavior of the combustor as a function of amplitude. Comparison with systematic experiments carried out by changing

the feeding manifold length and flame tube size are in agreement with experiments over a broad range of parameters. Calculations are quite reliable in the case of a short flame tube but they are slightly off in the case of a longer tube where a difference is observed in a finite range of feeding manifold lengths. This may be corrected by improving the procedure to determine the FDF but also by refining the model which includes simplifications of the boundary and matching conditions. It remains that the FDF analysis provides a suitable account of limit cycle amplitudes, hysteresis and mode switching observed in practice as demonstrated in the short flame tube case. Comparisons with systematic experiments on triggering and mode switching indicate that predictions of limit cycle amplitudes and mode switching are in good agreement with experimental data and highlight the necessity of a nonlinear analysis. It is demonstrated in particular that some of the unstable oscillation frequencies corresponding to large amplitude levels observed experimentally would not have been predicted with a linear analysis. This is illustrated in a case where the limit cycle oscillation is locked on a mode around 465 Hz with a large level of oscillation, whereas a linear stability analysis would have predicted an unstable mode around 765 Hz. This indicates that the stability map cannot be completely determined without taking into account the nonlinear flame response but that it is possible to keep a linear description of the other elements in the system. While the nonlinear gain influences the limit cycle prediction, the nonlinear phase also plays an important role. It controls hysteresis, mode switching and triggering and modifies the amplitude of the limit cycles. This latter point is studied in further detail in Appendix A, where one calculates a bifurcation diagram by using a FDF with a linear phase. Such calculation illustrates the phase influence with the loss of the nonlinearly unstable modes.

Chapter 8

Detailed dynamical analysis

The various modeling elements presented up to now are used in this chapter to study the dynamics of the burner configuration described in Chapter 1. The model uses a network formed by two ducts with a flame located at the interface. This model has been devised in Chapter 6. It was shown in Sec. 7.1.6 that there are differences between experiments and predictions. The initial model is improved by taking into account all the burner elements analyzed in Chapter 4. This includes upstream and downstream boundary conditions and the change in the surface area between the two cavities. A FDF measured under confined conditions is also considered. Predictions of this advanced model allow to retrieve frequencies and amplitudes experimentally observed with an improved agreement for a variety of geometrical ranges. This allows reconstructions of pressure and velocity in the burner. There are however cases where the limit cycles arising in experiments feature amplitude and frequency variations which are less well represented by this advanced FDF model and which need to be considered separately.

8.1 Experimental investigation for different flame tube sizes

Configurations examined in this chapter correspond to four different flame tube sizes progressively increased from $L_2 = 0.10$ m to 0.40 m by steps of 0.10 m. The exploration is carried out for different feeding manifold lengths L_1 by moving the piston in both directions for each flame tube configuration. The perforated plate of thickness $l = 15$ mm is used in all experiments. The FDF is slightly modified compared to that used in Chapter 7 with the thin perforated plate. This is to account for the change in velocity profile in the perforations which was seen to depend on the flame holder thickness. This change influences the flame front dynamics and its response to harmonic perturbations (see Chapter 5).

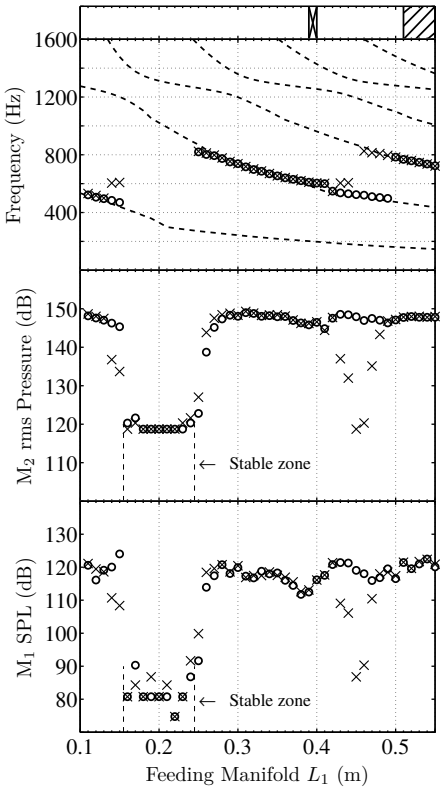

Figure 8.1: *Frequency and sound pressure level evolutions for a confinement tube L_2 = 0.10 m. The feeding manifold length L_1 is swept from 0.11 m to 0.55 m (○) and from 0.55 m to 0.11 m (×). Dashed lines indicate acoustic eigenmodes calculated without unsteady combustion. Upper frame on the top of the figure shows limit cycle ranges with variable amplitude and frequency. The cross is linked to the regular beating range, whereas the case of multiple modes corresponds to the hatched area.*

8.1.1 Flame tube $L_2 = 0.10$ m

The first set of results is presented in Fig. 8.1 for the smallest confinement tube (L_2 = 0.10 m). Frequencies and rms pressure amplitudes are plotted for the different lengths of feeding manifold L_1 explored. Open circle symbols (○) correspond to data gathered when L_1 is increased from 0.11 m to 0.55 m. Cross symbols (×) indicate the behavior obtained by diminishing L_1 from 0.55 to 0.11 m. The upper window above the frequency plot indicates limit cycle ranges where the amplitude features a fickle value whether it is regular or not. The different instabilities observed are examined in the present section. When the feeding manifold length L_1 is increased, oscillations evolve around the first acoustic eigenmode from L_1 = 0.11 m to 0.15 m. At L_1 = 0.16 m, one finds a stable band until L_1 = 0.24 m. For L_1 = 0.25 m, the system meets enters in an unstable range around the second mode. These oscillations are found from L_1

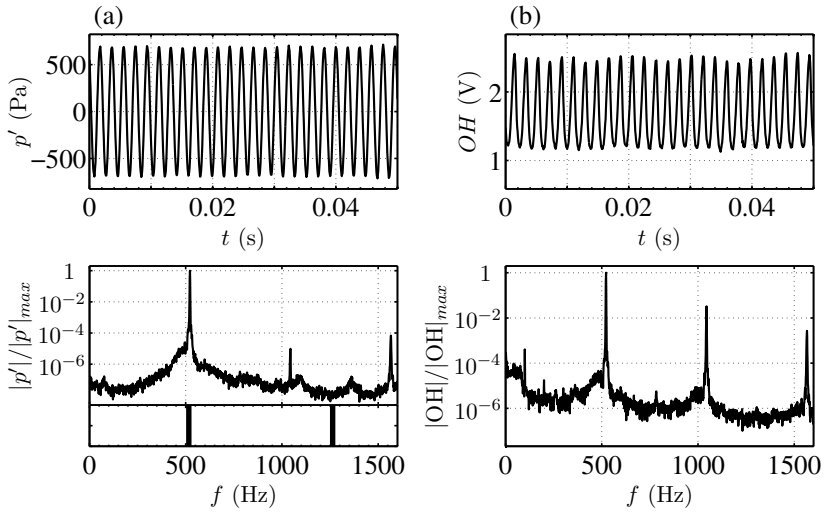

Figure 8.2: *Pressure signal recorded by microphone* M_2 *and OH* light emission for* $L_1 = 0.11$ *m and flame tube* $L_2 = 0.10$ *m. Corresponding spectral densities are shown below. The window under the pressure spectrum shows the acoustic eigenmodes positions as vertical solid lines (calculated by assuming that unsteady combustion is absent).*

= 0.25 m to 0.49 m. For $L_1 = 0.40$ and 0.41 m, the flame cannot stabilize on a well defined limit cycle. For the last range, $L_1 = 0.50$ m to 0.55 m, the system exhibits an unstable range around the third mode. In this case, the instability frequency is not a pure tone from $L_1 = 0.51$ m to 0.55 m. Frequencies and amplitudes represented in Fig. 8.1 for $L_1 = 0.40$ m and 0.41 m and $L_1 = 0.51$ m to 0.55 m correspond to the main peaks in the spectrum of the pressure signal detected by microphone M_2. These unstable amplitudes will be analyzed in a detailed fashion in Chapter 9.

In a second series of experiments, the feeding manifold length L_1 is decreased. In this way, oscillations first lie around the third mode from $L_1 = 0.55$ m to 0.46 m. As in the first direction of exploration, the flame does not oscillate on a pure tone from $L_1 = 0.55$ m to 0.51 m. At $L_1 = 0.45$ m flame oscillations nearly vanish. By diminishing L_1, mode 2 is triggered with a non negligible amplitude for $L_1 = 0.44$ m and 0.43 m. It is important to highlight that the second mode triggered for $L_1 = 0.44$ m and 0.43 m is slightly higher in frequency and lower in amplitude than in the first exploration direction. The limit cycle retrieved for $L_1 = 0.40$ m and 0.41 m is not well defined. An oscillation at the pure tone associated to mode 2 frequency is obtained until $L_1 = 0.25$ m. The stable band is found again from $L_1 = 0.24$ m to 0.16 m. Finally, the system switches again to the first mode at $L_1 = 0.15$ m. One can see that this time, as noted for $L_1 = 0.44$ m and 0.43 m, frequency and amplitude exhibit different values for $L_1 = 0.15$ m and 0.14 m. In summary this configuration ($L_2 = 0.10$ m) exhibits two hysteresis intervals.

Limit cycles with pure tone oscillations were found for most of feeding manifold lengths L_1 when L_2 is set to 0.10 m, but oscillations characterized by multiple frequencies were also identified for a set of conditions for mode 2 and mode 3. Pure tone oscillations are typified by a flame oscillation at a single frequency. This has been checked experimentally by analyzing pressure time traces and flame shapes recorded by means of high speed imaging. A typical case is displayed in Fig. 8.2 for pressure and photomultiplier (PM) signals when L_1 = 0.11 m. The time traces of these signals appear in the upper plots. The lower plot shows the power spectral densities estimated by means of Welch's method of averaging combined with a Hanning windowing. These spectral densities have been normalized by the amplitude reached by the main peak to exhibit the importance of harmonics. Acoustic eigenmodes, calculated without unsteady flame and different temperatures in each cavity (300 K in the feeding manifold and 900 K in the downstream flame tube), are shown as vertical solid lines in the lower window below the pressure spectrum. Time traces indicate that the flame oscillates in a nonlinear fashion whereas the pressure remains in the linear range. This is confirmed by analyzing the PM spectrum. The harmonics observed in the flame response feature a large amplitude compared to the ones noted on pressure spectrum.

One finds multiple frequency cases, for L_1 = 0.40 m and 0.41 m and for L_1 = 0.51 m to 0.55 m. In these ranges the pressure spectra show multiple peaks with high amplitudes. This is illustrated in Figure 8.3 for the pressure and PM signals for L_1 = 0.40 m. These signals exhibit modulations because oscillation frequencies are close. The flame spectrum is typified by a series of concentrated peaks around the main instability frequency. One can easily distinguish three main components with a main peak at 604 Hz, a lower peak at 570 Hz and a third component at 638 Hz. These three frequencies lie around the second acoustic mode of the system. The pressure signal is further analyzed by using the continuous wavelet transform with a complex Morlet mother wavelet to characterize the frequency evolution with time. The resulting analysis is presented in Fig. 8.4. This indicates that the instability frequency oscillates around a mean value and that the oscillation frequency reaches a maximum when the pressure oscillation reaches a minimum and conversely.

A second band featuring multiple frequencies is now investigated. The feeding manifold length L_1 = 0.52 m is chosen to illustrate this phenomenon. Result presented in Fig. 8.5 show that the power spectral densities of pressure and OH* signals exhibit two main peaks around mode 2 and mode 3 indicating that the system is locked on these modes. Oscillations may occur simultaneously or in an alternative fashion. By using the wavelet analysis, it is possible to shed light on this point. Figure 8.6 indicates that the main frequency 759 Hz associated to mode 3 is always present in the pressure signal. The same analysis around mode 2 shows the same type of signal, indicating that the flame oscillates simultaneously on mode 2 and mode 3.

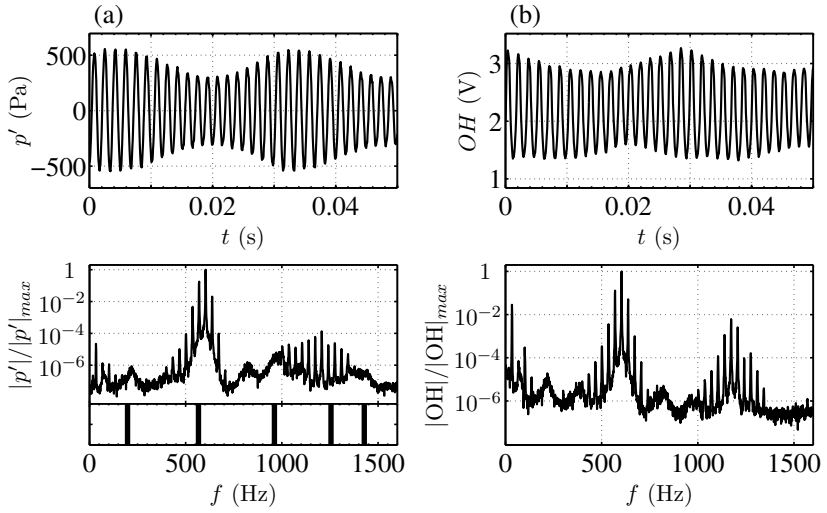

Figure 8.3: *Pressure signal recorded by microphone* M_2 *and OH* light emission for* $L_1 = 0.40$ *m and flame tube* $L_2 = 0.10$ *m. Corresponding spectral densities are shown below. The window under the pressure spectrum shows the acoustic eigenmodes positions as vertical solid lines (calculated by assuming that unsteady combustion is absent).*

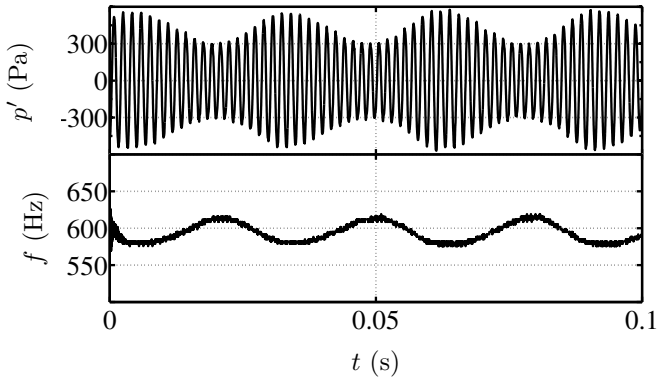

Figure 8.4: *Pressure signal from microphone* M_2 *for* $L_1 = 0.40$ *m and flame tube* $L_2 = 0.10$ *m. Time frequency signal analysis using a continuous wavelet transform with a complex Morlet mother wavelet to extract the evolution of frequency. This allows to see which frequency appears as the amplitude grows or decreases.*

At this point, it is interesting to use phase plane portraits to associate what has been found previously with a representation of limit or pseudo-limit cycle. Figure 8.7 represents three phase planes (a, b, c) respectively corresponding to L_1 = 0.11 m, 0.40 m and 0.52 m. Figure 8.7(a) is typified by a circular pattern corresponding to periodic oscillations. Modulation of the fixed amplitude induces a torus pattern in Fig. 8.7(b) for L_1 = 0.40 m. Period deformations lead to multiple circular patterns as displayed in Fig. 8.7(c).
In summary, one finds that unstable modes in the short confinement tube configuration present three types of limit cycle. The first is well defined (Fig. 8.7(a)), the second is linked to regular beating (Fig. 8.7(b)) while the last one features a period deformation with the simultaneous presence of two modes (Fig. 8.7(c)).

8.1.2 Flame tube L_2 = 0.20 m

A similar analysis is now carried out for a slightly longer flame tube L_2 = 0.20 m. The instability frequencies and corresponding amplitudes are shown in Fig. 8.8 when the feeding manifold length L_1 is first increased and then decreased. Oscillations lie around the first acoustic eigenmode from L_1 = 0.11 m to 0.19 m. The system then reaches a multiple frequency band between L_1 = 0.20 m and 0.25 m. In this latter band, the main frequency appearing in the pressure spectrum measured by microphone M_2 is displayed in the graph. A stable band follows for three lengths and an instability lying around the second mode is retrieved from L_1 = 0.29 m to 0.55 m. In this case, there is no hysteresis when the piston is moved in one direction or the other.
The same type of limit cycles with fixed or variable amplitude highlighted for L_2 = 0.10 m are retrieved in this configuration. The multiple frequency range appears between L_1 = 0.20 m and 0.25 m where the flame oscillation does not stabilize on a single frequency. This does not depend on the direction used to bring the piston to its position.
There are different types of limit cycles with variable amplitude as observed for the short flame tube L_2 = 0.10 m. One needs to analyze time traces to delineate these differences. Figure 8.9 shows the pressure and PM signals with their respective power spectral densities and the corresponding acoustic eigenmodes for L_1 = 0.20 m. This operating condition lies at the beginning of the multiple frequency band. The pressure signal is slightly distorted due to the presence of the second mode. It is interesting to note that in this case the second acoustic mode of the system is a harmonic of the first mode. In this special configuration a harmonic of a mode coincides with another eigenmode of the system.
Another interesting case is considered in Fig. 8.10 showing measurements for L_1 = 0.22 m. The oscillations are now characterized by irregular bursts galloping along the time axis. This instability features a broad main peak centered between mode 1 and mode 2 in the pressure spectrum and a second broad peak

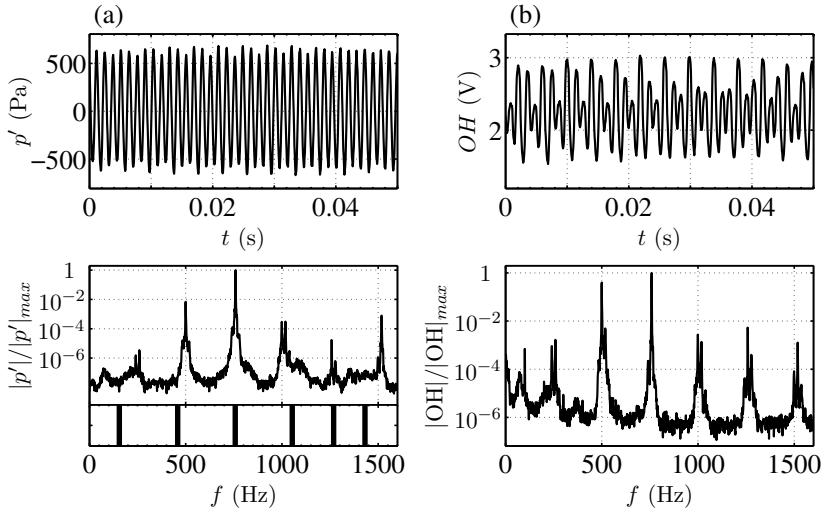

Figure 8.5: *Pressure signal recorded by microphone* M_2 *and OH* light emission for* $L_1 = 0.52$ *m and flame tube* $L_2 = 0.10$ *m. Corresponding spectral densities are shown below. The window under the pressure spectrum shows the acoustic eigenmodes positions as vertical solid lines (calculated by assuming that unsteady combustion is absent).*

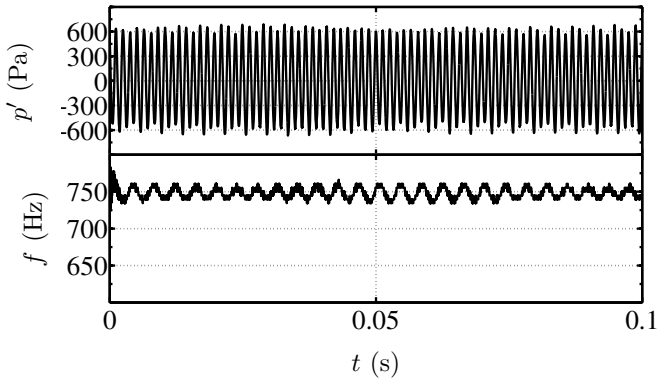

Figure 8.6: *Pressure signal from microphone* M_2 *for* $L_1 = 0.52$ *m and flame tube* $L_2 = 0.10$ *m. A time frequency analysis is done by using a continuous wavelet transform with a complex Morlet mother wavelet to extract the evolution of frequency along time. This allows to see which frequency appears as the amplitude grows or decreases.*

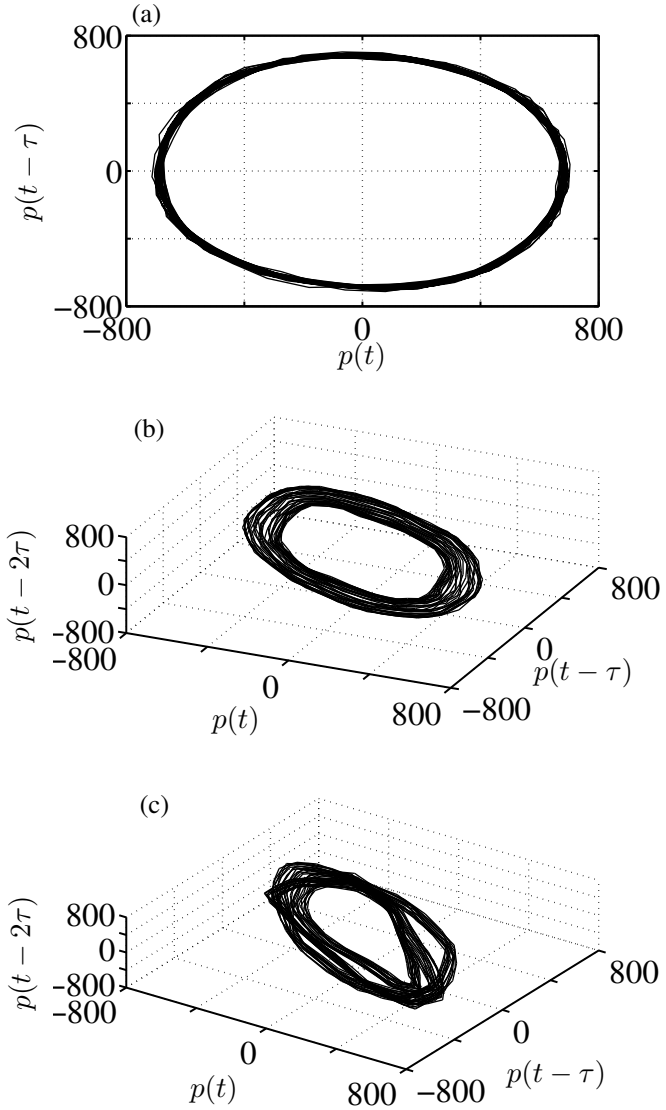

Figure 8.7: *Phase plane portraits of pressure signal from microphone* M_2*, determined for three lengths of feeding manifold* L_1*. (a) is linked to the stable limit cycle when* L_1 *= 0.11 m, (b) illustrates the regular beating noted for* L_1 *= 0.40 m and (c) corresponds to the case with two modes when* L_1 *= 0.52 m.*

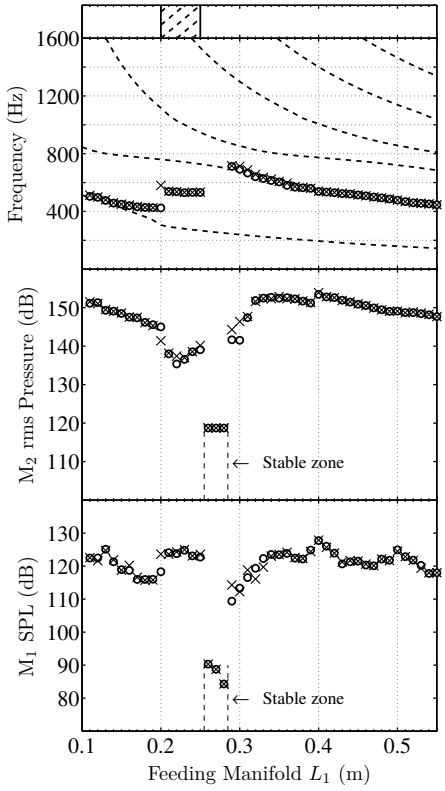

Figure 8.8: *Frequency and pressure level evolutions with the $L_2 = 0.20$ m confinement tube. The feeding manifold length L_1 is swept from 0.11 m to 0.55 m (○) and from 0.55 m to 0.11 m (×). Dashed lines indicate acoustic eigenmodes calculated without unsteady combustion. Upper frame on the top of the figure reveals limit cycle ranges with variable amplitude and frequency.*

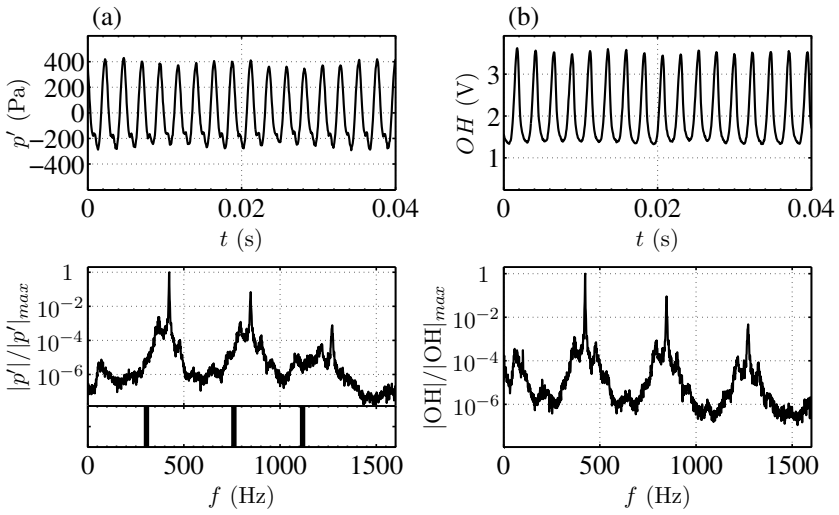

Figure 8.9: *Pressure signal recorded by microphone* M_2 *and OH* light emission for* $L_1 = 0.20$ *m and flame tube* $L_2 = 0.20$ *m. Corresponding spectral densities are shown below. The window under the pressure spectrum shows the acoustic eigenmodes positions as vertical solid lines (calculated by assuming that unsteady combustion is absent).*

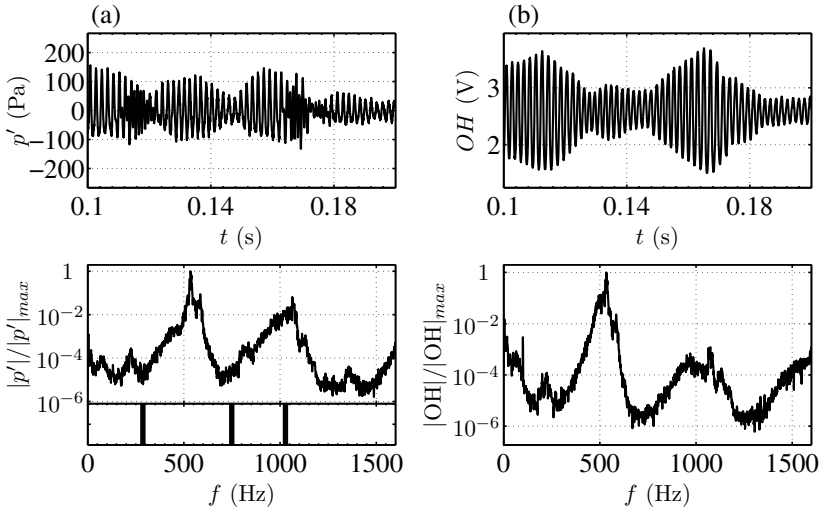

Figure 8.10: *Pressure signal recorded by microphone* M_2 *and OH* light emission for* $L_1 = 0.22$ *m and flame tube* $L_2 = 0.20$ *m. Corresponding spectral densities are shown below. The window under the pressure spectrum shows the acoustic eigenmodes positions as vertical solid lines (calculated by assuming that unsteady combustion is absent).*

located on mode 3. By analyzing this signal by means of a wavelet transform, as illustrated in Fig. 8.11, it is possible to see the frequency evolution along the bursts. The oscillation amplitude grows at a relatively constant oscillation frequency near 500 Hz, decreasing a little bit at high amplitudes, and suddenly switches to a higher frequency of about 1000 Hz. It is seen that this higher frequency component appears when the amplitude drops. This high frequency value corresponds to the harmonic of the signal. For example, at t = 0.11 s, the frequency reaches 500 Hz and suddenly switches to 1000 Hz. This phenomenon occurs when the amplitude is maximum and the frequency lies around 500 Hz. As already indicated for $L_1 = 0.20$ m, this peculiar configuration appears when one harmonic of the main instability frequency, here equal to 500 Hz, matches another eigenfrequency of the system. This occurs here for 1000 Hz which is linked to the third acoustic eigenmode.
A phase space reconstruction is undertaken for $L_1 = 0.20$ m and $L_1 = 0.22$ m in Fig. 8.12. Figure 8.12(a) shows that the period deformation, which is very slight in the present case, leading to the creation of a small cusp in the circular pattern without creation of a second form as noted in Fig. 8.7(c). Regarding the irregular burst sequences in Fig. 8.12(b), one can see that the phase space reconstruction fills a region of the embedding space without any regular structure. One can distinguish two remaining circles on the outer edge and in the center. The trajectory travels randomly in a three-dimensional volume indicating that the oscillation is chaotic in nature. In essence, the multiple frequencies noted for this confinement tube are linked to period deformations (Fig. 8.12(a)) or a new type of limit cycle with irregular bursts (Fig. 8.12(b)) which can be qualified as galloping limit cycle GLC. This type of oscillation is observed in various other fields like civil engineering and we have adopted the terminology introduced by Scanlan et al. (2004) in his analysis of velocity fluctuations in the wake of cables submitted to wind.

8.1.3 Flame tube $L_2 = 0.30$ m

A third configuration is now explored with a still longer flame tube $L_2 = 0.30$ m. The multiple frequency band is now broadened. Results are presented in Fig. 8.13 for increasing and decreasing feeding manifold lengths L_1. When combustion is initiated, oscillations evolve around the first mode from $L_1 =$ 0.11 m to 0.22 m. For feeding manifold lengths larger than $L_1 = 0.22$ m, an unstable range with multiple frequencies appears. The main frequency of the pressure spectrum is presented in Fig. 8.13. This behavior persists until L_1 = 0.32 m. At $L_1 = 0.33$ m, the instability features a single frequency located between the first and the second acoustic eigenmode calculated in the absence of unsteady combustion. A switching to the second mode is observed for L_1 = 0.36 m which is sustained until $L_1 = 0.55$ m. By diminishing the feeding manifold length L_1, the system exhibits a hysteresis. The instability frequency evolves around the second mode from $L_1 = 0.55$ m to 0.34 m. From $L_1 = 0.35$ m

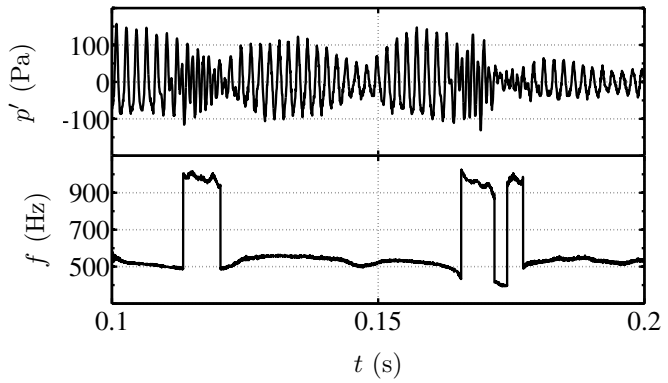

Figure 8.11: *Pressure signal from microphone* M_2 *for* $L_1 = 0.22$ *m and flame tube* $L_2 = 0.20$ *m. A time frequency analysis is carried out by using a continuous wavelet transform with a complex Morlet mother wavelet to extract the evolution of frequency along time. This allows to see which frequency appears as the amplitude grows or decreases.*

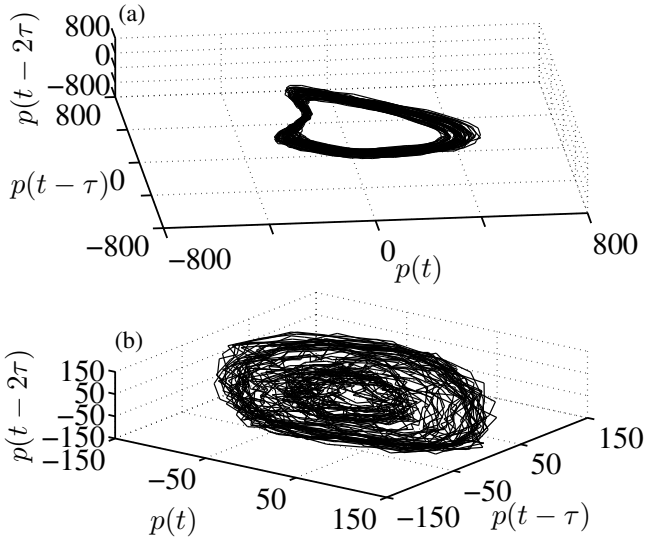

Figure 8.12: *Phase plane portraits of pressure signal from microphone* M_2 *determined for two feeding manifold sizes* L_1*. (a) is linked to the limit cycle slightly destabilized at* $L_1 = 0.20$ *m, (b) illustrates the irregular bursts noted for* $L_1 = 0.22$ *m.*

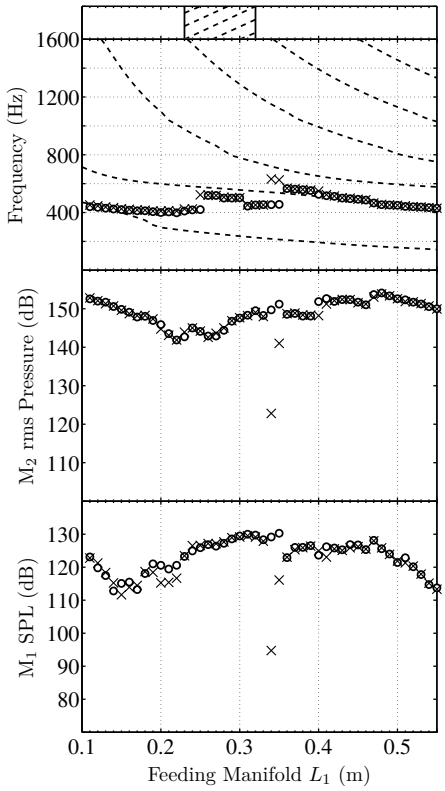

Figure 8.13: *Frequency and pressure level evolutions with the L_2 = 0.30 m confinement tube. The feeding manifold length L_1 is swept from 0.11 m to 0.55 m (○) and from 0.55 m to 0.11 m (×). Dashed lines indicate acoustic eigenmodes calculated without unsteady combustion. Upper frame on the top of the figure reveals limit cycle ranges with unfixed amplitude and frequency.*

to 0.34 m one finds a stable point. Oscillations take place at a lower amplitude and higher frequency than in the other direction of the piston motion. At L_1 = 0.33 m, the system switches to a single oscillation frequency between the first and the second mode. The multiple frequency zone appears just beyond that value for L_1 = 0.32 m until L_1 = 0.23 m. At L_1 = 0.22 m, the first mode is retrieved until L_1 = 0.11 m.

Outside the multiple frequency band, pressure and light emission signals show respectively linear and nonlinear behaviors as observed before. In the multiple frequency band, typical pressure and PM time traces plotted in Fig. 8.14 for L_1 = 0.32 m reveal irregular bursts with three main frequencies (390 Hz, 452 Hz and 515 Hz) appearing on the spectral densities. This is reminiscent of the beating structure observed previously with L_2 = 0.10 m. In this mode, spectral analysis exhibits a main peak with two side peaks. It is interesting to examine the PM trace presented in Fig. 8.14(b). Oscillations take place

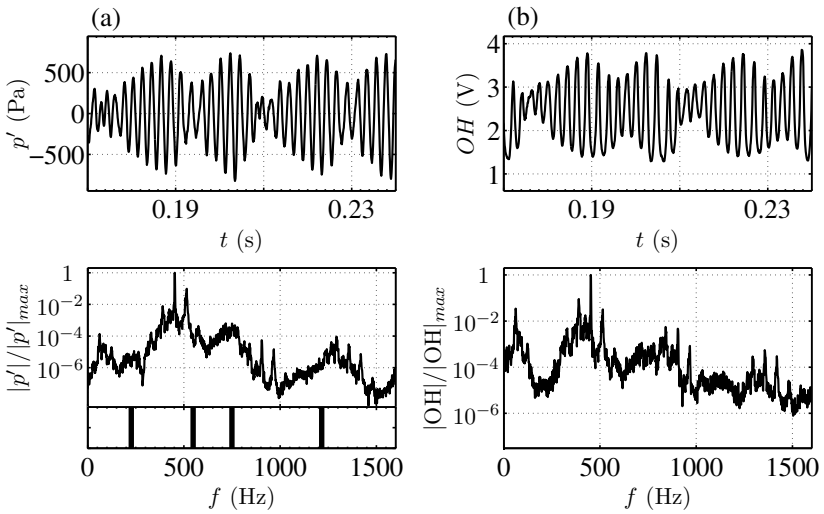

Figure 8.14: *Pressure signal recorded by microphone* M_2 *and OH* light emission for* $L_1 = 0.32$ *m and flame tube* $L_2 = 0.30$ *m. Corresponding spectral densities are shown below. The window under the pressure spectrum shows the acoustic eigenmodes positions as vertical solid lines (calculated by assuming that unsteady combustion is absent).*

at different amplitudes with an irregular increase and decrease in level. This variation highlights fluctuations of the flame motion amplitude during the oscillation cycle which can be examined with a high speed imaging camera at 6000 images/s. A sequence is presented in Fig. 8.15 for $L_1 = 0.32$ m. The upper window shows the PM signal linked to the images appearing in the lower part of the figure. The two symbols (◇ and ○) drawn on the time traces point out the phase of the image taken in the oscillation cycle. This figure indicates how the amplitude of the flame motion is stretched during the successive cycles (a), (b) and (c).

At the end of the multiple frequency band, the instability lies on a single frequency between mode 1 and mode 2 from $L_1 = 0.33$ m to 0.35 m. This phenomenon is illustrated in Fig. 8.16 for $L_1 = 0.33$ m. By using the phase plane representation, one is able to distinguish two types of limit cycles. The first, corresponding to a well defined oscillation amplitude, leads to a circular pattern as already observed in Fig. 8.7(a). The multiple frequency range noticed between $L_1 = 0.23$ m and 0.32 m features a perturbed pattern like the one observed in Fig. 8.12(b) for the flame tube $L_2 = 0.20$ m. It is typified by a circular structure as shown in Fig. 8.17. This third configuration is characterized by well defined limit cycles and a multiple frequency band with irregular pressure variations close to a regular beating.

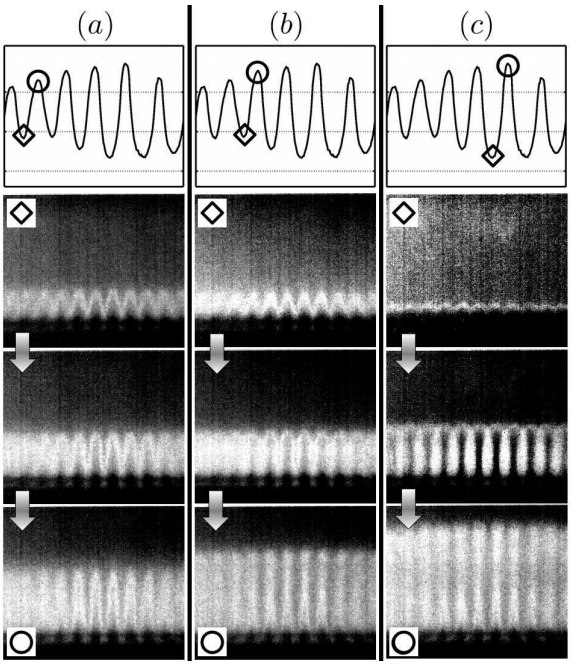

Figure 8.15: *Flame sequences during oscillation cycles for a feeding manifold length $L_1 = 0.32$ m and $L_2 = 0.30$ m. Three cycles (a),(b) and (c) are displayed in this figure. They correspond to a burst with a growing amplitude. Each cycle is displayed with three images where one is taken at the beginning (◇) of the cycle and one (○) at the end.*

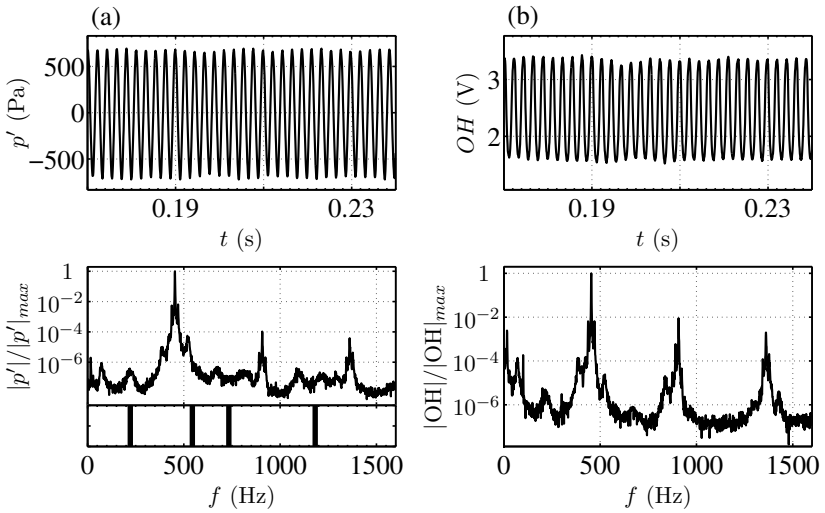

Figure 8.16: *Pressure signal recorded by microphone* M_2 *and OH* light emission for $L_1 = 0.33$ m and flame tube $L_2 = 0.30$ m. Corresponding spectral densities are shown below. The window under the pressure spectrum shows the acoustic eigenmodes positions as vertical solid lines (calculated by assuming that unsteady combustion is absent).*

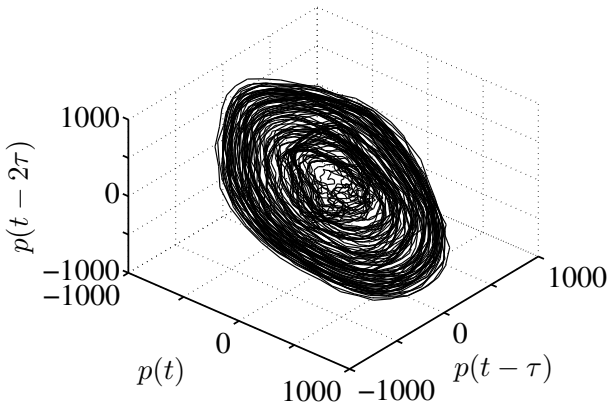

Figure 8.17: *Phase plane portrait of pressure signal from microphone* M_2 *estimated for* $L_1 = 0.32$ *m and* $L_2 = 0.30$ *m.*

8.1.4 Flame tube $L_2 = 0.40$ m

In the last configuration explored, the flame tube has the longest length $L_2 = 0.40$ m. Figure 8.18 shows the main instability frequency and the amplitude evolutions in the two way exploration when the piston position is modified. The hatched area above the frequency plot reveals the feeding manifold lengths L_1 where the instability amplitude and frequency do not take well defined values. It is worth noting that this confined case only features narrow bands of stable amplitude limit cycles and also no stable band. Due to the different types of instability observed, two different kinds of lines have been used in the hatched area. These various cases are examined in the following paragraph.

By increasing the feeding manifold length L_1, the pressure spectrum features multiple peaks with irregular acoustic beating from $L_1 = 0.11$ m to 0.14 m. Pressure and PM traces corresponding to this range are presented in Fig. 8.19 for $L_1 = 0.12$ m. The pressure signal exhibits an irregular beating accompanied by a fluctuation of the PM mean value. In this case, variations of the PM oscillation amplitude is less marked than that noticed in Fig. 8.14 for $L_2 = 0.30$ m and $L_1 = 0.32$ m. It indicates that flame stretching occurs more regularly from cycle to cycle. A flame sequence corresponding to $L_1 = 0.12$ m is presented in Fig. 8.20. It reveals a very large stretching of the flame during an oscillation cycle, but also merging and near destruction of the flame collection at some point in the cycle.

For a feeding manifold length $L_1 = 0.15$ m, the instability takes place around mode 1 at a single oscillation frequency until $L_1 = 0.20$ m. At $L_1 = 0.21$ m, multiple frequencies appear again. In this case, the shape of the pressure signal exhibits irregular bursts. Pressure and PM time traces, corresponding to $L_1 = 0.29$ m, are presented in Fig. 8.21. The mean value of the PM signal is still not constant. The oscillation level varies from cycle to cycle, revealing a variation

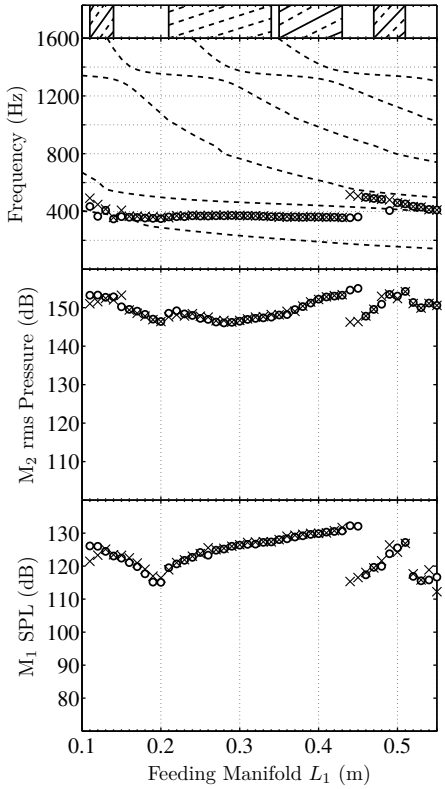

Figure 8.18: *Frequency and pressure level evolutions with the L_2 = 0.40 m confinement tube. The feeding manifold length L_1 is swept from 0.11 m to 0.55 m (○) and from 0.55 m to 0.11 m (×). Dashed lines indicate acoustic eigenmodes calculated without unsteady combustion. Upper frame on the top of the figure reveals limit cycle ranges with unfixed amplitude and frequency.*

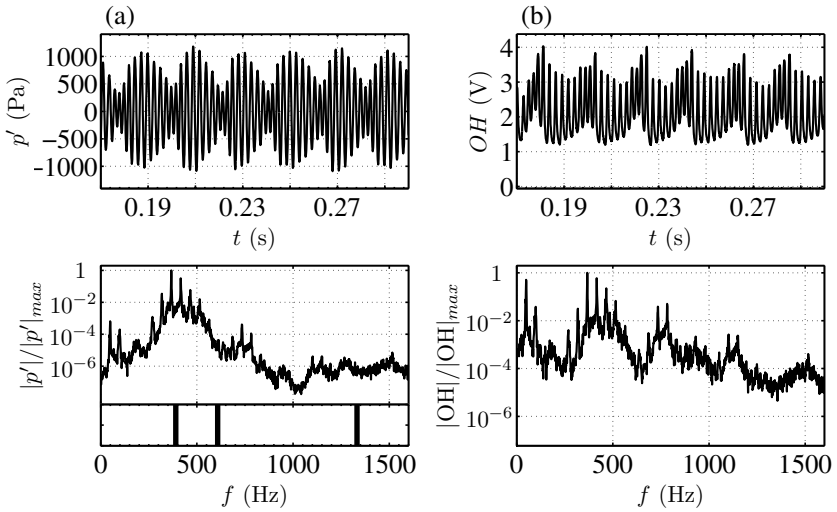

Figure 8.19: *Pressure signal recorded by microphone* M_2 *and OH* light emission for* $L_1 = 0.12$ *m and flame tube* $L_2 = 0.40$ *m. Corresponding spectral densities are shown below. The window under the pressure spectrum shows the acoustic eigenmodes positions as vertical solid lines (calculated by assuming that unsteady combustion is absent).*

of flame stretching. High speed imaging is displayed for this case in Fig. 8.22. One is able to distinguish three kinds of cycles. The first is characterized by a relatively weak stretching of conical flames (a), a second leads to a longer flame deformation (b) and the third one is accompanied by a destruction of the flame sheet (c) before anchoring and starting again a small oscillation cycle.
An irregular motion with a beating pattern is recovered at $L_1 = 0.35$ m until $L_1 = 0.43$ m. Within this range, the PM signal is still characterized by sequences where the amplitude increases and then decreases, but these variations are smoother. The mean value of the PM signal still features slight variations. High speed imaging also reveals an irregular stretch of the flame motion from cycle to cycle with phases of flame surface destruction that still takes place. At $L_1 = 0.44$ m, the flame oscillates at a single frequency located between mode 1 and mode 2 as observed for the preceding confinement tube $L_2 = 0.30$ m. The flame oscillation switches on a frequency around mode 2 at $L_1 = 0.46$ m. Instabilities characterized by multiple frequencies appear for $L_1 = 0.47$ m with irregular beating. This is exemplified for $L_1 = 0.49$ m in Fig. 8.23. One should note that small fluctuations of the PM mean value occur in this case, while the variation of the oscillation amplitude is quite regular. The same observations hold for the other lengths until $L_1 = 0.51$ m. The instability then switches to a frequency associated to mode 2 for $L_1 = 0.52$ m until 0.55 m.
In the second phase of the exploration when the feeding manifold length L_1 is decreased (crosses in Fig. 8.18), the instability remains locked on the second mode until $L_1 = 0.52$ m. At $L_1 = 0.51$ m, the instability is characterized by two

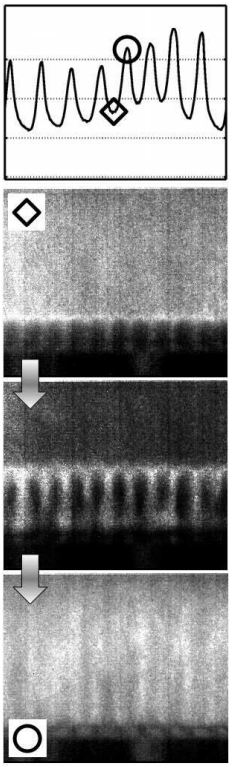

Figure 8.20: *Flame sequence during an oscillation cycle for a feeding manifold length $L_1 = 0.12$ m and $L_2 = 0.40$ m.*

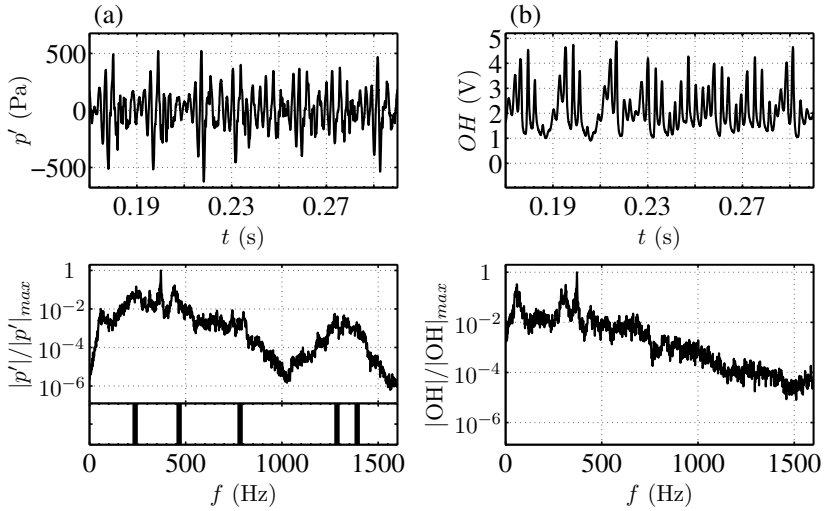

Figure 8.21: *Pressure signal recorded by microphone M_2 and OH* light emission for $L_1 = 0.29$ m and flame tube $L_2 = 0.40$ m. Corresponding spectral densities are shown below. The window under the pressure spectrum shows the acoustic eigenmodes positions as vertical solid lines (calculated by assuming that unsteady combustion is absent).*

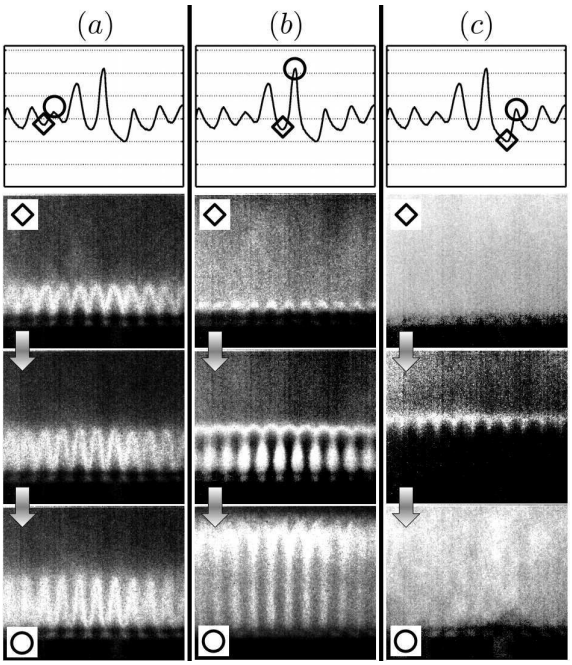

Figure 8.22: *Flame sequences during oscillation cycles for a feeding manifold length L_1 = 0.29 m and L_2 = 0.40 m. Three cycles (a),(b) and (c) are displayed in this figure. They correspond to a phase with a growing amplitude of the burst. Each cycle is displayed with three images where one is taken at the beginning (◇) of the cycle and the other one (○) is captured at the end.*

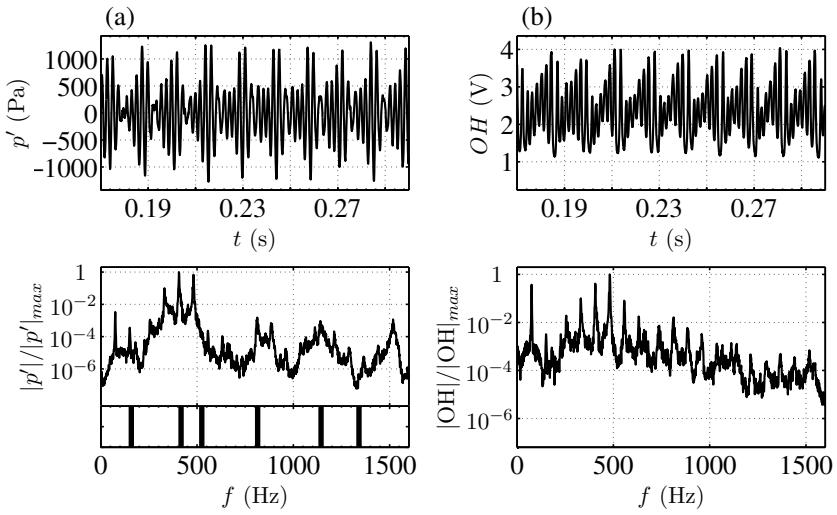

Figure 8.23: *Pressure signal recorded by microphone M_2 and OH* light emission for L_1 = 0.49 m and flame tube L_2 = 0.40 m. Corresponding spectral densities are shown below. The window under the pressure spectrum shows the acoustic eigenmodes positions as vertical solid lines (calculated by assuming that unsteady combustion is absent).*

main frequencies creating irregular acoustic beats. This persists until $L_1 = 0.46$ m. After that, the system presents a small hysteresis by oscillating on a single frequency close to the second mode for $L_1 = 0.45$ m and 0.44 m. It is worth noting that during the first phase of the exploration, the system lied around the first mode for these two lengths. At $L_1 = 0.43$ m, irregular beats are retrieved and persist until $L_1 = 0.35$ m. The PM time trace and high speed imaging show large oscillations of the flame with large flame surface destruction taking place at some phase of the cycle as observed during the first way of the exploration. From $L_1 = 0.36$ m to 0.21 m a multiple frequency domain is sustained. As shown previously, this domain is characterized by an intense destruction of the flame structure. This process disappears for $L_1 = 0.20$ m until $L_1 = 0.16$ m. In this range, the instability oscillation is locked on mode 1 with a well anchored flame. It is replaced by a multiple frequency oscillation from $L_1 = 0.15$ m to 0.11 m, with the same kind of behavior as the one observed during the first phase of exploration. Phase plane portraits correspond either to a circular pattern for periodic oscillations as drawn in Fig. 8.7(a) or to irregular structures as displayed in Fig. 8.12(b). Instabilities with this last flame tube present well defined limit cycles, or multiple frequencies with either irregular beating or bursts.

Regarding the four confined configurations investigated, it is interesting to note that instabilities with three flame tubes have highlighted hysteresis in the oscillation when the piston length L_1 is swept in the two directions. Besides, increasing the flame tube length L_2 gave rise to a large number of new phenomena that were not observed in the past experiments from Noiray et al. (2008) and Boudy et al. (2011b). It was shown that oscillations may reach very high amplitudes. It was also observed that the instability may feature multiple frequencies without fixed limit cycles for certain lengths of the feeding manifold L_1. Five types of limit cycles have been identified. This is gathered in Tab. 8.1 for the four flame tubes L_2. For each burner, a tick indicates the oscillation type encountered during the exploration with L_1.

8.2 Nonlinear modeling

A nonlinear dynamic model is briefly summarized in this section. It is based on the model B derived in Chapter 6. This model allows to examine the instabilities presented in the previous section. It is used to predict and understand the mechanisms of frequency switching, hysteresis or multiple frequencies observed in the system. For short flame tubes L_2, it has been seen previously that the system is unstable with mode switching and hysteresis phenomena. In addition, the flame does not oscillate on a single frequency for certain ranges of the feeding manifold lengths L_1. The multiple frequencies ranges widen when the confinement tube length L_2 is augmented. These phenomena cannot be

Table 8.1: *Limit cycles characterized for each flame tube L_2. Limit cycles with stable or unstable amplitudes correspond to the different phase space reconstructions indicated in the lower row. A tick indicates the types of limit cycle encountered for each flame tube L_2 by sweeping the feeding manifold length L_1.*

L_2 (m)	Single Freq.	Beating	Irregular Beating	Irregular Bursts	Multi-modes
0.10	✔	✔			✔
0.20	✔			✔	✔
0.30	✔			✔	
0.40	✔		✔	✔	
Phase plane		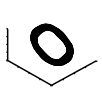			

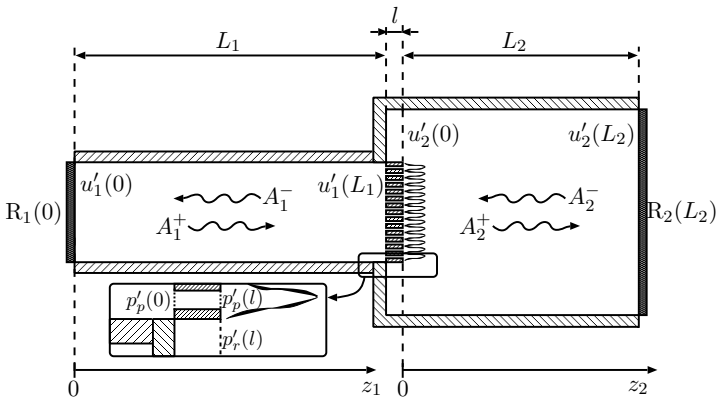

Figure 8.24: *Burner and symbol convention used for the analytical model.*

understood through a linear analysis and need to be modeled differently.
In the following analysis, fluctuating quantities are written as a sum of a mean and a fluctuation : $a = \bar{a} + a'$. The analysis is carried out in the frequency domain and each fluctuating quantity takes the form : $a' = \tilde{a}e^{-i\omega t}$ where $\omega = \omega_r + i\omega_i$ designates the complex angular frequency with $\omega_r = 2\pi f$ the angular frequency and ω_i the growth rate. A perturbation grows for positive values of growth rate while it decays for negative ones.
The burner is modeled as illustrated in Fig. 8.24. In each tube section, temperature, density, velocity and pressure are all subscripted with their respective numbers. Mean temperature and density $(\bar{T}, \bar{\rho})$ are considered uniform. It must be stressed that the temperature of the flame tube T_2 is not uniform for all the flame tubes lengths L_2. This has been underlined in Chapter 6. This temperature has been estimated by measurements with a K-thermocouple and these values are included in the calculations.
Model B is now considered. It provides an enhanced description of the acoustics

of the burner which yields to the following difference compared to model A :

- A better description of the reflection coefficient of the piston head.
- An improved description of the sound radiation at the flame tube outlet.
- A FDF measured with the thick perforated plate $l = 15$ mm used as flame holder and a small confinement tube $L_2 = 0.10$ m.
- An improved description of the acoustics in the connection between the two ducts with the ring cavity surrounding the flame.

Model B is derived in Chapter 6. By considering boundary and matching conditions between the two cavities. It leads to a set of four equations which can be written in a matrix form. This matrix is recalled here for completness :

$$\begin{pmatrix} 1 & -\mathrm{R}_1(0) & 0 & 0 \\ 0 & 0 & \mathrm{R}_2(L_2)e^{ik_2L_2} & -e^{-ik_2L_2} \\ \mathcal{A}_1 e^{ik_1L_1} & \mathcal{A}_2 e^{-ik_1L_1} & -1 & -1 \\ \mathcal{B}e^{ik_1L_1} & -\mathcal{B}e^{-ik_1L_1} & \mathcal{C}_1 & \mathcal{C}_2 \end{pmatrix} \begin{pmatrix} A_1^+ \\ A_1^- \\ A_2^+ \\ A_2^- \end{pmatrix} = 0 \quad (8.1)$$

where the complex coefficients $\mathcal{A}_1$, $\mathcal{A}_2$, $\mathcal{B}$, $\mathcal{C}_1$ and $\mathcal{C}_2$ correspond to :

$$\mathcal{A}_1 = 1 + \frac{i\omega l}{\mathcal{P}c_1}\left[1 + \frac{l_\nu}{r_p}(1+i)\right],\ \mathcal{A}_2 = 1 - \frac{i\omega l}{\mathcal{P}c_1}\left[1 + \frac{l_\nu}{r_p}(1+i)\right],$$

$$\mathcal{B} = \frac{S_1}{S_2}\frac{\rho_2 c_2}{\rho_1 c_1}\left[1 + Ge^{i\varphi}\left(\frac{T_f}{T_1} - 1\right)\right],$$

$$\mathcal{C}_1 = i\left(1 - \frac{S_1}{S_2}\right)\tan(k_2 l) - 1,\ \mathcal{C}_2 = i\left(1 - \frac{S_1}{S_2}\right)\tan(k_2 l) + 1$$

The reflection coefficient of the piston head presented in Fig. 4.5 is included in the model. As this boundary condition is insensitive to the amplitude, one uses the same reflection coefficient for all levels. The outlet of the flame tube is also considered with the radiation impedance detailed in Eqs. (4.8) and (4.9). This condition is also applied for all the amplitudes. The pressure jump depends on the analytical relation derived from Melling. The FDF measurements are plotted in Fig. 5.5 in terms of gain G and phase φ. To use these measurements for stability analysis, one has to interpolate and extrapolate FDF data in missing areas. The values considered for calculations are shown in Fig. 8.25.
The determinant of this system must equal zero to obtain non-trivial solutions. This condition provides the dispersion relation describing the dynamics of the system. This relation will be solved for the different FDF amplitudes with the continuation methodology described in Chapter 6, in the aim of finding complex roots $\omega = \omega_r + i\omega_i$ for each length of feeding manifold L_1 by treating separately each flame tube L_2.

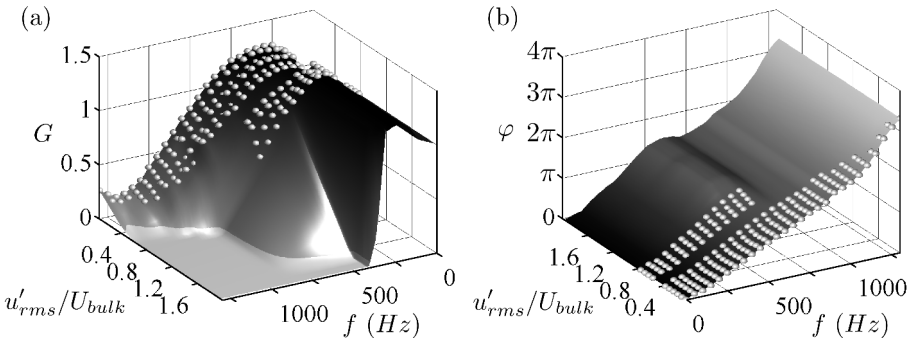

Figure 8.25: *Gain G (a) and Phase φ (b) of the interpolated and extrapolated FDF. u_{rms} corresponds to the rms value of the fluctuation amplitude and U_b the mean flow velocity within one hole. Experimental measurements are displayed as small spheres.*

8.3 Limit cycle prediction

The model B is now used to determine the frequencies and growth rates of the four confined configurations examined in Sec. 8.1. Roots of the dispersion relation are calculated with the continuation methodology detailed in Chapter 6. The dispersion relation is solved for increasing perturbation levels and each feeding manifold length L_1. This procedure yields a set of angular frequencies $\omega_r = 2\pi f$ and growth rates ω_i for each feeding manifold length L_1 evolving as a function of the perturbation level u_{rms}/U_b. The feeding manifold length L_1 is used as a bifurcation parameter for each confinement tube L_2.
Thus, it is possible to follow the evolution of frequency and growth rate from infinitesimally small amplitudes to the highest ones. When the growth rate vanishes, it is assumed that a limit cycle is reached. As mentioned in Sec. 8.1, there are many configurations typified by variable amplitudes and multiple frequencies. In the aim of understanding the different phenomena involved in these complex states of oscillation, the frequency associated to the main peak of the spectrum is considered to characterize the limit cycle and compared with predictions, but this is admittedly a simplification.
In the following figures, calculated growth rates ω_i are presented in a bifurcation diagram for each confinement tube L_2. These bifurcation diagrams are then used to predict flame oscillations as the feeding manifold length L_1 is modified. Figure 8.26 presents growth rate results for the shortest flame tube $L_2 = 0.10$ m and for the different lengths of feeding manifold L_1 as the perturbation amplitude u_{rms}/U_b grows. This bifurcation diagram shows positive values of ω_i for the three first eigenmodes of the system. These unstable bands are depicted by a yellow area for the first mode, the second unstable band being represented in blue and the third one in red. Light yellow is linked to the highest growth rate of the first mode approaching 500 s^{-1}, whereas dark yellow pertains to vanishing growth rates. Mode 2 and mode 3 color panels are inverted and the highest growth rate values appear respectively in dark blue

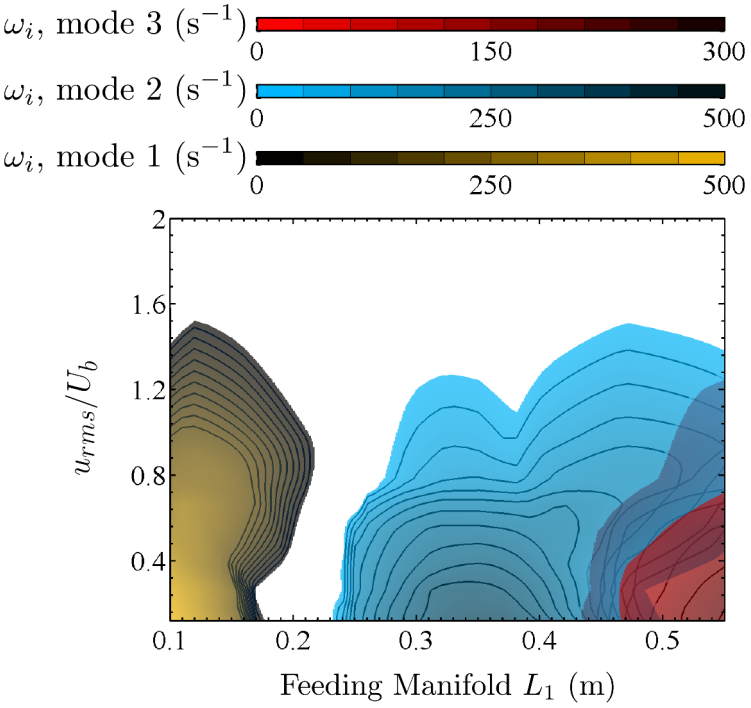

Figure 8.26: *Bifurcation diagram for the $L_2 = 0.10$ m confinement tube. The evolution of positive growth rate trajectories ω_i is presented for different lengths of feeding manifold between $L_1 = 0.10$ m and 0.55 m. Each trajectory evolves along the growing amplitude u_{rms}/U_b. The three first eigenmodes are displayed using different colors. The first mode corresponds to the yellow area, while the second and the third are displayed with blue and red.*

and dark red. By changing the feeding manifold length L_1, it is possible to obtain the amplitude and frequency reached at limit cycle by reading in the bifurcation diagram the value of the perturbation level u_{rms}/U_b corresponding to a vanishing growth rate ω_i. In the present investigation, it must be stressed that the main contributions to acoustic damping were taken into account in model B as most of the dissipation is associated with the piston head where reflection is not perfect, sound radiation at the flame tube outlet and in the perforated plate channels due to viscosity. It is then not necessary to include damping in the stability analysis by subtracting the measured damping rate α from the calculated growth rate $\omega_i - \alpha$ as it was done for example in Palies et al. (2011). In addition, relevance of this assumption will be tested by considering that limit cycles occur for $\omega_i = 0$ s^{-1}.

It is possible to determine the oscillation frequency at limit cycle by retaining the value calculated at the amplitude where growth rate ω_i vanishes. Figure 8.26 reveals different growth rate trajectories. Depending on the length L_1 considered, the growth rate ω_i is positive or negative for small perturbation

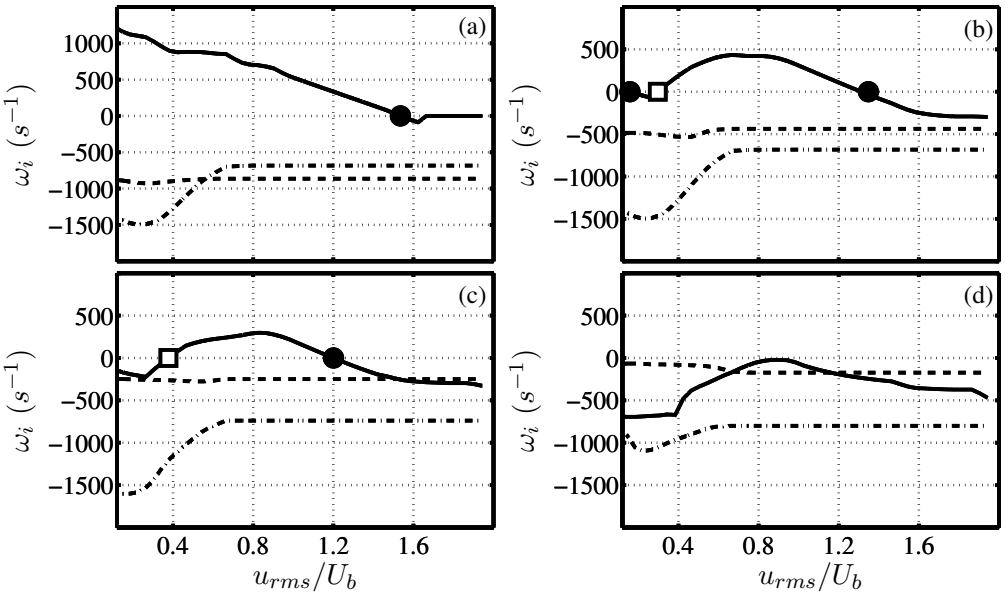

Figure 8.27: *State space trajectories ω_i encountered in the present study. (a), (b), (c) and (d) correspond to L_1 = 0.12 m, 0.175 m, 0.19 m and 0.22 m. Flame tube L_2 = 0.10 m. Bold line is linked to the growth rate of the first mode, while dashed line displays the second mode. The third mode also appears as dashed dotted line. Limit cycle (●) and triggering point (□) separate positive and negative growth rates.*

amplitudes u_{rms}/U_b. Results obtained for four fixed feeding manifold lengths L_1 are analyzed in Fig. 8.27 to illustrate the different possibilities. This figure synthesizes the different types of trajectory found by solving the dispersion relation. It shows the various possibilities encountered in this study with the different confinement tubes L_2 tested.

Figure 8.27(a) illustrates the case of a linearly unstable mode at $L_1 = 0.12$ m. This supercritical bifurcation is typified by a positive growth rate for infinitesimally small perturbation amplitudes, leading to a limit cycle at $u_{rms}/U_b \approx 1.5$ in this case.

A new type of trajectory that was not identified in the preceding studies (Noiray et al. (2008); Boudy et al. (2011b)) has been found in the present work. It is shown in Fig. 8.27(b) for $L_1 = 0.175$ m. The bifurcation diagram reveals a cusp bifurcation with two possible limit cycles for the same mode. Calculations exhibit a first mode (bold line) with positive growth rate for small perturbation amplitudes. A limit cycle is thus reached at $u_{rms}/U_b \approx 0.2$ where $\omega_i = 0$. Nonetheless, ω_i grows again from $u_{rms}/U_b \approx 0.3$ until it decreases leading to a new limit cycle found at $u_{rms}/U_b \approx 1.4$. When oscillations are stabilized at $u_{rms}/U_b = 0.2$ and a small finite impulse is introduced in the system, the oscillation amplitude increases again and the growth rate becomes positive. This leads to an oscillation growth with a new limit cycle reached at a much higher

level than the original oscillation. It should be noted that the high amplitude limit cycle $u_{rms}/U_b \approx 1.4$ is more stable than the initial one $u_{rms}/U_b \approx 0.2$. This latter situation was observed experimentally and it is reached by leaving the stable band during the reverse exploration with the piston, as presented in Sec. 8.1, Fig. 8.1. It is interesting to note that due to the peculiar frequency evolution with the perturbation level, the same unstable mode is able to reveal two oscillation frequencies which are very different. In this case, the shift between the two frequencies reaches 120 Hz.
A third situation is depicted in Fig. 8.27(c). It presents a positive growth rate for the first mode at $L_1 = 0.19$ m. These positive values only exist for a certain range of amplitudes. In this situation, one deals with a subcritical bifurcation and the system is linearly stable but nonlinearly unstable. A certain threshold of oscillation is needed to trigger an instability. In the last situation, corresponding to $L_1 = 0.22$ m and displayed in Fig. 8.27(d), all growth rate trajectories remain negative. This evolution is typical of a stable system. It is deemed to be linearly and nonlinearly stable.
Figure 8.26 reveals various bifurcation possibilities. By reading the bifurcation diagram, it is possible to predict mode switching when the bifurcation parameter L_1 is modified. This enables to predict triggering and hysteresis in the system. This particularity, made possible with this burner, has been observed in Sec. 8.1. These phenomena have been thoroughly investigated with the simplified model A in Chapter 7, Sec. 7.2.
Experiments and predictions are now compared in terms of amplitude and frequency at limit cycle. Figure 8.28(a) illustrates these evolutions by increasing the feeding manifold length L_1 after ignition at $L_1 = 0.11$ m. The reverse exploration, from $L_1 = 0.55$ m to 0.11 m, is displayed on the right hand side in Fig. 8.28(b). Bold lines correspond to predictions while square symbols (□) indicate self-sustained oscillations observed in experiments. The acoustic eigenmodes calculated without unsteady combustion are drawn as dashed lines when the temperatures in the feeding manifold and the flame tube are respectively fixed to $T_1 = 300$ K and $T_2 = 900$ K. Two colors have been used for the experiments. Open symbols indicate instabilities with a limit cycle of fixed amplitude and frequency. Gray symbols correspond to limit cycles featuring an unstable amplitude. In this latter case, the main frequency peak appearing on the pressure spectrum has been chosen for the diagram. One can draw four conclusions from the model :

- It is possible to predict mode switching when L_1 is modified. This is well verified in predictions of limit cycle frequencies. In addition, one is able to follow the frequency shift from the acoustic eigenmodes when the instability grows and reaches a limit cycle. Differences between the acoustic eigenmode frequency and the value reached at limit cycle by the instability may be large for certain operating conditions.

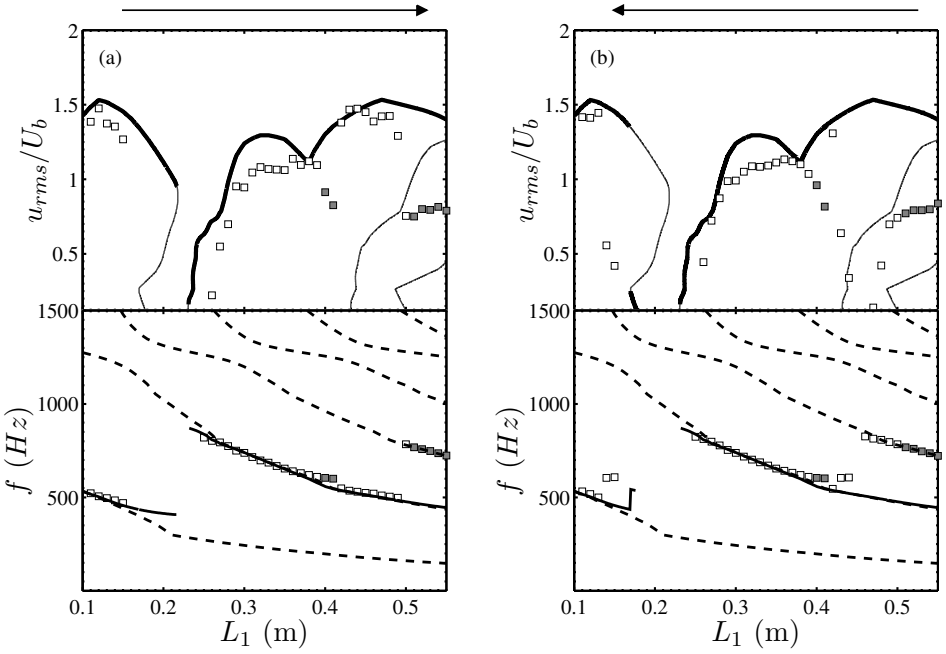

Figure 8.28: *Comparison between measurements and predictions for the shortest confinement tube $L_2 = 0.10$ m. The feeding manifold length L_1 is swept in both ways from $L_1 = 0.11$ m to 0.55 m (a) and $L_1 = 0.55$ m to 0.11 m (b). Bold lines indicate limit cycle predictions. Amplitudes and frequencies observed in the experiment are indicated by means of square symbols (□). Open symbols pertain to stable cases, while the gray ones reveal situations with unstable amplitude and frequency. In this latter case, the main frequency peak of the pressure spectrum has been chosen for the diagram.*

- Oscillation amplitudes at limit cycle are well predicted except for a few cases with a slight overestimate. This may be linked to the rough extrapolation of data for the FDF in the high amplitude range where it was difficult to measure it.

- The stable band is well retrieved between $L_1 = 0.21$ m and 0.23 m, which is embedded in the experimental range found from $L_1 = 0.16$ m to 0.24 m.

- Hysteresis is reproduced by the model when the bifurcation parameter L_1 is swept along the two ways of exploration. A small difference between predictions and experiments is noted. It is linked to the position L_1 corresponding to the calculated transition. In experiments, hysteresis was identified for $L_1 = 0.14$ m while in the calculations, it appears for $L_1 = 0.17$ m. As it was shown in Fig. 8.27(b), two limit cycles exist for the same mode when $L_1 = 0.17$ m. By leaving the stable band in the reverse way of exploration, from $L_1 = 0.55$ m to 0.11 m, a limit cycle with a small amplitude and a high frequency is well retrieved at $L_1 = 0.17$ m. In the first way of exploration when the feeding manifold length is increased from $L_1 = 0.11$ m to 0.55 m, the instability evolves on the first mode with a high amplitude. Then, if one considers $L_1 = 0.17$ m during the increase of L_1, the disturbance needed to trigger the high amplitude limit cycle is given by the high oscillation level of the previous length $L_1 = 0.16$ m.

These observations underline the effect of the amplitude on the evolution of the flame response to flow perturbations, i.e the FDF. By taking into account this amplitude dependency, it is possible to explain changes of flame oscillations observed in the burner.
The same type of analysis is conducted for the other flame tubes. The bifurcation diagram for $L_2 = 0.20$ m is presented in Fig. 8.29. First of all, the diagram exhibits larger growth rates for mode 1 and mode 2 than for mode 3. Mode 3 drawn in red is always overlapped by mode 2 which is typified by higher growth rate amplitudes. According to model B, third mode oscillations are not feasible in the range of feeding manifold length L_1 considered for this flame tube L_2. It is also worth noting that the growth rate values are higher compared to the calculations made with the short flame tube $L_2 = 0.10$ m for the two first modes. Comparisons between predictions and measurements at limit cycles are presented in Fig. 8.30.
Figure 8.30 indicate that prediction of limit cycle frequency are quite accurate. The oscillation amplitude is also well predicted for mode 1, but some differences arise for mode 2 at low amplitudes. The most important deviation appears around $L_1 = 0.26$ m, where switching occurs between the first and the second mode. A first difference concerns the stable band observed in the experiments

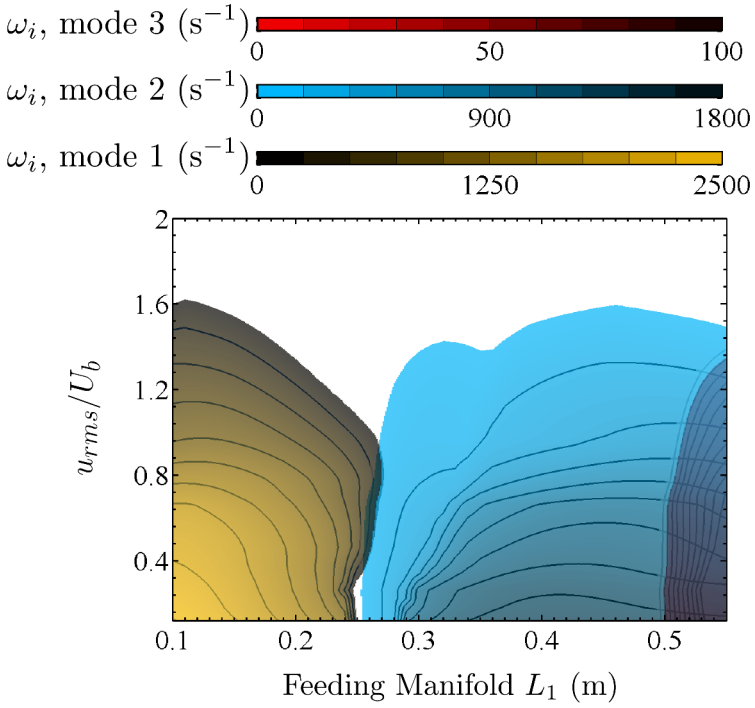

Figure 8.29: *Bifurcation diagram for the L_2 = 0.20 m confinement tube. The evolution of positive growth rate trajectories ω_i is represented for different lengths of feeding manifold between L_1 = 0.10 m and 0.55 m. Each trajectory is a function of the perturbation level u_{rms}/U_b. Unstable bands for the three first eigenmodes are displayed using different colors. The first mode corresponds to the yellow area, while the second and the third are displayed with blue and red.*

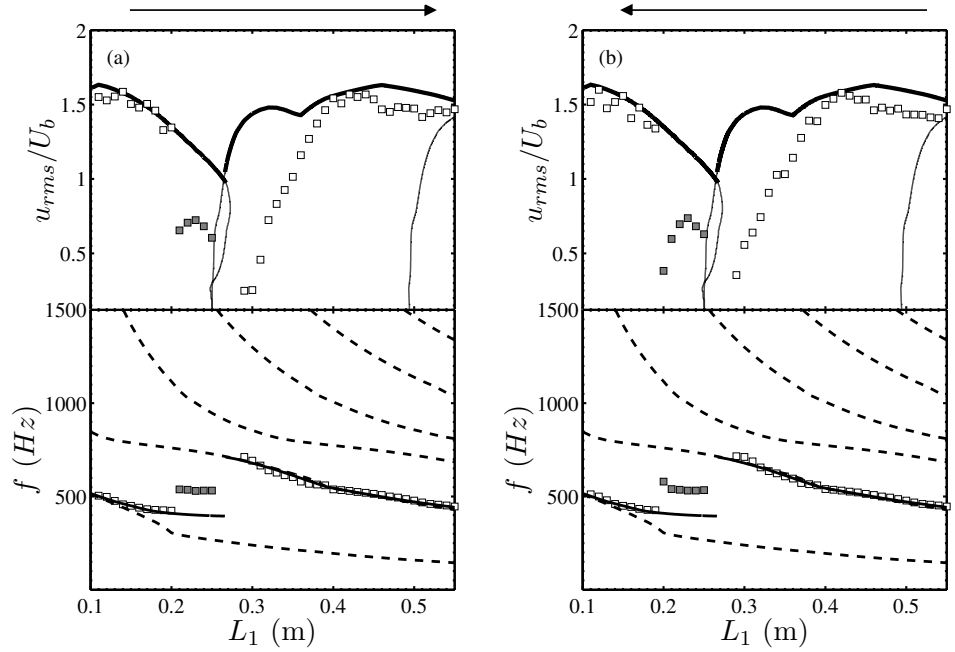

Figure 8.30: *Comparison between measurements and predictions for the L_2 = 0.20 m confinement tube. The feeding manifold length L_1 is swept in both ways from L_1 = 0.11 m to 0.55 m (a) and L_1 = 0.55 m to 0.11 m (b). Bold lines indicate limit cycle predictions. Amplitudes and frequencies observed in the experiment are indicated by means of square symbols (□). Open symbols pertain to stable cases, while the gray ones reveal situations with unstable amplitude and frequency. In this latter case, the main frequency peak of the pressure spectrum has been chosen for the diagram.*

from $L_1 = 0.26$ m to 0.28 m. In the calculations this band is unstable with oscillations locked on mode 2. A second issue is linked to the amplitude of the predicted limit cycle. From $L_1 = 0.29$ to 0.38 m, the predicted oscillation level is overestimated for mode 2. Frequency predictions show a better agreement with experiments, except in the multiple frequency band between $L_1 = 0.21$ m and 0.25 m. In this range, mode 1 is predicted unstable with a large oscillation level, but the system does not operate on a stable limit cycle and never reaches this prediction.

Results for the third flame tube with the length $L_2 = 0.30$ m are displayed in Fig. 8.31. Comparison between predictions and measurements of instability frequencies and amplitudes observed at limit cycles are shown in Fig. 8.32. First, one can note that frequencies and amplitudes are fairly well predicted. It is interesting to see that the large frequency shift between the acoustic eigenmode and the limit cycle frequency observed in the experiment is well captured by calculation from $L_1 = 0.17$ m to 0.22 m. As already observed with the flame tube $L_2 = 0.20$ m, switching from mode 1 to mode 2 is predicted at higher amplitudes compared to those observed in the experiments. This deviation is significant between $L_1 = 0.34$ m and 0.49 m. The hysteresis found by sweeping the piston in both directions is not predicted by the model because the associated unstable band for mode 1 fully overlaps that corresponding to mode 2 in Fig. 8.31. By examining the limit cycle frequencies in Fig. 8.32 it is seen that they are well predicted. An issue bears on the multiple frequency band between $L_1 = 0.23$ m and 0.32 m, where one expects an instability associated to the first mode using the FDF model.

The bifurcation diagram for the last confinement tube $L_2 = 0.40$ m is presented in Figs. 8.33. Comparisons with measurements are presented in Fig. 8.34. For many feeding manifold lengths L_1, the oscillation amplitude and frequency recorded are not fixed while predictions yield defined limit cycles. Thus, it is more difficult to distinguish differences with calculations in this case. One should delineate situations with a fixed amplitude (open symbols) from the unsteady cases (gray symbols).

Feeding manifold lengths corresponding to an oscillation at a single frequency are embedded from $L_1 = 0.15$ m to 0.20 m, 0.44 m to 0.46 m and 0.52 m to 0.55 m. The predicted amplitude and frequency match fairly well with measurements for the first mode. Nevertheless, deviations arise for the second one. In the multiple frequency cases, the flame motion does not stabilize on a well defined limit cycle hindering quantitative comparisons with calculations. The hysteresis noticed for $L_1 = 0.45$ m and 0.44 m in the experiments is not predicted. Growth rate trajectories remain positive during the switch from mode 1 to mode 2 and no gap exists in the bifurcation diagram for both way of sweeping L_1.

Regardless the problem of single or multiple frequencies, oscillations associated with mode 1 are predicted by the model until $L_1 = 0.42$ m in Fig. 8.33. An oscillation associated to mode 2 follows between $L_1 = 0.43$ m and 0.55 m. The

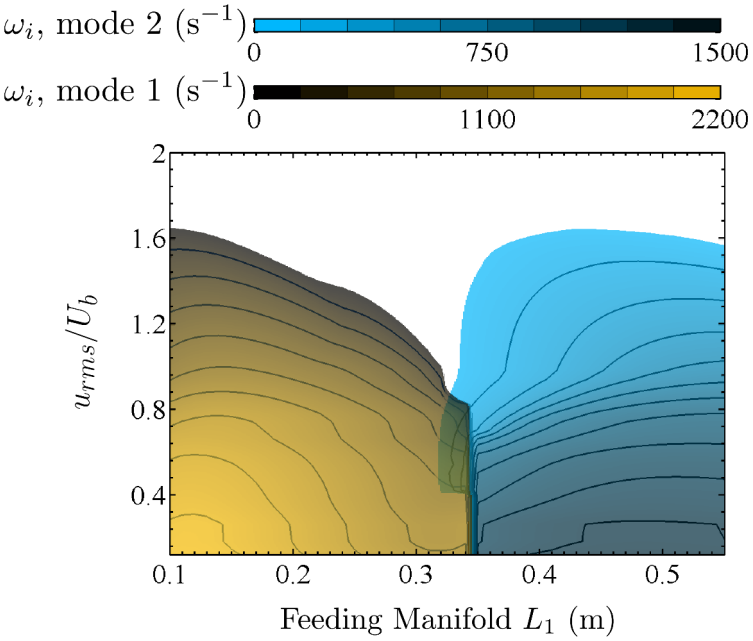

Figure 8.31: *Bifurcation diagram for the $L_2 = 0.30$ m confinement tube. The evolution of positive growth rate trajectories ω_i is represented for different lengths of feeding manifold between $L_1 = 0.10$ m and 0.55 m. Each trajectory is a function of the perturbation level u_{rms}/U_b. Unstable bands for the first two eigenmodes are displayed using different colors. The unstable band associated to mode 1 is drawn in yellow, while the second one linked to mode 2 appears in blue. In this range of lengths L_1, the third mode is always stable.*

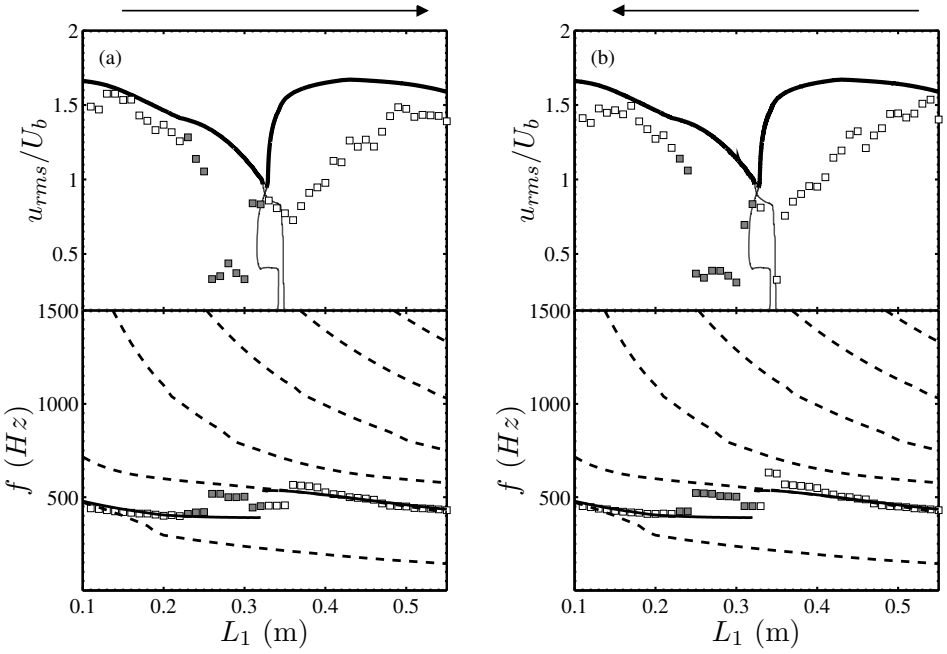

Figure 8.32: *Comparison between measurements and predictions for the L_2 = 0.30 m confinement tube. The feeding manifold length L_1 is swept in both ways from L_1 = 0.11 m to 0.55 m (a) and L_1 = 0.55 m to 0.11 m (b). Bold lines indicate limit cycle predictions. Amplitudes and frequencies observed in the experiment are indicated by means of square symbols (□). Open symbols pertain to stable cases, while the gray ones reveal situations with unstable amplitude and frequency. In this latter case, the main frequency peak of the pressure spectrum has been chosen for the diagram.*

dynamics of the system associated to this longer flame tube is complex. The origin of this issue lies in the roots of the dispersion relation. In this case, the eigenmodes calculated in the absence of unsteady combustion are found at very close frequencies. Recognizing that the solution corresponding to the instability may be shifted from its acoustic eigenmode, which was for example shown with the preceding flame tubes $L_2 = 0.20$ m and 0.30 m, and recognizing that roots of the dispersion relation are very close in the present configuration, it is more difficult to track the evolution of an unstable mode as the flame tube is lengthened. This is the reason why the transition from mode 1 to mode 2 presented in Fig. 8.33 is less clear as the feeding manifold length L_1 is increased. By examining the oscillation amplitude, it is interesting to see that switching from mode 1 to mode 2 is well defined for $L_1 = 0.43$ m in the bifurcation diagram. The oscillation level reached by the instability is higher than in the previous confined configurations. This is linked to the low frequency range of the instabilities. The unstable modes lie around 400 Hz and the FDF gain G takes very large values which overcomes unity in this frequency range. The flame continuously amplifies the instability and the gain does not fall to zero even at very large perturbation amplitudes u_{rms}/U_b. The limit cycle reached in these cases only depends on the change of phase lag φ of the FDF with the amplitude. Predictions yield a cancellation of growth rate when the phase lag is equal to π.

8.4 Predictions synthesis

A nonlinear stability analysis based on the FDF description was carried out for four different confined configurations with 45 feeding manifold lengths L_1. Considering all these cases, a good agreement between predictions and experiments has been found. It has been possible to estimate the amplitude and frequency of the observed limit cycles. The agreement with experiments is good for the shortest confinement tube $L_2 = 0.10$ m and for most of the feeding manifold lengths L_1 of the three longer flame tubes L_2. As the flame tube L_2 is lengthened, the instability amplitude increases and larger differences with experiments are observed.

It was shown that it is possible to predict limit cycle amplitudes and frequencies, mode switching when the feeding manifold depth L_1 is modified, triggering, frequency shift from the acoustic eigenmodes and hysteresis observed in experiments. Two difficulties were also identified in these calculations. First, the instability amplitude is often overestimated by the model for the long confinement tubes. Then, the multiple frequency bands found in the experiments show that FDF model predictions are not necessarily attained. These disrupted limit cycles correspond to flame oscillations occurring either with beating or irregular bursts, or even with period modifications which were described in Sec. 8.1.

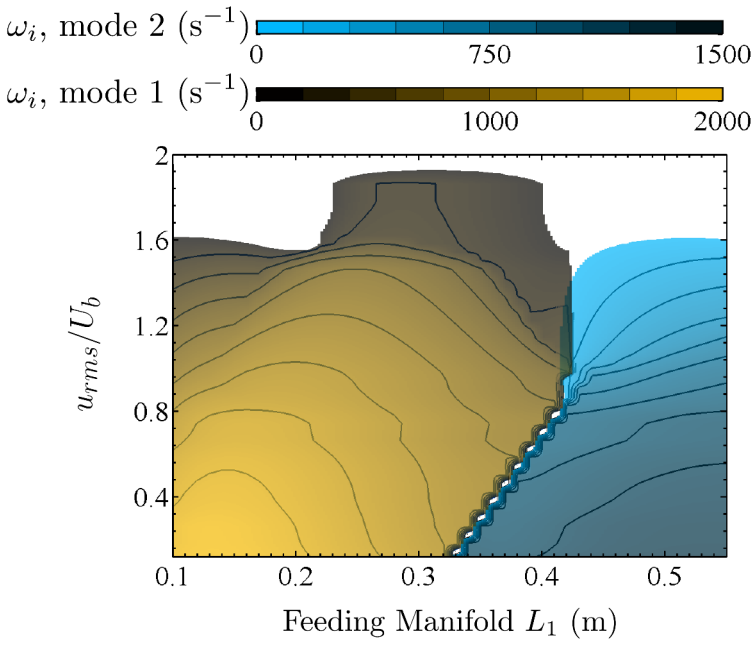

Figure 8.33: *Bifurcation diagram for the $L_2 = 0.40$ m confinement tube. The evolution of positive growth rate trajectories ω_i is presented for different lengths of feeding manifold between $L_1 = 0.10$ m and 0.55 m. Each trajectory is a function of the perturbation level u_{rms}/U_b. Unstable bands for the first two eigenmodes are displayed using different colors. The unstable band associated to mode 1 is drawn in yellow, while the second one linked to mode 2 appears in blue. In this range of lengths L_1, the third mode is always stable.*

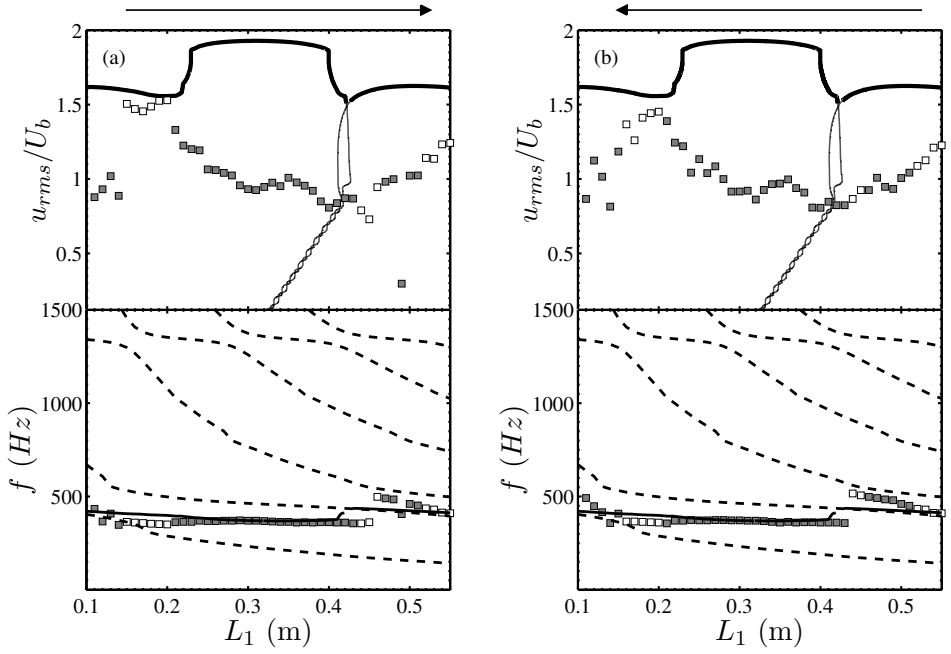

Figure 8.34: *Comparison between measurements and predictions for the L_2 = 0.40 m confinement tube. The feeding manifold length L_1 is swept in both ways from L_1 = 0.11 m to 0.55 m (a) and L_1 = 0.55 m to 0.11 m (b). Bold lines indicate limit cycle predictions. Amplitudes and frequencies observed in the experiment are indicated by means of square symbols (□). Open symbols pertain to stable cases, while the gray ones reveal situations with unstable amplitude and frequency. In this latter case, the main frequency peak of the pressure spectrum has been chosen for the diagram.*

To shed light on prediction failures, the model and its results are thoroughly examined. Regarding amplitude overestimations and also the unexplained hysteresis found for the $L_2 = 0.30$ m and 0.40 m confinement tubes, two elements have been investigated. First of all, if one reconsiders the thermoacoustic model defined in Eq. (8.1), only the temperatures in the cavities and the reflection coefficient at the combustor outlet remain potential parameters which may have been roughly estimated. The reflection coefficient of the piston head $R_1(0)$ was determined experimentally for different forcing amplitudes up to 130 dB. It remains uniform over the whole range of perturbation levels explored. The flame temperature T_f was chosen in agreement with the adiabatic flame temperature and stays constant. Thus, only the temperature T_2 in the flame tube and the reflection coefficient taken for the outlet $R_2(L_2)$ can be questioned. Calculations were conducted with a higher flame tube temperature T_2 or with different models for the outlet reflection coefficient $R_2(L_2)$.
Modifications of the temperature T_2 and the reflection coefficient $R_2(L_2)$ reveal variations in the bifurcation diagram. It was for example possible to reproduce the stable zone observed in the experiments for the $L_2 = 0.20$ m flame tube. By changing the temperature T_2 inside the flame tube, one was able to reproduce a stable band for certain ranges of L_1 for all the flame tubes L_2 of the study. Increasing the temperature T_2 decreases the growth rate ω_i which reaches negative values in the zone of switching from mode 1 to mode 2. The amplitude u_{rms}/U_b where the growth rate vanishes around this zone is also diminished. On the other hand, switching from mode 1 to mode 2 is shifted to shorter feeding manifold lengths L_1 from 0.02 to 0.03 m. This may explain the failure in predicting the hysteresis for the $L_2 = 0.30$ m and 0.40 m confinement tubes. The reverse exploration is made once the maximum extension L_1 has been reached several minutes after ignition. When experiments in the reverse direction are carried out the combustor is hotter than at the beginning of the exploration with the sliding piston. This temperature increase should be reflected in the calculations. This may be the reason why the calculations retrieve the small band of L_1 where oscillation almost stops in the reverse exploration for the $L_2 = 0.30$ m and 0.40 m flame tubes.
The reflection coefficient of the flame tube outlet $R_2(L_2)$ is more prone to change at high amplitudes and high frequencies. Thus, by considering modification of the outlet impedance at high frequency, leading to a decrease in the modulus of the reflection coefficient and a phase lying closer to $-\pi/2$ instead of $-\pi$, it is possible to reduce the amplitude of perturbations corresponding to vanishing growth rates. While this occurs at high frequency, it is interesting to see that it matches with the zone of switching from mode 1 to mode 2 where mode 2 frequencies take their larger values and show the worst agreement in amplitude prediction.
This parametric analysis highlights that prediction failures leading to overestimated amplitudes, the absence of hysteresis or even the absence of stable zone, in some of the calculated bifurcation diagrams, are probably linked to the

rough estimate of the flame tube temperature T_2 and the need of an improved model or measure for the outlet reflection coefficient $\mathrm{R}_2(L_2)$.
Regarding the multiple frequency bands, the close roots of the dispersion relation mentioned herein are thoroughly examined in the following chapter. It will be seen that these close roots may be related to the unstable oscillations.

8.5 Mode shape inside the combustor

The calculations undertaken in the preceding section yield the frequency f and amplitude u_{rms}/U_b of the different instabilities at limit cycle. These values can be injected back in the matrix (Eq. (8.1)) to determine the amplitudes A_n^+ and A_n^- and therefore evaluate pressure $p'_n(z_n)$ and velocity $u'_n(z_n)$ fluctuation along the geometry of the combustor. By using different microphones the pressure signal has been measured at different locations along the feeding manifold L_1. In addition, it is possible to obtain the pressure in the flame plane with microphone M_3 plugged on a waveguide (see Fig. 1.2). It is then possible to compare these values to calculations made by injecting back frequency and amplitude in the matrix. Besides, pressure measurements can also be used to estimate the velocity fluctutation by using a reconstruction of the signal by means of the reflection coefficient of the piston head $\mathrm{R}_1(0)$.

8.5.1 Estimation of pressure and velocity

The calculations of the previous section yield frequency f, growth rate ω_i and amplitude u_{rms}/U_b of the self-sustained combustion oscillations. These values are used to evaluate the matrix Eq. (8.1) but they allow also to read the gain G and phase φ of the flame response from the FDF which need to be injected back in Eq. (8.1). It should be noted that the values considered in these calculations correspond to the ones found with the model. One does not use the limit cycle frequency and amplitude measured in the burner.
The matrix $\boldsymbol{M}(\omega)$ Eq. (8.1) is fully determined and the vector $\boldsymbol{X}$ of amplitudes A_n^+ and A_n^- satisfaying to the system $\boldsymbol{M}(\omega)\boldsymbol{X} = 0$ can be evaluated. This is done by estimating the eigenvalues λ_n and eigenvectors V_n of the system. The eigenvector solution of the system $\boldsymbol{M}(\omega)\boldsymbol{X} = 0$ is linked to the eigenvalue $\lambda_n = 0$. This returns the eigenvector $(A_1^+, A_1^-, A_2^+, A_2^-)$. Multiplying this vector by a coefficient α, one obtains a non-trivial family of solutions for the system $\boldsymbol{M}(\omega)\boldsymbol{X} = 0$. But there is a single value α satisfying to the oscillation level u_{rms}/U_b reached at limit cycle.
This value is determined by using the value u_{rms}/U_b computed with model B in the flame plane in the previous section. This allows to calculate a theoretical mode shape with the limit cycle obtained from the FDF framework. This mode shape is compared to the results obtained from measurements on the multiple flame combustor by means of the different microphones. The pressure and velocity fluctuations are therefore obtained in two steps :

- In the first step, the system $\boldsymbol{M}(\omega)\boldsymbol{X} = 0$ is solved. Once the eigenvector corresponding to $\lambda_n = 0$ is determined, the pressure and velocity time traces are estimated at different locations z_n inside the combustor.

- In the second step, pressure and velocity found in the first step at each location z_n of the burner, are made dimensionless by the velocity fluctuation calculated on the flame plane $\widetilde{u}_1(L_1)$. Then, it is multiplied by the amplitude u_{rms} found with the FDF calculations in this plane when $\omega_i = 0$.

The following expressions are linked to the second step and provide the pressure and velocity distribution at each location in the combustor :

$$\begin{aligned} p'_n(z_n) &= \frac{p'_{th}(z_n)}{u'_{th}(L_1)} \frac{u_{rms}}{U_b} U_{b_n} \\ u'_n(z_n) &= \frac{u'_{th}(z_n)}{u'_{th}(L_1)} \frac{u_{rms}}{U_b} \end{aligned} \tag{8.2}$$

where $p'_{th}(z_n)$ and $u'_{th}(z_n)$ designate the reconstructed signals and U_{b_n} denotes the bulk velocity inside the cavity considered. In the feeding manifold $U_{b_1} = 1.05$ m.s^{-1}. The flame tube velocity is calculated by using the conservation of the mass flow rate $U_{b_2} = (\rho_1 S_1 U_{b_1})/(\rho_2 S_2)$.

8.5.2 Comparison between measurements and reconstruction

The reconstruction of the mode shape is now compared to measurements in some configurations. The plugs regularly spaced along the feeding manifold L_1 and the microphone M_3 with its waveguide connected on the plate supporting the flame tube L_2 (see Fig. 1.2) are used for these comparisons. These microphones provide the pressure oscillation inside the burner at different locations by setting a certain feeding manifold length L_1 and a flame tube L_2. Measurements are done with a sampling frequency $f_s = 16384$ Hz, with a duration of 4 s. These pressure signals are post-processed to obtain the corresponding velocity fluctuations. This is done by means of the reflection coefficient of the piston head $R_1(0)$. This enables to determine the velocity signal at the locations of pressure measurements. This may be written as follows :

$$u'_1(z_1) = \Re\left\{ \frac{1}{\rho_1 c_1} \frac{R_1(0)\, e^{ik_1 z_1} - e^{-ik_1 z_1}}{R_1(0)\, e^{ik_1 z_1} + e^{-ik_1 z_1}} \widetilde{p}_1(z_1)\, e^{-i\omega t} \right\} \tag{8.3}$$

where z_1 stands for the position in the tube, $R_1(0)$ is the reflection coefficient of the piston head and $\widetilde{p}_1(z_1)\, e^{-i\omega t}$ indicates the Hilbert transform of the microphone pressure signal. The velocity corresponds to the real part of this expression ($\Re$). In this estimation, the angular frequency ω is taken from the observed instability at limit cycle. One can see that all the values involved in

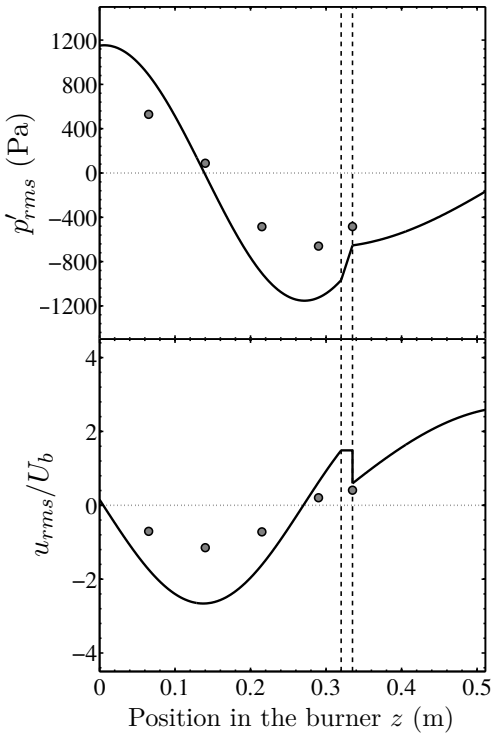

Figure 8.35: *Modal structure of pressure and velocity inside the combustor for $L_2 = 0.20$ m and $L_1 = 0.32$ m. The maximum pressure envelope is displayed in the upper part, while the velocity appears on the lower part. The multipoint injector is located between the two vertical dashed lines. Measurements made along the system are drawn by means of gray circle symbols on both graphs.*

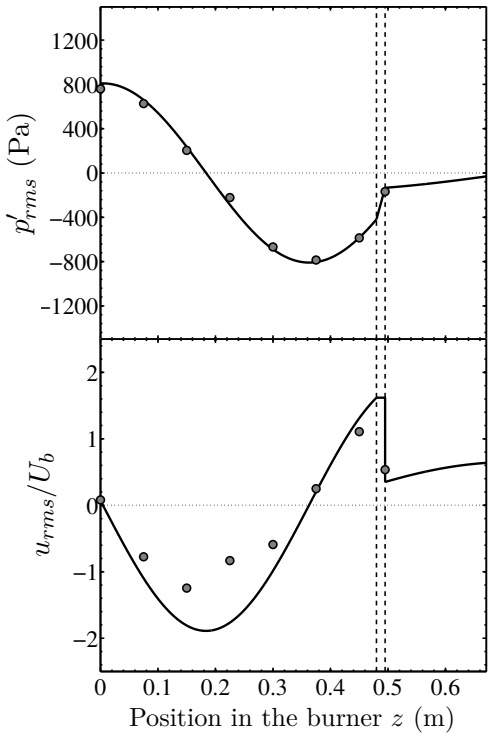

Figure 8.36: *Modal structure of pressure and velocity inside the combustor for $L_2 = 0.20$ m and $L_1 = 0.48$ m. The maximum pressure envelope is displayed in the upper part, while the velocity appears on the lower part. The multipoint injector is located between the two vertical dashed lines. Measurements made along the system are drawn by means of gray circle symbols on both graphs.*

this reconstruction depend on experiments contrary to calculations of pressure and velocity with Eq. (8.2), where all the terms come from the FDF model.
The distribution of pressure and velocity fluctuations at limit cycle are calculated and measured in three configurations. Results for two feeding manifold lenghts $L_1 = 0.32$ m and 0.48 m of the confinement tube $L_2 = 0.20$ m are firstly considered. A third case is considered with a longer flame tube $L_2 = 0.30$ m and a feeding manifold length $L_1 = 0.37$ m.
The results for the first flame tube $L_2 = 0.20$ m are presented in Figs. 8.35 and 8.36 for $L_1 = 0.32$ m and 0.48 m. The mode shape is drawn for its maximum amplitude at each location along the combustor. Gray symbols correspond to the measurements, while calculations are drawn with bold lines. These two cases show the second longitudinal eigenmode which establishes

in the system. Pressure measurement reaches its maximum amplitude on the piston head with a rms level of 600 Pa in the first case and 760 Pa in the second one. The velocity fluctuation is maximum inside the feeding manifold for $L_1 = 0.32$ m. Calculations indicate a maximum level $u_{rms}/U_b = 2.7$ reached in the middle of the feeding manifold. This maximum is also found inside the feeding manifold for $L_1 = 0.48$ m with $u_{rms}/U_b = 1.9$. Calculations with the FDF model enable to retrieve the mode shape inside the combustor. By comparing the two cases, one notes a better agreement between theory and measurements for $L_1 = 0.48$ m. In particular, the velocity discontinuity on the flame plane is fairly well retrieved at $z_1 = 0.495$ m. In this latter case, some differences appear for the velocity distribution at $L_1 = 0.15$ m and 0.225 m. This is probably linked to the single measurement of pressure at this location typified by a low pressure level (pressure antinode). For these two lengths, it would be better to set another microphone in front of the one used in this experiment to reduce measurement incertitudes.

Differences appear between measurements and calculations for $L_1 = 0.32$ m in Fig. 8.35. In this case, the FDF calculations overestimate the limit cycle amplitude compared to the experiment. As mentioned above, the values injected back in the matrix Eq. (8.1) correspond to these calculations and therefore influence the results. It is interesting to see that velocity and pressure fluctuations take large values inside the flame tube L_2 for $L_1 = 0.32$ m. This is not the case for $L_1 = 0.48$ m where velocity and pressure fluctuations are more important inside the feeding manifold L_1.

Results for the longer flame tube $L_2 = 0.30$ m and $L_1 = 0.37$ m are presented in Fig. 8.37. In this experiment, the limit cycle amplitude does not exceed $u_{rms}/U_b = 0.82$, which is largerly overestimated by the FDF calculations. This induces differences for the mode shape between measurements and calculations as shown in Fig. 8.37. In addition, it is important to note that the predicted frequency at limit cycle is lower than the one observed in experiment. This deviation reaches 36 Hz while it was limited to 15 Hz with the preceding flame tube $L_2 = 0.20$ m at $L_1 = 0.32$ m. The pressure fluctuation is maximum on the piston head with a rms level of 400 Pa, while the larger velocity fluctuation is found in calculations at the flame tube outlet with $u_{rms}/U_b = 5.4$. The velocity fluctuation remains limited inside the feeding manifold while the flame tube exhibits higher levels of oscillation. Regardless the differences between calculations and measurements, the mode shape is again well retrieved by the model.

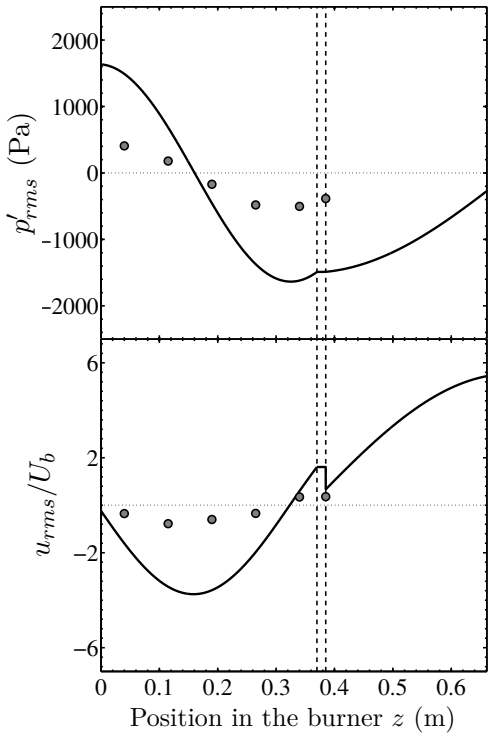

Figure 8.37: *Modal structure of pressure and velocity inside the combustor for L_2 = 0.30 m and L_1 = 0.37 m. The maximum pressure envelope is displayed in the upper part, while the velocity appears on the lower part. The multipoint injector is located between the two vertical dashed lines. Measurements made along the system are drawn by means of gray circle symbols on both graphs.*

Chapter 9

Limit cycles of variable amplitude

This chapter focuses on limit cycles of variable amplitude observed in the experiments. These dynamical behavior was reported in two publications which are reproduced here in sections 9.1 and 9.2. The first analysis deals with limit cycles sustained by the simultaneous oscillation of two modes. The second concentrates on oscillations without organized structure reminiscent of chaotic oscillations. The complete model "model B" is involved in the following calculations. This model takes into account the non ideal reflection coefficients of the system inlet and outlet and effects of the ring cavity surrounding the injection system.

9.1 Analysis of limit cycles sustained by two modes in the flame describing function framework

This section corresponds to a publication presented at the 3^{rd} *INCA workshop* and published in *Comptes Rendus Mécanique de l'Académie des Sciences* in 2013 :

Boudy, F., D. Durox, T. Schuller, and S. Candel. 2013. "Analysis of limit cycles sustained by two modes in the flame describing function framework." C. R. Mec. 341 (1–2): 181–90. doi:10.1016/j.crme.2012.10.014

For the sake of clarity, the present section has been shortened compared to the journal publication. The introduction is reduced and centers around the unstable amplitudes. The experimental setup was kept to allow an easier reading of the contents, but it can be skipped since it is described in Chapter 1.

9.1.1 Abstract

The Flame Describing Function (FDF) framework, developed for the nonlinear instability analysis of combustors, has been validated more recently in a generic configuration comprising an upstream manifold, an injection unit and a flame tube. It was shown that it is possible to predict limit cycles which exhibit a nearly stable amplitude and a single frequency. This system featuring a wide variety of dynamical phenomena, is used here to explore a new range of self-sustained flame oscillations. Depending on the geometry, the system exhibits stable or variable amplitude limit cycles. In the first case, oscillations have an essentially constant amplitude and are well retrieved with the FDF framework, whereas in the second case, limit cycles feature different types of amplitude unsteadiness and require some further consideration. The present article is concerned with one type of unstable oscillation in which a regular period modification occurs in the presence of two modes, leading to frequency heterodyning. It is found from the FDF analysis that such oscillations sustained by two modes may occur when there is an overlap between modes corresponding to super and subcritical bifurcations. An additional condition which has to be fulfilled to obtain this behavior is inferred from experiments.

9.1.2 Introduction

In the prediction of self-sustained combustion oscillations, problems arise when the limit cycle amplitude cannot be considered constant but evolves as a function of time. In some cases the amplitude modulations are irregular giving rise to "Galloping limit cycles" (GLCs), a term borrowed from civil engineering (Scanlan et al. (2004)) to define cable oscillations with varying amplitude. In the present case the limit cycle amplitude is modulated in a more regular fashion and the oscillation is sustained by two modes and will be designated in what follows as TMLC (Two Modes Limit Cycle). This behavior was not observed in the unconfined situation investigated in Noiray et al. (2008) but TMLCs arise in the generic system considered in the present study in a limited range of the bifurcation parameter.

In the analysis and calculation of thermoacoustic coupling it is generally assumed that the amplitude and frequency are fixed. It is known however that limit cycles are not always locked on an amplitude at a fixed frequency. This is for example found in the premixed laboratory combustor used by Sterling (1993) where quasi-periodic oscillations were identified and linked to the interaction of two acoustic eigenmodes. More recent experimental investigations in a multiple flame combustor equipped with a perforated plate comprising seven orifices have also revealed variable amplitude limit cycles (Kabiraj et al. (2011b); Kabiraj et al. (2011a)) which were uncovered by examining different combustion chamber lengths.

The present work complements our previous investigation of a multiple in-

jection combustor (Boudy et al. (2011b)). It specifically deals with TMLCs appearing in this system in which the multiple flame region is confined in a tube. This variable amplitude oscillation state, which can be qualified as "buzzing-blown" combustion due to its sound signature, is analyzed in the special case where two different modes coexist. The test rig is briefly presented in Sec. 9.1.3. Experimental results are reported in Sec. 9.1.4. The situation is examined with the FDF framework in Sec. 9.1.5. It is shown that TMLCs arise in a region where the domains of instability of two modes overlap.

9.1.3 Burner geometry and operating conditions

This section describes the experimental setup detailed in Part I of the present manuscript. The reader can skip this part which concerns the thickest flame holder l = 15 mm.

The experimental setup used in the present work is sketched in Fig. 9.1. Except for a thickened perforated plate, it features the elements used in our previous investigations (Boudy et al. (2011b); Boudy et al. (2011a)). An adjustable feeding manifold length L_1 of diameter $D_1 = 0.07$ m allows injection of a methane/air mixture. This mixture flows through a piston used to change the feeding manifold length L_1 and delivers the fresh stream through a peripherically holed flat head. Flames are anchored on a perforated plate. The thickness of this plate is $l = 15$ mm and there are $N = 421$ holes of diameter $d_p = 2$ mm. A confinement tube of length $L_2 = 0.10$ m and diameter $D_2 = 0.13$ m encloses the combustion region. Regimes of combustion are characterized at limit cycle by means of velocity and pressure measurements. Heat release rate fluctuation is estimated by measuring free radicals emissions. The mass flow rate is set here to $\dot{m} = 4.71{\times}10^{-3}$ kg.s^{-1} for an equivalence ratio of $\phi = 1.03$, providing a thermal power of 13.3 kW. This flow induces a bulk velocity $U_b = 3.1$ m.s^{-1} in each perforated plate channel.
Three microphones are used for pressure measurements. The first one M_1 is located 24.5 cm away from the burner axis. The second M_2 is connected to a waveguide which is plugged in the same section as a hot wire located 3 cm below the perforated plate. Microphone M_3 is also connected on a waveguide to scan the pressure evolution in the flame region. Free radical light emission is measured by a photodiode equipped with an OH* filter. This sensor placed at a distance from the flame tube collects the light radiated by the flame region. Another set of experiments has been used to characterize the flame response subjected to harmonic velocity perturbations of different amplitudes. The flow is excited by a loudspeaker placed at the bottom of the burner. It modulates the flow from 0 to 1300 Hz in a relative amplitude range (u_{rms}/U_b) swept from 6 to 77 % where U_b indicates the bulk flow velocity in the perforation. Loudspeaker efficiency bounds the amplitude and frequency range covered in these experiments. Nevertheless, thanks to the forced flame response measurements

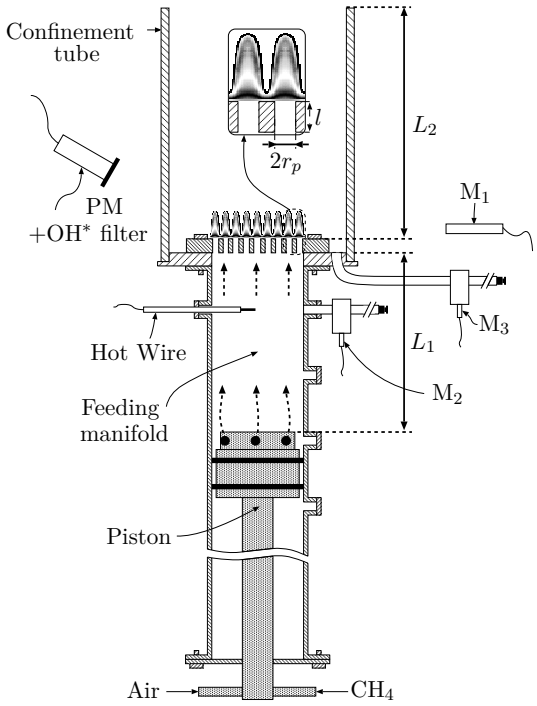

Figure 9.1: *Experimental setup and diagnostics used to characterize self-sustained instabilities.*

and the burner self-sustained combustion oscillations, the flame response is interpolated and extrapolated in missing areas. This flame response linked to a set of Flame Transfer Function at different amplitudes is designated as the Flame Describing Function (FDF). It is defined as the ratio of the relative heat release rate fluctuations to the relative velocity fluctuations :

$$\mathcal{F}\left(\omega_r, u_{rms}/U_b\right) = \frac{\widetilde{\dot{Q}}/\bar{\dot{Q}}}{u_{rms}/U_b} = G\left(\omega_r, u_{rms}/U_b\right) e^{i\varphi(\omega_r, u_{rms}/U_b)} \tag{9.1}$$

where ω_r indicates the angular forcing frequency and u_{rms} denotes the root mean square velocity fluctuation measured by LDV at 0.7 mm above one hole of the perforated plate.

9.1.4 Experimental analysis

The system described in Sec. 9.1.3 is now used to obtain the bifurcation diagram of self-sustained combustion oscillations for a confinement tube length $L_2 = 0.10$ m by varying the feeding manifold length L_1 between 0.11 m and 0.77 m. The experimental exploration consists of increasing L_1 by steps of 1 cm. Once the maximum extension has been reached the length of the upstream manifold is reduced from $L_1 = 0.77$ m to 0.11 m. Regimes of combustion oscillation are either stable or unstable. In the unstable case, a frequency and amplitude are

deduced from pressure, velocity and heat release rate records. In the stable case, the flame does not oscillate and a low level of noise is mainly generated by the fresh stream flowing in the duct.

Oscillatory combustion regimes present different types of limit cycles. One may distinguish two groups. The first features stable oscillation amplitudes which have already been documented in previous articles (Noiray et al. (2008); Boudy et al. (2011b); Boudy et al. (2011a); Palies et al. (2011)). In the second group, one finds GLCs where the oscillation exhibits either regular or irregular envelope modulations. These modulations result from the presence of multiple frequencies which are revealed by a spectral analysis of the signals. One surprising issue is that there is some variability in the limit cycles. The sound signal which is perceived under such conditions has the general character of a "buzzing" but with some irregular quasi-periodic low frequency modulations and it is designated as "buzzing-chugged" combustion.

The configuration used in the present work with a short flame tube exhibits variable amplitude limit cycles in two ranges of length L_1. Figure 9.2 shows the frequency evolution obtained by increasing the feeding manifold length L_1 from 0.11 m to 0.77 m. Two graphs display the frequencies corresponding to the major components in the velocity spectrum for each feeding manifold length L_1. The upper graph (Fig. 9.2(a)) shows the main frequency of the limit cycle whereas the lower graph (Fig. 9.2(b)) indicates the next most important spectral components in the multiple frequency cases. When these spectral components are close sidebands of the central frequency the two sideband frequencies are indicated. Otherwise, the lower plot only shows the frequency of the second most important component. An examination of Fig. 9.2(b), indicates the range of lengths L_1 corresponding to TMLCs, which is embedded between $L_1 = 0.52$ m and 0.64 m.

As L_1 is increased from its initial value of 0.11 m, oscillations appear around the first mode and remain in the vicinity of this mode until $L_1 = 0.15$ m. The system then reaches a stable band from $L_1 = 0.16$ m to 0.24 m. At $L_1 = 0.25$ m the system features a new unstable range around the second mode. This single mode oscillation persists until $L_1 = 0.51$ m. A first range of variable amplitude limit cycles is found for $L_1 = 0.40$ m and 0.41 m. In this interval the signal is regularly modulated as shown in Fig. 9.3, for $L_1 = 0.40$ m. The pressure spectrum features two side peaks located near the main frequency. This side band situation is marked by two black circle symbols plotted in Fig. 9.2(b). Phase space reconstruction provides some additional insight on the oscillation behavior. The time series analysis (Small (2005)) requires an embedding dimension d_e and an optimal time delay τ which are then used to plot the trajectories in phase space. The "False Nearest Neighbours" method provides d_e. As explained in Abarbanel et al. (1993), the time delay τ may be chosen by examining the signal autocorrelation function and finding the time value where it drops to zero. For $L_1 = 0.40$ m one finds $\tau = 7$ periods of the sampling frequency ($f_s = 16384$ Hz), i.e. almost one quarter of the main

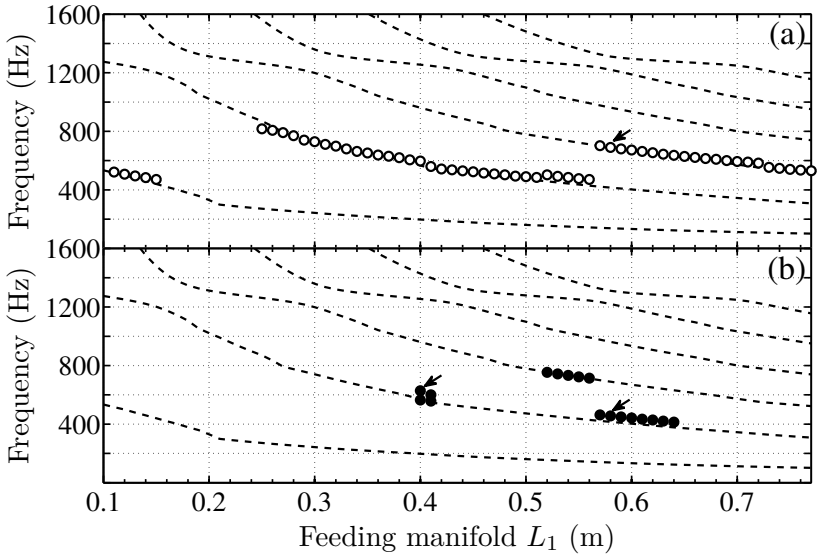

Figure 9.2: *Frequency evolution by increasing the feeding manifold length L_1 for the L_2 = 0.10 m flame tube. The six first acoustic eigenmodes calculated without an unsteady flame and different temperatures in each cavity are drawn with dashed lines. The feeding manifold temperature is fixed to T_1 = 300 K, while the flame tube is set to T_2 = 900 K. Top graph (a) represents the main frequency appearing on the velocity signal spectrum (○). Lower graph (b) shows the other frequencies found in multiple frequency cases. Two black circles (●) are used in the case of sidebands frequencies (first band of variable amplitude limit cycles) whereas only one circle shows the presence of another mode in the second multiple frequency band. The small arrows indicate the lengths studied and mentioned in the text.*

frequency period found at 600 Hz. The embedding dimension is estimated to be $d_e = 4$. It indicates the need to track the phase portrait in a four dimensional space. Nevertheless, it would be difficult to follow the trajectory in a such dimension. In this case, it is standard to consider a three-dimensional phase space. In addition, the rate of "false neighbours" is not so high with $d_e = 3$. The "False Nearest Neighbours" technique relies on the points evolution in the phase space when the dimension is progressively increased. When these points are "false neighbours", they move one from another with the increment. This gives a percentage of moving points decreasing along the dimension growth. A rate of 10 % is assumed to give the pattern exhibiting the proper dynamical behavior. In the present case, the use of three dimensions is a compromise between the difficulty to read the phase space reconstruction of higher value and the fact that the rate of false nearest neighbours falls to 20% when $d_e = 3$. One obtains a ring like structure confirming that the amplitude is modulated with a certain steadiness. This pattern features a flat ring which indicates that the frequencies of the different amplitudes are close. In the case of big differences this ring would have not been flat.
Beyond $L_1 = 0.51$ m, the third mode arises until $L_1 = 0.77$ m. This oscillation features multiple frequencies for $L_1 = 0.52$ m to 0.64 m as is well illustrated by analyzing the signal recorded for a particular value of $L_1 = 0.58$ m belonging to this range (Fig. 9.4). The pressure oscillates at a frequency corresponding to the third mode $f_{m3} = 690$ Hz. Its amplitude is modulated with a period which is equal to three times that corresponding to the fundamental frequency $f_c = f_{m3}$. The spectrum reveals the presence of modes 2 and 3. One also finds a low frequency at 234 Hz which corresponds to the difference between $f_{m3} - f_{m2}$. In the present case this gives rise to a period tripling phenomenon observed in the pressure record where one finds that three fundamental periods are necessary to recover the same signal value. Phase space reconstruction is obtained with the methodology described previously. One obtains an embedding dimension $d_e = 4$ while the optimal time delay τ corresponds to 6 periods of the sampling frequency f_s, i.e. 25.3 % of the f_{m3} frequency period. A three-dimensional space is used once more and the reconstruction exhibits three circular patterns corresponding to three amplitude levels induced by the period tripling characterizing this case. The phase space reconstruction allows to confirm a different behavior in comparison to the one analyzed before with $L_1 = 0.40$ m. Indeed with $L_1 = 0.58$ m, the circular patterns are not in the same plane. It reveals that the frequency changes largely with the amplitude compared to the previous case. This analysis is especially useful for the other lengths L_1 where the spectrum is not always as clear as the one presented here. It allows to delineate different circular patterns and helps to clarify the system dynamics.

In a nutshell, this configuration exhibits stable and variable amplitude limit cycles. In the first band of unstable oscillation amplitudes, between $L_1 = 0.40$

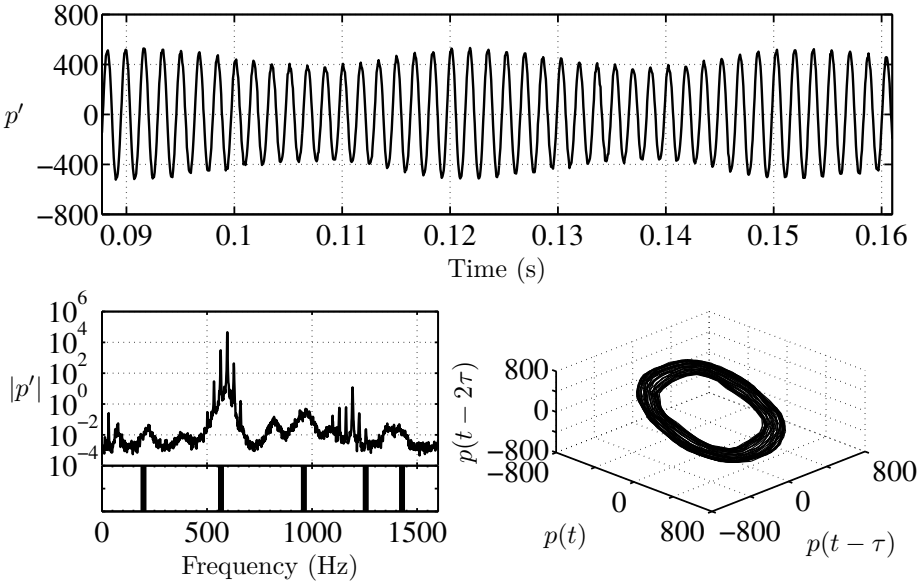

Figure 9.3: *Pressure evolution recorded by microphone* M_2 *(top) for* $L_2 = 0.10$ *m and* $L_1 = 0.40$ *m. The spectrum (left) and phase space reconstruction (right) are displayed below. Acoustic eigenmodes calculated without the flame but by assuming different temperatures in each cavity are drawn as vertical lines below the pressure spectrum.*

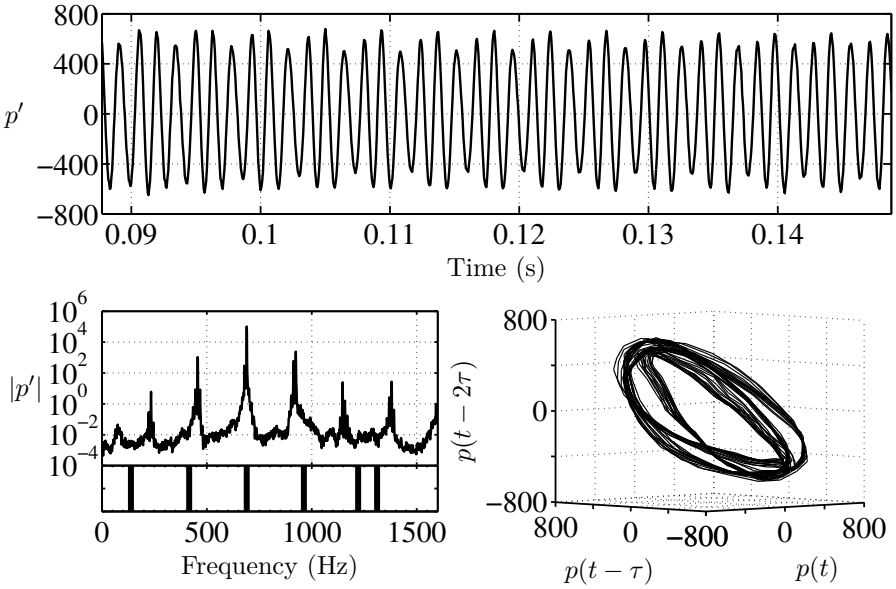

Figure 9.4: *Pressure evolution recorded by microphone* M_2 *(top) for* $L_2 = 0.10$ *m and* $L_1 = 0.58$ *m. The spectrum (left) and phase space reconstruction (right) are displayed below. Acoustic eigenmodes calculated without the flame but by assuming different temperatures in each cavity are drawn as vertical lines below the pressure spectrum.*

m and 0.41 m, the signal is regularly modulated and this corresponds to the presence of two side-peaks around the central frequency. In the second band pertaining to $L_1 = 0.52$ m to 0.64 m, two modes are simultaneously present and generate a frequency difference which in the range of observation produces a period tripling phenomenon. The study is now focused on this second kind of limit cycles sustained by two modes (TMLCs).

9.1.5 Theoretical interpretation

It is natural to seek an explanation for oscillations of the type described previously. We focus on unstable oscillations sustained by two modes which are probably the most commonly observed in practice. To this purpose we use the FDF framework to determine the growth rates of specific modes of oscillation. The analysis relies on the nonlinear dispersion relation derived by combining an acoustic network description of the system with a flame response represented by a family of transfer functions corresponding to different amplitude levels (the Flame Describing Function).
The model of the system is sketched in Fig. 9.5. A reflection coefficient defines the inlet and outlet of the combustion system. This can be represented as an acoustic network as in many studies of combustion instability (see Keller (1995); Paschereit et al. (2001)). A model of the perforated plate, used to anchor small conical flames, is also considered with a dynamical relation adapted from Melling (Melling (1973)) to link the pressure difference and the flow velocity in each channel. By considering boundary and matching conditions of acoustic variables between the upstream manifold and flame tube, one obtains the following system of equations written in a matrix form :

$$\begin{pmatrix} 1 & -\mathrm{R}_1(0) & 0 & 0 \\ 0 & 0 & \mathrm{R}_2(L_2)e^{ik_2L_2} & -e^{-ik_2L_2} \\ \mathcal{A}_1 e^{ik_1L_1} & \mathcal{A}_2 e^{-ik_1L_1} & -1 & -1 \\ \mathcal{B}e^{ik_1L_1} & -\mathcal{B}e^{-ik_1L_1} & \mathcal{C}_1 & \mathcal{C}_2 \end{pmatrix} \begin{pmatrix} A_1^+ \\ A_1^- \\ A_2^+ \\ A_2^- \end{pmatrix} = 0 \quad (9.2)$$

where $\mathcal{A}_1$, $\mathcal{A}_2$, $\mathcal{B}$, $\mathcal{C}_1$ and $\mathcal{C}_2$ correspond to :

$$\mathcal{A}_1 = 1 + \frac{i\omega l}{\mathcal{P}c_1}\Big[1 + \frac{l_\nu}{r_p}(1+i)\Big],\ \mathcal{A}_2 = 1 - \frac{i\omega l}{\mathcal{P}c_1}\Big[1 + \frac{l_\nu}{r_p}(1+i)\Big],$$

$$\mathcal{B} = \frac{S_1}{S_2}\frac{\rho_2 c_2}{\rho_1 c_1}\left[1 + \left(\frac{T_f}{T_1} - 1\right)Ge^{i\varphi}\right],$$

$$\mathcal{C}_1 = i\Big(1 - \frac{S_1}{S_2}\Big)\tan(k_2 l) - 1,\ \mathcal{C}_2 = i\Big(1 - \frac{S_1}{S_2}\Big)\tan(k_2 l) + 1$$

In this expression, $|\mathrm{R}_1(0)|\exp(i\phi_1(0))$ and $|\mathrm{R}_2(L_2)|\exp(i\phi_2(L_2))$ pertain to the reflection coefficients at the burner inlet and outlet. The FDF appears as $G\exp(i\varphi)$ and T_f denotes the flame temperature. The perforated plate

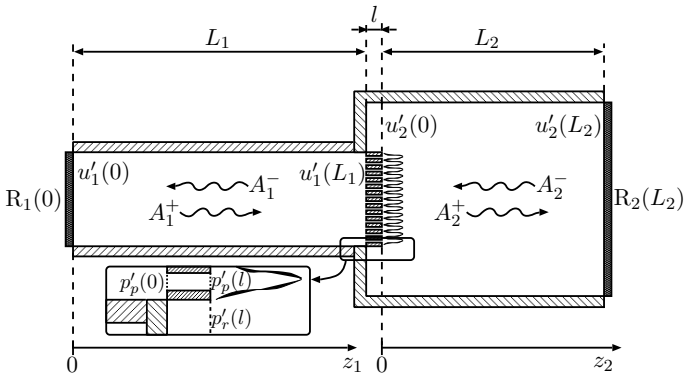

Figure 9.5: *Burner and symbol convention used for the analytical model.*

used as a flame holder is taken into account with a model due to Melling (Melling (1973)), where $l_\nu = (2\nu/\omega)^{1/2}$ stands for the thickness of the acoustic boundary layer in each channel. The porosity appears as $\mathcal{P} = N\pi r_p^2/\pi R_1^2$ where r_p and R_1 respectively designate the radius of a hole of the perforated plate and the one of the feeding manifold. Its surface area is noted S_1 while the one of the confinement tube corresponds to S_2. The determinant of the system must vanish to obtain non trivial solutions. This provides a dispersion relation which depends nonlinearly on the amplitude in a way defined by the FDF. The complex angular frequency $\omega = \omega_r + i\omega_i$ solution of the dispersion relation gives the angular frequency $\omega_r = 2\pi f$ and the growth rate ω_i of the oscillation. This solution is computed for each length L_1 belonging to the experimental range. This calculation is carried out for different amplitude levels and it is thus possible to follow the solution as a function of the amplitude.

By considering all the roots of the dispersion relation for a range of amplitudes and for each feeding manifold length L_1, it is possible to plot the bifurcation diagram shown in Fig. 9.6 which presents growth rate contours calculated for the first three eigenmodes. The growth rates are displayed with three different colors corresponding to the first three modes as indicated at the top of the figure. Contours plotted in the three domains provide the growth rates as a function of amplitude for each feeding manifold length L_1. When the growth rate vanishes $\omega_i = 0\ s^{-1}$ one obtains a boundary contour which possibly defines a limit cycle. It is interesting to note that there are regions where a single mode prevails and other regions where there is a modal overlap. When there is an overlap one expects to find a more complex behavior than in the situation featuring an isolated mode.

At this point it is useful to examine the experimentally observed amplitudes of oscillation. Oscillation amplitudes associated to the first mode are displayed as open circle symbols (○) while the second mode oscillation amplitudes appear as open square symbols (□). Amplitudes corresponding to the third mode are represented by open triangle symbols (△), but in the multiple frequency case

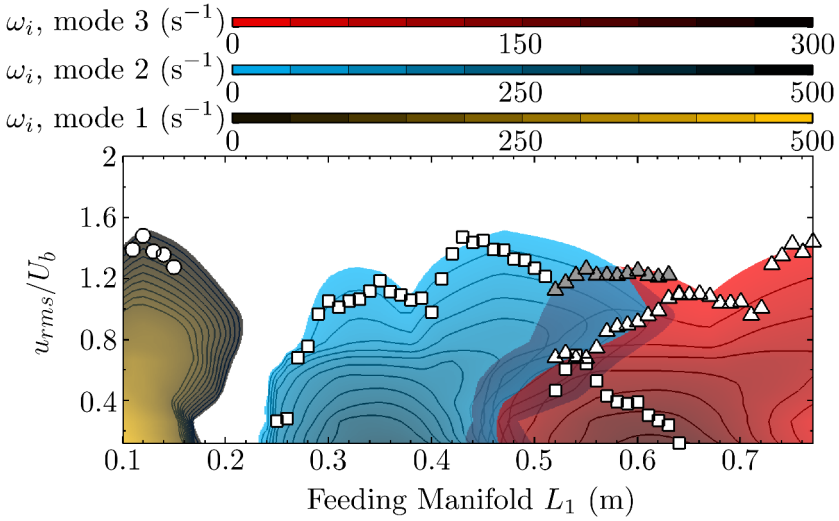

Figure 9.6: *Growth rate evolution for the $L_2 = 0.10$ m confinement tube and the sweeps of feeding manifold L_1 from 0.11 m to 0.77 m. Three colors are used for each eigenmode. The first is displayed in yellow, the second in blue and the third in red. Scale is given above to graph. Symbols correspond to experiments. ○ stands for the first mode while □ corresponds to the second one and △ to the third. Gray triangle symbols depict the sum of the 2 modes values in the multiple frequency band ($L_1 = 0.52$ m to 0.64 m).*

it is first necessary to separate the components corresponding to the different frequencies. This is accomplished by digital filtering of the record by setting two bandpass filters around the two main frequencies appearing in the power spectrum. This signal filtering is used to display the amplitudes associated to the two modes found in the multiple frequency range between $L_1 = 0.52$ m and 0.64 m. It is also interesting to calculate the sum of these two amplitudes without taking into account a possible phase shift. This defines the maximum amplitude which can be reached when the two components are mixed. This amplitude is marked by gray triangle symbols.

In the region where a single mode prevails one finds that the amplitude evolution observed experimentally by changing the feeding manifold length L_1 can be retrieved theoretically by reading this diagram. There is a reasonable match between the experimental points and the amplitude found for a vanishing ω_i. For these points one expects a stable amplitude limit cycle which is indeed observed almost everywhere. The first branches of the oscillation amplitude, i.e. mode 1 and mode 2 between $L_1 = 0.10$ m and 0.51 m, are well predicted. The last part between $L_1 = 0.65$ m and 0.77 m is also fairly well retrieved. There is however a small range of L_1 between 0.40 and 0.41 m where the system features a central frequency and two side bands giving rise to a modulated amplitude at limit cycle (see Fig. 9.2). It is possible to show that this particular behavior is related to the dependence of the boundary reflection coefficient with respect

to the amplitude level but this will not be examined here. For the stable limit cycle cases the real part of ω provides the oscillation frequency corresponding to the amplitude determined in the bifurcation diagram.

It is now interesting to examine the multiple frequency band between $L_1 = 0.52$ m and 0.64 m. One may first consider that the oscillation would behave as before and that the limit cycle would correspond to $\omega_i = 0\ s^{-1}$. If this were so, one would expect a limit cycle around the second mode between $L_1 = 0.52$ m and 0.58 m followed by a limit cycle around the third mode between $L_1 = 0.58$ m and 0.64 m. However, as observed in Fig. 9.4 for $L_1 = 0.58$ m, the oscillation is not locked on a single frequency. Pressure or velocity records feature two principal frequency components as observed in the power spectrum. By filtering the pressure or velocity signals, one finds that modes 2 and 3 coexist both with a nearly constant amplitude. One then finds that mode 3, represented by open triangle symbols ($\triangle$), stands for 50 % - or more - of the expected oscillation amplitude at $\omega_i = 0\ s^{-1}$. This is found by processing the signal in the range $L_1 = 0.55$ m to 0.62 m. Mode 2, represented by open square symbols ($\square$), also appears in this range. Its amplitude is found to be equal to the difference between the value calculated for the limit cycle at $\omega_i = 0\ s^{-1}$ and the amplitude of mode 3. One can see in Fig. 9.6 that the combined amplitude of the two modes (gray triangle symbols) closely matches the limit cycle boundary. This phenomenon appears in a case where mode 3 features a supercritical bifurcation (is linearly unstable) while mode 2 has a subcritical bifurcation and is nonlinearly unstable in the range of interest. There is an overlap region where mode 3 has a higher growth rate than mode 2. The third mode amplitude dominates that of the second mode but the third mode does not take over and oscillations at the second mode frequency persist. There is a crossing point in amplitudes which corresponds to coinciding growth rates of the two modes.

In addition to the growth rate ω_i it is interesting to examine the corresponding values of the angular frequency ω_r. Figure 9.7 displays the frequency calculated from the dispersion relation at the limit cycle amplitude predicted by reading the bifurcation diagram.

The frequencies are compared with experimental values plotted as symbols. Open circle symbols ($\circ$) correspond to the first mode frequencies while the second and the third modes are respectively displayed by means of open square ($\square$) and open triangle symbols ($\triangle$). Predictions corresponding to $\omega_i = 0\ s^{-1}$ are plotted as dark bold lines, whereas frequencies calculated in the multiple frequency cases are displayed as red bold lines. In this last condition, mode 2 and mode 3 frequencies are read at the amplitude where growth rates intersect. The multiple frequency cases clearly arise from a combination of two modes. In addition one finds that the frequencies mix and produce a signal with a difference frequency which is reminiscent of a similar situation found in wireless telecommunications where it is designated as frequency “heterodyning”. Heterodyning gives rise to the sum or difference of the two original frequencies

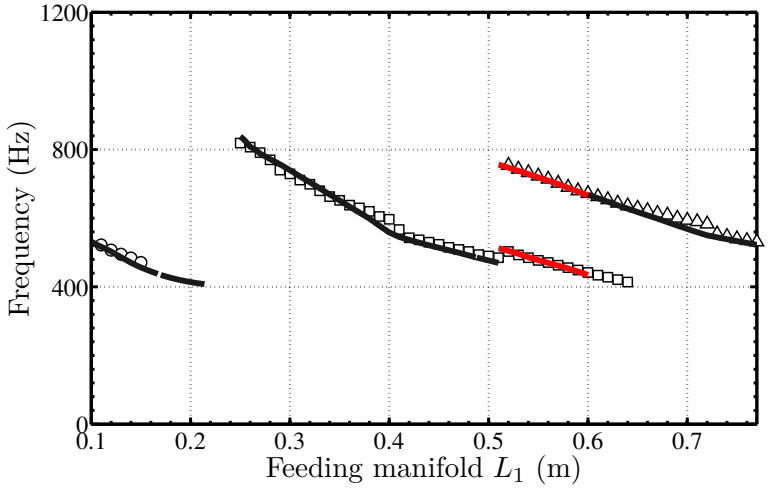

Figure 9.7: *Theoretical and experimental frequency at limit cycle. Open circle symbols (○) are linked to the first mode while the second mode appears as open square symbols (□) and the third mode as open triangle symbols (△). The dark bold lines represent predictions for $\omega_i = 0\ s^{-1}$ whereas the red ones correspond to the frequencies of the two modes limit cycles.*

input in a nonlinear system. There are some theoretical calculations indicating the possibility of double mode oscillations. For example, Culick and his co-workers (Awad et al. (1986)), show that this can happen if two modes exist of which one is stable and the other is unstable. This is only found for certain ranges of values of the growth rates but has not been observed in the present experiments and the double mode of oscillation arises when some other conditions are fulfilled as explained in what follows.

To predict the occurrence of multi-mode oscillations, it is natural to examine growth rate trajectories and derive conditions which gives rise to this behavior. First, it is found that dual mode oscillations appear when there is a modal overlap i.e. when the regions of positive growth rates of two modes intersect. A detailed examination reveals two types of overlap. The first type corresponds to two linearly unstable modes as shown in Fig. 9.6 between $L_1 = 0.43$ m and 0.48 m. In this case, exemplified in Fig. 9.8 for $L_1 = 0.45$ m, the second mode dominates over the whole amplitude range. By reading the bifurcation diagram, one expects that the oscillation will be locked on the mode which has the highest growth rate. This is well observed experimentally and in the corresponding range the second mode of oscillation prevails with an amplitude which closely matches that determined from the FDF calculation. It is well verified in this case that the third mode does not arise in the power spectrum. This kind of modal overlap has already been considered in previous calculations and experiments which all confirm that the mode with the highest growth rate values is dominant. For example, in Boudy et al. (2011b) two linearly unstable modes exist for a short flame tube of 0.10 m and a feeding manifold length L_1

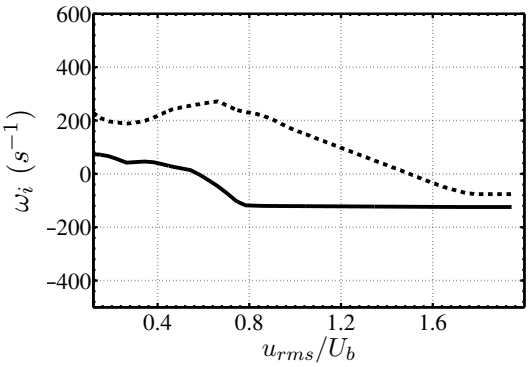

Figure 9.8: *Theoretical growth rate trajectories calculated with the FDF for the L_2 = 0.10 m confinement tube and L_1 = 0.45 m. The dashed line (- -) indicates the second mode growth rates whereas the bold line (—) corresponds to the third mode.*

between 0.28 m and 0.38 m (see Fig. 8 in Boudy et al. (2011b)). In this range, the second mode takes over and oscillations at the limit cycle correspond to a single frequency.

The second type of overlap is found in the present experiments when $L_1 > 0.48$ m, in the range where the second mode becomes nonlinearly unstable while the third mode is linearly unstable. In this range, the two modes are sustained. The existence of linearly and nonlinearly unstable modes is a necessary condition for a dual mode of oscillation but this is not sufficient. Indeed, previous experiments indicate that when this condition is verified the two modes do not always persist simultaneously. In the unconfined geometry discussed in Noiray et al. (2008) and in the confined configuration explored in Boudy et al. (2011a) it was found that the oscillation begins at the third mode frequency and that as the amplitude increases mode switching takes place and the second mode prevails. The final outcome is a limit cycle corresponding to a vanishing growth rate of the nonlinearly unstable mode ($\omega_i = 0\ s^{-1}$). It is then necessary to find the additional condition which distinguishes situations where a single mode takes over from that where the two modes are sustained. This is accomplished by examining the growth rate trajectories obtained by plotting this quantity with respect to the amplitude of oscillation.

An example is given in Figure 9.9 which shows two configurations where the trajectory of a linearly unstable mode (LUM) crosses that of a nonlinearly unstable mode (NLUM). The first case examined in Fig. 9.9(a) corresponds to experiments reported previously (Boudy et al. (2011a)) in which mode switching was observed and predicted for different operating conditions. The second case, shown in Fig. 9.9(b), pertains to the present investigation for $L_1 = 0.52$ m. The amplitude level where the linearly unstable mode (LUM) trajectory crosses the horizontal axis $\omega_i = 0$ is plotted as a vertical bold line in these two diagrams. Two arrows denote the tangent lines to the growth rate trajectories at this particular amplitude level designated as a_0. In the case shown

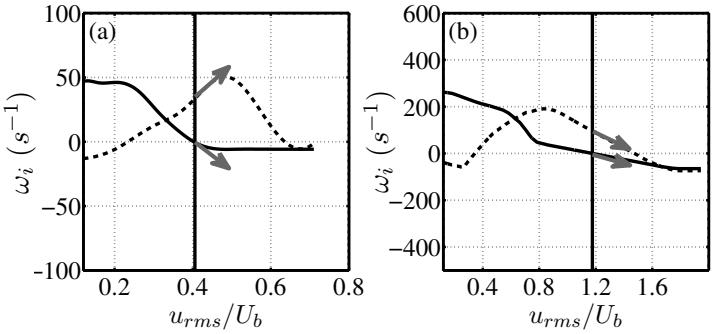

Figure 9.9: *Theoretical growth rate trajectories calculated with the FDF. The dashed line (- -) shows the second mode growth rate whereas the bold line (━) corresponds to the third mode. (a) pertains to calculations from previous work (Boudy et al. (2011a)) for $L_1 = 0.54$ m and a confinement tube of $L_2 = 0.10$ m. In this case, the crossing of trajectories leads to a mode switching during the growth of oscillation. (b) is obtained from the present investigation at $L_1 = 0.52$ m with the $L_2 = 0.10$ m confinement tube. Experiments reveal a dual mode oscillation. The first trajectory crossing $\omega_i = 0$ is indicated by means of a vertical line. Gray arrows at this point represent the tangent lines and provide the signs of the slopes for the two modes.*

in Fig. 9.9(a) which gives rise to mode switching, the slope of the third mode (LUM) growth rate is negative while the slope of the second mode (NLUM) growth rate is positive :

$$(d\omega_{i3}/da)_{a_0} < 0 \text{ and } (d\omega_{i2}/da)_{a_0} > 0 \tag{9.3}$$

In contrast, when the two modes are simultaneously sustained, the growth rate slopes are both negative as illustrated in Fig. 9.9(b) :

$$(d\omega_{i3}/da)_{a_0} < 0 \text{ and } (d\omega_{i2}/da)_{a_0} < 0 \tag{9.4}$$

The present experiments indicate that when there is a modal overlap involving a linearly unstable mode (LUM) and a nonlinearly unstable mode (NLUM) and when condition Eq. (9.4) is satisfied the oscillation takes place at the two frequencies. On the other hand, when condition Eq. (9.3) is satisfied, mode switching takes place and the nonlinearly unstable mode prevails.
By applying the previous criterion it is possible to delineate the region where one expects oscillations at two modal frequencies. This can be simply done by calculating the growth rate differentials with respect to the amplitude in the region of modal overlap. The region where the criterion has to be satisfied appears in gray in Fig. 9.10. For $L_1 < 0.50$ m the first condition on the existence of linearly and nonlinearly unstable modes is not fulfilled. Condition Eq. (9.4) is satisfied for $0.50 \leq L_1 \leq 0.61$ m and one expects to find a double mode oscillation. The boundaries of this range nearly match that found in the experiment which is located between 0.52 m and 0.64 m. Except for this small difference due to uncertainties in the FDF determination, the criterion

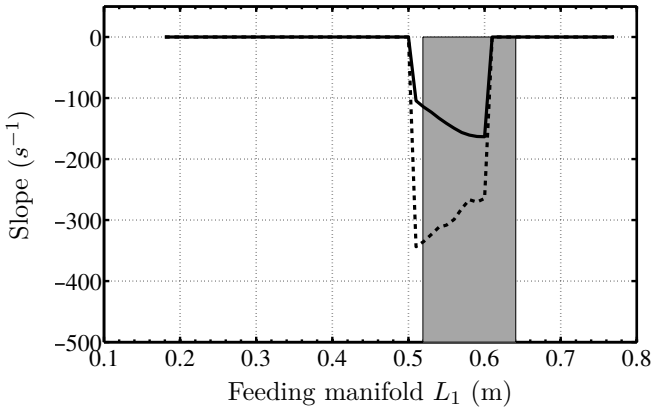

Figure 9.10: *Rates of change (slope) of the growth rates corresponding to mode 2 (dashed line - -) and mode 3 (bold line ━). The calculation is carried out in the region of overlap of the LUM and NLUM. The slope of each mode is determined at the amplitude where the linearly unstable mode (LUM) crosses $\omega_i = 0$. Gray area indicates the lengths where dual mode oscillation has been found in the experiment.*

stated previously suitably provides the range where two modes are sustained simultaneously.
In summary, it appears that double mode oscillations can be expected when a linearly and a nonlinearly unstable modes overlap and when in addition condition (9.4) on the rates of change of the growth rates is satisfied.

9.1.6 Conclusion

Thermoacoustic coupling is investigated in a generic combustion system featuring a feeding manifold, a multipoint injector and a small length flame tube confining the combustion region. Two classes of limit cycle have been identified. The first features a nearly stable oscillation amplitude, whereas the second shows an amplitude unsteadiness. These variations are of different kinds. In the present experiment, two types arise indicating that TMLCs can occur in different parametric ranges. The present study concentrates on a range of parameters where oscillations are sustained by two modes also giving rise to frequency mixing. In this range the limit cycle is regularly distorted via a low frequency formed by heterodyning. It is shown that such a process can be expected by examining FDF calculations. It is first observed that a nonlinear dispersion relation including a flame describing function provides predicted amplitudes and frequencies which are in good agreement with experimental values for stable limit cycle cases. In the TMLC cases, a double mode oscillation is shown to occur when two conditions are fulfilled. The first condition is an overlap between a supercritical bifurcation mode (LUM) and a subcritical bifurcation mode (NLUM). The second condition requires that the slopes of growth rate trajectories of these two modes have negative signs at the point

where the LUM would reach its limit cycle. In contrast when the signs of these slopes are distinct, i.e. the slope of the NLUM growth rate is positive, mode switching takes place and a single mode prevails at the limit cycle.

9.2 Analysis of galloping limit cycles featuring chaotic states

This section corresponds to a publication presented at the *ASME Turbo Expo 2012* :

Boudy, F., D. Durox, T. Schuller, and S. Candel. 2012. "Nonlinear flame describing function analysis of galloping limit cycles featuring chaotic states in premixed combustors." In *Proceedings of the ASME Turbo Expo, paper GT2012-68998*, New York: American Society of Mechanical Engineers.

The experimental setup and model (model B) used in this analysis are the same as those presented in Sec. 9.1. Thus, after the introduction which is shortened and focused on the unstable amplitudes, the experimental results are shown and followed by results of calculations carried out with model B. The abstract is kept to underline highlights of this section.

9.2.1 Abstract

Nonlinear prediction of combustion instabilities in premixed systems is undertaken on a generic configuration featuring an adjustable feeding manifold length, a multipoint injector composed of a perforated plate and a flame confinement tube. By changing the feeding manifold or flame tube lengths, the system exhibits different types of combustion regimes for the same flow operating conditions. Velocity, pressure and heat release rate measurements are used to examine oscillations during unstable operation. For many operating conditions, a limit cycle is reached at an essentially fixed oscillation frequency and quasi-constant amplitude. In another set of cases, the system features other types of oscillations characterized by multiple frequencies, amplitude modulation and irregular bursts which can be designated by "galloping" limit cycles or GLC. These situations are explored in this article. Imaging during GLCs indicates that the flame is globally oscillating but that the cycle is irregular. Prediction of these special oscillation states is tackled within the Flame Describing Function (FDF) framework. It is shown that it is possible to predict with a reasonable degree of agreement the ranges where a quasi-constant amplitude limit cycle will be established and ranges where the oscillation will be less regular and take the form of a galloping limit cycle. It is found that the FDF analysis also provides indications on the bounding levels of the oscillation envelope in the latter case.

9.2.2 Introduction

In combustion instabilities, there are few studies in which the oscillation on an unstable amplitude is characterized and calculations are attempted. This is for example found in the premixed laboratory combustor used in Sterling (1993) where quasi-periodic oscillations were identified and linked to the interaction of two acoustic eigenmodes. In the swirled combustor studied in Lamraoui et al. (2011) two unstable modes simultaneously present were associated to different triggering mechanisms of the flame response to flow perturbations. A theoretical investigation based on a multiple inputs and outputs flame model was used in J. P. Moeck et al. (2012) to examine limit cycles with multiple frequencies. A dual oscillator model was proposed in this study where energy transfer occurs and leads to an oscillating limit cycle between two modes. Nevertheless, no experimental comparison was carried out. More recent experimental investigations in a multiple flame combustor equipped with a perforated plate comprising seven orifices also revealed different states of limit cycles with modulated amplitudes (Kabiraj et al. (2011b); Kabiraj et al. (2011a)) which were uncovered by examining different combustion chamber lengths. In these studies, various types of unstable combustion regimes were identified and characterized including quasi-periodic as well as chaotic oscillations, but the flame response to flow perturbations was not considered.
The present work complements our previous investigation of a multiple injection combustor (Boudy et al. (2011b)). It specifically deals with GLCs (Galloping Limit Cycles) appearing in this system when the flame region is confined in a longer tube. Two types of GLCs can be distinguished. The first features a regular amplitude modulation, while the second exhibits irregular variations. An analysis of unstable oscillations featuring multiple frequencies was carried out in Boudy et al. (2013). The present study considers the case of GLCs featuring a richer spectral content and corresponding to time evolving amplitudes. This variable amplitude oscillation state is now analyzed in the special case of chaotic oscillations where the amplitude fluctuates in an irregular fashion. This analysis is based on the Flame Describing Function (FDF) framework. It is shown that this allows to delineate ranges where the limit cycle will have a special behavior and to obtain predictions for the peak and minimum amplitudes of oscillation. This article begins with a short description of the test rig and instrumentation. Experimental results are reported next. The model, including the FDF, is then briefly presented. Results of calculations are then discussed and the chaotic oscillations are interpreted on this theoretical basis. It is shown in particular that amplitude variable limit cycles arise when the nonlinear dispersion relation of the system feature roots with closely matching real parts.

9.2.3 Self-sustained combustion regimes

Experiments were carried out with the flame tubes $L_2 = 0.20$ m and 0.30 m. The measurements of the oscillation frequencies are plotted in Fig. 9.11 as a function of the feeding manifold length L_1.
Self-sustained combustion oscillation regimes are examined here when the feeding manifold length is varied. Combustion is initiated for $L_1 = 0.11$ m and the feeding manifold length L_1 is increased by steps of 1 cm until $L_1 = 0.55$ m. By increasing L_1, it is found that the flame oscillates around one of the acoustic eigenmodes of the system. This phenomenon takes place for most of the lengths L_1. Two flame tubes $L_2 = 0.20$ m and $L_2 = 0.30$ m are specifically examined. Thanks to these experiments, one can distinguish two classes of limit cycles. The first relies on oscillations at an essentially constant amplitude revealed in time traces and spectral analysis. In the second class, the oscillation amplitude can be regularly or irregularly modulated, leading to multiple frequencies in the power spectral densities of the different signals. The present study focusses on oscillations characterized by irregular variations in amplitude which give rise to what can be designated as a "galloping" limit cycle (GLC). These unstable amplitudes occur around the first mode in the two configurations explored with different flame tubes. Thus, for the sake of simplicity, only oscillations around this first acoustic eigenmode of the system are examined in this analysis.
Figure 9.11 displays oscillation frequencies observed for a limited range of feeding manifold lengths L_1 and for the two different confinement tubes $L_2 = 0.20$ m and 0.30 m. In the first case presented in Fig. 9.11(a) for $L_2 = 0.20$ m, oscillations associated to the first mode prevail from $L_1 = 0.11$ m to 0.25 m. A stable band is then found between $L_1 = 0.26$ m and 0.28 m. Beyond that value, the system switches to the second mode until $L_1 = 0.55$ m. In the second case presented in Fig. 9.11(b) for $L_2 = 0.30$ m, oscillations evolve around the first mode between $L_1 = 0.11$ m and 0.35 m. At that point the system switches to the second mode until $L_1 = 0.55$ m and there is no stable band.

9.2.4 Stable limit cycle

Analysis initiated in the present experiment reveals two types of limit cycles. Stable limit cycles are indicated in Fig. 9.11 as open circle symbols (○). One can see that the frequency lies close to the first acoustic mode of the combustor for the shortest lengths of feeding manifold L_1 between 0.11 m and 0.14 m. This appears for both flame tubes. For sizes greater than $L_1 = 0.14$ m, the oscillation frequency is shifted with respect to the acoustic eigenmode. It is interesting to note that this frequency shift may reach 100 Hz. It clearly shows that linear stability analyses only yield a rough estimate of the frequencies which may develop in the system. One can see in Fig. 9.11(a) that the oscillation frequency is shifted, but the limit cycle remains stable until $L_1 = 0.20$ m for the $L_2 = 0.20$ m flame tube. In Fig. 9.11(b), $L_1 = 0.22$ m represents the last

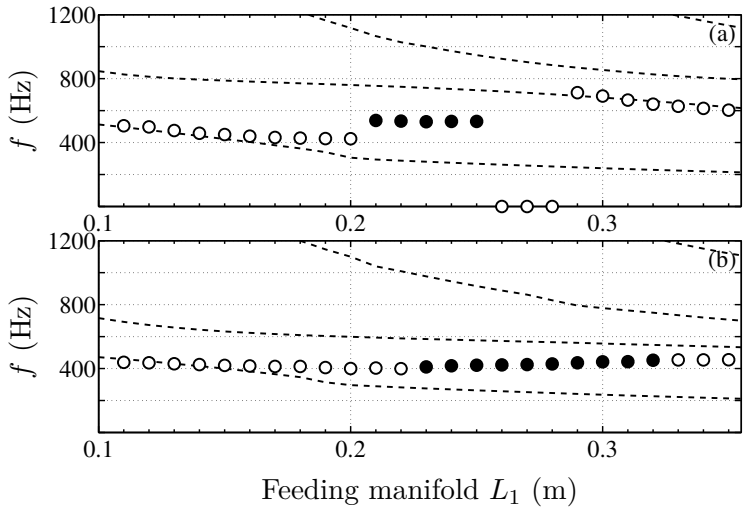

Figure 9.11: *Instability frequency evolution as a function of the feeding manifold length L_1. (a) and (b) are respectively linked to experiments conducted with $L_2 = 0.20$ m and 0.30 m flame tubes. Dashed lines correspond to the acoustic eigenmodes calculated without the flame but with 300 K in the feeding manifold and 1100 K in the $L_2 = 0.20$ m flame tube. The other case $L_2 = 0.30$ m is calculated with 1300 K. (○) symbols represent the peak frequency of the pressure spectrum measured by microphone* M_2 *for stable limit cycles. (●) symbols indicate the main frequency appearing in the spectrum of GLCs.*

stable limit cycle for this longer confinement tube ($L_2 = 0.30$ m). One example of stable limit cycle is presented in Fig. 9.12. Pressure measurements recorded with microphone M_2 for $L_1 = 0.16$ m and $L_2 = 0.20$ m are indicated together with the corresponding spectral distribution and phase space reconstruction. Welch's method of averaging combined with a Hanning windowing is used to estimate the power spectral densities. The phase space has been reconstructed using the methods presented in Abarbanel et al. (1993).

This reconstruction is divided in two steps. The first is devoted to the determination of the optimal embedding dimension d_e. In essence, one seeks to represent the signal time series in a space where trajectories do not cross (or do not come close) because the choice of the number of dimensions is too low. In a second step, one calculates the optimal time lag τ used to shift the values of the time series.

In practice, the embedding dimension d_e is deduced by using the so-called "False Nearest Neighbours" technique well explained in Small (2005). For the present case with $L_1 = 0.16$ m and $L_2 = 0.20$ m, d_e takes a low order of 2. The optimal time delay τ is determined with the autocorrelation function of the time series. As explained in Abarbanel et al. (1993), τ may be chosen by examining the signal autocorrelation function and finding the time lag where it drops to zero. For $L_1 = 0.16$ m and $L_2 = 0.20$ m, this gives $\tau \simeq 9/f_s$, where $f_s = 16384$ Hz indicates the sampling frequency.

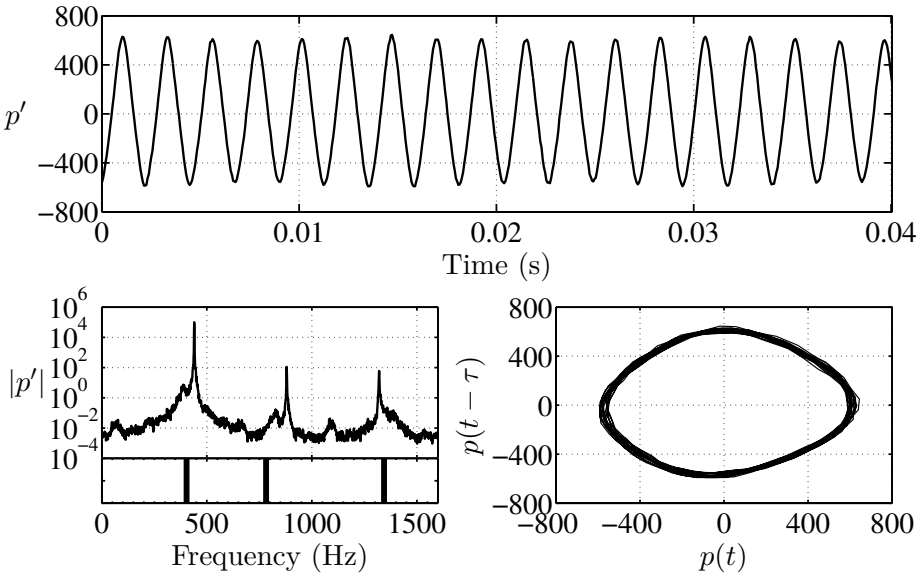

Figure 9.12: *Pressure evolution of microphone* M_2 *(top) for* L_2 *= 0.20 m and* L_1 *= 0.16 m. the corresponding spectrum is displayed below on the left and the phase plane is shown on the right. The acoustic eigenmodes calculated without the flame but with 300 K in the feeding manifold and 1100 K in the flame tube are drawn below the pressure spectrum.*

One can see that the pressure oscillation evolves with a quasi constant amplitude. The spectrum reveals a well marked peak at $f = 440$ Hz together with a few harmonics featuring a significantly reduced amplitude. The phase plane exhibits a circular pattern confirming the stability of this limit cycle. Galloping limit cycles are now analyzed in the same way. It is interesting to note that GLCs occur for an almost equal frequency shift observed in the two geometrical configurations investigated. This happens for $L_1 = 0.20$ m for the small flame tube $L_2 = 0.20$ m where the frequency shift is 118 Hz with respect to the acoustic eigenmode. In the second case with the longer flame tube L_2 = 0.30 m, this arises for $L_1 = 0.22$ m and the frequency shift reaches 117 Hz.

9.2.5 Chaotic limit cycles

Phase space reconstruction and spectral analysis give insight on the periodicity and chaotic behavior of the system dynamics. As explained in Henry et al. (2000) the "grassy appearance" of a pressure spectrum and the non periodic character of the autocorrelation function reveal the chaotic nature of the oscillation. The phase space reconstruction enables to follow trajectories and reveals possible periodic patterns or a less organized chaotic motion. It might be worth using system dynamics theoretical tools to define the attractor type and the route to chaos by calculating Lyapunov exponents or fractal dimension

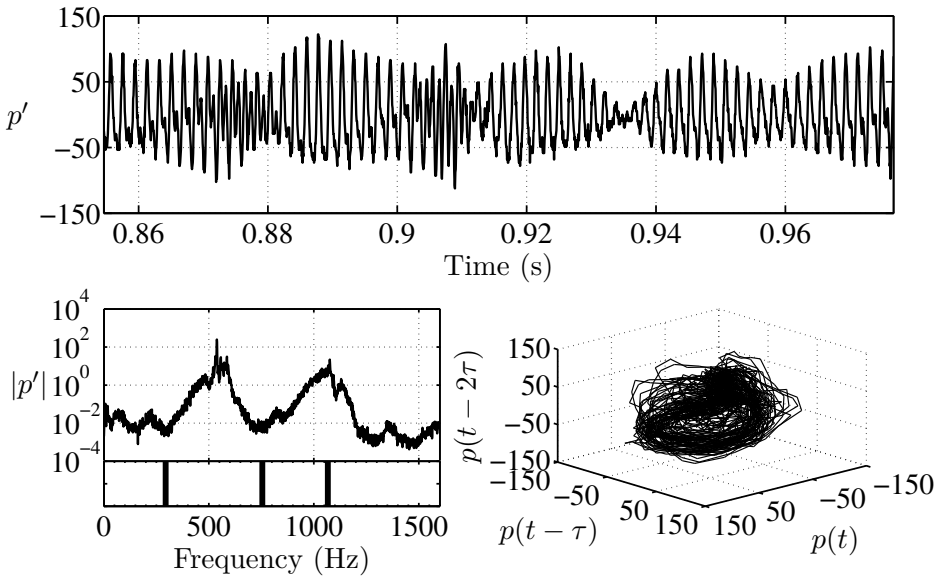

Figure 9.13: *Pressure evolution of microphone* M_2 *(top) for* $L_2 = 0.20$ *m and* $L_1 = 0.21$ *m. The corresponding spectrum is displayed below on the left and the phase plane is shown on the right. The acoustic eigenmodes calculated without the flame but with 300 K in the feeding manifold and 1100 K in the flame tube are drawn below the pressure spectrum.*

but this will not be pursued here because the aim is to interpret the dynamical behavior of GLCs in terms of FDF calculations.

The analysis of the microphone M_2 pressure signal is now considered. Figure 9.13 presents the time trace recorded for $L_1 = 0.21$ m and $L_2 = 0.20$ m. This unstable operating condition observed at the beginning of the GLCs band is characterized by a pressure oscillation between 0 and 100 Pa. The instability starts and stops randomly. By analyzing the pressure spectrum, one observes a wide peak base stretching over approximately 200 Hz. To characterize this limit cycle one uses the time series analysis presented in the previous section. False Nearest Neighbours method reveals an embedding dimension of $d_e = 4$. The optimal time delay τ takes 6 periods of the sampling frequency $\tau \simeq 6/f_s$. In such a case it is standard to examine a three-dimensional phase space. It should be noted that the embedding dimension, determined for the other GLCs appearing between $L_1 = 0.22$ m and 0.25 m, is also $d_e = 4$. One can see in Fig. 9.13 that the phase space reconstruction fills a region of the embedding space without any regular structure. The oscillation travels randomly in a three-dimensional volume indicating that its is chaotic in nature. The same behavior is observed for the whole range of lengths L_1 where GLCs prevail.

Galloping limit cycles are now explored for the longer flame tube $L_2 = 0.30$ m. Figure 9.14 displays the pressure signal of microphone M_2 for $L_1 = 0.28$ m. In this case, the time trace shows almost periodic patterns with growth and

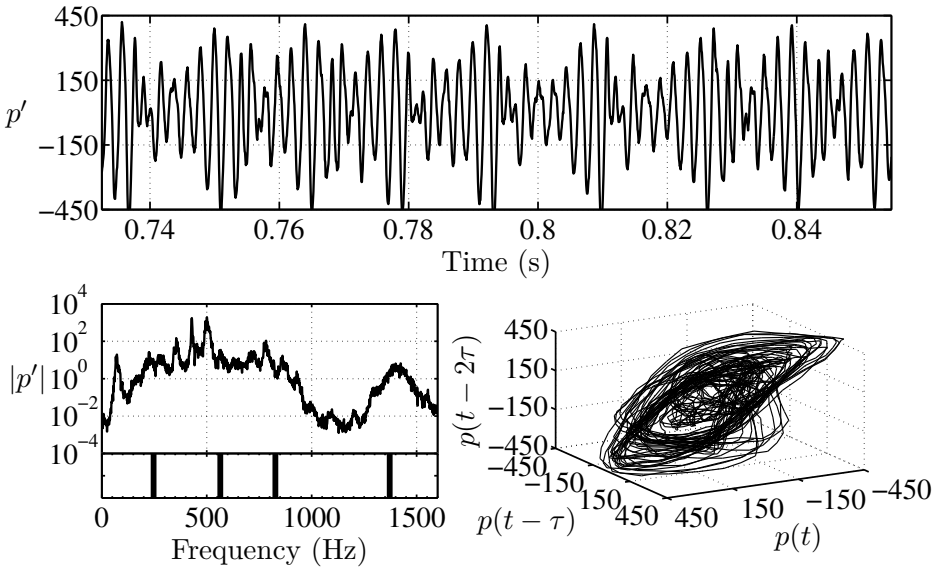

Figure 9.14: *Pressure evolution of microphone* M_2 *(top) for* $L_2 = 0.30$ *m and* $L_1 = 0.28$ *m. The corresponding spectrum is displayed below on the left and the phase plane is shown on the right. The acoustic eigenmodes calculated without the flame but with 300 K in the feeding manifold and 1300 K in the flame tube are drawn below the pressure spectrum.*

decay of the oscillation amplitude. Nevertheless, this regularity is not well defined as shown in the spectrum which now features a wide peak. There is also a broader base indicating that the different oscillation frequencies are being swept around the modal frequency as the amplitude is continuously changing. Regarding the phase space reconstruction, the embedding dimension is estimated to be $d_e = 5$. The time lag represents about 8 periods of the sampling frequency $\tau \simeq 8/f_s$. However, a three dimensional representation is adopted to view the trajectories. The reconstruction is not limited to a single plane and occupies a flattened volume in the embedding space. The structure tends to be more regular, but remains distinct from the closed trajectories observed for stable amplitude limit cycles (see Fig. 9.12). Based on these elements, one may consider that this oscillator also belongs to the chaotic category. Phase space reconstructions, and the pressure spectral densities, provide similar indications for the other feeding manifold lengths. It is found that the embedding dimension remains equal to 5 and the phase space reconstructions in three dimensions show flattened volume patterns typical of chaotic dynamics from $L_1 = 0.23$ m to 0.32 m.

Finally, it is interesting to investigate the recorded oscillation in a time-frequency representation for the limit cycle cases presented herein. This is carried out by using the continuous wavelet transform with a complex Morlet mother wavelet (Mallat (1998)). Wavelet scalograms are processed to determine the

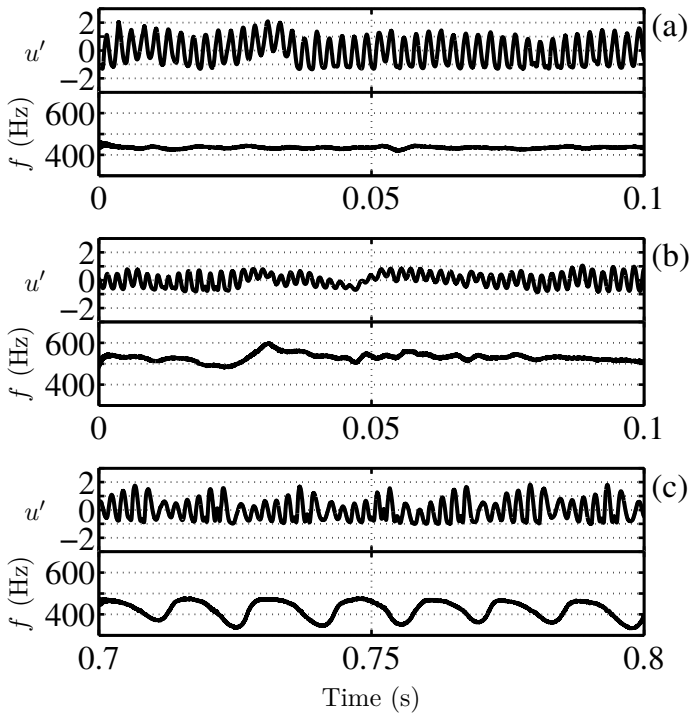

Figure 9.15: *Velocity time trace with the $L_2 = 0.20$ m and 0.30 m flame tubes. Each signal has been analyzed by continuous wavelet transform to obtain the scalogram of the frequencies. This scalogram is processed to draw the evolution of the peak frequency at each instant. This frequency is represented below each velocity time trace. (a) and (b) are respectively linked to $L_1 = 0.16$ m and 0.21 m with the $L_2 = 0.20$ m flame tube. The $L_1 = 0.28$ m case with $L_2 = 0.30$ m flame tube is shown in (c).*

evolution of the main oscillation frequency of the velocity signal as a function of time. Figure 9.15 displays this frequency on the bottom graph which evolves in a synchronized fashion with the velocity time trace represented on the top. Figures 9.15(a), (b) respectively correspond to $L_1 = 0.16$ m and 0.21 m for the $L_2 = 0.20$ m confinement tube. Figure 9.15(c) corresponds to $L_1 = 0.28$ m and $L_2 = 0.30$ m. For a stable limit cycle oscillation when $L_2 = 0.20$ m and $L_1 = 0.16$ m (Fig. 9.15(a)), the frequency is nearly constant as expected from the previous analysis of the spectral content. For the GLC at $L_1 = 0.21$ m with the $L_2 = 0.20$ m flame tube, the frequency evolves with amplitude. One can see in Fig. 9.15(b) that high oscillation frequencies always match with low oscillation amplitudes. Conversely, a low oscillation frequency characterizes the highest velocity fluctuation levels. In the last case corresponding to $L_1 = 0.28$ m and $L_2 = 0.30$ m presented in Fig. 9.15(c), the frequency also evolves with amplitude. In this case, it is interesting to note that a low frequency around 350 Hz follows the signal amplitude climax.

In summary the examination of pressure and velocity time traces, indicates that some of the limit cycles feature nearly constant amplitudes while others (designated as galloping limit cycles) are characterized by a variable amplitude which evolves in an irregular fashion. While stable amplitude limit cycles are well defined and easy to typify, the interpretation of galloping limit cycles requires a more elaborate analysis to characterize their dynamical behavior. It is in particular instructive to exploit *nonlinear time series analysis* tools (Small (2005)). In addition the wavelet transform can be used to track the peak frequency evolution as a function of time. Using these various tools, it has been shown that the GLCs identified in this study can be qualified as chaotic due to the randomness of their oscillations.

9.2.6 Instability predictions

Instability predictions are obtained with the same dynamical model (model B) used in Sec. 9.1.

Results are examined for the first acoustic eigenmode corresponding to the oscillations characterized experimentally. Calculations indicate that in this range of feeding manifold length L_1, positive growth rates exist only for the first mode and this is true for both confinement tube lengths L_2. Results for the growth rate ω_i, displayed in Fig. 9.16, are first examined. This figure shows positive growth rate values in the range of lengths L_1 investigated for the two flame tubes $L_2 = 0.20$ m and 0.30 m explored. It is assumed here that the limit cycle is reached when the growth rate vanishes $\omega_i = 0$. Figure 9.16(a) represents calculations for the $L_2 = 0.20$ m flame tube and Fig. 9.16(b) shows results for the second flame tube $L_2 = 0.30$ m. Measurements are depicted with the convention used in Fig. 9.11. Open circle symbols ($\circ$) indicate the oscillation amplitude of stable limit cycles. For GLCs, the main frequency of the pressure spectrum is considered and one filters the modulated signal with a Butterworth bandpass filter and extracts the amplitude which is represented by dark circle symbols ($\bullet$).

One first notes that the growth rates ω_i reach large values and that ω_i is only slightly lower than $\omega_r = 2\pi f$ presented in Fig. 9.11. The fact that these two quantities are close indicates that the mode is quite unstable and that one can expect to find a rapid growth to a large amplitude. It would then be difficult to measure such growth rates because the system almost immediately reaches a limit cycle. This underlines the necessity of a nonlinear analysis of the system dynamics as is carried out in the present article. The transitional states calculated by the FDF method may only be approximate, but the limit cycles are reached at the predicted amplitudes when the oscillation level remains quasi-constant. Thus, the final amplitude is suitably obtained from the FDF analysis and the open circle symbols ($\circ$) follow growth rate contours at $\omega_i = 0\ \mathrm{s}^{-1}$. For the GLC cases, one observes however that the amplitude does not reach the expected value. For the $L_2 = 0.20$ m flame tube, the amplitudes

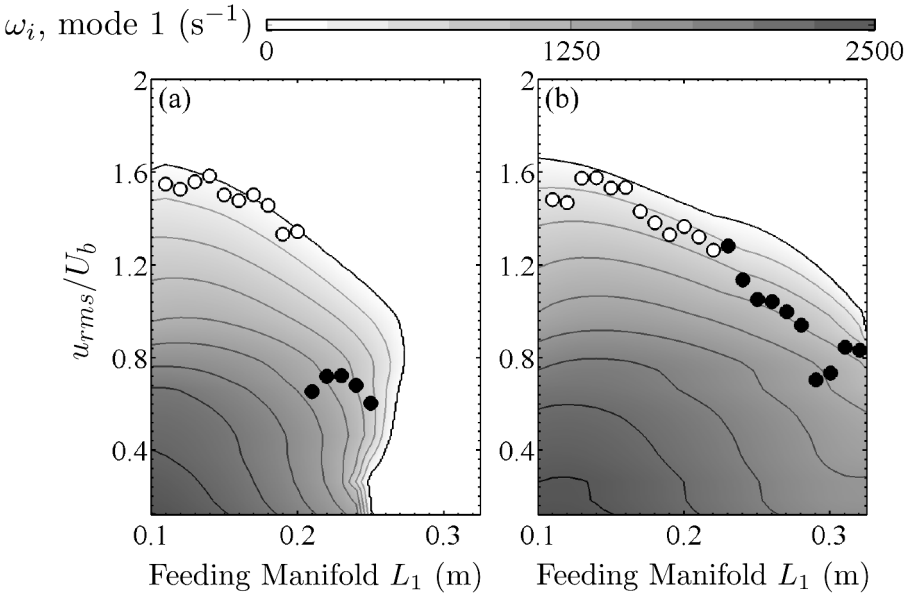

Figure 9.16: *Growth rate evolution for the two flame tubes (a) L_2 = 0.20 m and (b) L_2 = 0.30 m. Experiments are depicted by means of symbols. Open circle symbols (○) indicate stable limit cycles. Filled circle symbols (●) represent the peak amplitude of galloping limit cycles.*

of the GLCs reach values close $u_{rms}/U_b = 0.8$ while predictions yield higher values. The situation is roughly the same for the longer flame tube $L_2 = 0.30$ m, where the predicted value for the amplitude coincides with the observed oscillation level for stable limit cycles but is overestimated when the system operates in the GLC range.

In addition to the growth rate, it is possible to read the associated angular frequency $\omega_r = 2\pi f$ calculated at $\omega_i = 0$ and deduce the limit cycle frequency. This is represented in Fig. 9.17 which compares measurements, drawn as open circle symbols (○) for stable limit cycles and dark circle symbols (●) for GLCs. Calculations are represented with dark bold lines. Figure 9.17(a) presents this comparison for the flame tube $L_2 = 0.20$ m. Results for $L_2 = 0.30$ m are depicted in Fig. 9.17(b). One can see, first of all, that constant amplitude limit cycle frequencies are perfectly predicted. In addition, the frequency shift experimentally observed which reaches about 120 Hz, is also well retrieved.

However, the observed GLC frequencies feature large differences with the eigenmodes of the combustor and the predictions obtained with the FDF in Fig. 9.17(a). The observed frequency lies around 520 Hz for the feeding manifold lengths L_1 which produce GLCs. Since the measured oscillation amplitude is not obtained in the predictions, it is also natural to find a different frequency. However, by analyzing the calculated frequencies for lower oscillation levels, it is possible to show that the observed frequency suitably matches calculations

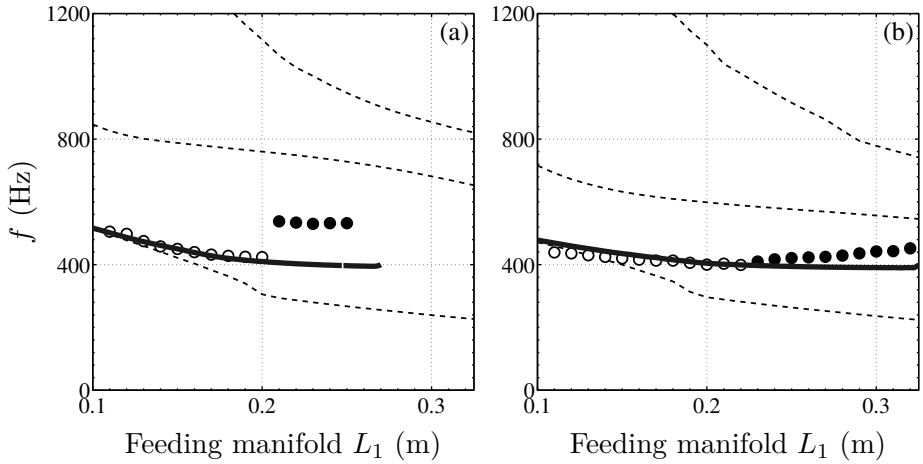

Figure 9.17: *Frequencies predicted for the two flame tubes investigated (a) L_2 = 0.20 m and (b) L_2 = 0.30 m. Experiments are depicted by means of symbols. Open circle symbols (○) indicate stable limit cycle amplitudes. Filled circle symbols (●) represent galloping limit cycle amplitudes. Predicted frequencies are displayed by means of dark bold lines, while acoustic eigenmodes calculated without the flame but different temperatures in each cavity are indicated through dashed lines.*

when the amplitude level is fixed to the correct value. For the second flame tube $L_2 = 0.30$ m, the oscillation amplitude reaches higher levels. Thus, predicted and experimental frequencies are expected to be closer than before as frequency found for $\omega_i = 0$ in Fig. 9.16 almost corresponds to the amplitude of the GLC. This is the case as one can see in Fig. 9.17(b). Dark circle symbols almost coincide with predictions in this case. The range where chaotic states are manifested is considered in the next section by analyzing calculations obtained with the FDF.

9.2.7 Chaotic states and FDF calculations

The continuation methodology employed to solve the nonlinear dispersion relation can be used to track the roots of this equation as a function of amplitude u_{rms}/U_b and for each length of feeding manifold L_1. This reveals some distinct features of the roots giving rise to oscillations around the first mode in the form of a GLC.

For unstable operating conditions characterized by positive growth rates $\omega_i > 0$, the solution of the dispersion relation normally features one or sometimes two modes with positive growth rates for each feeding manifold length L_1 and small disturbance amplitude levels u_{rms}/U_b. By solving the dispersion relation for increasing amplitudes, the solutions generally feature an imaginary component ω_i dropping to zero and defining the limit cycle. There are however cases where multiple solutions arise with nearly equal angular frequencies ω_r. It

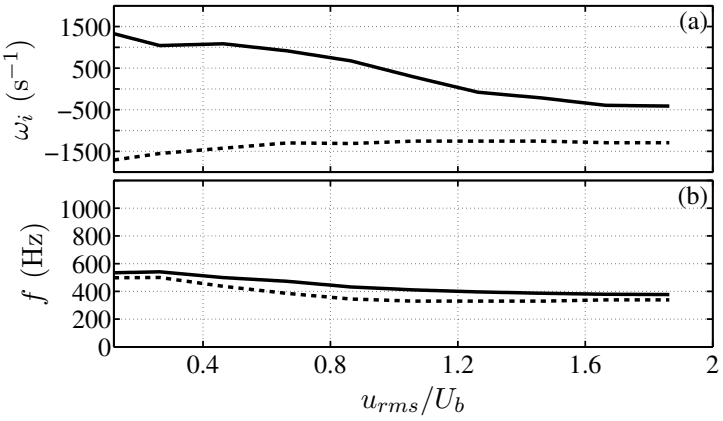

Figure 9.18: *Growth rate and frequency evolutions for the two solutions of the first mode calculated at $L_1 = 0.23$ m with $L_2 = 0.20$ m. (a) represents the growth rates ω_i. (b) corresponds to the frequencies. Dashed lines are linked to the negative growth rate solution whereas the bold line corresponds to the positive one.*

is then more difficult to track the roots in the complex plane as a function of amplitude. Multiple solutions may feature positive and negative ranges of growth rates ω_i. These multiple solutions are now examined and it is shown that they are present when one observes a chaotic limit cycle.

The evolution of the instability frequency and growth rate are examined here as a function of amplitude. Multiple solutions with positive and negative growth rates can be ignored when their oscillation frequencies differ. When the oscillation frequency ω_r of two solutions coincide or nearly coincide, one has to consider that the oscillation can grow ($\omega_i > 0$) or decay ($\omega_i < 0$).

Calculations reveal two types of such solutions. The first type is characterized by roots featuring a negative and a positive growth rate evolving at nearly the same frequency for all perturbation amplitudes. In the second type considered, the roots feature a positive and a negative growth rate with coinciding frequencies in a finite range of amplitudes. These two types of solutions are depicted in Figs. 9.18 and 9.19.

The overlap of the oscillation frequency in an amplitude interval for the two solutions corresponding to mode one is presented in Fig. 9.18 for a case where $L_2 = 0.20$ m and $L_1 = 0.23$ m. Analysis of the growth rates plotted in Fig. 9.18(a) shows that even if the negative contribution is of the same order as the positive one at low amplitude, it becomes more important when the perturbation level increases. This indicates a higher damping rate than a growth rate along the trajectory for $u_{rms}/U_b > 1$. The frequency evolution plotted in Fig. 9.18(b) shows that the overlap is quasi-perfect for oscillation amplitudes lower than $u_{rms}/U_b = 0.35$. The largest difference between the two frequency trajectories reaches 87 Hz. This type of multiple solutions with frequency match occurs for operating conditions between $L_1 = 0.22$ m to 0.27 m which includes the stable

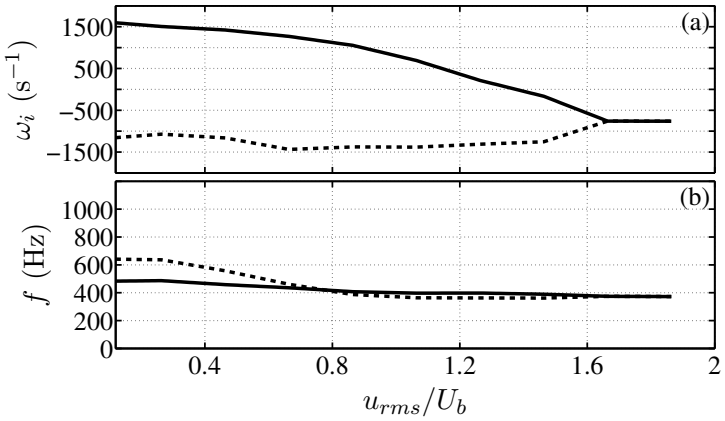

Figure 9.19: *Growth rate and frequency evolutions for the two solutions of the first mode calculated at $L_1 = 0.25$ m with $L_2 = 0.30$ m. (a) represents the growth rates ω_i. (b) Corresponds to the frequencies. Dashed lines are linked to the negative growth rate solution whereas the bold line corresponds to the positive one.*

band. In addition, it is also instructive to note that the dual solution band includes the chaotic limit cycles which occur between $L_1 = 0.21$ m and 0.25 m. Considering the overlap in oscillation frequency for the whole amplitude range, one expects that velocity disturbances will grow from $u_{rms}/U_b = 0$ to the limit cycle. However perturbations do not reach a constant amplitude limit cycle, because there is another modal solution at the same frequency which features a negative growth rate. A possible scenario is that of an energy transfer taking place between the modes, the growth rate becoming negative and the amplitude of the limit cycle dropping down.

For the second flame tube $L_2 = 0.30$ m, the predicted dual solution frequencies only overlap over a certain range of amplitudes as shown in Fig. 9.19. One first notes that the calculated overlap of frequency trajectories with dual solutions occurs between $L_1 = 0.17$ m and 0.31 m, while chaotic oscillations are found between $L_1 = 0.23$ m and 0.32 m. The solution amplitude corresponding to positive growth rate first increases to reach a limit cycle at $\omega_i = 0$, but a second solution with a matching frequency co-exists beyond $u_{rms}/U_b = 0.8$ (see Fig. 9.19) with a negative growth rate. In this case, the frequency difference between the two trajectories does not exceed 35 Hz. The scenario is that the oscillation amplitude of the unstable mode remains bounded in a finite interval with a lower bound defined by the perturbation amplitude where the two modal frequencies match. This scenario can be further analyzed by comparing the minimum and maximum oscillation levels reached in the experiments and calculations for all the GLCs of the two confinement tubes.

This is synthesized in Fig. 9.20 where growth rates have been plotted for the two flame tubes as in Fig. 9.16. One should note that only GLCs are considered in Fig. 9.20. Experiments are depicted by means of symbols. Black

circle symbols (•) pertain to the maximum amplitude reached while minimum amplitudes appear as open circle symbols (◦). These amplitudes have been determined by calculating the rms values of each velocity time trace at the minimum and maximum reached during the modulation. Calculated values from the model are plotted as bold and dashed lines. The minimum amplitude where frequency trajectories overlap pertain to the dark dashed lines. The expected limit cycle where $\omega_i = 0$ is shown by the dark bold line. By examining the amplitudes reached, one can see that predictions and experimental data roughly match. For the $L_2 = 0.20$ m flame tube, the frequency trajectories nearly overlap for all oscillation amplitudes and one expects that u_{rms}/U_b will drop to about 0 because the negative damping rate is always higher than the positive growth rate. This phenomenon is well retrieved experimentally where the minimum oscillation amplitude vanishes. The same phenomenon highlighted for $L_2 = 0.20$ m is observed for $L_2 = 0.30$ m except that the minimum oscillation level now differs from 0. This minimum is well retrieved by considering the parameter values where the frequency trajectories, associated to negative and positive growth rates, overlap in a certain range of amplitudes. The scenarios described previously may not give the full picture because at very high perturbation levels which prevail in these experiments, the flame evolves significantly giving rise to rapid departures in its response which might not be well accounted for in the FDF framework. It should be kept in mind that the FDF description assumes that the flame is perturbed around a mean state defined by the steady flow and that this may not quite reflect what is observed experimentally.

9.2.8 Conclusion

The present study is focused on the prediction of unstable combustion regimes in a generic configuration, comprising a variable size upstream manifold, a multipoint injector and a flame tube confining the combustion region. The stability of this system is analyzed for two confinement tube lengths L_2 by varying the feeding manifold length L_1 over a broad range of values. Experiments reveal two classes of limit cycles. In the first group, oscillations occur at an essentially constant amplitude, while in the second, oscillation amplitudes vary in an irregular fashion and the pressure and velocity signal envelopes are modulated accordingly. The last type of amplitude modulated limit cycles correspond to an irregular occurrence of starts and stops in the oscillation. These “galloping” or chaotic limit cycles (GLCs) occur in the present experiments when the system resonates in the vicinity of its first mode for small sizes L_1 of the feeding manifold cavity. On the theoretical level, calculations are carried out within the flame describing function (FDF) framework. It is found that the constant amplitude limit cycles are well retrieved and that the calculated amplitudes and frequencies agree well with measurements, thus confirming previous applications of the FDF framework. The interpretation of the GLCs is less easy but

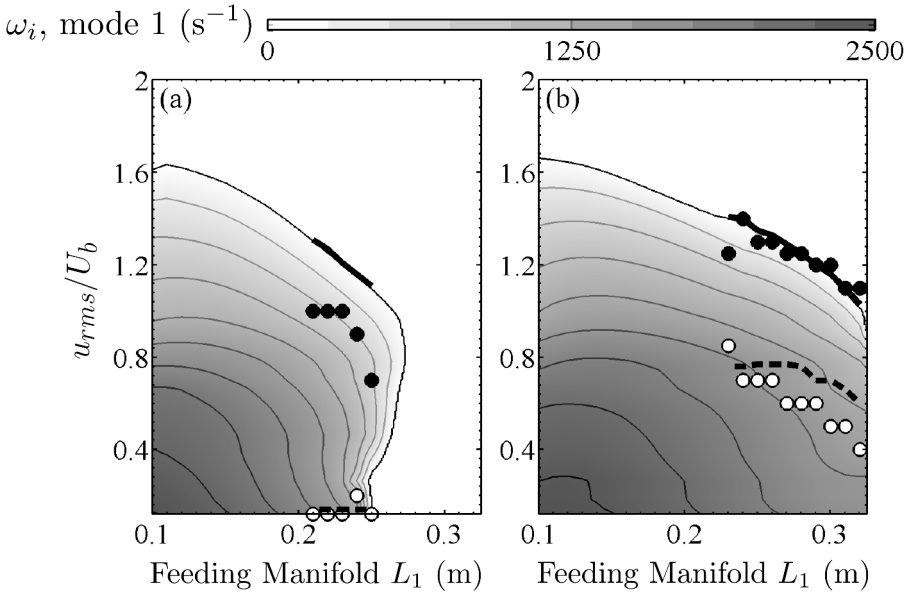

Figure 9.20: *Growth rate evolution for the two flame tubes (a) L_2 = 0.20 m and (b) L_2 = 0.30 m. The boundary amplitudes of the experimental galloping limit cycles are represented by means of symbols while the boundary amplitudes where frequency trajectories overlap in calculations pertain to bold and dashed lines. Open circle symbols (○) indicate the minimum amplitude reached in the experiments. Filled circle symbols (●) show the maximum amplitude attained. The overlap of the frequency trajectories, found in calculations, occurs for all or a part of the amplitude range. The predicted minimum amplitude is depicted through a dashed line (- -) while the bold line (—) shows the limit cycle amplitude expected at ω_i = 0 s^{-1}.*

it is found that their range of occurrence corresponds to parameter values for which the nonlinear dispersion relation of the system features roots which are closely matched in angular frequencies but have positive and negative growth rates. By determining the parameter values for which such unstable and stable modes with nearly similar eigenfrequencies simultaneously exist, it is possible to define ranges where one can expect to find GLCs. This can be used to explain the galloping features observed. It is shown that the calculated ranges nearly correspond to those identified experimentally. It is also shown that the FDF can be used to obtain some estimates of the maximum and minimum levels in the signal envelope.

Part IV

Passive control of combustion instabilities and cavity decoupling

Chapter 10

Acoustic damping with bias flow perforates (BFP)

This chapter is concerned with oscillation control by means of a damping system inserted in the multiple flame combustor investigated previously. This system comprises a perforated plate backed by a cavity and traversed by a bias flow (BFP : bias flow perforate). Of the two such devices considered in what follows, one has been designed to operate in the so called low Strouhal regime. BFP systems feature a sufficiently high mean flow velocity in the perforations to avoid reverse motion during unsteady operation. Theoretical aspects are covered first. Design of a BFP for the multiple flame combustor are described in a second stage. A nonlinear analysis based on the FDF framework is carried out to interpret experimental observations. It is shown that damping systems based on BFP can effectively damp oscillations over a wide frequency range and that they can be used to reduce large amplitude pressure perturbations. Cases where the BFP damping system could not reduce oscillations are also documented. In general, this occurs when the system shifts its resonance frequency outside the range where the damper effectively provides a low reflection coefficient. The important question of controller robustness is also analyzed by making use of non optimal set of parameters for the damper.

10.1 Introduction

Perforated liners are often used to control combustion instabilities. Such systems can be found in jet engine and industrial gas turbine combustors (Richards et al. (2003)). In general the perforated liner or plate is traversed by a bias flow and is backed by a cavity.
The acoustic damping is linked to the creation of vortices from the perforations edge as sketched in Fig. 10.1 for a single hole. These vortices are convected

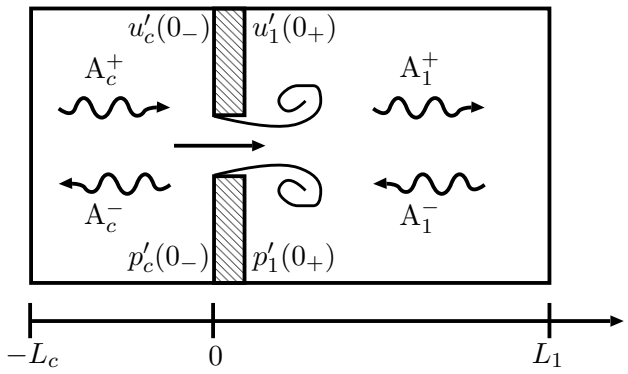

Figure 10.1: *Bias flow orifice backed by a cavity. A vortex is created at the edge of the perforation, while left and right acoustic waves propagate in the main tube and in the back cavity.*

away by the flow and they are eventually dissipated. Energy is transferred from the acoustic wave to the vortices, removing energy from the acoustic wave. This mechanism was theoretically explained by Howe (1979).

BFP systems do not always work as planned (Tran et al. (2009b)). The FDF framework is here used to analyze configurations equipped with a BFP damper. This is used to explain successes and failures in damping of self-sustained oscillations. It is specifically interesting to examine the different situations analyzed in Part III which have been systematically characterized in the absence of a damper and include a BFP. At this point it is important to review previous work concerned with BFP design and practical demonstrations.

Work which is closely linked to the present study is reported by Tran (2009) where it is shown that the nonlinearity in the BFP response induces a loss in damping characteristics. As the acoustic wave amplitude increases, the generation of vortices becomes less effective and damping is reduced when the oscillation reaches large amplitude levels.

Modeling and sizing of BFP systems is considered for a particular regime of operation by Hughes et al. (1990). The analysis based on Howe's theory (Howe (1979)) only considers acoustic plane waves. An optimum absorption is identified at low Helmholtz numbers $\mathrm{He} = kL \ll 1$ and for a resonance parameter $\mathrm{Q} = 1$. This latter quantity is defined as $\mathrm{Q} = (k/k_{\mathrm{He}})^2$ where $k_{\mathrm{He}} = [2r_a/(Ld^2)]^{1/2}$ is the wave number of the back cavity of volume Ld^2. The cavity acts in this regime as a Helmholtz resonator and the resonance parameter indicates that the unsteady flow in the perforation operates at large Strouhal number $\mathrm{St} \gg 1$ as shown by Scarpato et al. (2012). These set of conditions define compact dampers, designated in what follows as "A-dampers", which are characterized by a relatively narrow bandwidth of interest. This requires an accurate knowledge of the frequency to damp and one can immediately see that A-dampers will be difficult to tailor in practice because the frequency of unstable perturbations may feature excursions with respect to its nominal value.

Another interesting regime is considered by Scarpato et al. (2012) where the frequency band of interest is widened by operating at low Strouhal numbers St $\ll 1$ with a quarter wave mode in the back cavity. This allows to design robust low frequency dampers designated in what follows as "B-dampers" which are better suited than A-dampers for thermoacoustic instability suppression. This is specifically so when the oscillation has reached a limit cycle with a frequency shifted with respect to the acoustic eigenmode. It is shown here that the frequency may vary with the oscillation amplitude (Noiray et al. (2008); Boudy et al. (2011a)) and this has the consequence that cancellation provided by A-dampers in a narrow range is not robust.
All these studies indicate two important points concerning the control of thermoacoustic oscillations which are linked to the amplitude :

- The system can loose its damping characteristics under large amplitude levels because the damper orifices have a nonlinear response
- The frequency band of influence has to be widened to avoid a possible initiation of oscillation with a frequency varying with the amplitude in the vicinity of the acoustic eigenfrequency.

The detailed characterization of the multiple flame combustor will be used in what follows to select specific regimes of operation and analyze the instability in the whole range of amplitudes within the FDF framework. Two major topics will be considered in what follows.
The first is concerned with the cancellation of large amplitude limit cycles, up to relative values $u_{rms}/U_b = 1.5$. This is used to investigate the influence of the damper nonlinear response. Self-sustained oscillations of different amplitudes but almost similar frequencies will be considered. This is achieved by changing the confinement tube size L_2. The damper efficiency will be checked in this way for large oscillation levels and this will be interpreted with the FDF framework providing an understanding of experimental data. The present study thus differs from Tran (2009) where the FDF of the swirled burner was not available.
The second topic concerns the frequency bandwidth of the damping device and its ability to handle frequency shifts, with respect to the eigenmode resonances. The damper robustness will be tested by examining the special case of an oscillation sustained by two modes as described in Chapter 9. Modification of the back cavity size L_c is used to examine if a change in the optimal frequency can bring the system into an oscillatory state.
In what follows the BFP damper constitutes the boundary condition of the upstream manifold. Its reflection coefficient is derived from the impedance of the perforated plate which relies on the Rayleigh conductivity deduced from Howe's theory. The BFP is placed in the multiple flame combustor and the piston creates a back cavity. The model derived by Scarpato et al. (2012) is summarized and combined with the description of the multiple flame combustor

in the following sections. This model is then used to obtain predictions for selected geometries. These predictions are finally compared to experimental data.

10.2 Theoretical analysis of bias flow perforates

It is first useful to give a few details on the modeling of BFP. In a first step, the model is presented by closely following Scarpato et al. (2012). One has to recall however that the piston head is not a perfect rigid wall and the reflection coefficient of this head is taken into account in a second stage of modeling.

10.2.1 The ideal case of back cavity terminated by a rigid wall

The configuration is the same as the one sketched in Fig. 10.1 for a single hole. The perforated plate is backed by a cavity terminated by a rigid wall. Assuming harmonic disturbances for pressure p', velocity u' and flow rate q', one can write :

$$p' = \Re\{\widetilde{p}\exp(-i\omega t)\}\ ;\ u' = \Re\{\widetilde{u}\exp(-i\omega t)\}\ ;\ q' = \Re\{\widetilde{q}\exp(-i\omega t)\} \tag{10.1}$$

Using conventions defined in Fig. 10.1, the specific acoustic impedance on the downstream side of the perforated plate is :

$$\zeta_1(0_+) = \frac{\widetilde{p}_1(0_+)}{\rho_0 c_0 \widetilde{u}_1(0_+)} \tag{10.2}$$

The back wall at the longitudinal coordinate $z = -L_c$ is perfectly rigid and one can write the specific acoustic impedance $\zeta_c(0_-)$ on the upstream side of the perforation :

$$\zeta_c(0_-) = \frac{\widetilde{p}_c(0_-)}{\rho_0 c_0 \widetilde{u}_c(0_-)} = \frac{e^{ikL_c} + e^{-ikL_c}}{e^{ikL_c} - e^{-ikL_c}} \tag{10.3}$$

Using the conservation of the acoustic volume flow rate and a momentum balance between upstream and downstream sections one has :

$$\begin{aligned} &\widetilde{q} = \widetilde{u}_c(0_-)d^2 = \widetilde{u}_0 \pi r_a^2 = \widetilde{u}_1(0_+)d^2 \\ &i\rho_0\omega\widetilde{u}_c(0_-) = i\rho_0\omega\widetilde{u}_1(0_+) = \frac{K_R}{d^2}[\widetilde{p}_1(0_+) - \widetilde{p}_c(0_-)] \end{aligned} \tag{10.4}$$

where d designates the square mesh separation of orifices of diameter $d_a = 2r_a$ as illustrated in Fig. 10.2 and K_R is the Rayleigh conductivity of an aperture. This quantity links the pressure fluctuation difference between the two sides of the plate and the unsteady acoustic volume flow rate across the hole (Morse et al. (1986)).

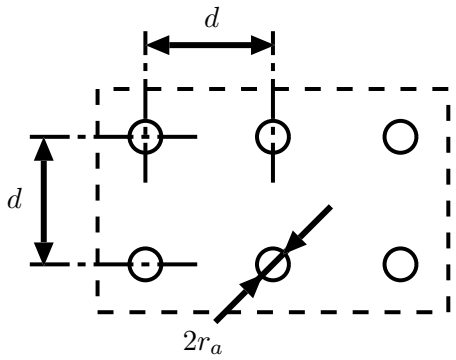

Figure 10.2: *Geometrical definitions of the perforated plate. The holes of diameter $d_a = 2r_a$ are equally spaced in a square pattern with a mesh size d.*

Combining Eqs. (10.3) and (10.4) one obtains the specific acoustic impedance on the downstream side :

$$\zeta_1(0_+) = \frac{\widetilde{p}_1(0_+)}{\rho_0 c_0 \widetilde{u}_1(0_+)} = i\left(\frac{kd^2}{K_R} - \frac{1}{\tan(\mathrm{He})}\right) \tag{10.5}$$

The response of the perforate submitted to an incident acoustic wave requires the determination of the Rayleigh conductivity. This can be obtained from Howe (1979), where an analytical expression is derived for a circular aperture with an initially irrotational jet emerging :

$$K_R = 2r_a(\gamma - i\delta) \tag{10.6}$$

where γ and δ take the following form[1] :

$$\gamma - i\delta = 1 + \frac{(\pi/2)\, I_1(\mathrm{St})\, \exp(-\mathrm{St}) - iK_1(\mathrm{St})\, \sinh(\mathrm{St})}{\mathrm{St}\left[(\pi/2)\, I_1(\mathrm{St})\, \exp(-\mathrm{St}) + iK_1(\mathrm{St})\, \cosh(\mathrm{St})\right]} \tag{10.7}$$

In the previous expression I_1 and K_1 are modified Bessel functions of the first and second kinds. The Strouhal number St is defined as $\mathrm{St} = \omega r_a / u_{cv}$ where r_a designates the perforation radius and u_{cv} is the vortex convection velocity taken equal to one half of the jet velocity in the contraction section of the vortex.
If the system operates in the low Strouhal number range ($\mathrm{St} \ll 1$), it is possible to reduce Eq. (10.7) and obtain a simpler expression for the Rayleigh conductivity :

$$K_R \simeq 2r_a\left(\frac{1}{3}\mathrm{St}^2 - i\frac{\pi}{4}\mathrm{St}\right) \tag{10.8}$$

[1]It should be noted that the Rayleigh conductivity defined in Hughes et al. (1990) takes a different form. However by factorizing the equation given in Hughes et al. (1990), one retrieves the simple formula of Eq. (10.7) used by Scarpato et al. (2012).

Using this relation one finds an analytical expression for $\zeta_1(0)$ which yields the reflection coefficient on the downstream side of the perforated plate :

$$\mathrm{R}_1(0) = \frac{\zeta_1(0)+1}{\zeta_1(0)-1} \tag{10.9}$$

Maximum damping is obtained when the reflection coefficient is led to vanish. This can be attained by searching the zeros of Eq. (10.9), which corresponds to solving $\zeta_1(0)+1=0$. Combining Eqs. (10.5) and (10.8), and limiting the analysis to second order, one has to solve :

$$\frac{\mathrm{M_c}}{\sigma_d}\frac{8}{3\pi}\mathrm{St} - \frac{1}{\tan(\mathrm{He})} + i\left(2\frac{\mathrm{M_c}}{\sigma_d}-1\right) = 0 \tag{10.10}$$

where $\mathrm{M_c} = u_{cv}/c$ designates the Mach number based on the convective velocity of the vortices. In this case, the convection velocity u_{cv} is taken equal to the bulk velocity $u_{cv} = U_b$ in each perforation. As one can see, the low Strouhal approximation yields a simple relation which defines a vanishing reflection coefficient. This corresponds to :

$$\mathrm{M_c} = \frac{\sigma_d}{2} \tag{10.11}$$

$$\frac{1}{\tan(\mathrm{He})} = \frac{4}{3\pi}\mathrm{St} \tag{10.12}$$

The reflection coefficient on the upstream side of the combustor vanishes when two conditions are fulfilled. The first regards the porosity of the perforated plate as shown in Eq. (10.11), the second is linked to the size of the back cavity L_c found from Eq. (10.12). The system operating in the low Strouhal number range $\mathrm{St} \ll 1$, induces a small value on the right hand side of Eq. (10.12), yielding :

$$\frac{1}{\tan(\mathrm{He})} \simeq 0 \tag{10.13}$$

One obtains a solution for $\mathrm{He} = (\omega L_c)/c = \pi/2$ corresponding to a certain length L_c of the back cavity :

$$L_c = \frac{c}{4f} \tag{10.14}$$

On the basis of this low Strouhal number analysis and on Howe's modeling of the Rayleigh conductivity, Scarpato et al. (2012) designed dampers which feature two positive characteristics :

- The cancellation frequency band is widened,
- The frequency to damp is only determined by selecting the size of the back cavity as defined in Eq. (10.14)

10.2.2 Model including the reflection coefficient of the piston head

The piston head is typified by a reflection coefficient $\mathrm{R}_c(-L_c)$ which can be written as follow :

$$\mathrm{R}_c(-L_c) = \frac{A_c^+ e^{-ikL_c}}{A_c^- e^{ikL_c}} \tag{10.15}$$

It is then possible to modify Eq. (10.3), and obtain :

$$\frac{\widetilde{p}_c(0_-)}{\rho_0 c_0 \widetilde{u}_c(0_-)} = \frac{\mathrm{R}_c(-L_c)e^{ikL_c} + e^{-ikL_c}}{\mathrm{R}_c(-L_c)e^{ikL_c} - e^{-ikL_c}} \tag{10.16}$$

The specific acoustic impedance is deduced from Eq. (10.4) in combination with the acoustic volume flow rate and the momentum balance :

$$\zeta_1(0) = \frac{\widetilde{p}_1(0_+)}{\rho_0 c_0 \widetilde{u}_1(0_+)} = i\frac{kd^2}{K_R} + \frac{\mathrm{R}_c(-L_c)e^{ikL_c} + e^{-ikL_c}}{\mathrm{R}_c(-L_c)e^{ikL_c} - e^{-ikL_c}} \tag{10.17}$$

It is found that the second term in the right hand side changes when one represents the piston behavior. For a perfectly reflecting boundary with $\mathrm{R}_c(-L_c) = 1$, one retrieves the expression $1/\tan(\mathrm{He})$ given in Eq. (10.5).
Using the low Strouhal approximation for the Rayleigh conductivity K_R, it is possible to write a new equation which yields a vanishing value of the reflection coefficient, i.e. $\zeta_1(0) + 1 = 0$. Limiting the analysis to second order, one finds :

$$\frac{\mathrm{M_c}}{\sigma_d}\frac{8}{3\pi}\mathrm{St} - i\frac{\mathrm{R}_c(-L_c)e^{ikL_c} + e^{-ikL_c}}{\mathrm{R}_c(-L_c)e^{ikL_c} - e^{-ikL_c}} + i\left(2\frac{\mathrm{M_c}}{\sigma_d} - 1\right) = 0 \tag{10.18}$$

This equation is very close to that introduced previously (Eq. (10.10)). The influence of the reflection coefficient of the piston head $\mathrm{R}_c(-L_c)$ only affects one term. This will be examined later on. It is first useful to measure the damper response and see if it agrees with the theoretical prediction.

10.3 Damping system design

10.3.1 Methodology

The model presented in the previous section is now used to design a damper comprising a perforated plate backed by a cavity. One considers the configuration of the multiple flame combustor illustrated in Fig. 10.3. The burner sketched on the left of this figure corresponds to the configuration investigated in previous chapters. For a certain feeding manifold length L_1 where an oscillation occurs at a fixed amplitude and frequency, one is able to determine the back cavity length L_c to suppress the oscillation. In this case, the perforated plate is set up at the position of the piston head and the back cavity size L_c

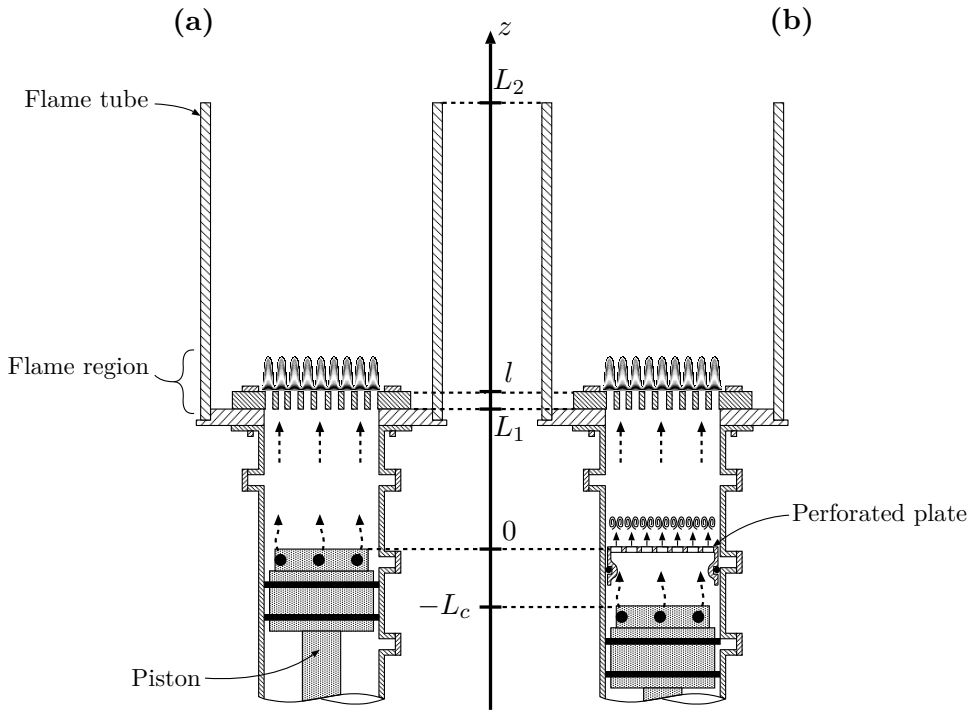

Figure 10.3: *Experimental setup equipped with the damper comprising a bias flow perforated plate backed by a cavity. (a) The left figure shows the burner used to characterize and predict self-sustained combustion oscillations. (b) The burner equipped with the perforated plate is sketched on the right. The piston has a dual use. It injects the methane-air mixture and defines the cavity back wall.*

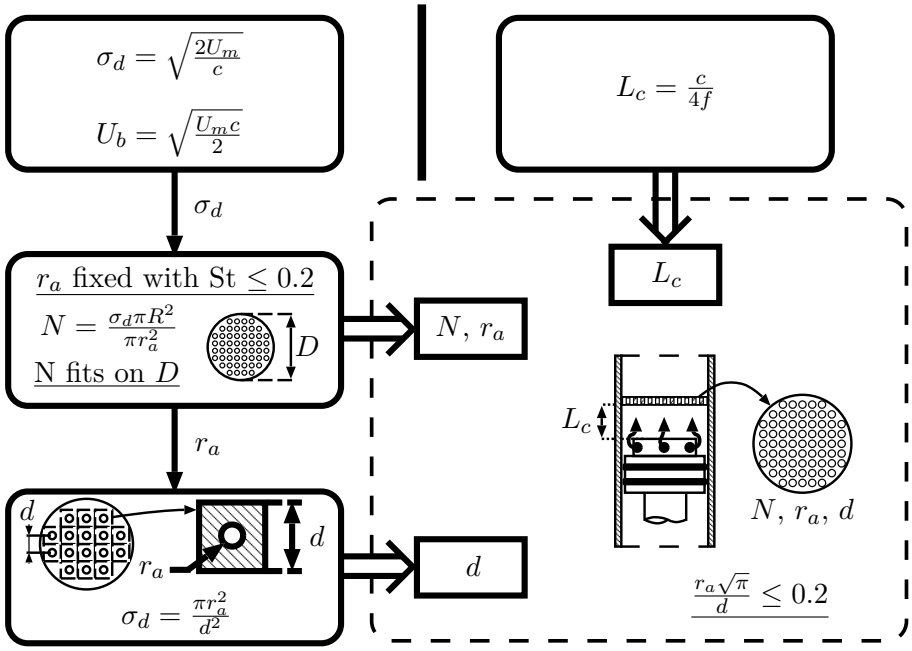

Figure 10.4: *Algorithm for the determination of the damper characteristics. Dimensions of the perforated plate are determined independently of the size of the back cavity. This design implies that three conditions are satisfied :* St $\leq$ *0.2, the number N of holes is compatible with the size D and* $r_a\sqrt{\pi} \leq 0.2d$*. These conditions are underlined in the graph.*

is adjusted by displacing the piston as shown in Fig. 10.3(b). To design the damper, one has to define the porosity σ_d, the number of holes N of the perforated plate and independently, the back cavity size L_c. As shown in Sec. 10.2 with Eq. (10.14), the size of the back cavity solely depends on the frequency of oscillation. Figure 10.4 summarizes the methodology used to determine the dimensions for the perforated plate and the back cavity. In the present case, all the flow traverses the perforated plate. Thus, in a first step, one has to link the mean velocity in the feeding manifold U_m and the bulk velocity U_b in the damper perforations. These two velocities are coupled by the porosity of the perforated plate :

$$U_m = \sigma_d U_b \tag{10.19}$$

where $\sigma_d = (N\pi r_a^2)/(\pi D^2/4)$ corresponds to the porosity. However, as the reflection coefficient is cancelled for $\mathrm{M_c} = U_b/c = \sigma_d/2$, one has to take into account the following relation :

$$U_b = \frac{\sigma_d c}{2} \tag{10.20}$$

Combining Eqs. (10.19) and (10.20), one obtains an expression for σ_d and U_b depending on the mean flow velocity U_m :

$$\sigma_d = \sqrt{\frac{2U_m}{c}}$$
$$U_b = \sqrt{\frac{U_m\, c}{2}} \tag{10.21}$$

In a second step, the porosity σ_d is used to calculate the number of holes. In this case, two conditions underlined in Fig. 10.4 must be fulfilled. The first regards the holes diameter. It is arbitrarily fixed, keeping in mind that the Strouhal number St has to be small (St $\ll 1$). It is safe to stay below a value of 0.2. The second condition is linked to technological possibilities. One determines a number of holes N which has to be drilled inside the limited diameter D of the perforated plate. In the present case, this dimension is that of the upstream manifold $D = 0.07$ m. As the square mesh for the holes position is not known at this stage, one has to see whether the number of holes is too large or not.
Finally, the last step concerns the calculation of the distance between the perforations d. The holes are located on a regular square mesh as illustrated in Fig. 10.4. Holes of diameter d_a are located on a square of side d. This pattern defines for the porosity $\sigma_d = \pi d_a^2/(4d^2)$, providing the distance d between the holes. One is therefore able to see if the number of holes N fits in a circle of diameter D. In addition, a last criteria has to be verified to assure that no interactions take place between holes and that vortex shedding occurs independently. According to Melling (1973), interaction are weak if $r_a\sqrt{\pi}/d \leq 0.2$.
Having defined the perforated plate dimensions, one may determine the back cavity length L_c and the damper can be manufactured and tested.

10.3.2 Damping system for the multiple flame combustor

The damper is defined as explained in the previous subsection. Experiments are carried out with a mean flow velocity $U_m = 1.05$ m.s^{-1}. This yields a porosity $\sigma_d = 0.0782$ and a bulk velocity $U_b = 13.4$ m.s^{-1} in the perforations. The diameter d_a is set to 1 mm. This gives a Strouhal number St $= 0.12$ for a frequency of 500 Hz. This value is typical of the instability frequencies observed in the experiments. Using the porosity σ_d, one finds the number of holes $N = 383$ and the spacing $d = 3.2$ mm between the holes. The interaction index $r_a\sqrt{\pi}/d = 0.28$ slightly exceeds 0.2 which is acceptable. One finds however that the number of holes N cannot fit in the limited diameter $D = 0.07$ m. An iterative process is used to obtain the final values gathered in Tab. 10.1.
The main change concerns the number of holes. It is decreased to 357 leading to a slight increase in bulk velocity U_b which becomes 14.4 m.s^{-1}. The Strouhal number is now 0.11 at 500 Hz. This ensures that the system operates in the

Table 10.1: *Damper geometrical parameters and corresponding Strouhal and spacing numbers. Nominal design and practical application.*

	N	r_a (mm)	d (mm)	St	$\frac{r_a\sqrt{\pi}}{d}$
Nominal Design	*383*	*0.5*	*3.2*	*0.12*	*0.28*
Application	*357*	*0.5*	*3*	*0.11*	*0.3*

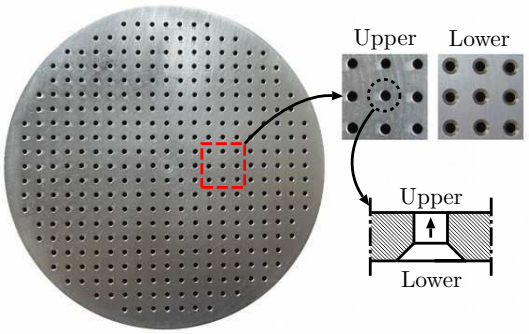

Figure 10.5: *Image of the machined perforated plate. Details on the right reveal the hole characteristics. The lower side of the perforations has been countersunk, a characteristic which was not initially planned. Experiments indicate that this does not modify the plate reflection response. The flow direction is indicated with an arrow.*

low Strouhal number range with a higher bulk velocity U_b. The higher velocity also allows a better handling of large amplitude oscillations retarding reverse flow in the damper channels (Scarpato et al. (2011)). On the other hand, the interaction coefficient $r_a\sqrt{\pi}/d$ rises to 0.3 which is not far from 0.2.
The damper geometry is shown in Fig. 10.5. As indicated in the right hand side of the figure, the perforations are countersunk on the lower side, a characteristic which was not planned at the beginning, because sharp edges are better suited to generate vortices. While this was not initially planned it was decided to keep this geometry and examine the influence of these chamfers on the reflection response of the damper.

10.3.3 Measurement of the reflection coefficient

The damper reflection response is now characterized experimentally in the impedance tube represented schematically in Fig. 10.6. Its response is determined with the method described in Sec. 4.2.1.
Pressure is recorded by three microphones M_1 to M_3. The back cavity is defined by the piston position with respect to the perforated plate. The transfer function H_{12} between microphones M_1 and M_2 is measured to estimate the specific acoustic impedance $\zeta_1(0)$ and subsequently the reflection coefficient $R_1(0)$. The loudspeaker subjects the perforated plate to harmonic fluctuations between 50 and 1100 Hz by steps of 50 Hz. A B-type damper is tested in this section. It is designated as “B-SH” for Small Holes. This system was designed

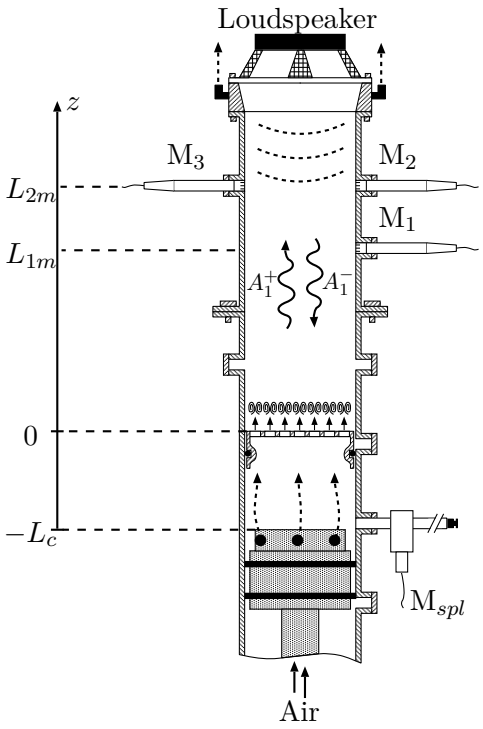

Figure 10.6: *Impedance tube used to measure the reflection coefficient of the BFP. An air flow rate equivalent to the methane-air mixture is used in these experiments.*

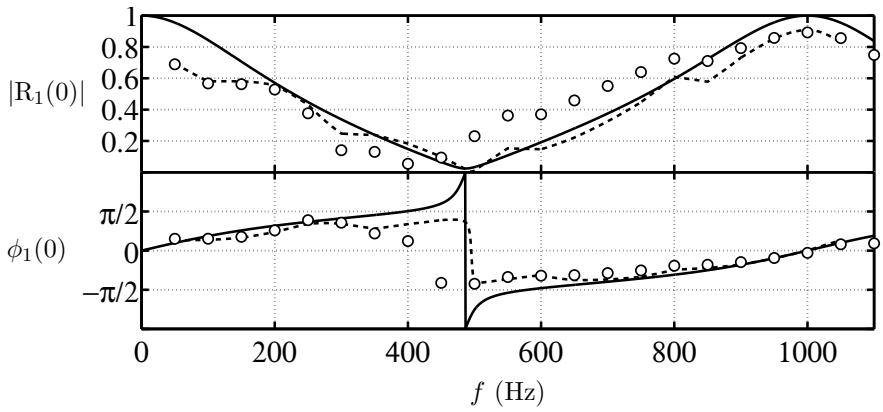

Figure 10.7: *Reflection coefficient of the damper B-SH. The back cavity is terminated by the piston. Measurements are displayed as open symbols (○). Two models are used to retrieve the reflection coefficient of the damper. Predictions from the first model plotted as a continuous line (—) correspond to the low Strouhal regime of Scarpato et al. (2012). Predictions from the second model appear as a dashed line (- -). It uses the low Strouhal approximation but accounts for the reflection coefficient of the piston.*

to cancel combustion oscillations around 500 Hz and the back cavity size is set to $L_c = c_1/(4f) = 0.173$ m.

The modulus $|\mathrm{R}_1(0)|$ and phase $\phi_1(0)$ of the reflection coefficient $\mathrm{R}_1(0) = |\mathrm{R}_1(0)| \exp(\mathrm{i}\phi_1(0))$, calculated using Eqs. (10.5), (10.8) and (10.9), are plotted in Fig. 10.7 as a function of the modulation frequency. The improved model Eq. (10.17) yields values displayed as dashed lines. Measurements by means of the three microphones technique are shown as open circle symbols (○) for a fixed sound pressure level SPL = 132 dB controlled by the microphone M_{spl}.

One notes that the expected behavior is well retrieved. The damping system has been designed to cancel oscillations at a frequency $f = 500$ Hz and the reflection coefficient features a low modulus $|\mathrm{R}_1(0)|$ with a phase shift $\phi_1(0)$ in the frequency range of interest.

Predictions from the first model of Scarpato et al. (2012) correspond to the bold line. The general shape is well retrieved. The modulus decreases and the phase increases around 500 Hz. There are some differences between predictions and experiments. The modulus $|\mathrm{R}_1(0)|$ is higher than the measured value between 50 Hz and 200 Hz and lower between 500 Hz and 800 Hz. The phase indicates a greater shift between 300 Hz and 700 Hz. This can be attributed to the piston head which does not perfectly close the back cavity. The second model takes into account the reflection coefficient of the piston head and yields improved predictions. The low frequency range perfectly matches measurements up to 300 Hz. Some differences remain between 300 Hz and 900 Hz for the modulus and between 300 Hz and 500 Hz for the phase. This is may be due to vortex interactions which are not taken into account in the model. Such interactions are possible since the interaction index exceeds the limiting value of 0.2 in the

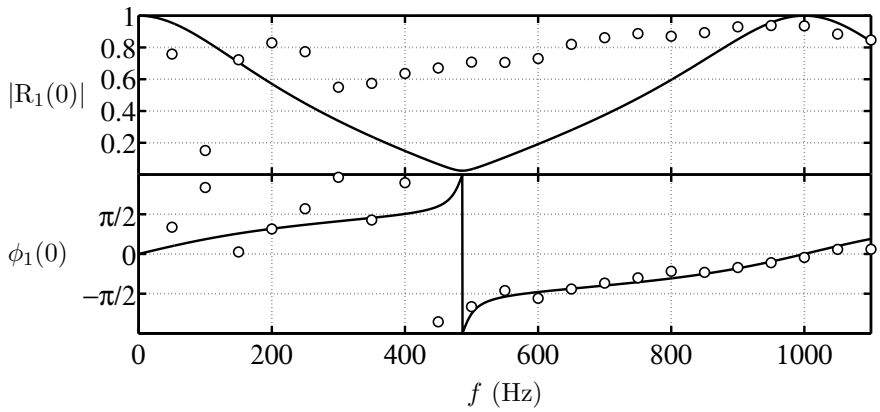

Figure 10.8: *Reflection coefficient of the damper B-SH. The back cavity is closed by the piston. There is no bias flow in the system. Measurements are displayed as open symbols (○). The low Strouhal approximation of Scarpato et al. (2012) is shown as a continuous line (—). Measurements indicate that the bias flow is essential if one wishes to reduce the reflection response.*

system as holes are close and do not quite satisfy the weak interaction condition defined by $r_a\sqrt{\pi}/d \leq 0.2$.

By switching off the flow rate, it is clearly shown that damping is linked to the bias flow velocity as illustrated in Fig. 10.8. Without flow, the reflection coefficient is modified and takes large values with a modulus around 0.8.

It is now interesting to estimate the influence of the chamfers machined on the lower side of the perforations presented in Fig. 10.5. The perforated plate is turned upside down and the evaluation of the reflection coefficient is repeated. Results are displayed in Fig. 10.9 and compared with measurements corresponding to the standard position of the perforations.

A large deviation appears at 400 Hz for the phase. Apart from this, one can see that the modulus $|\mathrm{R}_1(0)|$ and the phase $\phi_1(0)$ are close for all frequencies, indicating that the chamfer has a minor influence. The sharp edges needed to obtain vortices on the perforations is not a critical point for this damper. The holes countersink does not influence the reflection coefficient. The plate is used in what follows with the countersink placed on the lower side.

Finally, a second perforated plate is considered to illustrate the likelihood of an interaction phenomenon between vortices. The perforations are further apart and the measurement of the reflection coefficient is repeated. This perforated plate has been used to damp combustion instabilities in the unconfined configuration studied by Noiray (2007). This new damper, designated as "B-BH" for Big Holes, features 21 holes of diameter $2r_a = 4$ mm placed on a $d = 14$ mm square mesh. The flow rate remains the same and the bulk velocity U_b in the perforations reaches 15.3 m.s^{-1}. For a frequency of 500 Hz, the Strouhal number is now St = 0.41. The low Strouhal approximation is not valid anymore and the complete formula for the Rayleigh conductivity, given in Eq. (10.7),

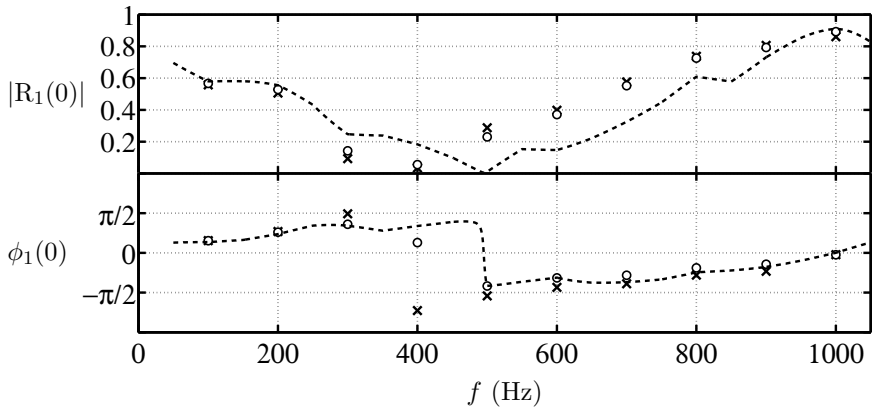

Figure 10.9: *Reflection coefficient of the damper B-SH. The back cavity is closed by the piston which is represented in the model. Predictions are plotted as a dashed line (- -). Measurements are displayed as symbols. Open circle symbols (○) show measurements corresponding to the standard plate installation on the first side. Cross symbols (×) exhibit values obtained when the plate is set upside down.*

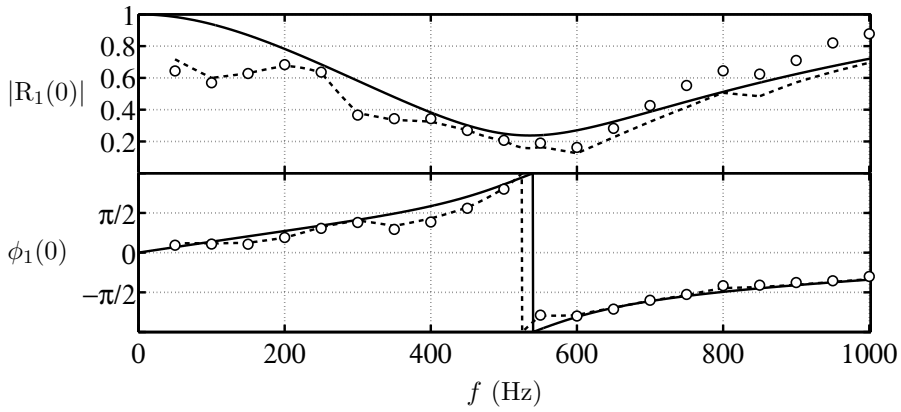

Figure 10.10: *Reflection coefficient of the damper B-BH (r_a = 2 mm). Measurements are displayed as open circle symbols (○). Two models are used to determine the reflection coefficient. The first plotted as a bold line (—) uses the Rayleigh conductivity derived by Howe (1979) but assumes that the piston is perfectly rigid. The second shown as a dashed line (- -) involves the same model but uses a finite reflection response for the piston. The convection velocity u_{cv} used in the Strouhal number corresponds to half of the bulk velocity $U_b/2$ = 7.65 $m.s^{-1}$.*

Table 10.2: *Characteristics of the two dampers used to suppress self-sustained oscillations. These dampers pertain to "B" type.*

Name	N	r_a (mm)	d (mm)	St (1 to 1000 Hz)
B-SH	357	0.5	3	$2.2\ 10^{-4}$ - 0.22
B-BH	21	2	14	$8.2\ 10^{-4}$ - 0.82

is used to calculate $\zeta_1(0)$. This provides the reflection coefficient $\mathrm{R}_1(0)$. The interaction coefficient $r_a\sqrt{\pi}/d$ is in this case 0.25 which is closer to 0.2.
The ideal or imperfect closure of the back cavity is integrated to determine the specific acoustic impedance $\zeta_1(0)$ by using either Eq. (10.5) or Eq. (10.17). In their experiments, Noiray (2007) found a better agreement between modeling and measurements when the convection velocity u_{cv} is taken equal to half of the bulk velocity U_b. Thus, it was decided to estimate the reflection coefficient with the same approximation ($u_{cv} = U_b/2$) with this damper.
Figure 10.10 displays results obtained with $u_{cv} = U_b/2$. Comparing the two models, one can see that the reflection coefficient of the piston head allows to obtain a perfect match between predictions and measurements. There are only small differences beyond 600 Hz for the modulus $|\mathrm{R}_1(0)|$.
The characteristics of the two dampers presented in this section are summarized in Tab. 10.2. For the two systems B-SH and B-BH, Howe's model of the Rayleigh conductivity is used to determine the reflection coefficient of the BFPs. A good agreement with experiments is obtained by modeling all the system components, and in particular the piston head which does not act as a perfectly rigid wall. Some differences subsist, but experiments on damper B-BH indicate that this may be linked to the interaction between adjacent vortices.

10.3.4 Influence of oscillation level

The two dampers devised previously are tested in the multiple flame combustor. It is known from Tran (2009) that the performances of a BFP drop down as the oscillation amplitude increases. The modulus tends to 1 and the phase to 0. A threshold exists where the system response is influenced by the sound pressure level. It has been demonstrated that this phenomenon occurs when the root mean square value of the acoustic velocity fluctuation $u'_p(0)$ within the perforation is of the order of the bias flow velocity $u'_p(0)/U_b \simeq 1$ (Tran (2009); Scarpato et al. (2011)).
In the present study, the velocity fluctuation level within the perforations of the damping system is not directly measured. This quantity is reconstructed from the reflection coefficient $\mathrm{R}_c(-L_c)$ and the pressure signal measured by

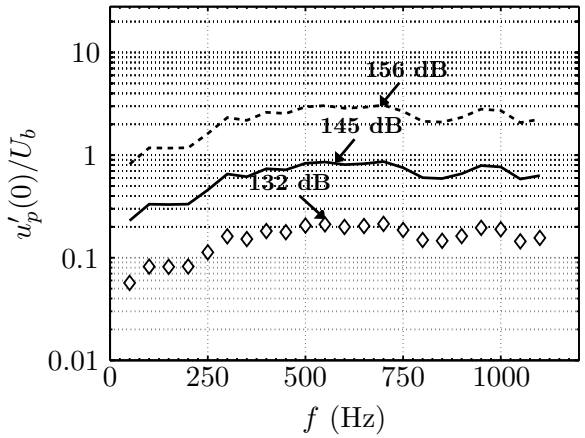

Figure 10.11: *Evolution of the relative velocity fluctuation $\widetilde{u}_p(0)/U_b$ within the holes ($2r_a$ = 4 mm) for the frequency range of interest. Three sound pressure levels (SPLs) are considered. The first of 132 dB corresponds to the level applied during the calibration of the damper in the impedance tube. The two other levels are used to define the SPL for which the oscillation overcomes the mean flow velocity in the perforation.*

the microphone M_{spl} as follows :

$$\Re\{\widetilde{u}_p(0)\, e^{-i\omega t}\} = \Re\left\{\frac{1}{\sigma_d \rho c(\mathrm{R}_c(-L_c)+1)}(\mathrm{R}_c(-L_c)e^{ikL_c} - e^{-ikL_c})\widetilde{p}_c(-L_c)\, e^{-i\omega t}\right\} \tag{10.22}$$

where $\widetilde{p}_c(-L_c)\, e^{-i\omega t}$ represents the Hilbert transform of the pressure time trace measured by microphone M_{spl}.

It is then possible to determine the relative velocity fluctuation level $\widetilde{u}_p(0)/U_b$ within a perforation. This is shown in Figs. 10.11 and 10.12 for the two perforated plates considered previously. These figures also display an extrapolation of the velocity fluctuation level by considering two higher pressure amplitudes at microphone M_{spl}. This helps to define the SPL threshold for which $\widetilde{u}_p(0)/U_b = 1$ is overcome.

For a value of 145 dB, the rms velocity fluctuation reaches the mean value U_b at a frequency $f = 500$ Hz in both cases. It should be noted that almost all relative velocity fluctuations are above unity when the SPL reaches 156 dB. For the perforated plate with small holes of diameter $d_a = 1$ mm, shown in Fig. 10.12, a safe zone exists above 900 Hz. In this range, relative velocity fluctuations are lower than unity.

Regarding the three SPL for the two systems, velocity oscillations within the perforations remain smaller than the bias flow velocity when the SPL is below 145 dB. The damping system response can be anticipated using the model defined in Eqs. (10.9) and (10.17). For larger values of the pressure level, velocity fluctuations exceed the bias flow value and the reflection coefficient

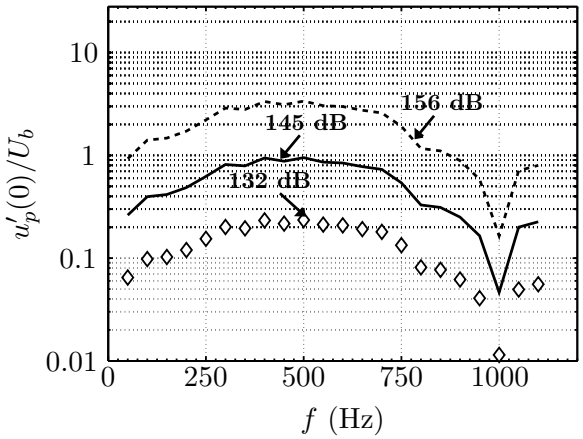

Figure 10.12: *Evolution of the relative velocity fluctuation $\widetilde{u}_p(0)/U_b$ within the holes ($2r_a$ = 1 mm) for the frequency range of interest. Three sound pressure levels (SPLs) are considered. The first of 132 dB corresponds to the level applied during the calibration of the damper in the impedance tube. The two other levels are used to define the SPL for which the oscillation overcomes the mean flow velocity in the perforation.*

deviates from the linear model. It is worth noting however that Tran (2009) showed that damping properties really deteriorate for a ratio $\widetilde{u}_p(0)/U_b$ above 3, with some degradation when $\widetilde{u}_p(0)/U_b$ exceeds unity. Finally, it is found that the damping systems feature robust characteristics because of the high value of their bias flow velocity U_b and that their reflection response will not deviate from the linear regime up to a level of 156 dB.

10.4 Nonlinear stability analysis

The configuration investigated in this section accounts for the interaction of two nonlinear elements. The first is the set of conical flames described with the FDF. The response of these flames has been examined in detail in the preceding chapters. Using the FDF, it has been possible to predict growth rates and frequencies of unstable modes as well as amplitudes reached at limit cycles. This investigation also reveals limit cycles with variable amplitude sustained by multiple modes. The flame was treated as the only nonlinear element, while the piston head response was described by a linear reflection coefficient $\mathrm{R}_1(0)$. Different amplitudes were tested and did not modify its response. This boundary condition is now replaced by the dampers devised previously. The back cavity is set to a length L_c depending on the frequency to damp. This new configuration now comprises two nonlinear elements at the two boundaries of the feeding manifold L_1 as represented schematically in Fig. 10.13. This typifies more complex situations were the dynamics of the reactive region interferes with the response of the chamber boundaries. A similar system was analyzed by Schuller et al. (2009) when the flame is unconfined. Nevertheless, in the

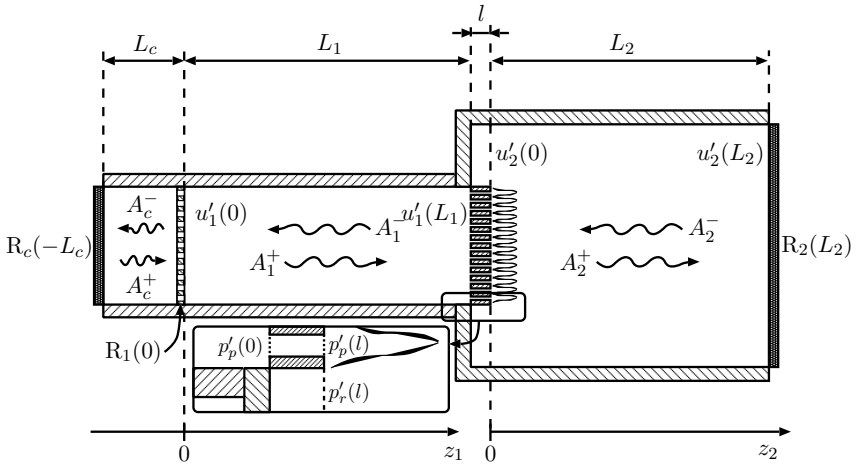

Figure 10.13: *Burner geometry and conventions used in the analytical model of the system response.*

present case the flame is confined by the quartz tube.
The reflection coefficient of the bias flow perforated plate $\mathrm{R}_1(0)$ and the flame are sensitive to velocity fluctuations. Thus, it is more consistent to also use velocity fluctuations to characterize the damper reflection coefficient $\mathrm{R}_1(0)$. This response is measured for incident waves at a reference level of 132 dB. The velocity fluctuations inside the perforations $\widetilde{u}_p(0)$ can be estimated with Eq. (10.22). It is also possible to link the velocity fluctuation in the perforations $\widetilde{u}_p(0)$ to those existing at the base of the flame $\widetilde{u}_1(L_1)$. The reflection coefficient $\mathrm{R}_1(0)$ is needed and may be written as :

$$\mathrm{R}_1(0) = \frac{A_1^+}{A_1^-} \tag{10.23}$$

Thus, the link between the two velocities $\widetilde{u}_1(L_1)$ and $\widetilde{u}_1(0)$ can be made. This takes the form :

$$\widetilde{u}_1(0) = \frac{\mathrm{R}_1(0) - 1}{\mathrm{R}_1(0)e^{ik_1L_1} - e^{-ik_1L_1}}\,\widetilde{u}_1(L_1) \tag{10.24}$$

Microphone M_2, placed 3 cm below the multipoint injection plate (see Fig. 1.2) can be used to determine the velocity fluctuation $\widetilde{u}_1(L_1)$. One uses Eq. (8.3) presented in Chapter 8 to compute velocity fluctuations as a function of feeding manifold length L_1. The Hilbert transform of this velocity signal is introduced in Eq. (10.24), giving the velocity fluctuation $u_1'(0)$ in the plane of the damping system. The velocity perturbation in the perforations is deduced by taking into account the porosity of the damper σ_d : $u_1'(0) = \sigma_d u_p'(0)$.
It was noted in Sec. 10.3.4 that the relative fluctuation amplitude $\widetilde{u}_p(0)/U_b$ has to lie below unity to avoid nonlinear effects. Moreover, the system is more prone to these nonlinearities when the velocity ratio exceeds 3 (Tran (2009); Scarpato

et al. (2011)). The amplitude of the self-sustained combustion oscillations are calculated in the perforations of the damping system using Eq. (10.24). This indicates that the relative fluctuation amplitude $\widetilde{u}_p(0)/U_b$ does not exceed 2.4 at this location for the $L_2 = 0.20$ m confinement tube. By examining the short confinement tube $L_2 = 0.10$ m, the maximum amplitude lies around $\widetilde{u}_p(0)/U_b = 1.8$ for the damping system with small holes and 2.1 for the one with larger holes $d_a = 4$ mm. One may then use the linear damper response in calculations carried out for all amplitudes.

The nonlinear analysis based on the FDF carried out in this section focuses on several different points. It is aimed at interpreting successes and failures sometimes encountered in damping the oscillations. One first examines the reliability of the BFP at high amplitude. In this context, the perforated plates feature a high bulk velocity U_b in each perforation to avoid flow reversal and deterioration of the damping characteristics. The two dampers are tested in the multiple flame combustor which provides a set of instabilities covering a wide variety of amplitudes and frequencies mapped in the preceding chapters. It is particularly interesting to consider configurations discussed in Chapter 8 which exhibit the same instability frequency at different amplitudes. These conditions are realized by changing the flame tube size L_2.

Another objective is to examine the benefits of the large frequency bandwidth obtained with damper B-SH but also with B-BH. This is examined by analyzing situations where a frequency shift occurs or in the situation where two unstable modes exist simultaneously in the burner. In a second step, the work investigates the influence of a change in the back cavity length L_c. The system is operated in its optimal arrangement and the back cavity size L_c is diminished in a progressive manner. By considering the damping response, this leads to move the optimal absorption frequency to a higher value. It is shown that B-type dampers characterized by a broad frequency absorption bandwidth offer more flexibility compared to A-dampers based on design rules derived by Hughes et al. (1990).

In what follows, we consider two frequencies. The first one lies around 600 Hz and is treated with the damper B-BH, while the second is 500 Hz and it is reduced by the damper B-SH. Table 10.3 synthesizes the geometrical configurations calculated with the FDF framework and investigated experimentally.

10.4.1 Damping of combustion instabilities for different amplitudes

The damper B-BH with the largest holes of diameter $d_a = 4$ mm is first considered. Flames are anchored on the perforated plate of thickness $l = 15$ mm. The system is investigated with the protocol adopted in Chapter 8. The model devised in Eq. (8.1) is applied to calculate complex roots $\omega = \omega_r + i\omega_i$ of the dispersion relation as a function of the feeding manifold length L_1. The reflection coefficient of the piston head $\mathrm{R}_1(0)$ is replaced by the reflection coefficient

Table 10.3: *Configurations investigated with the multiple flame combustor equipped with the dampers B-BH and B-SH. The two lower lines show values observed during self-sustained combustion oscillations without damper, while the upper part gathers the geometrical characteristics of the configurations.*

Damper	***B-BH***				***B-SH***		
Flame holder l (mm)	15			3	15		
L_2 (m)	0	0.10	0.20	0	0.10	0.30	0.10
L_1 (m)	0.35			0.34	0.43	0.35	0.50
f (Hz)	683	652	603	715	537	455	795
u_{rms}/U_b	0.27	1.20	1.02	0.35	1.45	0.78	0.7

of the perforated plate backed by the cavity, i.e. the damper. This is calculated with Eq. (10.17).

The first test is carried out in the unconfined version of the burner. This configuration offers a condition with self-sustained oscillations at low amplitude. The limit cycle is recorded for a frequency $f = 683$ Hz and an amplitude $u_{rms}/U_b = 0.28$ for $L_1 = 0.35$ m. The perforated plate is installed at this length and the back cavity is adjusted to $L_c = 0.125$ m to cancel the oscillation at 683 Hz. Calculations with the FDF framework and reflection coefficient are presented in Fig. 10.14. Calculations are shown on the left hand side of the figure. The growth rate ω_i appears in the upper box as a function of increasing amplitude u_{rms}/U_b. The frequency appears in the lower box. These trajectories pertain to the second mode. Growth rates computed for the first and third modes remain negative for all amplitudes and are not included in this figure. The growth rates and frequencies of the first mode are plotted as bold lines for the undamped burner. Dashed lines show the trajectories when the damper is placed in the system.

One finds negative growth rates for all amplitudes when the passive damper is placed in the system. This effectively leads to a stable combustion regime. Regarding the undamped burner, the limit cycle occurs at $u_{rms}/U_b = 1.06$ and $f = 672$ Hz. While frequency is well predicted, the amplitude is overestimated as found in Chapter 8 for other configurations. Under real test conditions one obtains the power spectral density of the signal recorded by microphone M_2 displayed in Fig. 10.15 in the absence or presence of a damper.

The power spectral density of the pressure in the absence of the BFP plotted as a dark bold line in subfigure (a) features a well marked peak at 683 Hz. The damper suppresses the instability as can be seen in the PSD plotted in subfigure (b). Other frequencies do not emerge. This confirms the results found in calculations and the burner is deemed to operate with a stable combustion process.

The previous case features a low amplitude combustion instability. This oscillation can be damped out by means of the BFP placed in the feeding manifold. The BFP is designed to avoid reverse flow in its perforations. This would lead to a nonlinear regime with degraded damping characteristics. The reflection

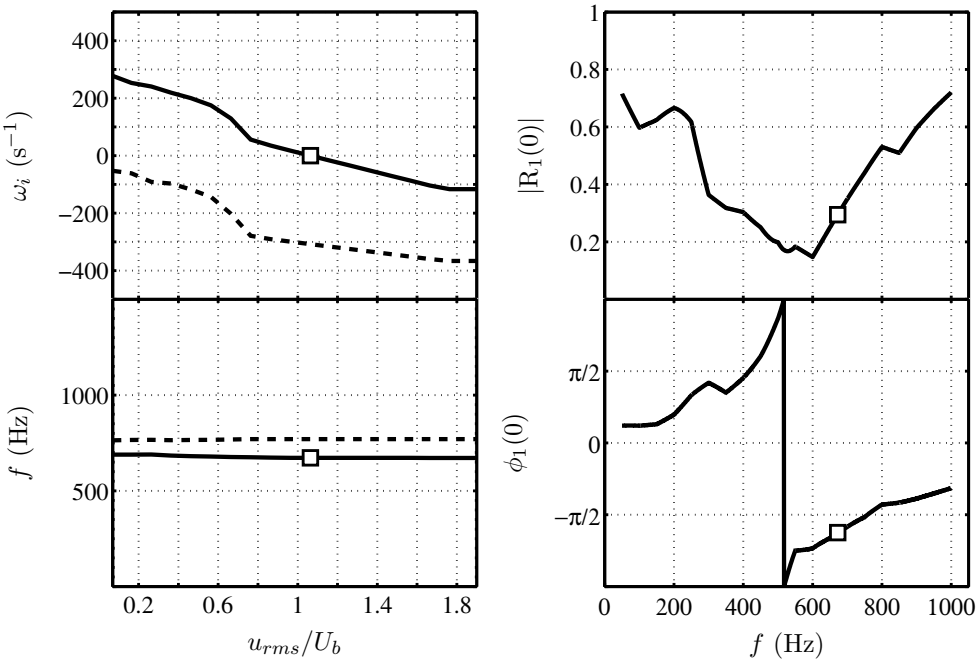

Figure 10.14: *Left : Evolution of growth rate (ω_i) and frequency (f) deduced from the FDF framework. Bold line (**—**) pertains to prediction of self-sustained oscillations without damper. Dashed line (**- -**) corresponds to calculations including the damper. Damper B-BH (d_a = 4 mm), back cavity size L_c = 0.125 m. The confinement tube is removed and the feeding manifold length is fixed to L_1 = 0.35 m. Without the damper, the system features self-sustained oscillations on the second mode at a frequency f = 683 Hz and the oscillation amplitude u_{rms}/U_b = 0.27. Limit cycle found at ω_i = 0 for the undamped burner is shown as an open square symbol (□). Right : Reflection coefficient of the perforated plate backed by its cavity. (□) indicates the limit cycle frequency found in calculations for the system without damper.*

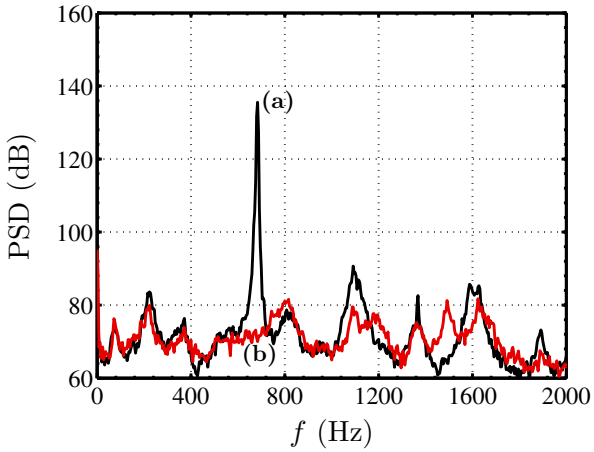

Figure 10.15: *Power spectral density of microphone* M_2*. This microphone is plugged on the feeding manifold. (a) The black bold line corresponds to an undamped condition (without the BFP). (b) The red bold line, shows results obtained when the damper is inserted in the burner. The feeding manifold length* $L_1 = 0.35$ *m while* $L_2 = 0$ *m (unconfined condition).*

coefficient does not deviate from the linear regime as the amplitude is growing and calculations with the FDF can be carried out with a fixed boundary condition $R_1(0)$.

It is now interesting to consider another instability around the same frequency but leading to a higher amplitude and see if the damper can be relied upon in this more difficult case. This analysis is motivated by previous studies where a BFP fails to cancel combustion acoustic coupling (Tran et al. (2009b)). The latter analysis is carried out with two BFPs, one of which is typified by a nonlinear response with degraded damping properties as the amplitude is growing, while the other is still adequate up to 140 dB. We are here following Tran et al. (2009b) analysis where it was shown that oscillations could be suppressed with a BFP designed to deal with large amplitudes. This was demonstrated experimentally, but not verified by calculations, as the flame response was not available in this study. It should be noted that the effective perforated plate does not suppress a higher frequency appearing in the system when the targeted one is cancelled. It is also interesting to examine why the damper which is not supposed to deviate from its linear regime does not effectively damp oscillations and prevent their growth to a high amplitude limit cycle. This question is investigated experimentally as in Tran et al. (2009b), but also theoretically within the present FDF framework. It will be shown that a BFP with diminishing damping characteristics reduces the growth rates in a limited range, creating a cusp in the bifurcation diagram as explained schematically in Fig. 10.16.

The cases considered in this figure idealize calculations with and without a

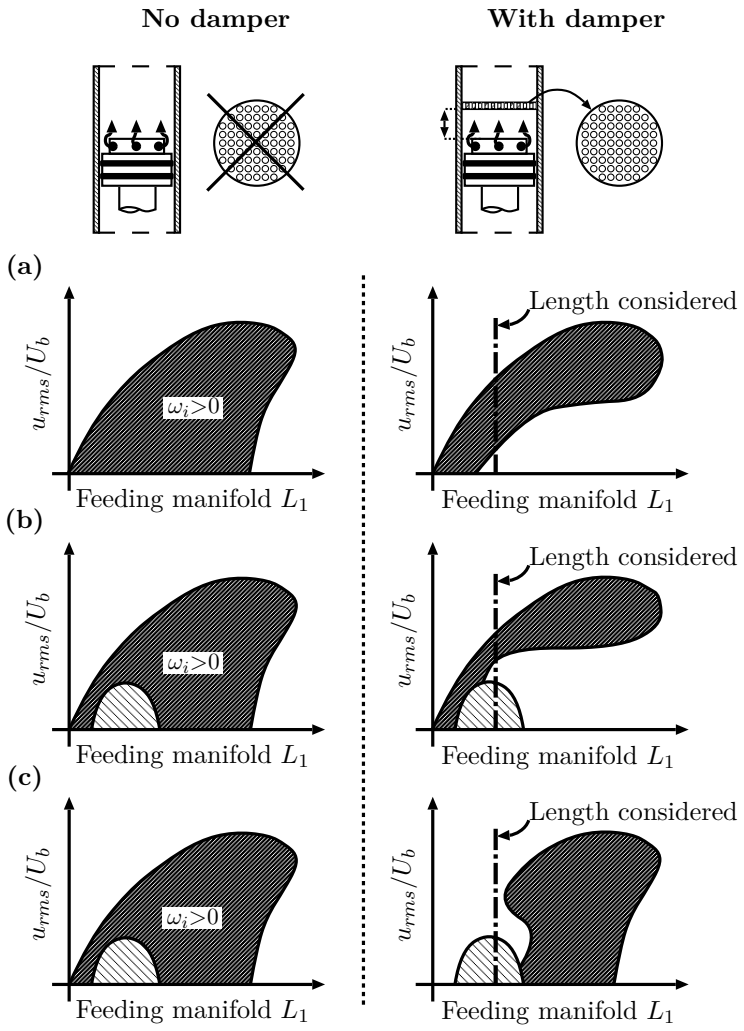

Figure 10.16: *Effect of a damper on positive growth rates ($\omega_i>0$). The system features similar instabilities to those found for the multipoint injection device considered in the present investigation. The damper features a nonlinear regime with a deterioration of its properties at high amplitudes. The operating length is indicated with the dashed-dotted line in the right part of the graph. One may distinguish three possible scenarios. (a) A linearly unstable mode (left) becomes nonlinearly unstable (right) when the damper operates. (b) Two modes exhibit positive growth rates indicated by the two different hatched areas. The damping system, acts on one mode, which becomes nonlinearly unstable while the other mode is unaffected. (c) The damper influences one of these modes. The smaller feeding manifold lengths are influenced and small amplitude limit cycles are suppressed but another mode which is linearly unstable prevails.*

nonlinear damping system, respectively drawn on the right and left parts of the figure. The first example (a) shows the influence of the damper at low amplitudes. The growth rates ω_i drops to a negative level (right graph) and the oscillation will occur if it is triggered. Considering that the unsteady flame flow interaction never reaches a perfectly null amplitude, the instability can start by itself. The right graph of (a) indicates that the amplitude needed to obtain positive growth rates may not be that high. In the second case (b), the target mode is not the only one featuring positive growth rates. Thus, another mode, with a different frequency, keeps its growth capacity and can trigger the target mode giving rise to a high amplitude limit cycle. Finally, in subfigure (c), two modes are present, but this time, one of the linearly unstable modes is completely suppressed but the other mode corresponding to a different frequency prevails.

Using the multipoint injection combustor, it is easy to select the desired combustion regime and test the damper. This is used to verify the scenarios shown in Fig. 10.16 and thus to explain failures in suppressing instabilities.

The confined version of the burner is more prone to self-sustained oscillations at high amplitude. Such regimes are found by confining the flame with a tube of length $L_2 = 0.10$ m. The feeding manifold length is fixed to $L_1 = 0.35$ m and the damper is introduced in the upstream part. The back cavity length L_c is adapted to the target frequency, which is not exactly the same as that investigated up to now. It is now $f = 652$ Hz instead of $f = 683$ Hz. The amplitude features a huge increase to $u_{rms}/U_b = 1.2$. Predictions of self-sustained combustion oscillations are carried out by successively considering undamped and damped systems. Results are presented in Fig. 10.17.

Examining the burner dynamics without damper, the limit cycle is predicted for $f = 652$ Hz and $u_{rms}/U_b = 1.26$, which match experimental data. When the BFP is inserted, calculations still predict a limit cycle at a lower amplitude $u_{rms}/U_b = 0.54$ with a higher frequency $f = 732$ Hz. It is interesting to see that the second unstable mode at $f = 652$ Hz shifts to a higher frequency with a larger reflection coefficient $|\mathrm{R}_1(0)| = 0.45$ instead of 0.29. The phenomenon illustrated in this calculation reflects changes in frequency with a growing amplitude. This also occurs when the boundary condition is modified by the presence of a damper. When the damper is centered on a specified frequency, the flame dynamics may adapt itself and the resonant frequency might be shifted in a range where the reflection response is less influential.

This raises an important issue for passive control solutions. If the control device has a reduced frequency bandwidth, it may not be able to cancel the thermoacoustic oscillation. This is typical of A-type dampers. B-type dampers designed according to Scarpato et al. (2012) extend the band of influence and will be more effective.

To illustrate this fact, calculations have been carried out in the case $L_1 = 0.35$ m and $L_2 = 0.10$ m. One uses the damper B-SH featuring 357 holes of $d_a = 1$ mm. This system works at low Strouhal number and exhibits a large

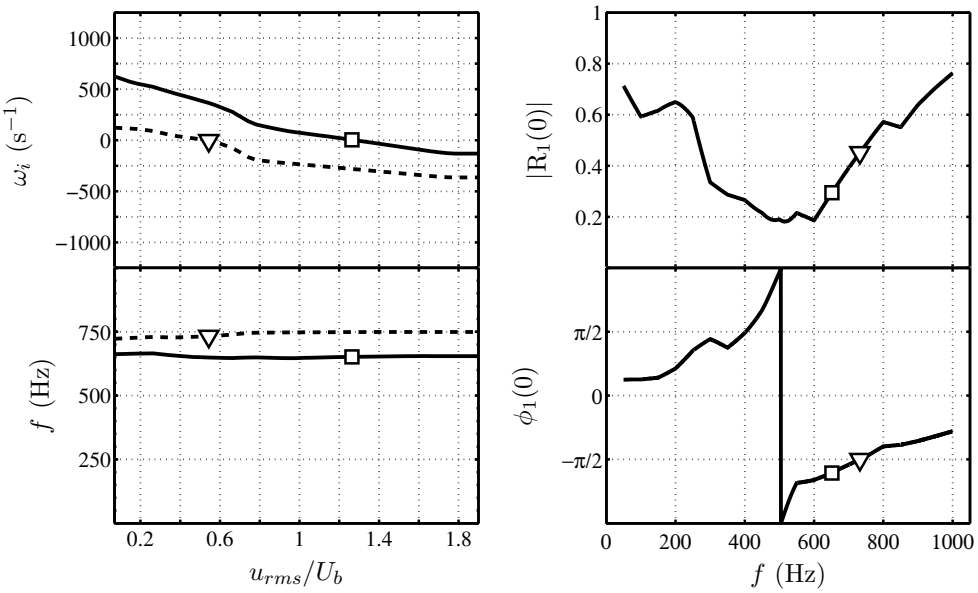

Figure 10.17: *Left : Growth rate (ω_i) and frequency (f) deduced from the FDF framework. Bold line (**—**) pertains to predictions of self-sustained oscillations without damper. Dashed line (**- -**) corresponds to calculations including the damper. Damper B-BH ($d_a = 4$ mm), back cavity size $L_c = 0.133$ m. A short confinement tube $L_2 = 0.10$ m is used and the feeding manifold length is fixed to $L_1 = 0.35$ m. Without damper the burner features self-sustained oscillations near the second modal eigenfrequency at $f = 652$ Hz leading to an amplitude $u_{rms}/U_b = 1.2$. Limit cycles found at $\omega_i = 0$ for the undamped and damped burners are respectively displayed as open square symbols (□) and open triangle symbols (▽). Right : damper reflection coefficient. (□) and (▽) respectively indicate the limit cycle frequency found in calculations for the undamped and damped burners.*

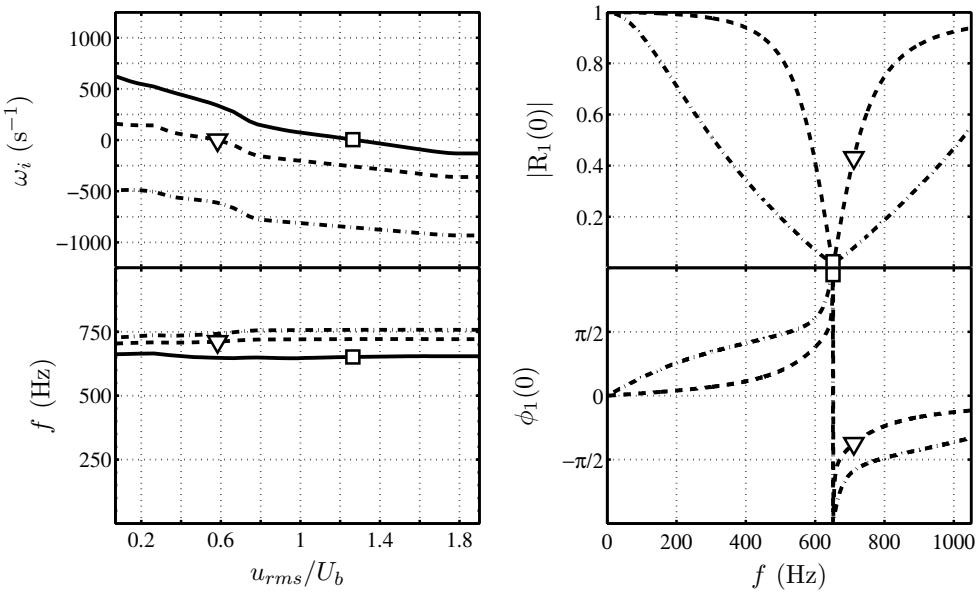

Figure 10.18: *Left : Growth rate (ω_i) and frequency (f) deduced from FDF calculations. Bold line (**—**) pertains to predictions of self-sustained oscillations without damper. Dashed line (- -) corresponds to calculations with an A-damper. Results for a B-damper (B-SH) which features 357 holes (d_a = 1 mm) are shown as a dashed-dotted line (·-), the cavity size L_c = 0.138 m is used to cancel the frequency found without damper, i.e. f = 629 Hz. The feeding manifold length L_1 = 0.35 m while the confinement tube L_2 = 0.10 m. Limit cycles found at ω_i = 0 for the undamped and damped systems are respectively displayed by open square symbols (□) and open triangle symbols (▽). Right : Reflection coefficient of the A-damper dashed line (- -) and B-damper dashed-dotted line (·-). Open symbols (□) and (▽) respectively indicate the limit cycle frequency found in calculations for the undamped burner and for burner equipped with an A-damper.*

damping bandwidth. Results are compared to those obtained by considering an A-type damper designed with the method of Hughes et al. (1990) which features a smaller band of interest. Results for these two cases are displayed in Fig. 10.18.

When a B-damper is used, the growth rate ω_i dives in the negative part, indicating that the oscillations will be cancelled. This is not the case when one uses an A-damper. Even if the lowest reflection coefficient centers around the target frequency, the flame adapts its frequency and shifts to a higher value. The oscillation persists and the amplitude is only slightly diminished.

Experiments are now considered. By placing the B-BH damper (d_a = 4 mm), one observes the suppression of the oscillation even if calculations presented in Fig. 10.17 indicate that oscillations will persist at a lower amplitude u_{rms}/U_b = 0.54. This is shown by analyzing the pressure records of microphone M$_2$ in Fig. 10.19.

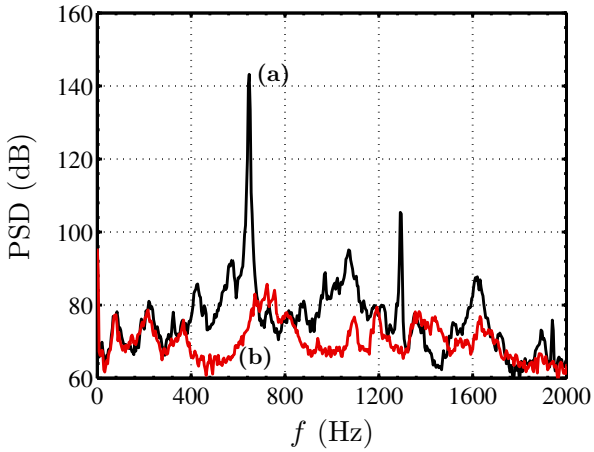

Figure 10.19: *Power spectral density of microphone* M_2 *plugged on the feeding manifold. The black bold line (a) corresponds to the undamped condition (without BFP). The red bold line (b) is obtained when the damper is placed in the burner. In both cases, the feeding manifold length* $L_1 = 0.35$ *m while* $L_2 = 0.10$ *m (short flame tube).*

The power spectrum indicates that control is effective. The unstable frequency is completely suppressed and the other modes do not arise. This indicates that the method is applicable in a case where the limit cycle would reach a very high amplitude. The slight difference in prediction may be linked to the phenomenon evoked in Chapter 8 and is probably related to uncertainties in the natural damping or in the temperature T_2 estimate.

In the two cases investigated, control has been applied with a robust damper when the system features small and high amplitude limit cycles. In each case, the oscillation is cancelled. In addition, calculations reveal the ability of the flame to shift its frequency of oscillation. The failure scenarios proposed in Fig. 10.16 do not arise in the present experiment. The BFP operates effectively at the high oscillation amplitudes under consideration.

It is however possible to demonstrate the mechanism sketched in Fig. 10.16(c) with another configuration. This is found in the unconfined version of the burner. The configuration retained was studied by Noiray (2007). In this latter case, the perforated plate is also effective for all amplitudes, but a length L_1 featuring two modes can be explored. These two modes are linearly unstable. Without damper, this length exhibits a second mode instability with a constant amplitude. The damper B-BH ($d_a = 4$ mm) is set up and one aims to cancel this second mode frequency at 715 Hz. The result, shown in Fig. 10.20, indicates that this frequency is eliminated, but a higher frequency appears at 1283 Hz. The bifurcation diagram obtained in Noiray (2007) is recalculated by making use of the flame response and parameters used in this experiment. The damper B-BH ($d_a = 4$ mm) backed by a cavity $L_c = 0.12$ m, is then included and a new bifurcation diagram is determined. The damper geometry is fixed while

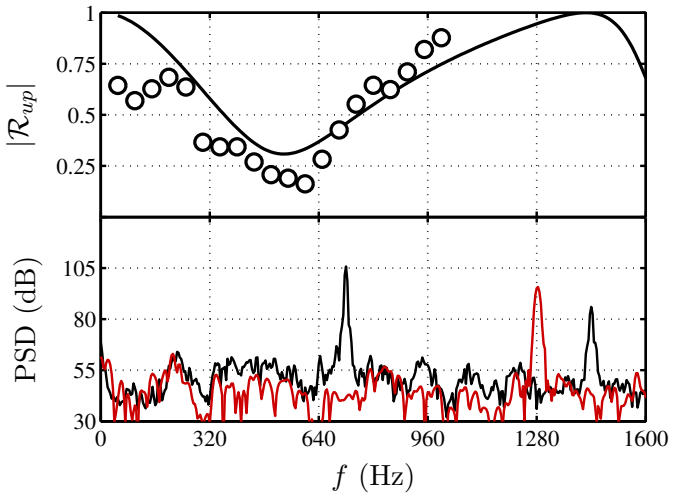

Figure 10.20: *Reflection coefficient (upper part) and power spectral density of the microphone signal (lower part). The microphone is located 35 cm away from the burner axis. The dark bold line corresponds to the unconfined flame configuration without damper, while red bold line corresponds to the burner when the damper is placed in the feeding manifold. In both cases $L_1 = 0.34$ m. From Noiray (2007).*

the feeding manifold length L_1 is varied. Results without and with damper are plotted in Fig. 10.21.

The length investigated $L_1 = 0.34$ m is marked as a dash-dotted line. By examining the diagram of Noiray (2007) also shown in Fig. 10.21(a), one observes positive growth rates until $u_{rms}/U_b = 0.2$ for the third mode (red area). These growth rates have lower values around 100 s^{-1} when compared to those of the second mode. They are hidden behind the blue area. By using the damper, one retrieves the scenario shown in Fig. 10.16(c). The second mode is completely suppressed while the third one remains as shown in Fig. 10.21(b). This explains the result found by Noiray (2007). By considering the predicted frequency, one finds that $f = 1270$ Hz, which is close to the experimental value $f = 1283$ Hz. The amplitude in the feeding manifold is not available and hinders any further comparison with theory. It is however possible to determine the amplitude in Fig. 10.20, retrieved from Noiray (2007). This value is recorded by a microphone located 35 cm away from the burner axis. One finds a lower amplitude for the high frequency $f = 1283$ Hz than for the one without the damper. This indicates that the lower amplitude found in calculations may be in agreement with the experimental value.

The flame tube configuration treated previously is relatively short ($L_2 = 0.10$ m), while that investigated by Tran et al. (2009b) on a different system is much longer $L = 0.50$ m. Another configuration with a longer confining tube $L_2 = 0.20$ m is therefore tested. The feeding manifold length is set to $L_1 = 0.35$ m with the same damper B-BH ($d_a = 4$ mm). The back cavity length

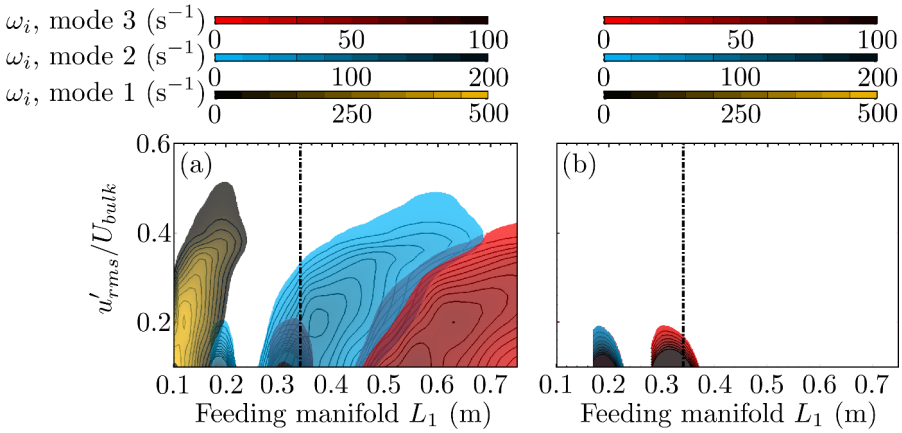

Figure 10.21: *Bifurcation diagrams calculated for the configuration of Noiray (2007). Left graph (a) corresponds to the burner with a perfectly reflecting boundary condition for the upstream boundary. Right graph (b) shows results obtained by replacing this boundary condition with damper B-BH (d_a = 4 mm) set with a back cavity L_c = 0.12 m. This damping system is not modified when the length is swept from L_1 = 0.10 m to 0.75 m. The dashed-dotted line drawn on each graph corresponds to the length examined L_1 = 0.34 m.*

L_c is adapted to maximize absorption at the frequency f = 603 Hz. This yields L_c = 0.145 m. The amplitude to damp reaches u_{rms}/U_b = 1.02 which lies in the same range as that studied with the short flame tube L_2 = 0.10 m (where an oscillation amplitude u_{rms}/U_b = 1.2 was suppressed). Calculations and reflection coefficient are displayed in Fig. 10.22.

Results obtained in this case reveal an unexpected behavior. While the limit cycle without the damper is fairly well predicted, a strong oscillation persists when the damper is included. Its amplitude lies around 0.98 for a frequency f = 462 Hz. This behavior is confirmed by experiments. One observes a strong oscillation with a significant amplitude u_{rms}/U_b = 0.55 at f = 592 Hz. This experimental result is depicted in Fig. 10.23. It indicates that the damper hardly modifies the pressure spectrum and is unable to control the system.

The loss of effectiveness is well predicted through the FDF framework. The model highlights three important points. The first one centers around the perforated plate efficiency. The frequency does not change to a value corresponding to a higher reflection coefficient as observed with the small confinement tube L_2 = 0.10 m. It is shifted to a value where $|R_1(0)|$ is lower (see the open triangle symbol in the right part of Fig. 10.22). The second point is linked to the prediction of self-sustained oscillations. While the prediction agrees with experiment, there are some differences. The amplitude is overestimated although it is reduced when compared to the calculated value without the perforated plate. The frequency appears to be lower than that found in the experiment. Finally, one is surprised to see that control is not achieved

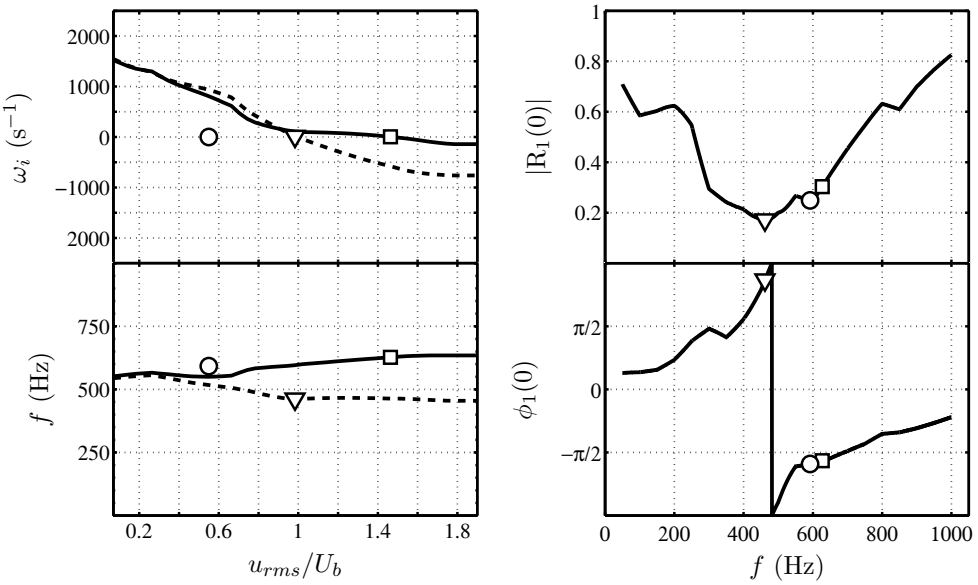

Figure 10.22: *Left : Evolution of growth rate (ω_i) and frequency (f) deduced from the FDF framework. Bold line (**—**) pertains to predictions of self-sustained oscillations without damper. Dashed line (**- -**) corresponds to calculations including the damper. Damper B-BH (d_a = 4 mm), back cavity size L_c = 0.145 m. The feeding manifold length L_1 = 0.35 m while the confinement tube L_2 = 0.20 m. Without the damper, the system features self-sustained oscillations at the second mode frequency f = 603 Hz for an amplitude u_{rms}/U_b = 1.02. The limit cycle found at ω_i = 0 for the undamped burner is shown as an open square symbol (□) while the limit cycle corresponding to the damped burner is displayed as an open triangle symbol (▽). In spite of the damper, the experiment reveals self-sustained oscillations at a frequency f = 592 Hz and an amplitude u_{rms}/U_b = 0.55. This is shown as an open circle symbol (○). Right : Reflection coefficient of the perforated plate backed by its cavity. (□) and (▽) respectively indicate the limit cycle frequency found in calculations for the undamped and damped burners.*

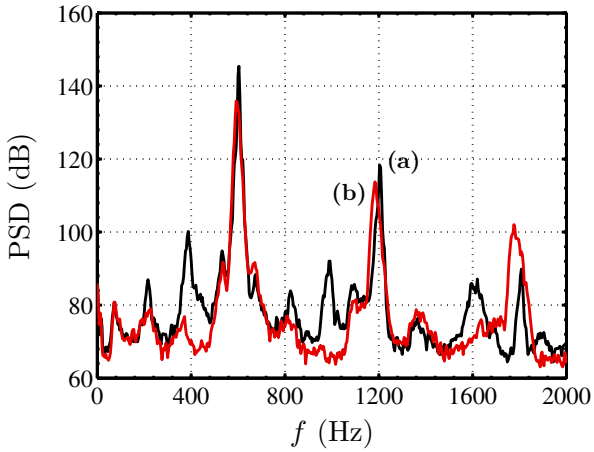

Figure 10.23: *Power spectral density of microphone* M_2 *plugged on the feeding manifold. The black bold line (a) corresponds to the undamped condition (without BFP). The red bold line (b) shows the result when the damper is inserted in the burner. In both conditions, the feeding manifold length* $L_1 = 0.35$ *m while* $L_2 = 0.20$ *m.*

in this situation where the oscillation level remains moderate. Indeed, for the small confinement tube $L_2 = 0.10$ m and without damper, self-sustained combustion oscillations reach a level $u_{rms}/U_b = 1.2$ and they are suppressed by the damper. In the present situation with $L_2 = 0.20$ m, it is found that the fluctuation level $u_{rms}/U_b = 1.02$ but the damper is ineffective. This cannot be attributed to the nonlinearity of its response. This unexpected behavior is linked to the acoustic response of the burner when the damping system is introduced in the upstream. This induces a cavity decoupling effect which will be investigated in Chapter 11.

The other damper B-SH ($d_a = 1$ mm) is now tested in the same way. This device operates in the low Strouhal number range and offers the benefits of a broad frequency absorption bandwidth with a low reflection coefficient. By using the back cavity length L_c, it is possible to tune its response with a minimum modulus and a maximum phase. The work centers around the same guideline and aims to damp out an almost equal frequency at different amplitudes. In addition, the confinement tube L_2, used to obtain a high amplitude of oscillation, is increased to a length $L_2 = 0.30$ m. Three configurations are examined and their respective conditions are gathered in Tab. 10.4.

The damper effectively suppresses self-sustained oscillations up to $u_{rms}/U_b = 1.45$. This is found for $L_1 = 0.43$ m with the flame tube $L_2 = 0.10$ m. The suppression of all the eigenmodes is obtained both in calculations and experiments. The damper also suppresses an oscillation for the same confinement tube at $L_1 = 0.50$ m. Nevertheless, it was not possible to cancel the instability for the longer confinement tube $L_2 = 0.30$ m. By considering experiments with the small confinement tube $L_2 = 0.10$ m at $L_1 = 0.50$ m, one notes the presence

Table 10.4: *Configurations examined with the damper B-SH (d_a = 1 mm) used as control device in the multiple flame combustor. The lower line indicates the success or failure to damp the self-sustained oscillations considered.*

L_2 (m)	*0.10*	*0.10*	*0.30*
L_1 (m)	0.5	0.43	0.35
Frequency (Hz)	795	537	455
Amp. u_{rms}/U_b	0.7	1.45	0.78
Damped out ?	✔ ☺	✔ ☺	✖ ☹

of two modes. This situation studied in Chapter 9 was obtained for $L_1 = 0.52$ m, while in the present experiment, the two modes exist at $L_1 = 0.50$ m. This is linked to the burner temperature T_2. As mentioned at the end of Chapter 6, the flame tube temperature T_2 modifies the eigenmodes distribution and so, the bifurcation diagram. Thus, as the experimental points are acquired in another series of experiments, the behavior slightly changes in the transition zone where the two modes appear. The back cavity is set up by considering the frequency of the third mode $f = 795$ Hz. Results of calculations are displayed in Fig. 10.24. One observes that growth rate ω_i trajectories represented by dashed lines become negative indicating full suppression of oscillation. This indicates that the damper stabilizes the flame in this configuration. This phenomenon is well retrieved experimentally.
Stabilization is not feasible anymore for the longer confinement tube $L_2 = 0.30$ m where one wishes to cancel a frequency $f = 455$ Hz featuring an oscillation amplitude $u_{rms}/U_b = 0.78$. Oscillations persist but amplitude is lowered. This is reminiscent of what is found previously with the $L_2 = 0.20$ m flame tube and the damper B-BH. This latter system, without nonlinearities in its response, was not able to suppress an instability at a moderated amplitude. Damper B-SH leads to the same result. It is found effective for an oscillation level $u_{rms}/U_b = 1.45$ when $L_2 = 0.10$ m. Thus, by using the $L_2 = 0.30$ m confinement tube which features oscillations at lower amplitude $u_{rms}/U_b = 0.78$, one would have expected the suppression of the instability. Experiment and calculations reveal that this is not attained. This surprising result comes from the decoupling effect mentionned before when $L_2 = 0.20$ m and will be explained in Chapter 11.

10.4.2 Influence of the back cavity length

The back cavity length L_c is set to an optimal value to obtain a vanishing reflection coefficient. This is accomplished by setting $\mathrm{He} = \pi/2$ where He designates the Helmholtz number. This method allows to lower the reflection coefficient on a wide frequency band and it is interesting to modify the back cavity size L_c to see the sensitivity of the system. The wide frequency band of the damper is supposed to keep the reflection coefficient at low values and avoid the initiation of self-sustained oscillations even if the back cavity L_c is modified.

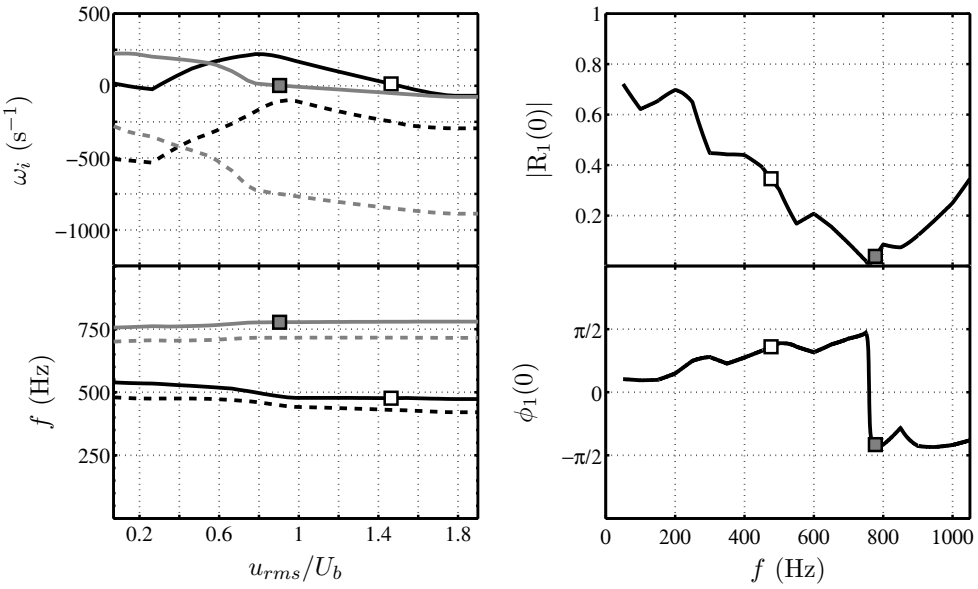

Figure 10.24: *Left : Growth rate (ω_i) and frequency (f) deduced from the FDF framework. Bold line (**—**) pertains to predictions of self-sustained oscillations without damper. Dashed line (**- -**) corresponds to calculations including the damper. Damper B-SH (d_a = 1 mm), back cavity size L_c = 0.109 m. Black color represents the second mode while the gray lines are linked to the third mode. The feeding manifold length L_1 = 0.50 m while the confinement tube L_2 = 0.10 m. Without damper the burner features oscillations sustained by two modes. Limit cycles found at ω_i = 0 for the second and third modes of the undamped burner are respectively displayed as open and gray square symbols. Right : Reflection coefficient of the damper. Open and gray square symbols respectively indicate the second and third mode frequency found at limit cycle for the undamped condition.*

The modification is considered in two configurations. The first corresponds to the small confinement tube $L_2 = 0.10$ m and the second to a longer tube $L_2 = 0.20$ m, a situation where the damper does not suppress the oscillations. The two configurations are investigated by calculations and experiments.

In the first case the flame tube is set to $L_2 = 0.10$ m and the damper B-SH ($d_a = 1$ mm) is inserted in the feeding manifold L_1. The point of operation examined corresponds to $L_1 = 0.50$ m. The optimal back cavity length is set to $L_c = 0.109$ m. In this situation, one obtains a minimum reflection coefficient for $f = 764$ Hz. This is displayed in Fig. 10.24 of the previous section. One is able in this case to avoid modes 2 and 3. The modulus $\mathrm{R}_1(0)$ remains lower than 0.5 from $f = 285$ Hz to 1000 Hz and the phase $\phi_1(0)$ exhibits a big shift of $\pi/2$ in this range. It is interesting to see if this broad band allows to move the piston without initiating oscillations. Calculations are done with the FDF by sweeping the back cavity length L_c by steps of 1 cm.

One observes that frequency trajectories are almost the same for the growing amplitudes u_{rms}/U_b of each damper. The piston is moved until $L_c = 0.039$ m. These calculations indicate that the system is effective until $L_c = 0.079$ m. Below this length, the growth rate trajectories enter in the positive range. The two targeted frequencies lie around 750 Hz and 500 Hz. Regarding the reflection coefficient $\mathrm{R}_1(0)$ for the optimal cavity depth L_c, it is seen that the frequency around 500 Hz exhibits the highest value for the modulus $|\mathrm{R}_1(0)|$. If one examines this value during the reduction of the back cavity, the modulus reaches 0.5 for $L_c = 0.079$ m. The experiment has been done by diminishing the back cavity with the same steps and shows a stable combustion regime for the lengths found in calculations. This regime persists until $L_c = 0.049$ m which slightly differs from the predicted value.

This analysis reveals that the damping methodology is robust and does not require a fine tuning of the back cavity length L_c. This is due to the wide frequency band of action for the damper. It is however required to calculate or measure the reflection coefficient to keep a sufficiently low value for the modulus.

The same analysis has been undertaken in the confined configuration $L_2 = 0.20$ m, where the damping device shows its inefficiency. The burner is equipped with damper B-BH ($d_a = 4$ mm). The case studied corresponds to the feeding manifold length $L_1 = 0.21$ m. The back cavity is fixed to $L_c = 0.206$ m. By reducing this length, one finds an insensitive condition for the self-sustained oscillations. The frequency evolves slightly around 600 Hz. This is represented in Fig. 10.25. This indicates that the flame oscillation is weakly influenced by upstream conditions. This agrees with what was found previously for the $L_2 = 0.20$ m flame tube. In this latter case, the damper was not able to cancel a self-sustained oscillation of moderate amplitude. In the present configuration, by using the modification of the back cavity L_c, it is possible to see that the damping system does not act on the instability. This confirms that the oscillations observed in this case are insensitive to damping in the upstream

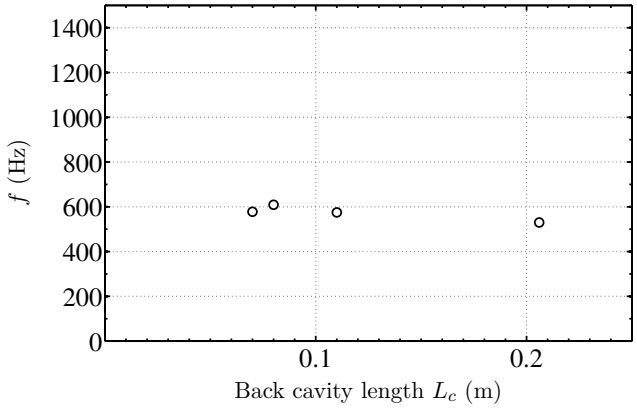

Figure 10.25: *Evolution of the frequency of self-sustained combustion oscillations obtained by sweeping the size L_c from 0.206 m to 0.07 m. Damper B-BH (d_a = 4 mm). The confinement tube is set to L_2 = 0.20 m and the feeding manifold length is L_1 = 0.21 m.*

manifold. This point is considered in the next chapter.

10.5 Chapter summary

A passive control of the self-sustained combustion oscillations characterized in Chapter 8 was undertaken by using bias flow perforates.
A suitable model was obtained by using the Rayleigh conductivity derived by Howe (1979). It is chosen to work at low Strouhal number, a regime studied by Scarpato et al. (2012), which widens the frequency bandwidth and allows to determine independently the back cavity size L_c for the peak absorption frequency. This low order modeling was improved by taking into account the imperfect closure of the back cavity made with the piston in the present experiment.
Two dampers were designed for the multiple flame combustor. The mean flow velocity inside the perforations is set to a high value to avoid nonlinear effects.

- The first one B-SH works at low Strouhal numbers and its response is fairly well predicted by the improved model of Scarpato et al. (2012). It is seen that chamfers of the holes, not planned at the design stage, do not change the response.

- The second damper B-BH works at higher Strouhal numbers but is typified by a wide frequency bandwidth. Its optimal peak absorption frequency is fairly well tuned with the back cavity size L_c. In this latter case, it was possible to obtain a perfect match between modeling and experiments.

- An uncertainty persists with the convection velocity u_{cv} of the vortices. It is generally considered that the value is one half of the jet velocity in the vena contracta (Howe (1979)).

A nonlinear analysis based on the FDF was finally undertaken. The goal was to investigate the cancellation of self-sustained combustion oscillations with the two dampers and explain failures in damping combustion oscillations encountered in some cases. This was done through the analysis of two points : cancellation of large oscillation levels and the benefits of the large frequency bandwidth. This leads to the following results :

- The two dampers were able to suppress instabilities featuring large velocity fluctuations up to $u_{rms}/U_b = 1.45$.
- Even if the amplitude does not exceed large values, it was not possible to cancel the self-sustained oscillations encountered in the long confinement tubes $L_2 = 0.20$ m and 0.30 m.
- In all the cases, the FDF was able to predict the observed results with some differences for some configurations.
- The large frequency bandwidth allowed to suppress oscillations sustained by two modes identified in Chapter 9.

By using the FDF and the detailed characterization of the multiple flame combustor, it has been possible to understand why damping sometimes fails. This is due to different reasons. Some of these reasons were deduced from the FDF framework but not verified experimentally, while others were investigated for both. This list may not be exhaustive :

- The nonlinearity of the damper induces that a linearly unstable mode becomes nonlinearly unstable. This mode can be triggered by another mode, itself or a finite impulse. This was not found in the present experiments.
- The nonlinearity of the damper does not avoid the suppression of a moderate limit cycle amplitude but self-sustained oscillations persist with another mode. This was found in calculation and experiments with a configuration examined by Noiray (2007).
- The frequency variation with the growing amplitude allows the initiation of oscillations if the damper frequency bandwidth is too sharp. The large frequency bandwidth of the dampers used in the present study circumvented this issue.
- For a damper characterized by a narrow frequency bandwidth, the flame

is able to oscillate on a shifted frequency regarding the optimal absorption value, which precludes the cancellation of oscillations.

- In the case of long confinement tube when $L_2 = 0.20$ m or 0.30 m, the oscillations seem to be insensitive to the damper. By using another study (Tran (2009)) it has been possible to delineate that it may be linked to a flame tube oscillation. In this latter situation a nonlinear damper does not prevent the start and the establishment of an unstable mode in the whole burner. For a robust BFP, which is the case here, the oscillation persists if the flame is able to feed energy to the eigenmode of its cavity. This has been characterized by experiments and FDF calculations with some differences between the two.

It is found that the passive control of self-sustained combustion oscillations from the upstream part of a combustor is an efficient technique when it is well designed. Nevertheless, it was seen that it can fail in various cases and that this narrows its relevance. In the absence of a nonlinear damper, one is able to suppress large amplitudes of oscillation but the frequency bandwidth with a low reflection coefficient has to be widened. A worst case is that where the flame is in a long confinement tube, a situation usually found in applications. This features oscillations which are essentially localized in the flame tube and are insensitive to upstream damping.

Chapter 11

Decoupling cavities

Dans ce chapitre, on s'intéresse à l'effet d'un découplage acoustique des cavités amont et aval du brûleur MIC (Multiple Injection Combustor) étudié dans ce manuscrit. Il s'agit ici de mieux comprendre le changement de comportement associé à une modification de la condition à l'entrée du brûleur. On s'intéresse notamment à l'effet d'un changement du coefficient de réflexion sur les fréquences de résonance du système. La possibilité de découpler l'analyse acoustique de cavités a déjà fait l'objet d'une étude qui traite de l'influence de la géométrie (Schuller et al. (2012)). Afin de simplifier le problème, un modèle comportant deux tubes et possédant des conditions aux limites idéales est envisagé. Il est montré que l'amortissement de l'onde dans le tube d'alimentation permet de découpler les cavités avec un fonctionnement autonome dans le tube de confinement de la flamme. Ce résultat assez logique se démontre facilement par l'analyse de la relation de dispersion de deux cavités couplées. Il est possible dans ces conditions de déterminer la fréquence d'oscillation de l'instabilité dans le tube à flamme lorsque le système est bien découplé et de s'intéresser à sa dynamique propre. On montre dans cette situation que le fonctionnement autonome du tube aval L_2 perdure quel que soit le coefficient de réflexion amont $R_1(0)$. Ceci se produit dans le cas où la longueur de la géométrie amont L_1 possède une dimension de l'ordre de celle du tube à flamme L_2.

11.1 Découplage de cavité dans un brûleur

L'analyse effectuée dans les chapitres précédents a montré qu'une modélisation au moyen d'éléments compacts (voir par exemple Poinsot et al. (2012) pour une explication de la méthode) permet de déterminer les modes propres des différentes géométries considérées. La méthode de l'équivalent harmonique (FDF) est utilisée pour prendre en compte la réponse non-linéaire de la flamme. Elle fournit également les fréquences et les amplitudes d'oscillation au cycle limite (Noiray et al. (2008); Boudy et al. (2011b)). Enfin, il est important

de noter que l'amortissement α peut être inclus dans ces analyses en tenant compte des vrais conditions aux limites comme expliqué dans le Chapitre 8. Ainsi, dans ces conditions, il a été montré qu'il est possible de retrouver par le calcul les amplitudes et les fréquences mesurées. Le décalage en fréquence par rapport aux modes acoustiques est également bien estimé par ce biais.
Ce chapitre vise à montrer qu'un découplage de cavité peut survenir dans le brûleur lorsqu'un système d'amortissement est utilisé dans la partie amont. Cela se produit dans le cas où l'impédance amont est adaptée pour supprimer l'oscillation qui apparaît dans le système. Le découplage des éléments composant le système de combustion a déjà été examiné sur différentes configurations par Schuller et al. (2012). Dans cette étude les auteurs se penchent sur le découplage induit par la géométrie et les différences de température dans le système. Suivant la valeur d'un paramètre Ξ, faisant intervenir les températures des différentes sections T_n ainsi que leur surface S_n, la relation de dispersion peut être modifiée. Comme cela a déjà été exposé dans les chapitres précédents, cette relation décrit la dynamique du brûleur et permet de calculer les modes propres du système. Lorsque le paramètre Ξ prend des valeurs petites, la relation se simplifie et permet de montrer que les cavités du brûleur possèdent chacune leur propre fréquence. Ces solutions spécifiques, révèlent le découplage des cavités. Ceci permet d'expliquer les phénomènes d'oscillation rencontrés dans certaines chambres de combustion présentant des fréquences différentes de celles liées aux modes des cavités couplées. Cette notion de découplage peut avoir un intérêt pour la conception, car elle peut être utilisée pour supprimer les instabilités auto-entretenues. Ceci est utilisé par exemple dans les moteurs fusées (F. Culick et al. (1995)) où une perte de charge est volontairement introduite entre les lignes d'injection et la chambre de combustion. Cette perte de charge empêche le couplage entre cette dernière et les parties supérieures. De plus, comme mentionné par Schuller et al. (2012), connaître les conditions de découplage permet de dimensionner un système afin d'éviter une réponse de la flamme aux fréquences propres de la chambre.
Comme il l'a été montré dans les chapitres précédents, les modes propres du brûleur peuvent être calculés à l'aide d'un réseau de cavités couplées. Ainsi, un modèle à deux cavités est utilisé dans une première section afin d'identifier les conditions de découplage acoustique sur le foyer MIC. La seconde partie décrit une expérience et des calculs dans des conditions plus réalistes. Ce type d'analyse, de l'influence du coefficient de réflexion de la cavité amont sur les instabilités de combustion, a déjà été envisagé avec une mise en oeuvre concrète dans le cas d'un brûleur swirlé par Tran et al. (2009a); Tran et al. (2009b). Dans ces études, le coefficient de réflexion du système de prémélange a été diminué jusqu'à une valeur suffisamment basse pour atténuer les instabilités observées dans le foyer. On peut trouver un travail détaillé sur ces phénomènes dans les manuscrits de thèse de Tran (2009) et Lamraoui (2011) en l'absence de combustion instationnaire. L'étude développée ci-dessous suit celles engagées par Lamraoui et al. (2011) et Richecoeur et al. (2013) dans des configurations

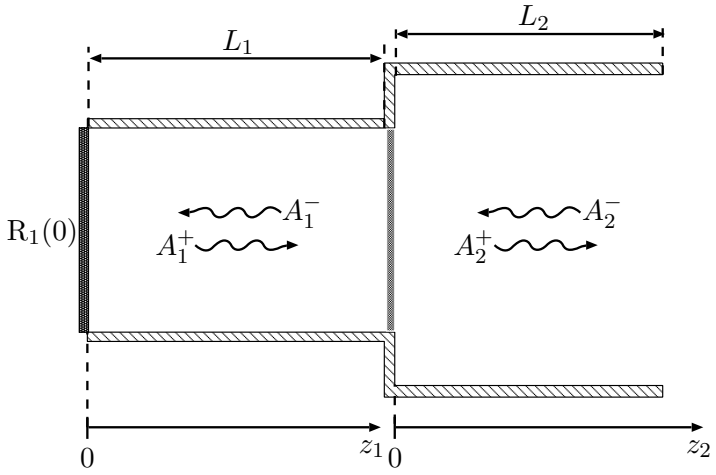

Figure 11.1: *Modèle de brûleur utilisé pour l'analyse du découplage sous l'influence de la condition amont. Une flamme est positionnée à l'interface entre les 2 tubes de longueur L_1 et L_2.*

similaires, mais où l'influence de la flamme n'a pas été prise en compte.

11.2 Modes couplés sur deux cavités idéales

Le cas de deux cavités couplées au travers d'un changement de section est tout d'abord considéré. On peut facilement déduire dans ce cas l'effet des modifications de l'impédance amont sur les modes propres du système. Le modèle est présenté dans le paragraphe suivant et l'analyse est effectuée dans un deuxième temps.

11.2.1 Modèle à deux cavités

Le brûleur est présenté à la Fig. 11.1. Le modèle correspond à une version simplifiée des équations détaillées dans le Chapitre 8. La grille d'injection ainsi que sa cavité annulaire ne sont pas prises en compte. Le coefficient de réflexion à la sortie du confinement est idéal $R_2(L_2) = -1$. Un coefficient de réflexion $R_1(0)$ est appliqué à l'extrémité de la partie amont. Ce coefficient inclut le piston et le système d'amortissement. La matrice $\boldsymbol{M}$, décrivant la dynamique du système, peut donc s'écrire sous la forme suivante :

$$\begin{pmatrix} 1 & -R_1(0) & 0 & 0 \\ 0 & 0 & e^{ik_2L_2} & e^{-ik_2L_2} \\ e^{ik_1L_1} & e^{-ik_1L_1} & -1 & -1 \\ \mathcal{B}e^{ik_1L_1} & -\mathcal{B}e^{-ik_1L_1} & -1 & 1 \end{pmatrix} \begin{pmatrix} A_1^+ \\ A_1^- \\ A_2^+ \\ A_2^- \end{pmatrix} = 0 \qquad (11.1)$$

où le terme $\mathcal{B}$ correspond à :

$$\mathcal{B} = \frac{S_1}{S_2}\frac{\rho_2 c_2}{\rho_1 c_1}\left[1 + Ge^{i\varphi}\left(\frac{T_f}{T_1} - 1\right)\right] \tag{11.2}$$

La relation de dispersion se déduit en calculant le déterminant de la matrice $\boldsymbol{M}$ dont les racines ($\det(\boldsymbol{M}) = 0$) déterminent les solutions non triviales du système à 4 équations. Cette relation peut s'écrire sous cette forme :

$$\begin{aligned}
&e^{ik_2L_2}\left\{e^{-ik_1L_1} - \Xi\left[1 + Ge^{i\varphi}\left(\frac{T_f}{T_1} - 1\right)\right]e^{-ik_1L_1}\right\}\\
&+e^{-ik_2L_2}\left\{e^{-ik_1L_1} + \Xi\left[1 + Ge^{i\varphi}\left(\frac{T_f}{T_1} - 1\right)\right]e^{-ik_1L_1}\right\}\\
&+\mathrm{R}_1(0)\,e^{ik_2L_2}\left\{e^{ik_1L_1} + \Xi\left[1 + Ge^{i\varphi}\left(\frac{T_f}{T_1} - 1\right)\right]e^{ik_1L_1}\right\}\\
&+\mathrm{R}_1(0)\,e^{-ik_2L_2}\left\{e^{ik_1L_1} - \Xi\left[1 + Ge^{i\varphi}\left(\frac{T_f}{T_1} - 1\right)\right]e^{ik_1L_1}\right\} = 0
\end{aligned} \tag{11.3}$$

Cette relation permet de calculer les modes propres du brûleur composé de deux cavités. Ces modes propres prennent une forme particulière lorsque le coefficient de réflexion $\mathrm{R}_1(0)$ est réglé pour amortir les oscillations qui peuvent apparaître.
On peut tout d'abord examiner la relation de dispersion dans le cas d'une réflexion parfaite au niveau de la cavité amont, $\mathrm{R}_1(0) = 1$. Ainsi, l'Eq. (11.3) se simplifie comme suit :

$$\begin{aligned}
&\cos(k_1L_1)\cos(k_2L_2) -\\
&\Xi\left[1 + \left(\frac{T_f}{T_1} - 1\right)Ge^{i\varphi}\right]\sin(k_1L_1)\sin(k_2L_2) = 0
\end{aligned} \tag{11.4}$$

Dans le cas où un système d'amortissement est mis en place dans la partie amont à la même position que la tête du piston, comme étudié dans le Chapitre 10, Fig. 10.3, le coefficient de réflexion diminue et l'amplitude de l'onde réfléchie (A_1^+) est réduite par rapport à celle de l'onde incidente (A_1^-). Si on considère le cas idéal où $\mathrm{R}_1(0) = 0$, la relation de dispersion prend une forme très particulière :

$$e^{-ik_1L_1}\left\{\cos(k_2L_2) - i\,\Xi\left[1 + Ge^{i\varphi}\left(\frac{T_f}{T_1} - 1\right)\right]\sin(k_2L_2)\right\} = 0 \tag{11.5}$$

Cette nouvelle forme révèle un comportement qui diffère de celui de l'Eq. (11.4). En effet, les seules solutions s'obtiennent grâce au deuxième terme de l'équation

:

$$\cos(k_2 L_2) - i\,\Xi\left[1 + Ge^{i\varphi}\left(\frac{T_f}{T_1} - 1\right)\right]\sin(k_2 L_2) = 0 \tag{11.6}$$

Cette relation ne dépend que de la longueur du confinement L_2 et n'est plus influencée par une modification de la longueur amont L_1. Ainsi, il apparaît que l'impédance amont supprime complètement la possibilité d'une oscillation dans la cavité d'alimentation mais l'instabilité subsiste dans le tube de confinement de manière autonome (Lamraoui (2011)).
Ce phénomène est analysé dans la section suivante qui présente les calculs effectués au moyen de cette relation de dispersion en tenant compte de la réponse de flamme mesurée pour la grille d'épaisseur $l = 15$ mm.

11.2.2 Analyse non-linéaire des instabilités amorties

L'analyse non-linéaire de la dynamique du brûleur composé de deux cavités couplées avec ou sans système d'amortissement consiste à effectuer les mêmes calculs que dans le Chapitre 8. La relation de dispersion (Eq. (11.3)) est résolue pour différentes longueurs d'alimentation L_1 après avoir réglé une taille de confinement L_2. La dynamique de flamme est représentée par la réponse mesurée sur la grille d'épaisseur $l = 15$ mm. Les courbes sont données à la Fig. 5.5. L'influence de la grille d'épaisseur 15 mm n'est pas considérée dans la modélisation développée dans la partie précédente.
Le cas du confinement $L_2 = 0.10$ m est d'abord analysé. Le balayage en L_1 est effectué entre 0.10 m et 0.55 m. Sans système d'amortissement, le comportement du brûleur se rapproche du cas plus réel traité dans le Chapitre 8. Le calcul du diagramme de bifurcation est présenté à la Fig. 11.2. On peut d'abord constater que trois modes sont toujours présents quand on fait varier L_1. Cependant, ces résultats diffèrent par rapport à ceux du Chapitre 8 du fait de l'idéalisation des conditions aux limites qui ne tiennent plus compte d'un amortissement. En effet, le piston est parfaitement réfléchissant $R_1(0) = 1$ et la fluctuation de pression est supposée nulle en sortie de confinement $p'_2(L_2) = 0$, associée à un coefficient de réflexion idéal $R_2(L_2) = -1$. En lisant le diagramme de bifurcation, on constate que le mode 1 est instable de $L_1 = 0.10$ m à 0.27 m. Aucune bande stable n'existe et le passage au mode 2 s'effectue à $L_1 = 0.27$ m jusqu'à $L_1 = 0.55$ m. La présence sous-jacente du mode 3 de $L_1 = 0.40$ m à 0.55 m, avec une amplitude identique à celle du mode 2 de $L_1 = 0.48$ m à 0.55 m, indique la possibilité d'une oscillation simultanée sur deux modes comme étudié dans le Chapitre 9.
Cette configuration est maintenant étudiée avec le système d'amortissement idéal placé dans la cavité amont L_1. Le coefficient de réflexion est fixé à $R_1(0) = 0$ pour observer l'effet sur les calculs d'instabilités. Le calcul est tout d'abord effectué pour la plus petite amplitude d'oscillation, c'est-à-dire $u_{rms}/U_b = 0.0638$. En considérant la plage de fréquence des trois premiers

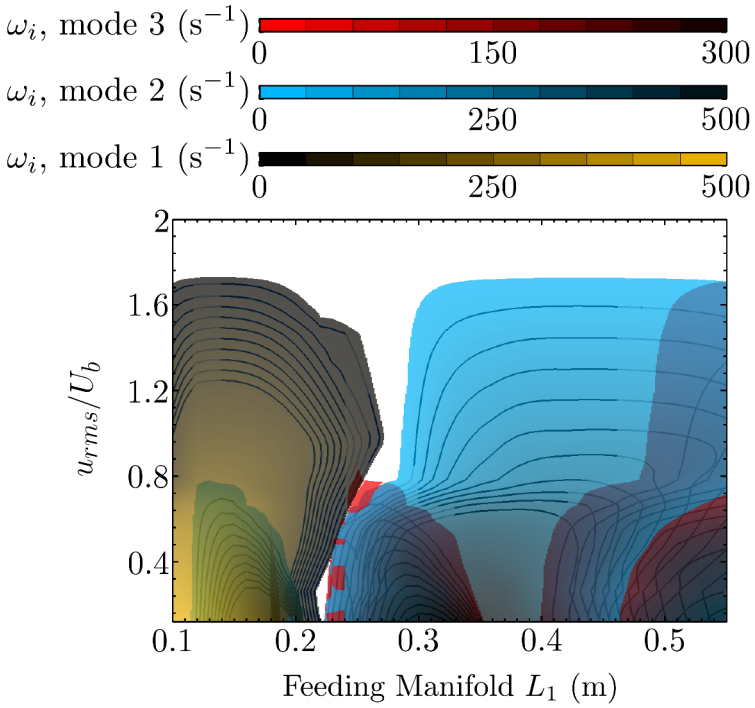

Figure 11.2: *Taux de croissance ω_i pour la configuration confinée à $L_2 = 0.10$ m. Le calcul est effectué pour des longueurs L_1 allant de 0.10 m à 0.55 m. Les conditions aux limites sont idéales et la plaque perforée supportant la flamme n'est pas représentée.*

modes, une seule solution existe pour la relation de dispersion. Cette solution est située à plus haute fréquence f = 1301 Hz pour un taux de croissance négatif ω_i = -208 s^{-1}. Lorsque l'amplitude u_{rms}/U_b augmente, la fréquence f et le taux de croissance ω_i de la solution de la relation de dispersion ne changent presque pas. L'oscillation ne peut pas démarrer, ce qui paraît normal étant donné que le gain s'effondre pour les hautes fréquences, traduisant ainsi l'absence d'un apport d'énergie par la flamme. Cette solution à plus haute fréquence correspond au mode 1 de la cavité aval L_2 (le tube de confinement) qui fonctionne indépendamment de la partie amont L_1. Cette fréquence est proche de celle que l'on peut calculer en représentant la partie confinée L_2 par un tube fermé-ouvert $c_2/4L_2$ = 1503 Hz.

Le découplage semble logique dans la mesure où l'onde réfléchie dans le tube amont de longueur L_1 est complètement supprimée car le coefficient de réflexion est nul $\mathrm{R}_1(0) = 0$. Ces calculs ont aussi été effectués pour les autres confinement L_2 et permettent de trouver les fréquences de résonance. Il apparaît que dans les autres cas de confinement L_2, la première racine de la relation de dispersion possède un taux de croissance ω_i positif et une fréquence f qui décroît lorsque la longueur du tube L_2 augmente. Les résultats pour les quatre confinements sont présentés à la Fig. 11.3. On retrouve ainsi le comportement du brûleur avec une condition $\mathrm{R}_1(0) = 0$ optimale. Il est maintenant intéressant d'utiliser le modèle pour estimer la limite au-delà de laquelle les cavités ne peuvent plus être considérées comme découplées.

Le coefficient de réflexion est augmenté par pas de 0.1 afin d'observer l'apparition des solutions correspondants aux cavités couplées dans la relation de dispersion. Le tube de confinement court L_2 = 0.10 m est d'abord analysé. Pour L_1 = 0.10 m les modes des cavités couplées apparaissent lorsque le système d'amortissement présente un module $|\mathrm{R}_1(0)| = 0.1$ quelle que soit la phase $\phi_1(0)$ utilisée. Néanmoins, la solution du tube de confinement L_2 subsiste de manière séparée. La cavité aval est découplée du reste du brûleur. Pour $|\mathrm{R}_1(0)| = 0.2$ la solution dans la cavité aval existe pour certaines phases $\phi_1(0)$. Cependant, pour $|\mathrm{R}_1(0)| = 0.3$ cette séparation n'existe plus et la racine rejoint la valeur trouvée pour un système couplé. Dans cette configuration de confinement, il apparaît que le découplage persiste jusqu'à $|\mathrm{R}_1(0)| = 0.2$.

En analysant les autres longueurs du tube d'alimentation L_1, on peut observer que la séparation des solutions n'existe plus à partir de L_1 = 0.12 m dès que le coefficient de réflexion devient non nul, c'est-à-dire lorsque $|\mathrm{R}_1(0)| = 0.1$. Ainsi, le découplage constaté pour L_1 = 0.10 m n'apparaît que lorsque $L_1 \approx L_2$. Dans le but d'expliciter ce phénomène, les autres tubes à flamme L_2 sont examinés.

Le tube L_2 = 0.20 m est utilisé et le coefficient de réflexion $\mathrm{R}_1(0)$ est augmenté de 0 à 0.1. Les solutions présentent le même comportement que celui observé précédemment. Une racine apparaît pour un coefficient de réflexion nul $|\mathrm{R}_1(0)| = 0$ et persiste lorsque le coefficient de réflexion est augmenté à 0.1. De plus, contrairement au cas précédent, la solution séparée subsiste quelle que

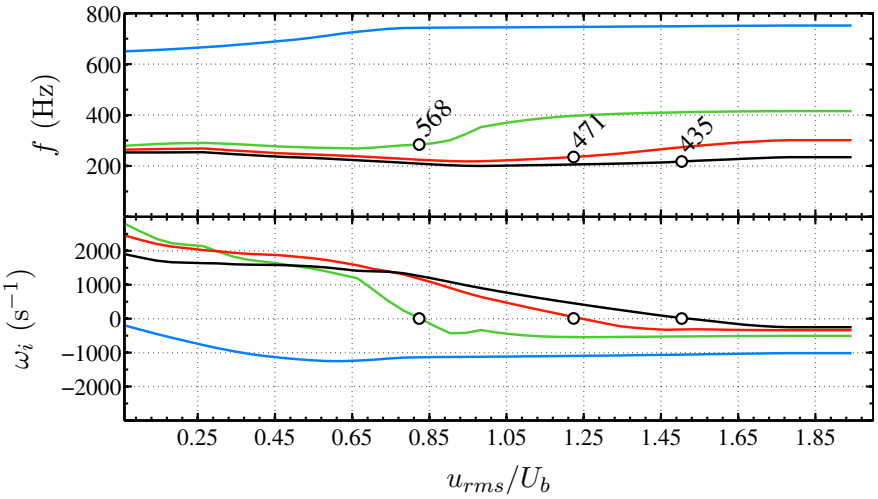

Figure 11.3: *Fréquence f et taux de croissance ω_i de la cavité aval L_2 calculés avec un coefficient de réflexion $R_1(0) = 0$ dans la cavité amont. Les différentes couleurs indiquent la longueur L_2 du tube de confinement. Le plus court $L_2 = 0.10$ m correspond au bleu (−), $L_2 = 0.20$ m est tracé en vert (−), $L_2 = 0.30$ m apparaît en rouge (−) et le plus grand $L_2 = 0.40$ m est représenté par une ligne noire (−). Un symbole circulaire (○) indique la fréquence f du cycle limite à $\omega_i = 0$ s^{-1}. Cette fréquence f est indiquée au-dessus du symbole.*

soit la valeur du coefficient de réflexion mis en place dans la cavité amont L_1 (les calculs sont effectués pour un niveau d'amplitude faible $u_{rms}/U_b = 0.0638$). On retrouve le même comportement pour les deux derniers tubes à flamme L_2 = 0.30 m et 0.40 m. Ce comportement est illustré dans les Figs. 11.4 et 11.5 qui présentent le module de la relation de dispersion dans le plan fréquence, taux de croissance (f en fonction de ω_i) pour le tube à flamme $L_2 = 0.20$ m et un coefficient de réflexion amont $R_1(0) = 1$. La Figure 11.4 correspond au cas $L_1 = 0.10$ m alors que la Fig. 11.5 présente l'évolution du module pour L_1 = 0.20 m. Le coefficient de réflexion $R_1(0) = 1$ est maximum afin de montrer que la solution séparée subsiste quelle que soit la valeur de celui-ci.
Ces deux figures montrent les racines de la relation de dispersion correspondant aux fréquences propres du brûleur. L'échelle de couleur, présentée sur la droite, indique l'amplitude du module de la relation de dispersion. Les minima du module, représentant les racines de la relation de dispersion, apparaissent en blanc au creux des zones décroissantes bleues. L'utilisation de la couleur blanche pour indiquer les minima a été effectuée afin de distinguer les minima globaux des minima locaux qui ne passent pas par zéro. Ces derniers ne représentent pas une racine de la relation de dispersion et ne correspondent pas à des modes propres du système. Sur la première figure (Fig. 11.4), une solution présente un taux de croissance positif lorsque la flamme oscille à u_{rms}/U_b = 0.0638. Un autre minimum ayant presque la même fréquence apparaît dans

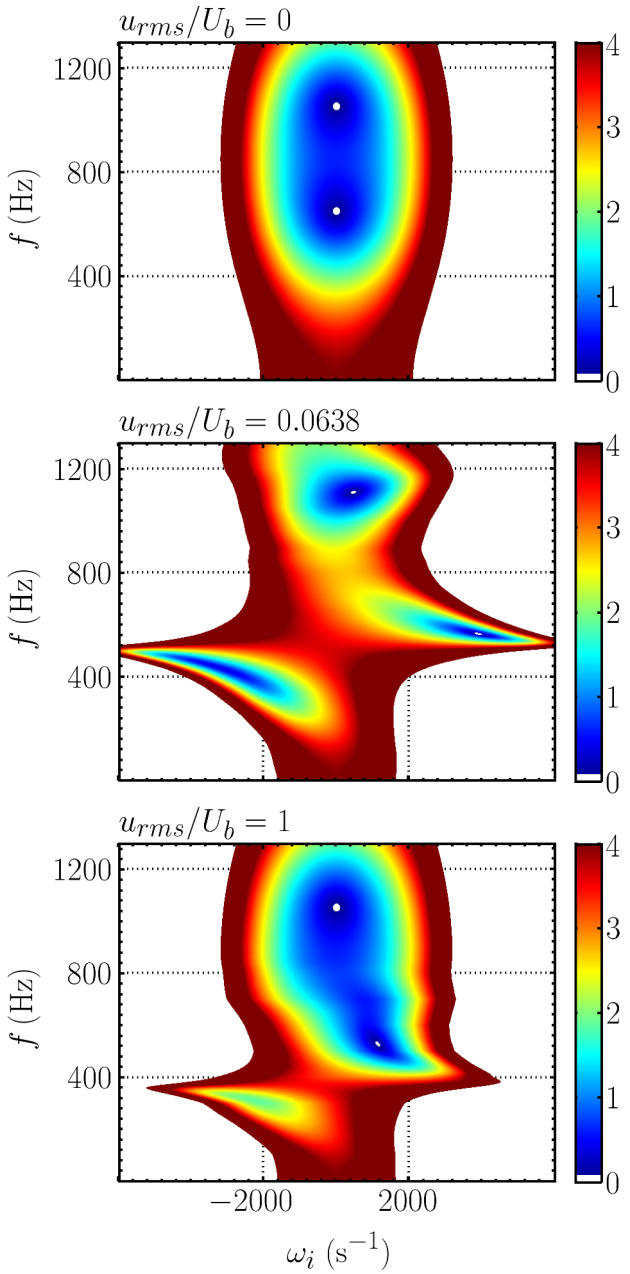

Figure 11.4: *Module de la relation de dispersion présentant les racines correspondant aux modes propres d'oscillation dans le brûleur. La fréquence f est située sur l'axe des ordonnées, tandis que le taux de croissance ω_i se trouve en abscisse. Chaque graphique correspond à une amplitude u_{rms}/U_b indiquée en haut à gauche. Les cas représentés ici sont liés à la géométrie $L_2 = 0.20$ m et $L_1 = 0.10$ m. Le coefficient de réflexion amont $\mathrm{R}_1(0) = 1$ correspond à une surface parfaitement réfléchissante. L'échelle de l'amplitude du module est indiquée sur la droite. Les minima du module de la relation de dispersion passant par 0 sont coloriés en blanc, en modifiant l'échelle de couleur, afin d'être différenciés des minima locaux ne passant pas par 0.*

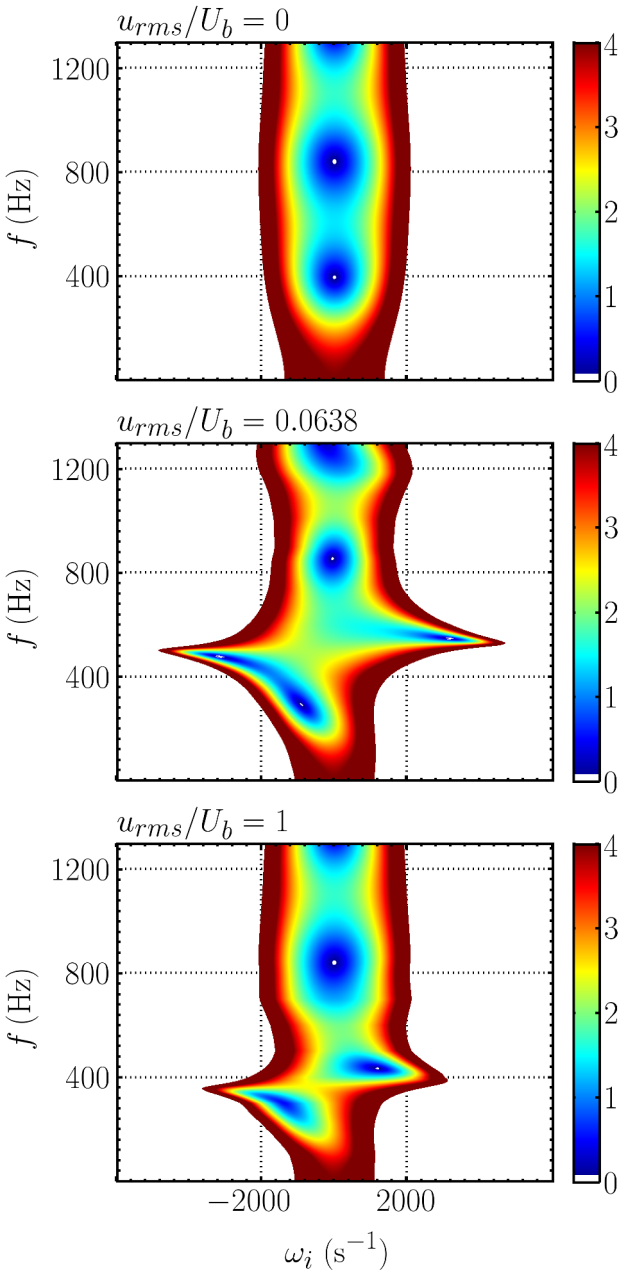

Figure 11.5: *Module de la relation de dispersion présentant les racines correspondant aux modes propres d'oscillation dans le brûleur. La fréquence f est située sur l'axe des ordonnées, tandis que le taux de croissance ω_i se trouve en abscisse. Chaque graphique correspond à une amplitude u_{rms}/U_b indiquée en haut à gauche. Les cas représentés ici sont liés à la géométrie $L_2 = 0.20$ m et $L_1 = 0.20$ m. Le coefficient de réflexion amont $\mathrm{R}_1(0) = 1$ correspond à une surface parfaitement réfléchissante. L'échelle de l'amplitude du module est indiquée sur la droite. Les minima du module de la relation de dispersion passant par 0 sont coloriés en blanc, en modifiant l'échelle de couleur, afin d'être différenciés des minima locaux ne passant pas par 0.*

la zone des taux de croissance négatif. Néanmoins, ce minimum ne passe pas par zéro et ne représente donc pas un mode propre. Lorsque l'amplitude augmente à $u_{rms}/U_b = 1$, cette solution tend vers $\omega_i = 0$. La solution apparaît à une fréquence de 561 Hz, proche de celle trouvée dans l'analyse de la cavité aval L_2 présentée dans la Fig. 11.3.
Si on analyse la deuxième géométrie $L_2 = 0.20$ m de la Fig. 11.5, on observe un comportement très différent. En effet, dans la zone de fréquence située aux alentours de $f = 500$ Hz, on remarque que les solutions sont beaucoup plus nombreuses. Pour l'amplitude $u_{rms}/U_b = 0.0638$, le premier mode des cavités couplées correspond à $f = 280$ Hz et $\omega_i = -720$ s^{-1}. Le second mode se trouve à $f = 840$ Hz et $\omega_i = -90$ s^{-1}. Contrairement à la longueur précédente $L_1 = 0.10$ m, deux autres solutions existent. La première se positionne à $f = 546$ Hz et $\omega_i = 3130$ s^{-1}, alors que la deuxième présente un taux de croissance négatif $\omega_i = -3122$ s^{-1} à $f = 476$ Hz. Là aussi, la fréquence caractérisée par un taux de croissance positif correspond à la fréquence de la cavité aval analysée précédemment dans la Fig. 11.3. Néanmoins, l'existence de solutions multiples indique que la cavité aval L_2 est indépendante des solutions des cavités couplées situées dans la zone de taux de croissance négatif.
Le comportement détaillé ci-dessus se retrouve pour les tubes de confinement plus longs $L_2 = 0.30$ m et 0.40 m.

11.2.3 Analyse théorique de la relation de dispersion

La relation de dispersion est analysée pour le modèle des deux cavités couplées idéales et on envisage le cas particulier $L_1 = L_2$. Ce modèle est considéré lorsque le coefficient de réflexion amont est $\mathrm{R}_1(0) = 1$. La relation de dispersion obtenue correspondant à l'Eq. (11.4) est rappelée ci-dessous :

$$\begin{aligned} &\cos(k_1 L_1)\cos(k_2 L_2) - \\ &\Xi\left[1 + \left(\frac{T_f}{T_1} - 1\right) G e^{i\varphi}\right] \sin(k_1 L_1)\sin(k_2 L_2) = 0 \end{aligned} \tag{11.7}$$

Compte tenu des températures dans les deux cavités, $T_1 = 300$ K et $T_2 = 1100$ K ($L_2 = 0.20$ m), on va aussi supposer que $c_1 \approx c_2/2$. Comme $L_1 = L_2$, la relation 11.7 prend la forme suivante :

$$\begin{aligned} &\cos(2k_2 L_2)\cos(k_2 L_2) - \\ &\Xi\left[1 + \left(\frac{T_f}{T_1} - 1\right) G e^{i\varphi}\right] \sin(2k_2 L_2)\sin(k_2 L_2) = 0 \end{aligned} \tag{11.8}$$

Ainsi, les termes qui apparaissent en $2k_2L_2$ peuvent être développés et conduisent à la relation suivante :

$$\begin{aligned}&\cos(k_2L_2)\Bigg\{\cos^2(k_2L_2)-\\&\left\{1+2\,\Xi\left[1+\left(\frac{T_f}{T_1}-1\right)Ge^{i\varphi}\right]\right\}\sin^2(k_2L_2)\Bigg\}=0\end{aligned} \tag{11.9}$$

On constate que la relation de dispersion se décompose en un produit de trois termes. Le terme situé à l'intérieur de la parenthèse est de la forme $a^2 - b^2$ et peut être factorisé. Finalement, on trouve que les racines de la relation de dispersion sont données par :

$$\begin{aligned}&\cos(k_2L_2)=0\\&\cos(k_2L_2)-\sqrt{1+2\,\Xi\left[1+\left(\frac{T_f}{T_1}-1\right)Ge^{i\varphi}\right]}\sin(k_2L_2)=0\\&\cos(k_2L_2)+\sqrt{1+2\,\Xi\left[1+\left(\frac{T_f}{T_1}-1\right)Ge^{i\varphi}\right]}\sin(k_2L_2)=0\end{aligned} \tag{11.10}$$

La décomposition de la relation de dispersion aux alentours d'une géométrie mettant en jeu une longueur de cavité amont L_1 du même ordre que celle de la cavité aval L_2 a permis de montrer que les cavités du système peuvent fonctionner de manière indépendante, conduisant à des solutions multiples. Ces solutions multiples ont été étudiées au Chapitre 9. Ainsi, il a été trouvé que les cycles limites ne peuvent pas osciller à amplitude constante lorsqu'une même fréquence d'oscillation apparaît avec des taux de croissance ω_i positif et négatif.

Dans le présent chapitre, l'amortissement par la cavité amont L_1 a montré que le tube de confinement peut entrer en oscillation de manière indépendante, dans la mesure où sa fréquence de résonance se situe dans une zone où la flamme peut apporter de l'énergie.

Cette analyse, montre que la fréquence instable aux alentours de 500 Hz, trouvée dans le Chapitre 9 pour les confinements $L_2 = 0.20$ m et 0.30 m, est liée à la partie aval du brûleur. Dans certain cas, cette cavité agit indépendamment du reste du brûleur, expliquant les observations du Chapitre 9.

Conclusion

The present study is focused on combustion instabilities resulting from a resonant coupling between the acoustic eigenmodes of a system and the flame. This phenomenon, also designated as thermoacoustic coupling, is commonly found in practical devices and in particular in gas turbine combustors, aero-engines, industrial burners or rocket engines.
The two milestones of the present investigation concern the prediction of such phenomena and their control. This investigation pursues a range of studies initiated in recent years at EM2C laboratory which have relied on various experiments to highlight a wide variety of physical processes of combustion dynamics. Previous research can be found in doctoral theses Ducruix (1999), Schuller (2003), A.-L. Birbaud (2006), Noiray (2007) and Palies (2010) and in many articles published by the combustion dynamics team. The present investigation is more closely linked to the thesis of Noiray (2007) where the unified FDF framework was devised and exploited to predict nonlinear features of combustion instabilities of an open flame configuration comprising an upstream manifold of variable size and a multipoint injection element. The work of Noiray is continued here to predict the limit cycles recorded in various configurations involving a confined combustion zone. The system comprises the same upstream manifold but the flame region is now confined by tubes of different sizes. As in the works carried out previously the present investigation relies on experimentation and theoretical and numerical modeling. The use of experiments in parallel to modeling efforts allows to check analytical tools devised in this research. The present study extends previous work in many different ways :

- The FDF framework is applied to confined configurations for a range of geometries. This is achieved with a piston, allowing an easy change of feeding manifold length L_1. The analysis relies on systematic comparisons between modeling results and experiments. Changes in geometries allow to test calculations in a generic configuration and for a large set of experiments.

- An improved description of the combustor acoustics is developed by accounting for the complex acoustic boundaries and details of the burner geometry in the modeled system.

- The broad experimental range reveals new kinds of limit cycles which are essentially typified by a variation of their amplitude and frequency as a function of time. This variety is sometimes described in the literature, but not in a systematic fashion.

- Tools of dynamical system theory, including nonlinear time series analysis, are applied to these variable amplitude limit cycles.

- FDF calculations are considered to examine ranges where such limit cycles arise and are used to uncover the subtending processes.

- A passive control method, involving a bias flow perforated plate backed by a cavity (BFP), is then used as a damper and its influence on combustion instability is investigated. This perforated plate operates in a flow regime which was recently studied by Tran (2009) and Scarpato et al. (2012). In this application to control self-sustained combustion instabilities, the FDF framework is used to understand the various oscillations or stable states encountered.

The experimental setup comprises a feeding manifold of variable length L_1. This length is obtained with a piston used to premix reactants and deliver the mixture to the system. The head is machined to offer a quasi perfect reflecting boundary condition. At the top of the feeding manifold, a perforated plate is set to anchor a collection of small laminar conical flames. Two perforated plates of different thickness have been considered. One features a thickness $l =$ 3 mm while the other is increased to $l = 15$ mm. The flame region is enclosed in a quartz tube of length L_2 open to the atmosphere. Four lengths were available stretching from $L_2 = 0.10$ m to 0.40 m by steps of 10 cm. The feeding manifold length L_1 has been swept from 0.10 m to 0.55 m by steps of 1 cm. In addition, it has been possible to extend this feeding manifold to $L_1 = 0.77$ m with an additional tube. By setting a feeding manifold length L_1 with a certain confinement tube L_2, the burner features combustion regimes which are either stable or unstable. The unstable combustion regime is typified by amplitude-frequency couples. In some cases, the amplitude-frequency couple never reaches a fixed value. The various kinds of limit cycles are analyzed theoretically by making use of the FDF framework. This enables to take into account the nonlinearity of the flame, which is considered as the central mechanism of oscillation in the present study. The particularity of the burner is to allow a continuous sweep of feeding manifold length L_1 for each confinement tube L_2. This enables to obtain various combustion regimes and follow their evolution by sweeping L_1. It has the advantage to provide a cluster of data and not an isolated point which is often difficult to interpret.

Main contributions

- In terms of flame response :
  - The flame response is acquired on a separate set of experiments. Two flame holders are successively set in the burner and the corresponding FDFs are measured. One of the two FDFs is characterized with a small confinement tube $L_2 = 0.10$ m. The confined and unconfined FDFs indicate that the confinement tube does not influence the gain G and phase φ. The quartz tube diameter is sufficiently large to preclude any interaction with the flame sheet.
  - It is found that the flame response cannot be considered as a separate module grafted on the perforated plate, because the perforations of the thin and thick flame holders do not feature the same velocity profile and therefore the same flame front deformations.
  - The flame response is also represented in terms of reflection coefficient. This technique allows to measure this important characteristic without any optical access. Nevertheless, one has to measure the velocity fluctuation level to obtain the reflection coefficient amplitude.
- In terms of prediction of limit cycles with constant amplitude :
  - A basic model has been devised and the amplitude-frequency couples are suitably predicted. Some differences appear but predictions remain reliable for most of the feeding manifold lengths L_1. This work has been presented during the ASME Turbo Expo, Glasgow, UK (2010) and published in the Journal of Engineering for Gas Turbines and Power (Boudy et al. (2011b)).
  - The basic model allows to predict specific phenomena like mode switching during the growth of oscillation. Calculations can be used to examine the influence of the FDF. While the evolution of the gain G with the amplitude modifies the oscillation level of limit cycle, the phase φ influences some special features like triggering, hysteresis, mode switching and also modification of the limit cycle amplitude. This work has been presented during the 33^{rd} International Symposium on Combustion, Beijing, China (2010) and published in the Proceedings of the Combustion Institute (Boudy et al. (2011a)).
  - A detailed model with the second flame holder has been derived by taking into account an improved description of the burner acoustic response to flow perturbations. It is found that : (1) Predictions match reasonably the experiments in all the confined configurations, (2) A frequency shift from the acoustic eigenmodes up to 100 Hz is observed and retrieved by calculations for some geometries, (3) Mode shape recon-

struction confirms the choice of Melling's model (Melling (1973)) in the description of the flame holder dynamics. (4) It is also shown that a new triggering range exists for some geometries.

- The detailed system model yields improved predictions for frequency-amplitude couples. The analysis of growth rate ω_i overlapping trajectories indicates that three factors are important in order to have a good estimate of the trajectories evolution as a function of amplitude : (1) The flame tube gas temperature T_2, (2) The flame temperature T_f which differs from the value of the gas temperature T_2 in the flame tube, (3) The nonlinear response of the boundary condition which influences the damping in the system.

- In terms of prediction of limit cycles with variable amplitude :

  - It is first shown that in certain ranges the system features Galloping Limit Cycles (GLCs) conveying the idea of a traveling amplitude variation as a function of time. The GLCs are easily identified from their specific auditive signature, but best analyzed by using dynamical tools in addition to the classical spectral analysis. The wavelet and the nonlinear time series analysis provide additional informations. It is shown that the variable amplitude limit cycles observed in the present experiments belong to four general categories.
  - One kind of GLCs is sustained by two modes and the FDF allows to delineate conditions for the occurrence of such oscillations. This work has been presented during the 3^{rd} INCA workshop, Toulouse, France (2011) and published in Comptes Rendus Mécanique de l'Académie des Sciences (Boudy et al. (2013)).
  - Another kind featuring irregular variations of the amplitude is qualified as chaotic oscillation and is observed for small lengths of the feeding manifold L_1 and involves a low frequency instability around the first acoustic eigenmode. The FDF calculations allow to find the feeding manifold lengths L_1 where these states exist and also the minimum and maximum of the signal envelope observed in experiments. This work has been presented during the ASME Turbo Expo, Copenhagen, Denmark (2012) (Boudy et al. (2012)).

- In terms of control of instability:

  - The analysis is concerned with two bias flow perforates (BFPs). One of the two devices is designed to operate in the so-called low Strouhal number range. It is shown that the reflection coefficients of the BFPs are suitably retrieved with theoretical models. One of the two BFPs features chamfers but it is found that its perforation edges do not influence the response of the system.

- It is shown that the use of a well designed perforated baffle allows to cancel large velocity fluctuations up to $u_{rms}/U_b = 1.45$.
- It is confirmed that a broad frequency bandwidth of the damper is obtained by operating at low Strouhal numbers leading to the cancellation of various oscillations. This is also obtained when the oscillation is sustained by two modes or when the frequency is shifted from the target value.
- The role of the nonlinear response in the failure to suppress oscillations is investigated. As the system should damp low amplitude perturbations, the growth rate ω_i must be reduced, hindering any initiation of instability. In certain cases, it is found that the damper fails to suppress the oscillation for various reasons. On the one hand, the oscillation may be driven by another mode characterized by a frequency which is sufficiently different from the target frequency used in the damper design. On the other hand, it is shown that some of the combustion dynamics are decoupled from the response of the upstream manifold and are therefore insensitive to the damper. This decoupling is in fact the result from the change in boundary condition induced by the damper.

Perspectives

The analysis of combustion instabilities in the generic multiple flame combustor has allowed to answer various questions, but gives rise to new issues which need to be tackled in the future. Two guidelines emerge from the present study :

- Firstly, it would be interesting to close various remaining questions concerning the geometry under investigation :
  - As mentioned in Chapter 8, prediction of frequencies and amplitudes relies on a good estimate of the damping in the burner. This damping is mainly linked to the boundary conditions in the present system. It would be interesting to have a nonlinear model to represent the response of the outlet of the flame tube which features large velocity fluctuations.
  - The temperature T_2 also influences the predictions in the system. Thus, it would be important to have a better estimate of what is happening in this zone of hot combustion products.
  - Concerning the flame response one would like to have values for large oscillation levels. From a technical point of view, this response has been measured in a limited range of amplitudes and extrapolated to the higher levels. It would be interesting to try to measure the FDF in a wider range of amplitudes and frequencies.

  - By analyzing predictions, it is found that the growth rate ω_i features large values compared to the ones found, for example, in an unconfined geometry. Thus, it would be interesting to undertake a comparison of the growth rates with the calculations by using for example active control methods. This would give access to the growth rate which could then be compared with predictions.

- The second point is linked to the next steps in the application of the FDF. This framework is deemed to be an efficient and reliable tool for the prediction of combustion instabilities. It provides a full view on the combustion dynamics in a burner.

  - It would be worth applying this framework to other well controlled systems and generalize the method to full annular configurations with multiple injectors featuring azimuthal instabilities. More specifically it would be interesting to test the use of the same FDF for each flame which may interact and thus modify the response. Besides, the use of small laminar conical flames as done here could be of value. These flames present advantages for combustion instability study. They are typified by a phase evolution of their response for growing amplitudes and they are able to provide energy at high frequency. This could be used in the annular configuration now being studied at EM2C.
  - The FDF could be included in an Helmholtz solver to calculate more complicated systems. This work is already engaged in collaboration with the "Institut de Mathématiques et de Modélisation" of Montpellier (I3M), France and the AVSP code for two experimental configurations studied at EM2C. The first concerns the analysis of the swirled burner used by Palies et al. (2011) and the other deals with the multiple flame combustor of the present study, which is a part of the PhD thesis of Cuquel (2013).
  - The simultaneous oscillation of two modes and the chaotic states have been analyzed through the frequency domain representation of the FDF framework. The overlap of positive growth rate ω_i trajectories or the presence of one mode with two solutions has to be considered in the time domain. It is worth deriving a dynamical nonlinear model reflecting the evolution of the oscillation as a function of time by using the FDF calculation results. This would help in the interpretation of the FDF calculations and confirm the origins of the variable amplitude states.

Appendices

Appendix A

Influence of the nonlinearity of the FDF phase lag

This appendix examines changes in the bifurcation diagrams predicted with two different FDF. The first one features a gain and a phase lag which are a function of frequency and perturbation level as shown in Chapter 5, while the second FDF is typified by a frequency dependent phase lag. The phase lag of this modified FDF is taken equal to the value measured for the smallest perturbation amplitude. Then, two bifurcation diagrams are calculated with these two FDF for the small confinement tube $L_2 = 0.10$ m. These calculations reveal changes induced in the bifurcation diagram. As mentioned in the second part of Chapter 7, when the phase lag does not change with the perturbation level, it is shown that nonlinearly unstable modes do not exist. The nonlinear behavior of the phase lag is responsible for the appearance of nonlinearly unstable modes and this is shown to give rise to hysteresis, mode switching and triggering.

Model B presented in Chapter 6 is used to calculate the bifurcation diagram of the burner equipped with the smallest confinement tube $L_2 = 0.10$ m by sweeping the feeding manifold between $L_1 = 0.10$ m and 0.77 m. This configuration was studied in Chapters 8 and 9. The FDF corresponds to the values measured with the thick perforated plate $l = 15$ mm drawn in Fig. 5.5, Chapter 5. In the following analysis, two FDF are used. These two flame responses are presented in Fig. A.1. In the upper graph, the flame response corresponds to the FDF used in the preceding chapters, while in the lower graph, the FDF features a phase lag independent of the input level. This latter component is locked to the first amplitude of perturbation $u_{rms}/U_b = 0.065$.
The bifurcation diagrams calculated with the two different FDF are plotted in Fig. A.2. This figure shows the positive growth rate areas found for the first

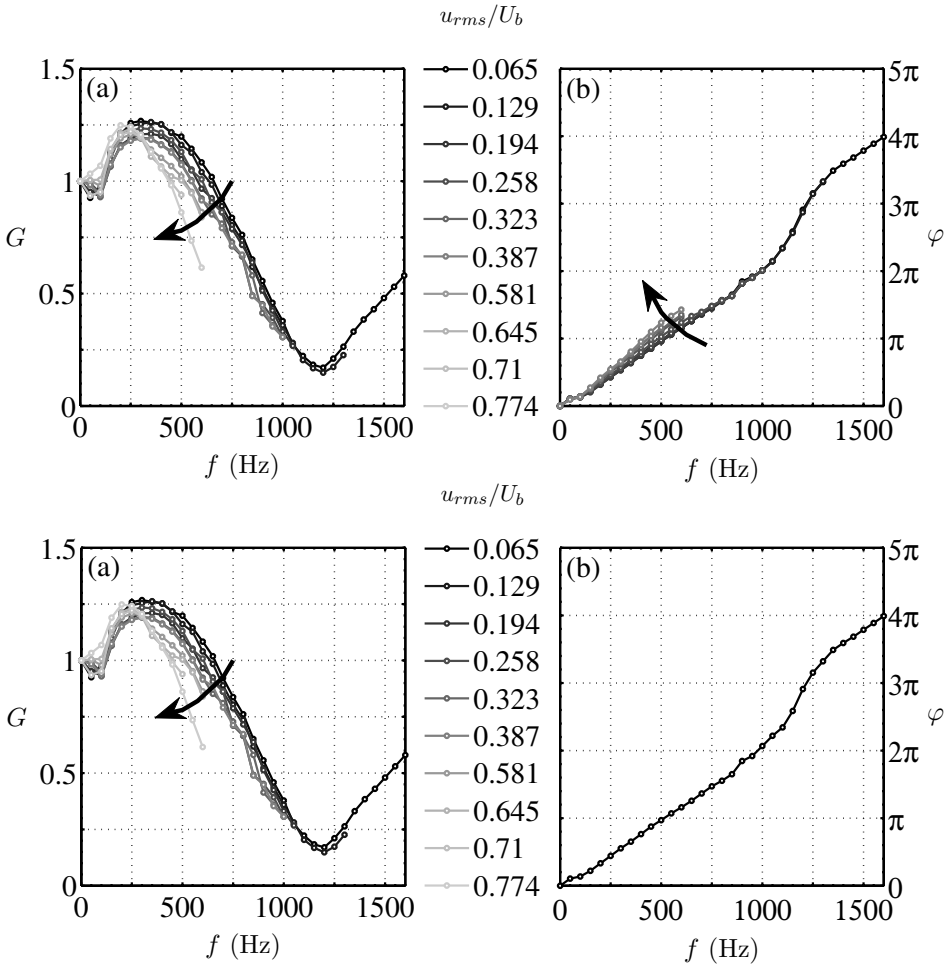

Figure A.1: *FDF measurements for the whole range of amplitudes and frequencies. The perforated plate thickness is set to l = 15 mm with a small flame tube L_2 = 0.10 m. A gray scale shows the increasing level of fluctuations. (a) shows the gain G, while (b) corresponds to the phase φ. The upper graph displays the FDF measured on the experimental setup while the lower graph corresponds to the same FDF with a phase independent of the input level.*

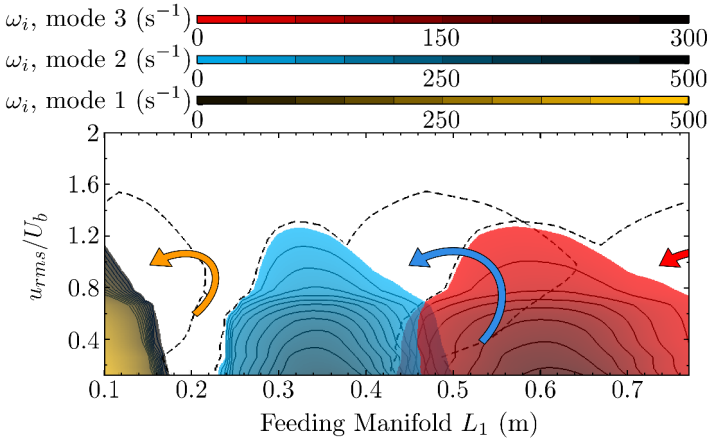

Figure A.2: *Growth rate evolution for the L_2 = 0.10 m confinement tube and the sweeps of feeding manifold L_1 from 0.11 m to 0.77 m. Three colors are used for each eigenmode. The first displayed in yellow, the second in blue and the third in red. Scale is given above to graph. The dashed lines indicate results of calculations at ω_i = 0 s^{-1} by using the FDF with its nonlinear gain and phase. It allows to distinguish the nonlinearly unstable modes. The three arrows, linked to each eigenmode, show the changes brought by the use of a linear phase.*

three eigenmodes. The first mode is drawn in yellow, the second one in blue and the third in red. The dashed line contours shows results of calculations presented in Chapter 9 by using the complete FDF (Fig. A.1 upper graph). These three contours correspond to vanishing growth rates ($\omega_i = 0$ s^{-1}). It is possible to distinguish the ranges of feeding manifold L_1 typified by nonlinearly unstable modes (L_1 = 0.17 m to 0.22 m for mode 1 and L_1 = 0.49 m to 0.64 m for mode 2). The three arrows highlight changes induced by the use of the modified FDF (Fig. A.1 lower graph).

This configuration synthesizes results obtained in the absence of a nonlinear evolution of the phase lag. The nonlinearly unstable modes vanish when the phase lag does not depend on the amplitude of perturbation u_{rms}/U_b. Thus, in the absence of a nonlinear evolution of the phase lag, hysteresis, mode switching and triggering phenomena, found in the preceding chapters, do not exist. This is due to the loss of superposition between a linearly unstable mode and a nonlinearly unstable mode. Nevertheless, the bifurcation diagram reveals possible interactions between two linearly unstable modes between L_1 = 0.44 m and 0.50 m. These two modes vanish around the same oscillation amplitude u_{rms}/U_b. This is reminiscent of what was found for the limit cycles examined in Chapter 9 which featured a simultaneous oscillation of two modes.

Appendix B

Sensitivity analysis of instability predictions

This appendix examines changes in stability predictions resulting from the different elements included in the thermoacoustic model B. The analysis is carried out for the small confinement tube $L_2 = 0.10$ m. In a first stage, bifurcation diagrams obtained with models A and B are compared. Then, model A is used by examining one by one the influence of the different acoustic boundary and matching conditions between the feeding manifold and the flame tube. Finally, the same calculations are undertaken with model B by analyzing one by one the same parts of the model.

B.1 Model A versus Model B

Two bifurcation diagrams are calculated in this section. The first corresponds to the results obtained with model B detailed in Chapter 6. This model includes more realistic conditions at the boundaries and in the matching relations between the upstream manifold and downstream combustion chamber. The second diagram is calculated with model A which considers ideal reflection coefficients at the boundaries and simplified jump relations between the manifold and the chamber. These different conditions are gathered in Tab. 6.1 which is reproduced here for completeness.

Table B.1: *Details of the two models devised for the acoustic analysis of the burner.*

	R piston	***R outlet***	***Pressure jump***	***Velocity jump***
model A	$R_1(0) = 1$	$R_2(L_2) = -1$	Melling model	No ring cavity
model B	$R_1(0) = R(f)$ (measured)	$R_2(L_2) = R(f)$ (modeled)	Melling model	Ring cavity

Comparisons between predictions and measurements are displayed in Figs. B.1

and B.2. When model A is employed, results reveal two important features :

- The limit cycles amplitudes and frequencies are approximately predicted
- The predicted unstable modes do not always correspond to the ones observed experimentally.

In the aim of finding the most influential parameters, two series of calculations are undertaken. The first series is presented in the next section. In this series, model A is considered and one parameter is modified toward a more realistic condition. Results are examined by considering the amplitude and frequency of limit cycles.

B.2 Sensitivity analysis with model A

The bifurcation diagram is calculated on the basis of the thermoacoustic model A. One of the following conditions is changed :

- The reflection coefficient of the piston $R_1(0)$
- The reflection coefficient of the flame tube outlet $R_2(L_2)$
- The matching condition with the ring cavity.

Predictions are then compared to experiments carried out at limit cycle.

B.2.1 The piston reflection coefficient

Calculations are first carried out by inserting in model A the reflection coefficient of the piston head instead of using $R_1(0) = 1$ (Fig. 4.5, Chapter 4). Results plotted in Fig. B.3 reveal a strong influence on the predicted limit cycles. It is seen that the predicted amplitude is too small. Predictions also show second mode oscillations around $L_1 = 0.15$ m and third mode oscillations around $L_1 = 0.25$ m, while these instabilities are not observed in experiments.

B.2.2 The reflection coefficient of the flame tube outlet

Calculations are next carried out by changing the reflection coefficient of the flame tube outlet. The ideal condition $R_2(L_2) = -1$ is replaced by the radiation impedance of an unflanged open pipe (Fig. 4.7, Chapter 4). Results obtained are displayed in Fig. B.4. In this case, amplitudes of oscillation are overestimated and the frequency difference between prediction and measurement increases. The stable zone is not obtained, but the correct unstable modes are retrieved.

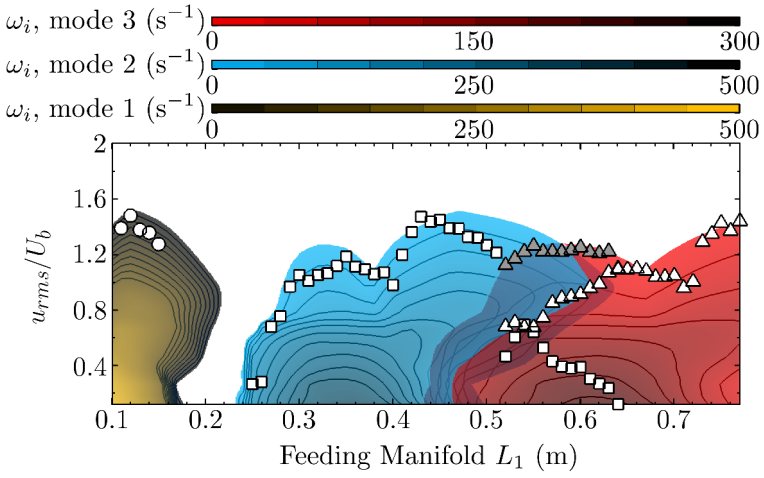

(a)

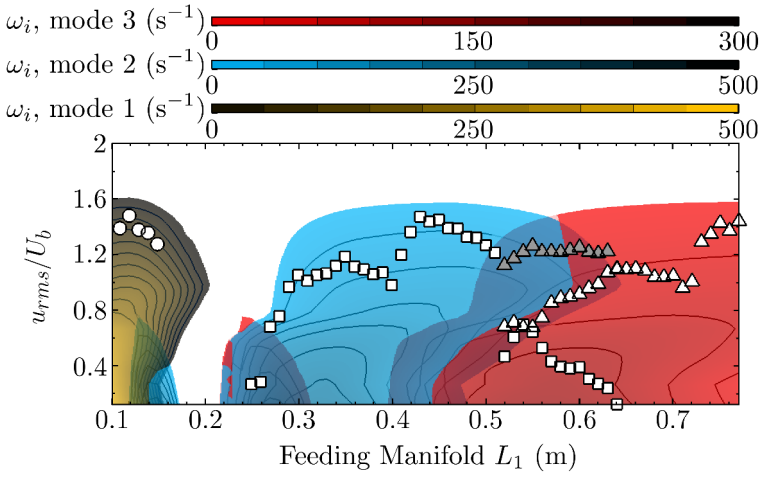

(b)

Figure B.1: *Growth rate evolution for the L_2 = 0.10 m confinement tube and the sweeps of feeding manilfold L_1 from 0.11 m to 0.77 m. Three colors are used for each eigenmode. The first displayed in yellow, the second in blue and the third in red. Scale is given above to graph. Symbols correspond to experiments : ○ stands for the first mode, □ corresponds to the second one and △ to the third mode. Gray triangle symbols depict the sum of the 2 mode values (see Chapter 9) in the multiple frequency band (L_1 = 0.52 m to 0.64 m). (a) corresponds to calculations with model B while (b) shows results with model A.*

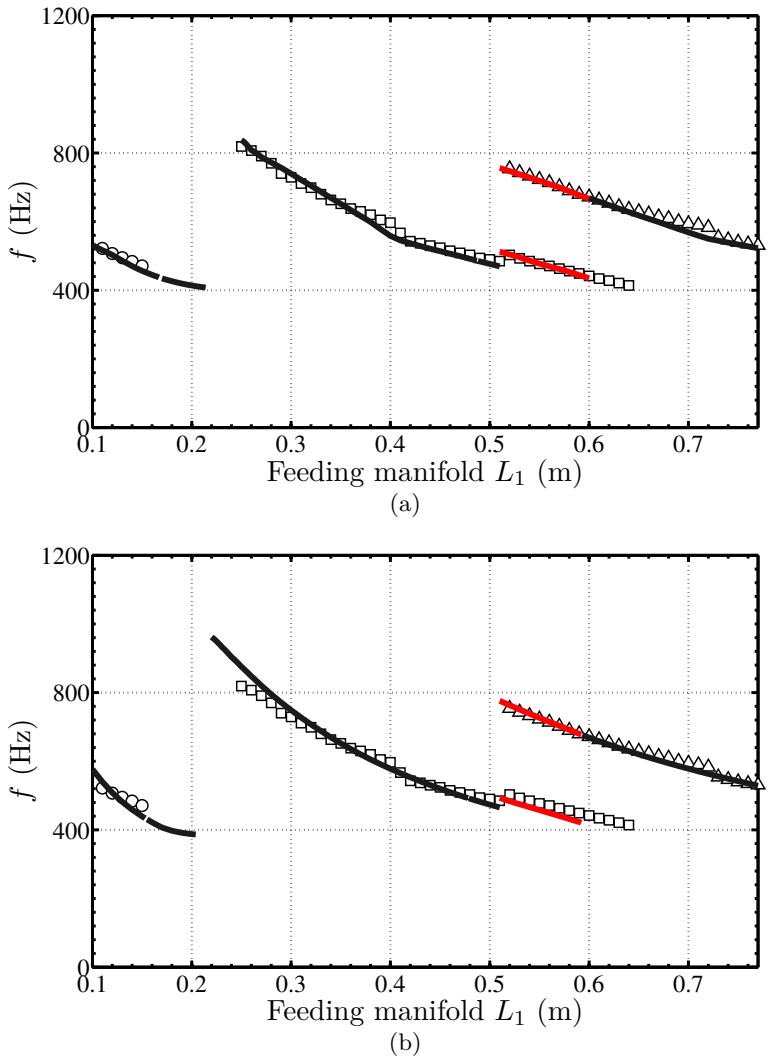

Figure B.2: *Theoretical and measured frequencies at limit cycle. Open circle symbols (○) are linked to the first mode while the second mode appears as open square symbols (□) and the third mode as open triangle symbols (△). Dark bold lines represent predictions at $\omega_i = 0\ s^{-1}$. The red lines correspond to the dual mode frequencies limit cycle examined in Chapter 9. (a) corresponds to calculations with model B while (b) shows results by considering model A.*

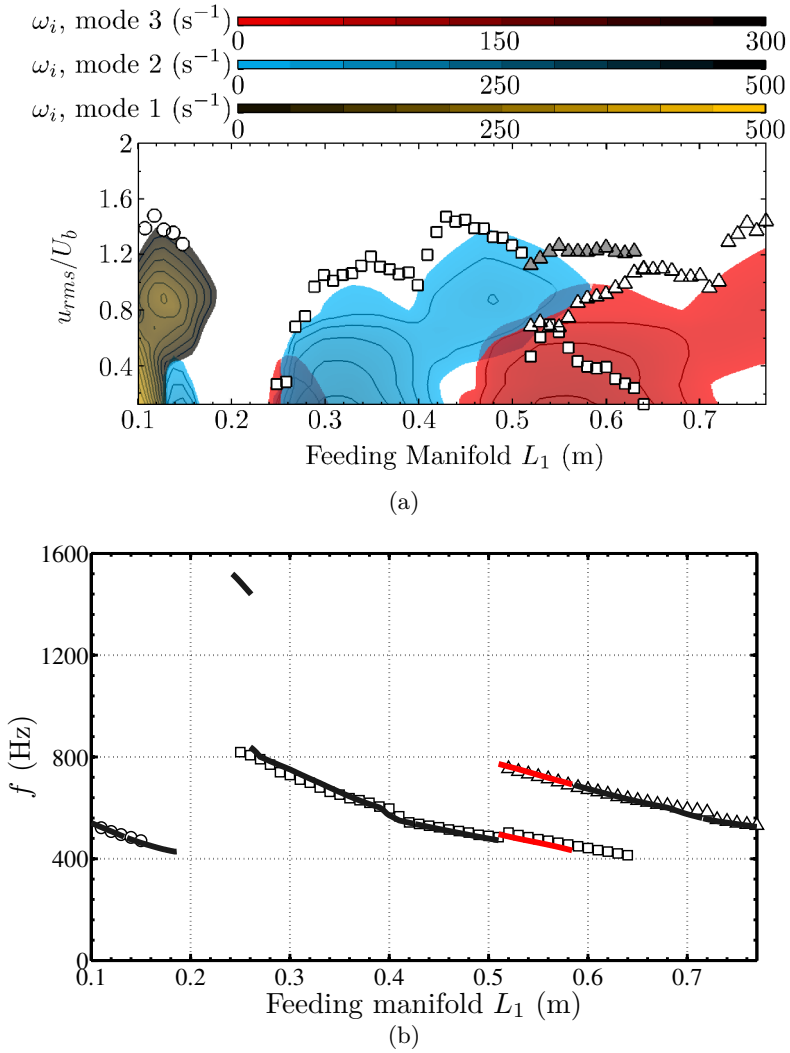

Figure B.3: *Theoretical and measured amplitudes (a) and frequencies (b) of unstable modes at limit cycle. Calculations are done with model A and the measurements of* $R_1(0)$. *Experiments are represented by symbols. Open circle symbols (○) are linked to the first mode while the second mode appears as open square symbols (□) and the third mode as open triangle symbols (△). Gray triangle symbols depict the sum of the 2 mode amplitudes (see Chapter 9) in the multiple frequency band (L_1 = 0.52 m to 0.64 m). For the frequency plot (b), the dark bold lines represent predictions for* $\omega_i = 0\ s^{-1}$ *whereas the red ones correspond to the frequencies of the two modes limit cycles.*

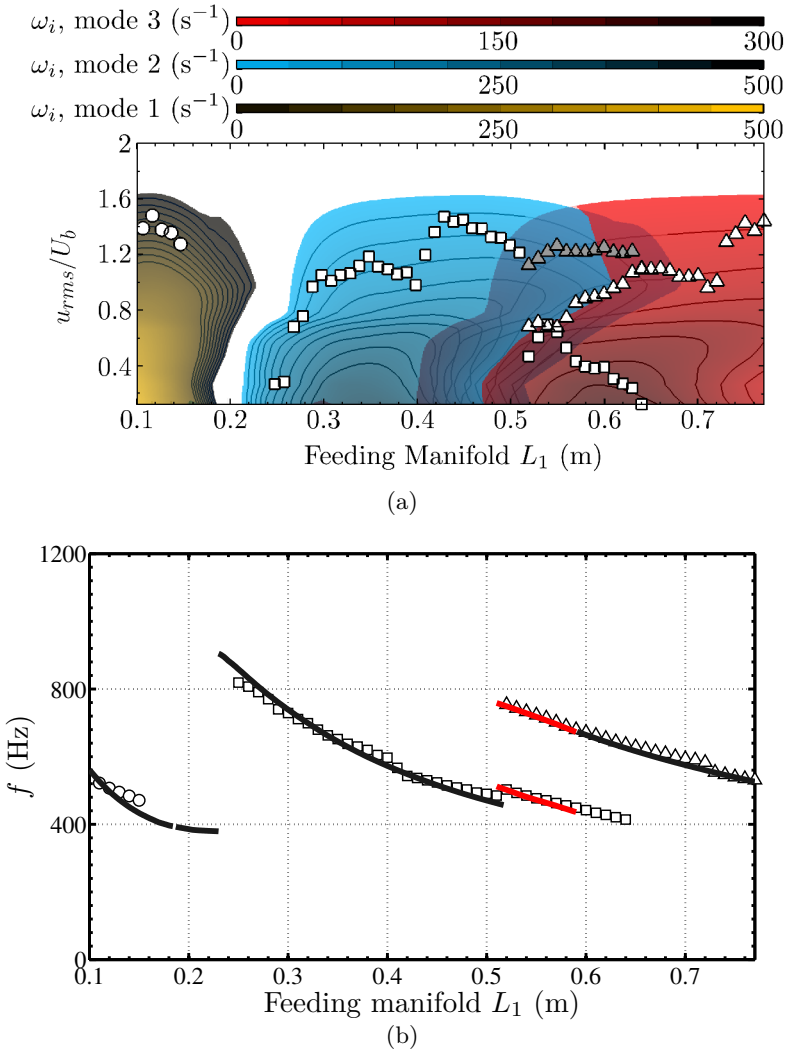

Figure B.4: *Theoretical and measured amplitudes (a) and frequencies (b) of unstable modes at limit cycle. Calculations are done with model A and the reflection coefficient of an unflanged open pipe ($R_2(L_2)$). Experiments are represented by symbols. Open circle symbols ($\circ$) are linked to the first mode while the second mode appears as open square symbols ($\square$) and the third mode as open triangle symbols ($\triangle$). Gray triangle symbols depict the sum of the 2 mode amplitudes (see Chapter 9) in the multiple frequency band (L_1 = 0.52 m to 0.64 m). For the frequency plot (b), the dark bold lines represent predictions for $\omega_i = 0$ s^{-1} whereas the red ones correspond to the frequencies of the two modes limit cycles.*

B.2.3 The ring cavity

In the third set of calculations, the ring cavity around the flame holder is included in model A. Results are plotted in Fig. B.5. The bifurcation diagram shows a rough prediction of limit cycles amplitudes and frequencies. In addition, other modes not seen in the experiments appear with positive growth rates.
The conclusion of this analysis is that the most influential parameter of model A corresponds to the reflection coefficient of the piston head $R_1(0)$. This reflection coefficient allows to reduce the difference between predictions and measurements both in frequency and amplitude. Nevertheless, by taking into account the measurements of the reflection coefficient $R_1(0)$, it is seen that the predicted growth rates are too small. Besides, one predicts positive growth rates for the second and third modes respectively around $L_1 = 0.15$ m and $L_1 = 0.25$ m, while these instabilities are not observed in the experiments for these geometries.

B.3 Sensitivity analysis with model B

In the second series of calculations model B is used to calculate the bifurcation diagram and compare predictions to experiments. The framework remains the same as the one used in the previous section, i.e. that the model B is successively modified by changing one by one boundary and matching conditions.

B.3.1 The piston reflection coefficient $R_1(0)$

Predictions with model B are analyzed with a perfect reflecting boundary condition for the piston head $R_1(0) = 1$. The calculations are displayed in Fig. B.6. Results indicate that the limit cycle amplitudes are overestimated and the stable band is not predicted. In addition, the oscillation frequencies remain roughly predicted in this case.

B.3.2 The reflection coefficient of the flame tube outlet

Model B is now employed with a perfect reflection coefficient at the flame outlet $R_2(L_2) = -1$. The predicted amplitudes and frequencies of the unstable modes are displayed in Fig. B.7. On the one hand, this figure shows the weak influence of this condition without big changes on the predicted frequencies (see Fig. B.2(a) for the full model). On the other hand, the ideal condition for the flame tube outlet $R_2(L_2)$ and the measured values of $R_1(0)$ (not modified here) induce too much damping for the growth rates and the prediction of unstable modes being not observed in the experiment. This is found for the second mode around $L_1 = 0.15$ m and the third mode around $L_1 = 0.25$ m.

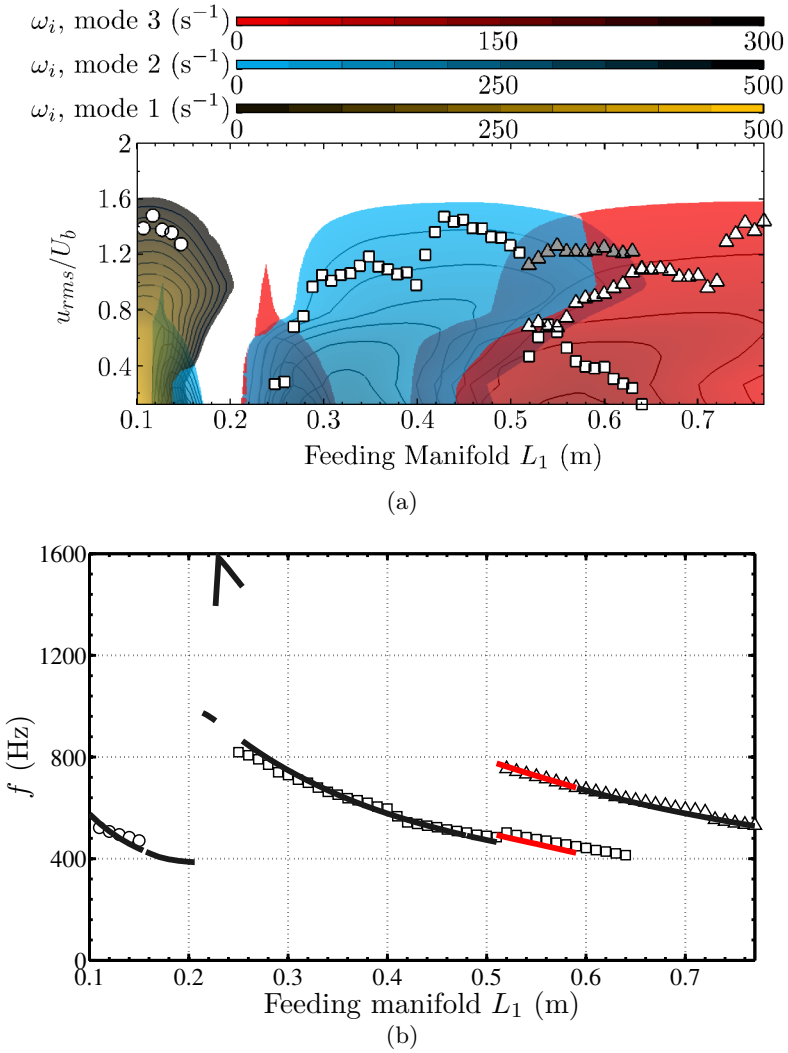

Figure B.5: *Theoretical and measured amplitudes (a) and frequencies (b) of unstable modes at limit cycle. Calculations are done with model A and the ring cavity between the two tubes. Experiments are represented by symbols. Open circle symbols (○) are linked to the first mode while the second mode appears as open square symbols (□) and the third mode as open triangle symbols (△). Gray triangle symbols depict the sum of the 2 mode amplitudes (see Chapter 9) in the multiple frequency band (L_1 = 0.52 m to 0.64 m). For the frequency plot (b), the dark bold lines represent predictions for $\omega_i = 0\ s^{-1}$ whereas the red ones correspond to the frequencies of the two modes limit cycles.*

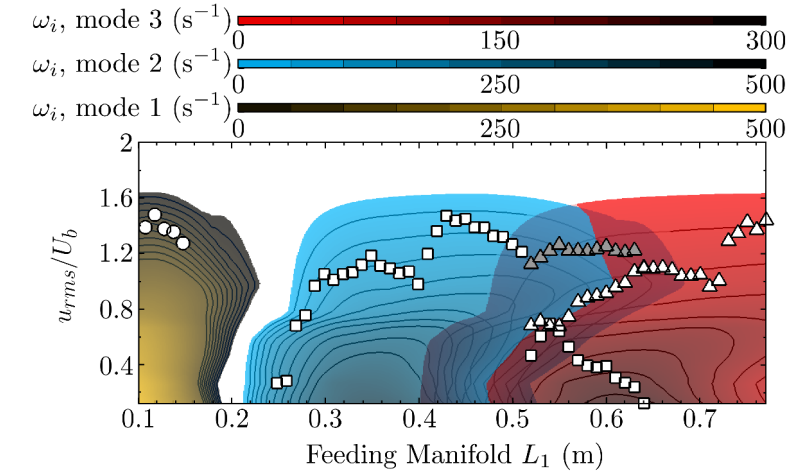

(a)

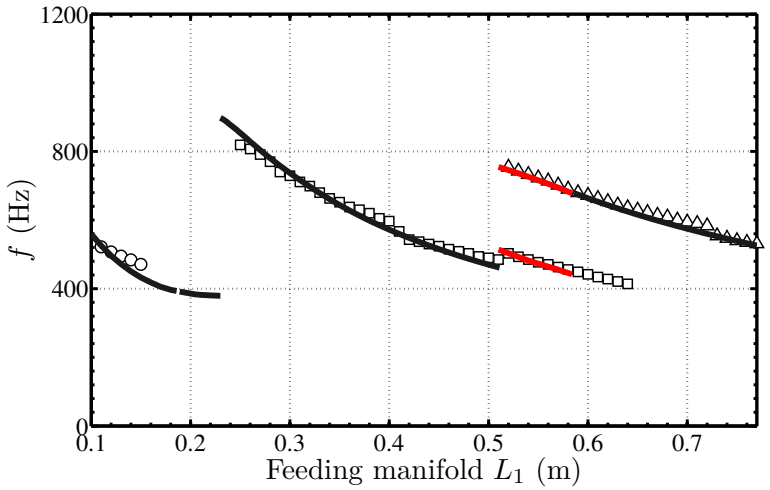

(b)

Figure B.6: *Theoretical and measured amplitudes (a) and frequencies (b) of unstable modes at limit cycle. Calculations are done with model B and a perfect condition for the reflection coefficient of the piston head* ($R_1(0) = 1$). *Experiments are represented by symbols. Open circle symbols* ($\circ$) *are linked to the first mode while the second mode appears as open square symbols* ($\square$) *and the third mode as open triangle symbols* ($\triangle$). *Gray triangle symbols depict the sum of the 2 mode amplitudes (see Chapter 9) in the multiple frequency band* ($L_1 = 0.52$ *m to* 0.64 *m). For the frequency plot (b), the dark bold lines represent predictions for* $\omega_i = 0$ s^{-1} *whereas the red ones correspond to the frequencies of the two modes limit cycles.*

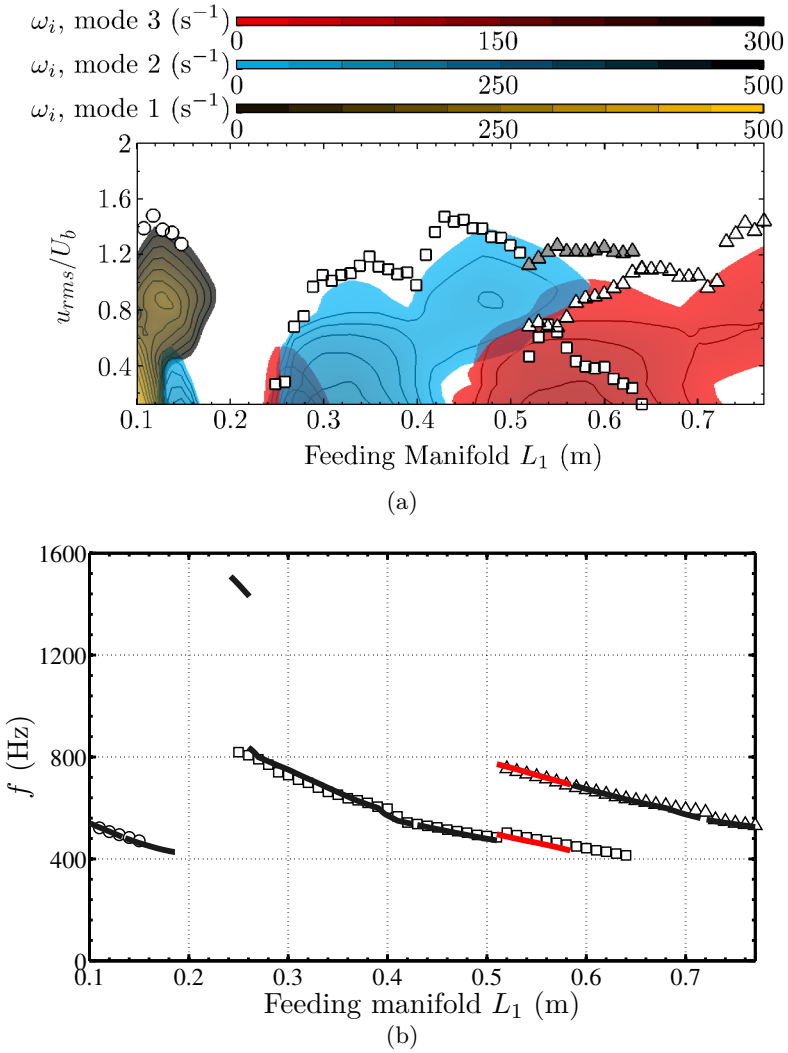

Figure B.7: *Theoretical and measured amplitudes (a) and frequencies (b) of unstable modes at limit cycle. Calculations are done with model B and a perfect reflecting condition for the flame tube outlet* ($R_2(L_2) = -1$). *Experiments are represented by symbols. Open circle symbols* ($\circ$) *are linked to the first mode while the second mode appears as open square symbols* ($\square$) *and the third mode as open triangle symbols* ($\triangle$). *Gray triangle symbols depict the sum of the 2 mode amplitudes (see Chapter 9) in the multiple frequency band* ($L_1 = 0.52$ *m to* 0.64 *m). For the frequency plot (b), the dark bold lines represent predictions for* $\omega_i = 0$ s^{-1} *whereas the red ones correspond to the frequencies of the two modes limit cycles.*

B.3.3 The ring cavity

In the last calculations, model B is used without considering the ring cavity around the flame holder in the matching conditions between the two tubes. Predictions, presented in Fig. B.8, match fairly well experiments. The small differences between results obtained with model B (see Fig. B.1(a)) and the ones without the ring cavity reveal a slight influence of this element. The predicted oscillation amplitudes diminish slightly while the frequencies are nearly the same in the two calculations.

B.4 Appendix synthesis

All things considered, the predicted amplitudes and frequencies of limit cycles are influenced by a set of conditions included in the model.
By using model A and a more realistic model for the different parts of the burner, it is seen that oscillation amplitudes and frequencies are strongly influenced by the reflection coefficient of the piston head $R_1(0)$. Predictions of oscillation frequencies are improved, but the growth rates and the amplitudes of limit cycles are too small. In addition, two modes which are not observed in the experiments do appear in these predictions, indicating that the model remain incomplete.
Stability diagrams calculated with model B and different conditions for the boundaries and the matching conditions indicate that the reflection coefficient of the piston head $R_1(0)$ has also a strong impact on predictions. This latter case is characterized by some differences with calculations obtained from model A set with the same boundary condition $R_1(0)$. It is however possible to show that predictions are in good agreement with experiments by using model B including the measurements of the reflection coefficient $R_1(0)$ and the radiation impedance of the flame tube outlet $R_2(L_2)$ without considering the ring cavity. In this latter case, even if the ring cavity is not included in the model, results are nearly the same as those calculated with the full model B. Thus, it is possible to conclude that the acoustic boundaries are the most influential parameters which need to be taken into account in the thermoacoustic model.

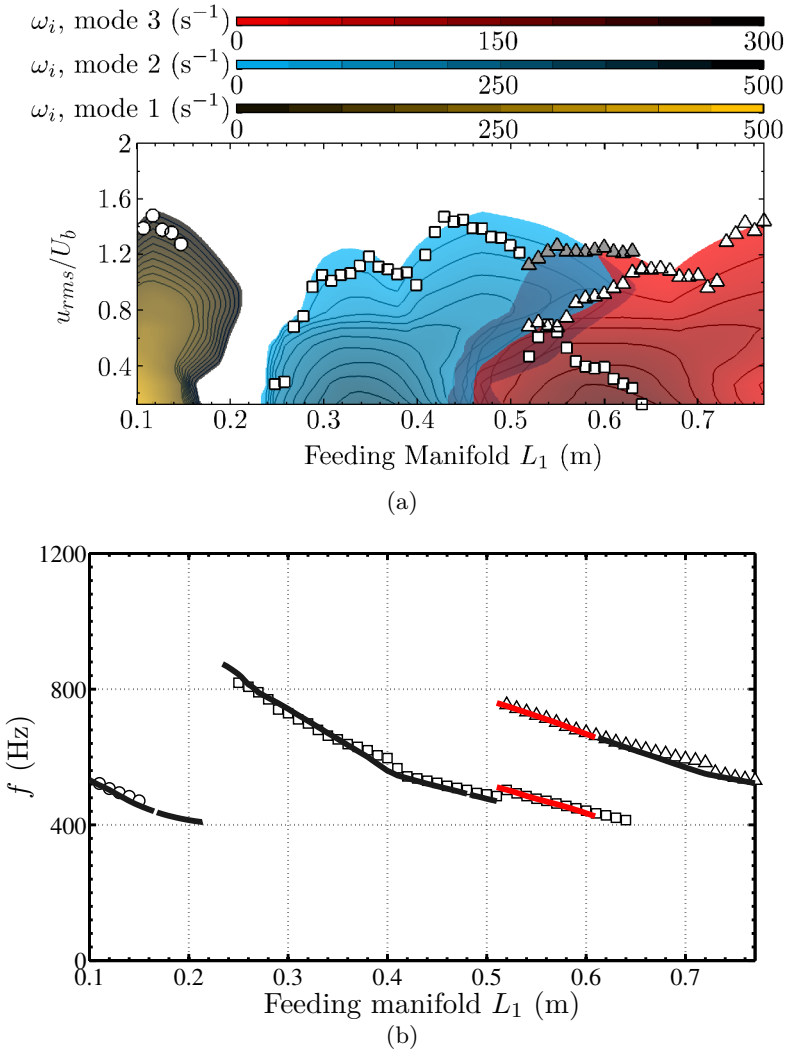

Figure B.8: *Theoretical and measured amplitudes (a) and frequencies (b) of unstable modes at limit cycle. Calculations are done with model B by discarding the ring cavity between the two tubes. Experiments are represented by symbols. Open circle symbols (○) are linked to the first mode while the second mode appears as open square symbols (□) and the third mode as open triangle symbols (△). Gray triangle symbols depict the sum of the 2 mode amplitudes (see Chapter 9) in the multiple frequency band (L_1 = 0.52 m to 0.64 m). For the frequency plot (b), the dark bold lines represent predictions for $\omega_i = 0\ s^{-1}$ whereas the red ones correspond to the frequencies of the two modes limit cycles.*

References

Abarbanel, H. D. I., R. Brown, J. J. Sidorowich, and L. S. Tsimring. 1993. "The analysis of observed chaotic data in physical systems." *Reviews of Modern Physics* 65 (4): 1331–92. *(pp. 151, 166)*
doi:10.1103/RevModPhys.65.1331

Ananthkrishnan, N., S. Deo, and F. Culick. 2005. "Reduced-order modeling and dynamics of nonlinear acoustic waves in a combustion chamber." *Combust. Sci. Technol.* 177 (2): 221–48. *(p. 6)*
doi:10.1080/00102200590900219

Armitage, C., R. Balachandran, E. Mastorakos, and R. Cant. 2006. "Investigation of the nonlinear response of turbulent premixed flames to imposed inlet velocity oscillations." *Combust. Flame* 146 (3): 419–36. *(p. 9)*
doi:10.1016/j.combustflame.2006.06.002

Awad, E. and F. E. C. Culick. 1986. "On the existence and stability of limit cycles for longitudinal acoustic modes in a combustion chamber." *Combust. Sci. Technol.* 46 (3-6): 195–222. *(p. 159)*
doi:10.1080/00102208608959800

Baillot, F., A. Bourehla, and D. Durox. 1996. "The characteristics method and cusped flame fronts." *Combust. Sci. Technol.* 112 (1): 327–50. *(p. 8)*
doi:10.1080/00102209608951963

Balachandran, R., B. Ayoola, C. Kaminski, A. Dowling, and E. Mastorakos. 2005. "Experimental investigation of the non linear response of turbulent premixed flames to imposed inlet velocity oscillations." *Combust. Flame* 143 (1-2): 37–55. *(p. 9)*
doi:10.1016/j.combustflame.2005.04.009

Barrere, M. and F. Williams. 1969. "Comparison of combustion instabilities found in various types of combustion chambers." *Symposium (International) on Combustion* 12 (1): 169–81. *(p. 2)*
doi:10.1016/S0082-0784(69)80401-7

Bellows, B., Q. Zhang, Y. Neumeier, T. Lieuwen, and B. Zinn. 2003. "Forced response studies of a premixed flame to flow disturbances in a gas turbine combustor." In *Proceedings of the 41st AIAA Aerospace Sciences Meeting,*

paper 2003-0824, Reston: American Institute of Aeronautics and Astronautics. *(pp. 9, 11)*
doi:10.2514/6.2003-824

Birbaud, A., D. Durox, S. Ducruix, and S. Candel. 2007. "Dynamics of confined premixed flames submitted to upstream acoustic modulations." *Proc. Combust. Inst.* 31 (1): 1257–65. *(pp. 8, 11, 60)*
doi:10.1016/j.proci.2006.07.122

Birbaud, A.-L. "Dynamique d'interactions - sources des instabilités de combustion." PhD diss., Ecole Centrale Paris, 2006. *(p. 231)*

Blackshear Jr., P. L. 1953. "Driving standing waves by heat addition." *Symposium (International) on Combustion* 4 (1): 553–66. *(p. 62)*
doi:10.1016/S0082-0784(53)80077-9

Boudier, G., N. Lamarque, G. Staffelbach, L. Y. M. Gicquel, and T. Poinsot. 2009. "Thermo-acoustic stability of a helicopter gas turbine combustor using large eddy simulation." *Int. J. Aeroacoust.* 8 (1-2): 69–93. *(p. 6)*
doi:10.1260/147547209786234975

Boudy, F., D. Durox, T. Schuller, and S. Candel. 2011a. "Nonlinear mode triggering in a multiple flame combustor." *Proc. Combust. Inst.* 33 (1): 1121–28. *(pp. 13, 15, 149, 151, 160, 161, 183, 233)*
doi:10.1016/j.proci.2010.05.079

———. 2012. "Nonlinear flame describing function analysis of galloping limit cycles featuring chaotic states in premixed combustors." In *Proceedings of the ASME Turbo Expo, paper GT2012-68998*, New York: American Society of Mechanical Engineers. *(pp. 16, 234)*

Boudy, F., D. Durox, T. Schuller, G. Jomaas, and S. Candel. 2011b. "Describing function analysis of limit cycles in a multiple flame combustor." *J. Eng. Gas Turb. Power* 133 (6): 061502.1–061502.8. *(pp. 13, 15, 123, 128, 149, 151, 159, 160, 164, 219, 233)*
doi:10.1115/1.4002275

Boudy, F., D. Durox, T. Schuller, and S. Candel. 2013. "Analysis of limit cycles sustained by two modes in the flame describing function framework." *C. R. Mec.* 341 (1-2): 181–90. *(pp. 15, 164, 234)*
doi:10.1016/j.crme.2012.10.014

Bourehla, A. and F. Baillot. 1998. "Appearance and stability of a laminar conical premixed flame subjected to an acoustic perturbation." *Combust. Flame* 114 (3-4): 303–18. *(p. 8)*
doi:10.1016/S0010-2180(97)00323-4

Candel, S. 2002. "Combustion dynamics and control: progress and challenges." *Proc. Combust. Inst.* 29 (1): 1–28. *(pp. 2, 4)*
doi:10.1016/S1540-7489(02)80007-4

Candel, S., C. Huynh, and T. Poinsot. 1996. "Some modeling methods of combustion instabilities." In *Unsteady combustion*, 1st ed. Edited by F. Culick, M. Heitor, and J. Whitelaw, 83–112. Dordrecht: Kluwer Academic Publishers. *(p. 4)*

Chung, J. Y. and D. A. Blaser. 1980a. "Transfer function method of measuring in-duct acoustic properties. I. theory." *J. Acous. Soc. Am.* 68 (3): 907–13. *(pp. 39, 41)*
doi:10.1121/1.384778

———. 1980b. "Transfer function method of measuring in-duct acoustic properties. II. experiment." *J. Acous. Soc. Am.* 68 (3): 914–21. *(pp. 39, 41)*
doi:10.1121/1.384779

Crandall, I. B. 1926. *Theory of vibrating systems and sound*. New York: D. Van Nostrand Company. *(p. 53)*

Crocco, L. 1951. "Aspects of combustion stability in liquid propellant rocket motors part I: fundamentals. low frequency instability with monopropellants." *J. Am. Rocket Soc.* 21 (6): 163–78. *(p. 2)*
doi:10.2514/8.4393

———. 1969. "Research on combustion instability in liquid propellant rockets." *Symposium (International) on Combustion* 12 (1): 85–99. *(p. 10)*
doi:10.1016/S0082-0784(69)80394-2

Culick, F. E. C. 2006. *Unsteady motions in combustion chambers for propulsion systems*. Neuilly-sur-Seine: RTO/OTAN. *(p. 85)*

Culick, F. 1994. "Some recent results for nonlinear acoustics in combustion-chambers." *AIAA Journal* 32 (1): 146–69. *(p. 4)*
doi:10.2514/3.11962

Culick, F. and V. Yang. 1995. "Overview of combustion instabilities in liquid-propellant rocket engines." In *Liquid rocket engine combustion instability*, vol. 169, 1st ed. Edited by W. Anderson and V. Yang, 3–38. Reston: American Institute of Aeronautics and Astronautics. *(p. 220)*

Cuquel, A., D. Durox, and T. Schuller. 2013. "Scaling the flame transfer function of confined premixed conical flames." *Proc. Combust. Inst.* 34 (1): 1007–14. *(p. 60)*
doi:10.1016/j.proci.2012.06.056

Cuquel, A. "Dynamics and nonlinear thermoacoustic stability analysis of premixed conical flames." PhD diss., Ecole Centrale Paris, 2013. *(p. 236)*

De Goey, L., J. Van Oijen, V. Kornilov, and J. Ten Thije Boonkkamp. 2011. "Propagation, dynamics and control of laminar premixed flames." *Proc. Combust. Inst.* 33 (1): 863–86. *(p. 8)*
doi:10.1016/j.proci.2010.09.006

Dowling, A. 1997. "Nonlinear self-excited oscillations of a ducted flame." *J. Fluid Mech.* 346: 271–90. *(p. 10)*
doi:10.1017/S0022112097006484

———. 1999. "A kinematic model of a ducted flame." *J. Fluid Mech.* 394: 51–72. *(p. 10)*
doi:10.1017/S0022112099005686

Dowling, A. and S. Stow. 2003. "Acoustic analysis of gas turbine combustors." *J. Propul. Power* 19 (5): 751–64. *(p. 85)*
doi:10.2514/2.6192

Duchaine, F., F. Boudy, D. Durox, and T. Poinsot. 2011. "Sensitivity analysis of transfer functions of laminar flames." *Combust. Flame* 158 (12): 2384–94. *(p. 6)*
doi:10.1016/j.combustflame.2011.05.013

Ducruix, S., D. Durox, and S. Candel. 2000. "Theoretical and experimental determinations of the transfer function of a laminar premixed flame." *Proc. Combust. Inst.* 28 (1): 765–73. *(p. 8)*
doi:10.1016/S0082-0784(00)80279-9

Ducruix, S. "Dynamique des interactions acoustique-combustion." PhD diss., Ecole Centrale Paris, 1999. *(p. 231)*

Durox, D., F. Baillot, G. Searby, and L. Boyer. 1997. "On the shape of flames under strong acoustic forcing: a mean flow controlled by an oscillating flow." *J. Fluid Mech.* 350: 295–310. *(p. 8)*
doi:10.1017/S0022112097006940

Durox, D., S. Ducruix, and F. Lacas. 1999. "Flow seeding with an air nebulizer." *Exp. Fluids* 27 (5): 408–13. *(p. 43)*
doi:10.1007/s003480050365

Durox, D., T. Schuller, and S. Candel. 2005. "Combustion dynamics of inverted conical flames." *Proc. Combust. Inst.* 30 (2): 1717–24. *(pp. 8, 11, 22, 35)*
doi:10.1016/j.proci.2004.08.067

Durox, D., T. Schuller, N. Noiray, A. Birbaud, and S. Candel. 2009a. "Rayleigh criterion and acoustic energy balance in unconfined self-sustained oscillating flames." *Combust. Flame* 156 (1): 106–19. *(pp. 22, 35, 92)*
doi:10.1016/j.combustflame.2008.07.016

Durox, D., T. Schuller, N. Noiray, and S. Candel. 2009b. "Experimental analysis of nonlinear flame transfer functions for different flame geometries." *Proc. Combust. Inst.* 32 (1): 1391–98. *(pp. 8, 9, 11, 60, 82, 87)*
doi:10.1016/j.proci.2008.06.204

Franzelli, B., E. Riber, L. Y. M. Gicquel, and T. Poinsot. 2012. "Large eddy

simulation of combustion instabilities in a lean partially premixed swirled flame." *Combust. Flame* 159 (2): 621–37. *(p. 6)*
doi:10.1016/j.combustflame.2011.08.004

Gelb, A. and W. Vander Velde. 1968. *Multiple-input describing functions and nonlinear system design*. New York: McGraw-Hill. *(p. 10)*

Giauque, A., L. Selle, L. Gicquel, T. Poinsot, H. Buechner, P. Kaufmann, and W. Krebs. 2005. "System identification of a large-scale swirled partially premixed combustor using LES and measurements." *J. Turbulence* 6: 1–21. *(p. 6)*
doi:10.1080/14685240512331391985

Gullaud, E., S. Mendez, C. Sensiau, F. Nicoud, and T. Poinsot. 2009. "Effect of multiperforated plates on the acoustic modes in combustors." *C. R. Mec.* 337 (6-7): 406–14. *(p. 6)*
doi:10.1016/j.crme.2009.06.020

Henry, B., N. Lovell, and F. Camacho. 2000. "Nonlinear dynamics time series analysis." In *Nonlinear biomedical signal processing, dynamic analysis and modeling*, vol. 2, edited by M. Akay, 1–39. New York: Wiley-IEEE Press. *(p. 167)*

Higgins, B., M. McQuay, F. Lacas, J. Rolon, N. Darabiha, and S. Candel. 2001. "Systematic measurements of OH chemiluminescence for fuel-lean, high-pressure, premixed, laminar flames." *Fuel* 80 (1): 67–74. *(pp. 24, 44)*
doi:10.1016/S0016-2361(00)00069-7

Howe, M. S. 1979. "On the theory of unsteady high reynolds number flow through a circular aperture." *Proc. R. Soc. London* A 366 (1725): 205–23. *(pp. 53, 182, 185, 195, 216, 217)*
doi:10.1098/rspa.1979.0048

Huang, Y. and V. Yang. 2009. "Dynamics and stability of lean-premixed swirl-stabilized combustion." *Prog. Energy Combust. Sci.* 35 (4): 293–364. *(pp. 5, 10)*
doi:10.1016/j.pecs.2009.01.002

Hughes, I. and A. Dowling. 1990. "The absorption of sound by perforated linings." *J. Fluid Mech.* 218: 299–335. *(pp. 16, 182, 185, 200, 207)*
doi:10.1017/S002211209000101X

Hurle, I., R. Price, T. Sudgen, and A. Thomas. 1968. "Sound emission from open turbulent premixed flames." *Proc. R. Soc. London* A 303 (1475): 409–27. *(pp. 24, 44, 81)*
doi:http://www.jstor.org/stable/2415909

Janardan, B., B. Daniel, and B. Zinn. 1976. "Measurements of acoustic re-

sponses of gaseous propellant injectors." *J. Sound Vib.* 47 (4): 559–69. *(p. 22)*
doi:10.1016/0022-460X(76)90882-8

Kabiraj, L. and R. Sujith. 2011a. "Investigation of subcritical instability in ducted premixed flames." In *Proceedings of the ASME Turbo Expo, paper GT2011-46155*, 969–77. New York: American Society of Mechanical Engineers. *(pp. 148, 164)*
doi:10.1115/GT2011-46155

Kabiraj, L., R. Sujith, and P. Wahi. 2011b. "Experimental studies of bifurcations leading to chaos in a laboratory scale thermoacoustic system." In *Proceedings of the ASME Turbo Expo, paper GT2011-46149*, 959–68. New York: American Society of Mechanical Engineers. *(pp. 148, 164)*
doi:10.1115/GT2011-46149

Kabiraj, L., R. I. Sujith, and P. Wahi. 2012. "Bifurcations of self-excited ducted laminar premixed flames." *J. Eng. Gas Turb. Power* 134 (3): 031502.1–031502.7. *(pp. 13, 35)*
doi:10.1115/1.4004402

Kagiya, S. 2000. "New burner design technique for suppression of combustion oscillations." Short communication. Tokyo Gas Co., Ltd. – Energy and Environmental Technology Lab. – Combustion and Fluid Dynamics. *(p. 21)*

Karimi, N., M. Brear, S. Jin, and J. Monty. 2009. "Linear and non-linear forced response of a conical, ducted, laminar premixed flame." *Combust. Flame* 156 (11): 2201–12. *(pp. 8, 11)*
doi:10.1016/j.combustflame.2009.06.027

Kaufmann, A., F. Nicoud, and T. Poinsot. 2002. "Flow forcing techniques for numerical simulation of combustion instabilities." *Combust. Flame* 131 (4): 371–85. *(p. 6)*
doi:10.1016/S0010-2180(02)00419-4

Keller, J. 1995. "Thermoacoustic oscillations in combustion chambers of gas turbines." *AIAA Journal* 33 (12): 2280–87. *(pp. 69, 155)*
doi:10.2514/3.12980

Kim, K. and D. Santavicca. 2009. "Linear stability analysis of acoustically driven pressure oscillations in a lean premixed gas turbine combustor." *J. Mech. Sc. Tech.* 23 (12): 3436–47. *(p. 10)*
doi:10.1007/s12206-009-0924-0

Kornilov, V., R. Rook, J. ten Thije Boonkkamp, and L. de Goey. 2009. "Experimental and numerical investigation of the acoustic response of multi-slit bunsen burners." *Combust. Flame* 156 (10): 1957–70. *(pp. 60, 87)*
doi:10.1016/j.combustflame.2009.07.017

Lamraoui, A., F. Richecoeur, S. Ducruix, and T. Schuller. 2011. "Experimen-

tal analysis of simultaneous non-harmonically related unstable modes in a swirled combustor." In *Proceedings of the ASME Turbo Expo, paper GT2011-46701*, 1289–99. New York: American Society of Mechanical Engineers. *(pp. 35, 164, 220)*
doi:10.1115/GT2011-46701

Lamraoui, A. "Acoustique et dynamique de flamme dans un foyer turbulent prémélangé swirlé : application à l'étude du bruit de combustion dans les chambres de turbines à gaz." PhD diss., Ecole Centrale Paris, 2011. *(pp. 220, 223)*

Lang, W. 1991. "Harmonic frequency generation by oscillating flames." *Combust. Flame* 83 (3-4): 253–62. *(p. 6)*
doi:10.1016/0010-2180(91)90073-K

Langhorne, P. 1988. "Reheat buzz: an acoustically coupled combustion instability. part 1. experiment." *J. Fluid Mech.* 193: 417–43. *(p. 10)*
doi:10.1017/S0022112088002204

Le Helley, P. "Etude théorique et expérimentale des instabilités de combustion et de leur contrôle dans un brûleur laminaire prémélangé." PhD diss., Ecole Centrale Paris, 1994. *(p. 62)*

Lee, J. G. and D. A. Santavicca. 2003. "Experimental diagnostics for the study of combustion instabilities in lean premixed combustors." *J. Propul. Power* 19 (5): 735–50. *(p. 8)*
doi:10.2514/2.6191

Levine, H. and J. Schwinger. 1948. "On the radiation of sound from an unflanged circular pipe." *Physical Review* 73 (4): 383–406. *(p. 50)*
doi:10.1103/PhysRev.73.383

Lieuwen, T. and K. McManus. 2003. "Introduction: combustion dynamics in lean-premixed prevaporized (LPP) gas turbines." *J. Propul. Power* 19 (5): 721–21. *(p. 5)*
doi:10.2514/2.6171

Lieuwen, T. and V. Yang, eds. 2005. *Combustion instabilities in gas turbine engines: operational experience, fundamental mechanisms and modeling*. Vol. 210. Reston: American Institute of Aeronautics and Astronautics. *(p. 2)*

Lieuwen, T. 2002. "Experimental investigation of limit-cycle oscillations in an unstable gas turbine combustor." *J. Propul. Power* 18 (1): 61–67. *(p. 10)*
doi:10.2514/2.5898

Lieuwen, T. and Y. Neumeier. 2002. "Nonlinear pressure-heat release transfer function measurements in a premixed combustor." *Proc. Combust. Inst.* 29 (1): 99–105. *(p. 8)*
doi:10.1016/S1540-7489(02)80017-7

Mallat, S. 1998. *A wavelet tour of signal processing*. 1st ed. Burlington: Academic Press. *(p. 169)*

Melling, T. H. 1973. "The acoustic impedance of perforates at medium and high sound pressure levels." *J. Sound Vib.* 29 (1): 1–65. *(pp. 15, 53, 70, 71, 86, 155, 156, 190, 234)*
doi:10.1016/S0022-460X(73)80125-7

Moeck, J. P. and C. O. Paschereit. 2012. "Nonlinear interactions of multiple linearly unstable thermoacoustic modes." *Intl J. Spray Combust. Dyn.* 4 (1): 1–28. *(pp. 13, 35, 164)*
doi:10.1260/1756-8277.4.1.1

Moeck, J., M. Bothien, S. Schimek, A. Lacarelle, and C. Paschereit. 2008. "Subcritical thermoacoustic instabilities in a premixed combustor." In *Proceedings of the 14th AIAA/CEAS Aeroacoustics Conference, paper 2008-2946*, Reston: American Institute of Aeronautics and Astronautics. *(p. 10)*
doi:10.2514/6.2008-2946

Morse, P. M. and K. U. Ingard. 1986. *Theoretical acoustics*. 1st ed. Princeton: Princeton University Press. *(pp. 47, 184)*

Noiray, N., D. Durox, T. Schuller, and S. Candel. 2006. "Self-induced instabilities of premixed flames in a multiple injection configuration." *Combust. Flame* 145 (3): 435–46. *(pp. 10, 11)*
doi:10.1016/j.combustflame.2006.01.006

———. 2007. "Passive control of combustion instabilities involving premixed flames anchored on perforated plates." *Proc. Combust. Inst.* 31 (1): 1283–90. *(p. 15)*
doi:10.1016/j.proci.2006.07.096

———. 2008. "A unified framework for nonlinear combustion instability analysis based on the flame describing function." *J. Fluid Mech.* 615: 139–67. *(pp. 2, 11–14, 21, 22, 35, 82, 123, 128, 148, 151, 160, 183, 219)*
doi:10.1017/S0022112008003613

———. 2009. "A method for estimating the noise level of unstable combustion based on the flame describing function." *Int. J. Aeroacoust.* 8 (1-2): 157–76. *(pp. 85, 92)*
doi:10.1260/147547209786234957

Noiray, N. "Analyse linéaire et non-linéaire des instabilités de combustion, application aux systèmes à injection multipoints et stratégies de contrôle." PhD diss., Ecole Centrale Paris, 2007. *(pp. 2, 53, 64, 65, 67, 194, 196, 208–210, 217, 231)*

Palies, P., D. Durox, T. Schuller, and S. Candel. 2010. "The combined dynamics

of swirler and turbulent premixed swirling flames." *Combust. Flame* 157 (9): 1698–717. *(pp. 9, 11)*
doi:10.1016/j.combustflame.2010.02.011

———. 2011. "Nonlinear combustion instability analysis based on the flame describing function applied to turbulent premixed swirling flames." *Combust. Flame* 158 (10): 1980–91. *(pp. 11, 127, 151, 236)*
doi:10.1016/j.combustflame.2011.02.012

Palies, P. "Dynamique et instabilités de combustion des flammes swirlées." PhD diss., Ecole Centrale Paris, 2010. *(p. 231)*

Paschereit, C., P. Flohr, and B. Schuermans. 2001. "Prediction of combustion oscillations in gas turbine combustors." In *Proceedings of the 39th AIAA Aerospace Science Meeting and Exhibit, paper 2001-0484*, Reston: American Institute of Aeronautics and Astronautics. *(p. 155)*
doi:10.2514/6.2001-484

Peracchio, A. and W. Proscia. 1999. "Nonlinear heat-Release/Acoustic model for thermoacoustic instability in lean premixed combustors." *J. Eng. Gas Turb. Power* 121 (3): 415–21. *(p. 10)*
doi:10.1115/1.2818489

Poinsot, T., D. Veynante, F. Bourienne, S. Candel, E. Esposito, and J. Surget. 1989. "Initiation and suppression of combustion instabilities by active control." *Symposium (International) on Combustion* 22 (1): 1363–70. *(p. 6)*
doi:10.1016/S0082-0784(89)80147-X

Poinsot, T. and D. Veynante. 2012. *Theoretical and numerical combustion.* 3rd ed. Toulouse - Paris: Poinsot T. and Veynante D. *(pp. 2, 6, 62, 69, 85, 219)*

Preetham, B., H. Santosh, and T. Lieuwen. 2008. "Dynamics of laminar premixed flames forced by harmonic velocity disturbances." *J. Propul. Power* 24 (6): 1390–402. *(p. 8)*
doi:10.2514/1.35432

Pun, W. "Measurements of thermo-acoustic coupling." PhD diss., California Institute of Technology, 2001. *(p. 2)*

Putnam, A. A. 1971. *Combustion-driven oscillations in industry.* New York: American Elsevier Pub. Co. *(p. 22)*

Richards, G. A., D. L. Straub, and E. H. Robey. 2003. "Passive control of combustion dynamics in stationary gas turbines." *J. Propul. Power* 19 (5): 795–810. *(p. 181)*
doi:10.2514/2.6195

Richecoeur, F., T. Schuller, A. Lamraoui, and S. Ducruix. 2013. "Analytical

and experimental investigations of gas turbine model combustor acoustics operated at atmospheric pressure." *C. R. Mec.* 341 (1-2): 141–51. *(p. 220)* doi:10.1016/j.crme.2012.11.008

Rienstra, S. and A. Hirschberg. 2010. *An introduction to acoustics*. Eindhoven: Eindhoven University of Technology. *(pp. 47, 50)*

Roux, A., S. Reichstadt, N. Bertier, L. Gicquel, F. Vuillot, and T. Poinsot. 2009. "Comparison of numerical methods and combustion models for LES of a ramjet." *C. R. Mec.* 337 (6-7): 352–61. *(p. 6)* doi:10.1016/j.crme.2009.06.008

Scanlan, R. and E. Simiu. 2004. "Aeroelasticity in civil engineering." In *A modern course in aeroelasticity*, vol. 116, 4th rev. and enlarged ed. Edited by E. H. Dowell, 299–376. Dordrecht: Kluwer Academic Publishers. *(pp. 113, 148)*

Scarpato, A., S. Ducruix, and T. Schuller. 2011. "A LES based sound absorption analysis of high-amplitude waves through an orifice with bias flow." In *Proceedings of the ASME Turbo Expo, paper GT2011-45639*, 613–22. New York: American Society of Mechanical Engineers. *(pp. 191, 196, 199)* doi:10.1115/GT2011-45639

Scarpato, A., N. Tran, S. Ducruix, and T. Schuller. 2012. "Modeling the damping properties of perforated screens traversed by a bias flow and backed by a cavity at low strouhal number." *J. Sound Vib.* 331 (2): 276–90. *(pp. 16, 40, 53, 182–186, 193, 194, 205, 216, 232)* doi:10.1016/j.jsv.2011.09.005

Schuermans, B., F. Guethe, D. Pennell, D. Guyot, and C. Paschereit. 2010. "Thermoacoustic modeling of a gas turbine using transfer functions measured under full engine pressure." *J. Eng. Gas Turb. Power* 132 (11): 111503.1–111503.9. *(pp. 10, 66)* doi:10.1115/1.4000854

Schuller, T., D. Durox, and S. Candel. 2003a. "A unified model for the prediction of laminar flame transfer functions: comparisons between conical and v-flame dynamics." *Combust. Flame* 134 (1-2): 21–34. *(pp. 8, 11, 60, 87)* doi:10.1016/S0010-2180(03)00042-7

———. 2003b. "Self-induced combustion oscillations of laminar premixed flames stabilized on annular burners." *Combust. Flame* 135 (4): 525–37. *(pp. 8, 22, 35)* doi:10.1016/j.combustflame.2003.08.007

Schuller, T., T. Tran, N. Noiray, D. Durox, S. Ducruix, and S. Candel. 2009. "The role of nonlinear acoustic boundary conditions in Combustion/Acoustic coupled instabilities." In *Proceedings of the ASME Turbo Expo, paper GT2009-*

59390, 325–39. New York: American Society of Mechanical Engineers. *(pp. 53, 65, 198)*
doi:10.1115/GT2009-59390

Schuller, T. "Mécanismes de couplage dans les interactions acoustique-combustion." PhD diss., Ecole Centrale Paris, 2003. *(p. 231)*

Schuller, T., D. Durox, P. Palies, and S. Candel. 2012. "Acoustic decoupling of longitudinal modes in generic combustion systems." *Combust. Flame* 159 (5): 1921–31. *(pp. 72, 219, 220)*
doi:10.1016/j.combustflame.2012.01.010

Selle, L., L. Benoit, T. Poinsot, F. Nicoud, and W. Krebs. 2006. "Joint use of compressible large-eddy simulation and helmholtz solvers for the analysis of rotating modes in an industrial swirled burner." *Combust. Flame* 145 (1-2): 194–205. *(p. 6)*
doi:10.1016/j.combustflame.2005.10.017

Sensiau, C., F. Nicoud, and T. Poinsot. 2009. "A tool to study azimuthal standing and spinning modes in annular combustors." *Int. J. Aeroacoust.* 8 (1-2): 57–67. *(p. 6)*
doi:10.1260/147547209786235037

Small, M. 2005. *Applied nonlinear time series analysis: applications in physics, physiology and finance*. Vol. 52. Singapore: World Scientific Publishing Co. Pte. Ltd. *(pp. 151, 166, 171)*

Sterling, J. 1993. "Nonlinear analysis and modelling of combustion instabilities in a laboratory combustor." *Combust. Sci. Technol.* 89 (1-4): 167–79. *(pp. 13, 35, 148, 164)*
doi:10.1080/00102209308924107

Tay-Wo-Chong, L., S. Bomberg, A. Ulhaq, T. Komarek, and W. Polifke. 2011. "Comparative validation study on identification of premixed flame transfer function." *J. Eng. Gas Turb. Power* 134 (2): 021502.1–021502.8. *(p. 6)*
doi:10.1115/1.4004183

Tay-Wo-Chong, L., T. Komarek, R. Kaess, S. Foeller, and W. Polifke. 2010. "Identification of flame transfer functions from LES of a premixed swirl burner." In *Proceedings of the ASME Turbo Expo, paper GT2010-22769*, 623–35. New York: American Society of Mechanical Engineers. *(p. 6)*
doi:10.1115/GT2010-22769

Tay-Wo-Chong, L. and W. Polifke. 2012. "LES-based study of the influence of thermal boundary condition and combustor confinement on premix flame transfer functions." In *Proceedings of the ASME Turbo Expo, paper GT2012-68796*, New York: American Society of Mechanical Engineers. *(p. 6)*

Tran, N., S. Ducruix, and T. Schuller. 2009a. "Damping combustion instabili-

ties with perforates at the premixer inlet of a swirled burner." *Proc. Combust. Inst.* 32 (2): 2917–24. *(pp. 41, 220)*
doi:10.1016/j.proci.2008.06.123

Tran, N. "Influence de la condition limite acoustique amont sur les instabilités de combustion de grande amplitude : conception d'un système robuste de contrôle d'impédance." PhD diss., Ecole Centrale Paris, 2009. *(pp. 39, 64, 182, 183, 196, 198, 199, 218, 220, 232)*

Tran, N., S. Ducruix, and T. Schuller. 2009b. "Passive control of the inlet acoustic boundary of a swirled burner at high amplitude combustion instabilities." *J. Eng. Gas Turb. Power* 131 (5): 051502.1–051502.7. *(pp. 41, 182, 203, 209, 220)*
doi:10.1115/1.3078206

Wicker, J., W. Greene, S.-I. Kim, and V. Yang. 1996. "Triggering of longitudinal combustion instabilities in rocket motors: nonlinear combustion response." *J. Propul. Power* 12 (6): 1148–58. *(p. 6)*
doi:10.2514/3.24155

Wolf, P., R. Balakrishnan, G. Staffelbach, L. Y. M. Gicquel, and T. Poinsot. 2012. "Using LES to study reacting flows and instabilities in annular combustion chambers." *Flow Turbul. Combust.* 88 (1-2): 191–206. *(p. 6)*
doi:10.1007/s10494-011-9367-7

Zinn, B. T. and L. Narayanaswami. 1982. "Application of the impedance tube technique in the measurement of the driving provided by solid propellants during combustion instabilities." *Acta Astronaut.* 9 (5): 303–15. *(p. 64)*
doi:10.1016/0094-5765(82)90004-2

Zinn, B. and M. Lores. 1971. "Application of the galerkin method in the solution of non-linear axial combustion instability problems in liquid rockets." *Combust. Sci. Technol.* 4 (1): 269–78. *(p. 4)*
doi:10.1080/00102207108952493

Index

Symbols

A

B

E

F

G

H

I

J

L

M

N

O

P

R

S

T

U

V

W